Finite Element Modeling of the Foot

Vara Isvilanonda

A dissertation
submitted in partial fulfillment of the
requirements for the degree of

Doctor of Philosophy

University of Washington
2015

Reading Committee:
William R. Ledoux, Chair
Randal P. Ching
Per G. Reinhall

Program Authorized to Offer Degree:
Department of Mechanical Engineering

University of Washington

Abstract

Finite Element Modeling of the Foot

Vara Isvilanonda

Chair of the Supervisory Committee:
Affiliate Associate Professor William R. Ledoux
Departments of Mechanical Engineering and Orthopaedics & Sports Medicine

Finite element (FE) foot modeling is a useful tool for investigating foot and ankle biomechanics. Such models can provide insight into internal soft tissue behavior of the foot and are ideal for conducting parametric analyses. Many of the previous FE foot models simulated quasi-static loads and imposed major simplifications on anatomy and material properties, which could compromise their accuracy and usefulness. The purpose of this study was to develop and validate two subject-specific FE foot models (normal and diabetic) capable of simulating both quiet stance (quasi-static loading) and the stance phase of gait (dynamic loading), and to explore the plantar pressure and internal soft tissue stress distribution under these two loading conditions.

The models included subject-specific bone, skin, muscle and fat anatomy obtained from CT and MR imaging data. Subject-specific hyperelastic material properties for each soft tissue were determined from inverse FE analysis of gated MRI compression experiments. Ligaments, tendons, and joint cavities were modeled more accurately based on the medical images. Four regions of the plantar aponeurosis were modeled with non-linear material properties obtained from cadaveric mechanical testing. The models were validated with *in vivo* experimental data collected in-house and with literature data under three loading conditions: passive compression, quiet stance, and the stance phase of gait, by analyzing bone kinematics, ground reaction forces (GRFs), plantar pressure, plantar aponeurosis force and ankle joint force.

The subject-specific models were capable of simulating physiologic quiet stance and dynamic gait conditions. The vertical GRF, plantar pressure distribution, bone kinematics, plantar aponeurosis force and ankle joint force were reproduced in the model. The von Mises and hydrostatic stress predictions provided insight into the specific location and time of the peak internal stress, which suggested regions of elevated injury risk as well as possible mechanisms of injury. The model's ability to effectively perform parametric analyses was demonstrated by investigating the effect of soft tissue simplifications on plantar pressure and internal stress. The protocols and mechanical test data outlined in this study will serve as a guide line for future FE foot model development. The models of the normal and diabetic subject developed in this dissertation are useful tools for exploring and generating clinically effective treatments for foot and ankle pathology.

TABLE OF CONTENTS

LIST OF FIGURES

LIST OF TABLES

ACKNOWLEDGEMENTS

I would like to express my sincere gratitude to my advisor, Dr. William Ledoux, for his guidance and support throughout my doctoral studies. Working with you has taught me innumerable lessons that help me achieve my long-term career goals.

I would like to thank my committee members: Professor Duane Storti , Professor Per Reinhall, Professor Peter Mackenzie-Helnwein, Professor Randal Ching, and Professor Wanpracha Chaovalitwongse, for their insightful discussions, comments and hard questions.

I would also like to thank Joseph Iaquinto and Matthew Kindig for their helpful ideas in every weekly research meeting, and their assistant in writing this manuscript. My thanks also go to Dr. Baocheng Chu, Dr. David Haynor, Professor Peter Cavanagh, Eric Whittaker, Evan Dengler, Evan Williams, Jane Shofer, Michael Fassbind, Michael Stebbins, QuocBao Vu, and Shruti Pai. This work would not have been possible without your contributions.

Finally and most importantly, I am truly grateful to have encouragement and emotional support from my family, especially my parents, Somporn and Orawan. Your stories about Seattle and UW inspired me to return to this rainy city. To my sister Wanaporn, brother Warin and fiancée Suchada, I thank you for being in my life.

This work was funded in part by the Veteran Affairs Research and Development grant A6973R.

DEDICATION

To my parents for their love, encouragement and support.

Chapter 1. Introduction

1.1 Prevalence and factors influencing diabetic foot ulceration

Diabetic foot ulceration is one of the leading causes of non-traumatic lower-limb amputations (LLA) in the United States (US). More than 60% of 73,000 LLA in 2010 were performed in the diabetic population (CDCP, 2014); 84% of these were preceded by ulceration (Pecoraro et al., 1990). The increasing diabetic population—9.3% of the US population in 2012 (CDCP, 2014) and 33% projected by 2050 (Boyle et al., 2010))—speaks to the prevalence and risk of LLA in the population. Preventing foot ulceration in this high-risk group can be a very effective strategy to reduce the number of LLA (Apelqvist and Larsson, 2000; Pecoraro et al., 1990).

Diabetic foot ulcers are often caused by multiple factors, including peripheral neuropathy (nerve damage) as a result of prolonged exposure to high levels of blood glucose (James A. Birke, 1991; Singh et al., 2005). The results from diabetic neuropathy are loss of sensation, intrinsic muscle weakness and foot deformity. These complications often result in elevated plantar pressure and foot injury (Bus et al., 2005; James A. Birke, 1991) and due to the sensory loss, such early signs of likely ulcer formation go unnoticed in the patient. When subjected to elevated plantar pressure, the tissue will eventually develop calluses, an important indication of pre-ulcerative lesion in the neuropathic foot (Edmonds and Foster, 2006; Murray et al., 1996). It is believed that this thick callused region injures the deeper soft tissue and causes ulceration (Figure 1.1) (Edmonds and Foster, 2006; Murray et al., 1996). Studies have also shown that diabetic subjects have abnormal soft tissue micro structures (Wang et al., 2011), soft tissue atrophy/migration (Bus et al., 2004) and altered material properties (Pai and Ledoux, 2010).

Coupled with a compromised vascular network (and thus reduced healing and diminished immune response) these aforementioned mechanical factors are believed to contribute to diabetic foot ulcer formation. However, difficulties gaining insight into the internal soft tissue behavior in *in vivo* or *in vitro* experiments have limited researchers' understanding of the development of diabetic foot ulcers.

Figure 1.1: (left) Callus over the first metatarsal head, (center) the roof of the blister and the associated callus are cut away, (right) ulcer is revealed underneath. *(adapted from (Edmonds and Foster, 2006)).*

1.2 Finite element model of the foot

Finite element (FE) models have been used to explore the biomechanics of normal (Chen et al., 2010; Cheung et al., 2004, 2006a) and diabetic feet (Cheung et al., 2005; Gefen, 2003). The models overcome limitations in *in vitro* and *in vivo* studies by allowing for force, displacement and boundary conditions to be prescribed and measured precisely. Results that are difficult or impossible to measure in experiments (e.g., internal stress, strain and deformation) can easily be quantified and visualized from the simulation. Further, such modeling allows for very controlled, repeatable testing.

The general use of FE foot models are for predicting plantar pressures (Chen et al., 2012; Chen et al., 2003; Chen et al., 2010; Gefen, 2003; Guiotto et al., 2014; Yu et al., 2008), internal stresses (Chen et al., 2010; Cheng et al., 2008; Cheung et al., 2005; Gefen, 2003; Lin et al., 2014; Thomas et al., 2003a; Yu et al., 2008) and performing parametric analyses (Chen et al., 2003; Cheung et al., 2004; Gefen, 2002; Iaquinto and Wayne, 2011; Isvilanonda et al., 2012). Clinical applications, such as designing custom pressure-relieving insoles, predicting injury-prone areas, and optimizing surgical techniques, are a few of the many areas where FE foot models can be used for personalized medicine to improve the effectiveness of diabetic foot ulcer prevention.

Many of the previously-developed FE foot models incorporate skin, fat and muscle into a homogeneous generic soft tissue (Chen et al., 2001; Chen et al., 2010; Cheng et al., 2008; Cheung and Zhang, 2008; Guiotto et al., 2014; Qiu et al., 2011; Spyrou and Aravas, 2011). Further, they tend to use *in vivo* material properties that represent some population average or representative value. These simplifications (i.e., generic soft tissue, non subject-specific material) can lead to substantial error in the predicted plantar pressures (Erdemir et al., 2006; Guiotto et al., 2014; Petre et al., 2013; Spears et al., 2007; Spirka et al., 2014).

In addition, the models often assume fused distal joints (Chen et al., 2012; Cheung and Zhang, 2008; Guiotto et al., 2014) and simplify materials and anatomy for ligaments and plantar aponeurosis (Chen et al., 2001; Chen et al., 2010; Chen et al., 2014b; Cheung and Zhang, 2008; Guiotto et al., 2014; Qiu et al., 2011). These oversimplifications can potentially cause non-physiologic bone kinematics and force distributions (Actis et al., 2006; Guiotto et al., 2014). Moreover, most simulations are performed and validated under quasi-static conditions, such as passive foot compression, quiet stance or fixed gait positions, using implicit FE analysis (Camacho et al., 2002; Chen et al., 2001; Chen et al., 2010; Chen et al., 2014b; Cheng et al., 2008; Cheung and Zhang, 2008; Garcia-Aznar et al., 2009; Gefen, 2002; Guiotto et al., 2014; Qiu et al., 2011; Sun et al., 2011; Wu, 2007). These types of (implicit) quasi-static analyses require that the model satisfies an equilibrium condition at every iteration. This requirement substantially limits the model’s usage and accuracy, as the foot is more likely to experience higher loads and deformations during dynamic activities compared to the quasi-static condition.

1.3 Objective

Simplifications to the FE foot models can negatively affect analysis results. The prediction accuracy can be improved by utilizing subject-specific anatomy and material properties and avoiding unnecessary model simplifications. The goal of this dissertation is to develop and validate two subject-specific FE foot models (healthy/normal and diabetic). The model development methodology as well as *in vivo* and *in vitro* experimental data will be presented. Improvements from prior models in terms of subject-specific inputs (anatomy, soft tissue material properties, bone kinematics), highly detailed model components (plantar aponeurosis, ligament, tendon and joint articulation) and thorough validation protocols (static and dynamic conditions, experimental and literature data) will be implemented. The internal stresses and plantar pressures exhibited by the diabetic foot during gait will be investigated and compared to the normal foot. The goal will be accomplished in four Specific Aims:

Specific Aim 1

To improve and utilize the cadaveric FE foot model previously created from our group. Knowledge and limitations from this work will be used to design experiments to obtain required model inputs (Specific Aim 2 and 3) and develop the subject-specific FE foot models (Specific Aim 4).

Specific Aim 2

To quantify the material properties of a cadaveric plantar fat pad and *in vivo* plantar skin, fat and muscle. The material properties will be determined from both isolated tissue compression (*in vitro*) and hindfoot gated MRI compression (*in vivo*) experiments using an inverse FE analysis. Ogden hyperelastic coefficients of the cadaveric subcalcaneal fat and subject-specific (normal and diabetic) hindfoot skin, fat and muscle will be determined.

Specific Aim 3

To characterize the regional cross-sectional area, stress-strain relationships, and material properties of the plantar aponeurosis. The functional contribution of four regions of the plantar aponeurosis (proximal middle, distal middle, medial and lateral) will be determined from cadaveric specimens such that this structure is better represented in the FE foot model.

Specific Aim 4

To develop subject-specific FE foot models of a healthy/normal and a diabetic feet. A representative (gold standard) FE foot model will be created from a healthy living subject (instead of a cadaveric foot). Specific improvements in model components (plantar aponeurosis, ligament, joint cavity/contact, and subject-specific plantar soft tissue material properties) and validation protocols (static and dynamic) will be implemented. The diabetic foot model will be based on the gold standard model and customized to the diabetic subject by utilizing subject-specific anatomy and soft tissue material properties. Ligament and plantar aponeurosis force-deformation curves, tendon paths and joint contact offsets will be fine-tuned based on the subject’s bone anatomy (taken from medical images). The normal and diabetic foot models will be validated and used to explore plantar pressures and internal stresses during gait.

1.4 Significance of the studies

Preventing foot ulcers in the diabetic population can be a very effective strategy to reduce the incidence of LLA. This study aims to contribute to the fundamental knowledge of diabetic foot ulceration by introducing computer models that can estimate soft tissue internal stresses and other important biomechanical measurements (e.g., bone kinematics, joint force, and ligament tension) during gait. The published model development protocols and mechanical test data will be beneficial for improving existing FE foot models and reducing unnecessary model simplifications.

1.5 Chapter layout

This dissertation is organized into 8 chapters. Chapter two includes relevant background on foot anatomy, the influence of diabetes on plantar soft tissue, previously-developed FE models of the foot (including inverse FE analysis), and mechanical testing of the plantar aponeurosis. Chapter 3 to 7 are written in the form of self-contained manuscripts. Chapter 3 was previously published in the Clinical Biomechanics. Chapter 4 and 5 will be submitted to the Journal of Biomechanics, Chapter 6 to the Clinical Biomechanics, and Chapter 7 to the Annals of Biomedical Engineering. The first study (Chapter 3) focuses on the development and utilization of the cadaveric FE foot model. The model is used to determine the effectiveness of two surgical procedures for correcting the clawed hallux deformity. From this first study, the potential limitations of the cadaver model, and areas for improvement, are identified. The methodology behind developing an entirely new FE foot model of a healthy normal subject is discussed in the subsequent chapters. The soft tissue material property inputs are determined utilizing both mechanical testing (inverse FE optimization (Chapter 4 and 5; plantar soft tissue) and Chapter 6; plantar aponeurosis). The knowledge gained from Chapters 4 to 6 are used in Chapter 7 to develop normal and diabetic subject-specific FE models. The models are used to predict plantar pressure and internal soft tissue stresses in normal and diabetic feet during gait. Chapter 8 includes a final discussion, summary and future work. Appendix I contains detailed information about the response surface optimization method used in the inverse FE analysis. Appendix II gives an overview of the digital image correlation (DIC) technique used in the plantar aponeurosis experiments. Appendix III describes calculation of the Ogden hyperelastic constitutive equation from the strain energy density function. Appendix IV provides mesh convergence analysis results.

Chapter 2. Literature review

The human foot is a complex structure designed for balance and mobility. It is comprised of 26 bones, 33 joints, approximately 110 ligaments, 12 extrinsic muscle tendons and 20 intrinsic muscles, as well as the skin, plantar fat, cartilage, fascia, nerves, and blood vessels.

2.1 Functional anatomy of the foot

2.1.1 Bones

The foot bones can be anatomically divided into three groups; the hind-, mid- and forefoot (Figure 2.1a). The hindfoot is composed of the talus and the calcaneus; the midfoot includes the navicular, cuboid and three cuneiforms (medial, intermediate and lateral); the forefoot consists of five sets of metatarsals, proximal, and distal phalanges (Gould, 1988). The second to fifth rays also have intermediate phalanges located between the proximal and the distal phalanges. Foot bones are aligned such that they form the medial longitudinal arch in the sagittal plane (Figure 2.1b)(Sarrafian, 1993). When loaded vertically at the apex, the arch deflection is mainly limited by tension in the plantar ligaments, intrinsic musculature, and the plantar aponeurosis (Figure 2.1c).

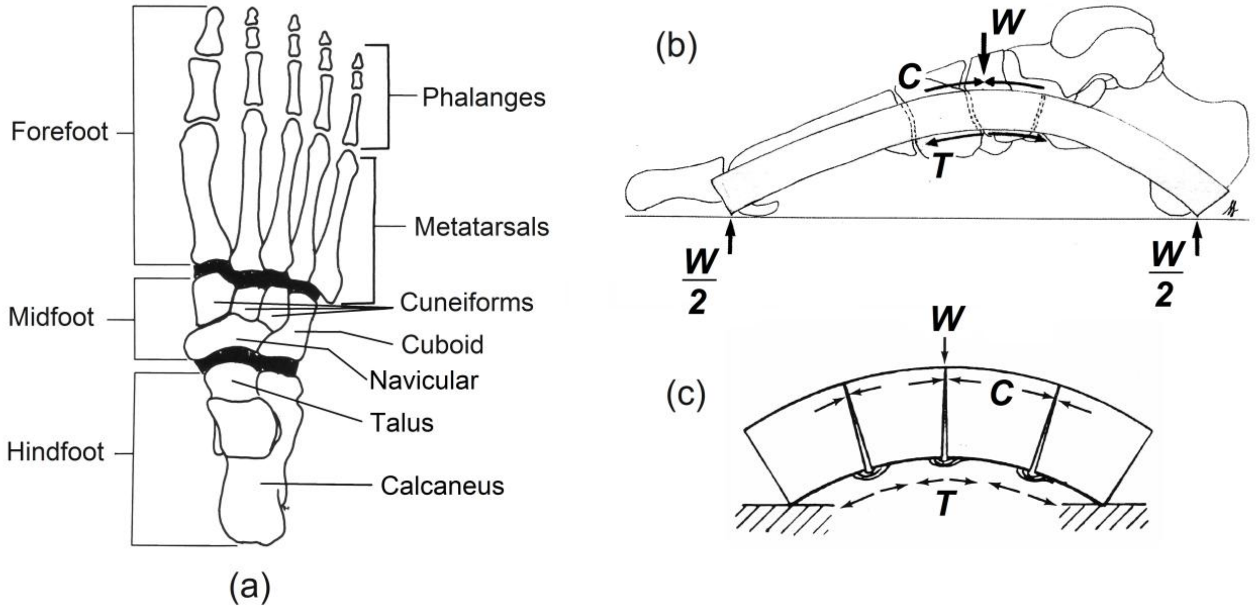

Figure 2.1: (a) Dorsal view of the foot showing the forefoot, the midfoot and the hindfoot. (b) Body weight (*W*) generates compressive force (*C*) on the superior aspect and tensile force (*T*) on the inferior aspect of the foot arch. (c) To prevent arch collapse, concave surfaces of the arch are bounded by strong ligaments similar to the plantar aspect of the foot. (*adapted from Gould, 1988 and Sarrafian, 1993*).

2.1.2 Ligaments and tendons

Ligaments and tendons are comprised of strong fibrous connective tissue that bears the tensile load in the direction parallel to the fibers. Ligaments connect one bone to another bone across a joint or joints, stabilize the articular surfaces and guide the joint kinematics. Tendons, on the other hand, connect muscle to bone and transmit a muscle's contractile force to bone. Due to anatomical muscle insertion locations, muscle forces generate torque across joints – this torque commonly results in motion or in joint stabilization. Twelve extrinsic foot muscles are located in the lower leg (Table 2.1). The tendons from these muscles continue distal to the ankle joint and insert into the foot bones. The extrinsic muscle tendons of the foot can be categorized (roughly) by function into two groups: dorsiflexors and plantar flexors. Ten extrinsic muscle tendons are included in this study; the peroneus tertius and plantaris, which are quite small, were excluded.

Table 2.1: Extrinsic muscles of the foot (Richardson, 2011; Sarrafian, 1993).

Muscle	Origin	Insertion	Function
Dorsiflexors			
Tibialis anterior (TA)	Upper half of the tibia lateral shaft and interosseous membrane	Inferomedial aspect of the first metatarsal base and medial dorsal surface of the medial cuneiform	Dorsiflex and invert the ankle
Extensor hallucis longus (EHL)	Anterior surface of the fibula and interosseous membrane	Dorsal base of the first distal phalanx	Dorsiflex the hallux and the ankle
Extensor digitorum longus (EDL)	Lateral condyle of the fibula, upper 60-75% of the medial fibula shaft surface, upper part of the interosseous membrane	Splits into 4 distal slips after inferior extensor retinaculum. Each slips inserts on the dorsum of the middle phalanx and the capsule of the proximal interphalangeal joint of toes 2-5. Each slip also inserts on the dorsal capsule of the distal interphalangeal joint and the base of the distal phalanx of each toe	Extend toes 2-5 and dorsiflex the ankle
Peroneus tertius (PT)	Arises with the EDL muscle from the medial fibula shaft surface and the anterior intermuscular septum	Superior surface of the fifth metatarsal base	Works with EDL to dorsiflex, evert and abduct the ankle
Plantar flexors			
Peroneus longus (PL)	Head of the fibula, upper 50-60% of the lateral fibula shaft surface	Plantar posterolateral aspect of the medial cuneiform, lateral side of the first metatarsal base	Evert and plantar flex the ankle
Peroneus brevis (PB)	Upper 60% of the inferolateral fibula surface	Lateral surface of the styloid process of the fifth metatarsal base	Evert and plantar flex the ankle
Tibialis posterior (TP)	Posterior aspect of the interosseous membrane, upper 60% of the medioposterior fibula surface, superoposterior aspect of the tibia	Navicular tuberosity, medial and intermediate cuneiforms, plantar surface of the metatarsals 2-4	Invert, adduct and plantar flex the ankle
Flexor hallucis longus (FHL)	Lower 60% of the posterior fibula surface, lower part of the interosseous membrane	Plantar surface of the base of the first distal phalanx	Plantar flex the hallux and the ankle
Flexor digitorum longus (FDL)	Posterior surface of the tibia distal to the popliteal line	Splits into four slips after the plantar medial intermuscular septum. Each slip inserts on the base of the distal phalanges (toes 2-5)	Plantar flex toes 2-5 and the ankle
Gastrocnemius and Soleus (Achilles)	Gastrocnemius: medial head from the posteromedial femoral condyle; Lateral head from the lateral femoral condyle Soleus: posterior aspect of the fibular head, upper 25-30% of the posterior fibula surface, middle 30% of the medial tibial shaft	Middle 1/3 of the posterior calcaneal surface	Powerful ankle plantar flexor
Plantaris	Inferolateral supracondylar line of the femur	Posterior calcaneal surface medial to the Achilles tendon	Plantar flex the ankle

The intrinsic muscles of the foot are relatively small muscles whose origin and insertion are both within the foot itself. These muscles produce substantially lower forces when compared to the extrinsic musculature. Their main function is to maintain stability of the foot arch and toes. Several important intrinsic muscles, from a stability standpoint, are the abductor hallucis longus, flexor hallucis brevis, flexor digitorum brevis and abductor digiti minimi (Gould, 1988). The intrinsic muscle weakness/imbalance is associated with Charcot-Marie-Tooth disease (Chung et al., 2008), clawed hallux deformity (Myerson and Shereff, 1989), claw toe deformity (Myerson and Shereff, 1989), hammer toe deformity (Kwon et al., 2009; Myerson and Shereff, 1989) and hallux valgus (Arinci Incel et al., 2003; Hoffmeyer et al., 1988).

2.1.3 Plantar aponeurosis

The plantar aponeurosis, or plantar fascia, is a strong fibrous tissue located at the plantar aspect of the foot deep to the plantar fat and superficial to the intrinsic muscle layer. The plantar aponeurosis can be divided into medial, central and lateral components (Figure 2.2) (Sarrafian, 1993). The central plantar aponeurosis, which is the most robust portion, originates from the posteromedial calcaneal tuberosity and divides into five longitudinal segments at the mid metatarsal level (Bojsen-Moller and Flagstad, 1976; Chen et al., 2014a; Hedrick, 1996; Moraes Do Carmo et al., 2008; Sarrafian, 1993). Towards the forefoot, the fibers blend into the metatarsophalangeal joint complex and the subcutaneus tissue.

Tensile force within the plantar aponeurosis is essential in maintaining stability of the foot arch during weight bearing (Arangio et al., 1997; Hicks, 1954). Hicks (1954) described the biomechanical function of the plantar aponeurosis by comparing it to a windlass mechanism (Figure 2.2). The drum of the windlass is the metatarsal head, the handle is the proximal phalanx and the cable attached to the handle is the plantar aponeurosis (Hicks, 1954; Sarrafian, 1993). Dorsiflexion of the toes winds the plantar aponeurosis around the metatarsal heads, thus decreases the distance L, increases arch height H and creates tension in the plantar aponeurosis (Figure 2.2). During push-off phase of gait (i.e., peak toe dorsiflexion), the foot is propelled forward with the help from potential energy stored in the plantar aponeurosis. The reverse windlass mechanism also benefits foot stability: as body weight is applied to the ankle, the foot arch deforms (*L* increases, *H* decreases). Tension in the plantar aponeurosis helps maintain proper arch height while simultaneously plantar flexing the toes (reverse windlass), creating a gripping action of toes to the ground.

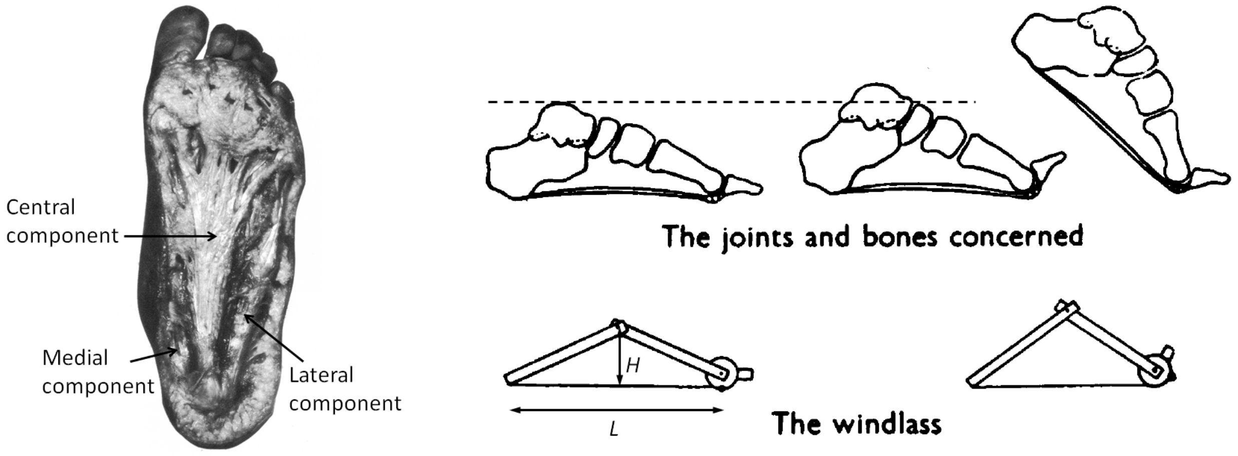

(a) (b)

Figure 2.2: (a) Planter view of the foot (skin and fat removed) showing medial, central and lateral components of the plantar aponeurosis (*adapted from Sarrafian, 1993*). (b) Plantar aponeurosis and the windlass mechanism (*adapted from Hicks, 1954*).

2.1.4 Articular cartilage and joint capsule

Articular cartilage is composed of a dense extracellular matrix which contains water, collagen and proteoglycans. These components create a unique biphasic (fluid and solid) mechanical system. The main function of the articular cartilage is to provide a smooth and lubricated surface for load transfer between bones (Sophia Fox et al., 2009). In order to keep the lubricated synovial fluid in position, a joint capsule forms a seal around the joint. The fibrous connective tissue of the joint capsule provides stability by limiting excessive joint movement (Ralphs and Benjamin, 1994).

2.1.5 Plantar fat

Plantar fat is generally comprised of fat cells that are held together by elastic septa (i.e., fat filled microchambers and macrochambers). The plantar fat pad is specifically structured to serve as an efficient shock absorber and cushioning layer to the sole of the foot (Sarrafian, 1993). Previous studies suggested that age (increase in thickness and stiffness, decrease in elasticity), foot deformity (decrease thickness) and diabetes (increase stiffness, decrease elasticity) can affect the plantar fat pad anatomy and material properties (Bus et al., 2004; Hsu et al., 2009; Hsu et al., 1998; Pai and Ledoux, 2010). The effect of diabetes on plantar fat pad is further discussed in Section 2.2.3.

2.1.6 Plantar skin

Plantar skin is designed to provide sensory feedback and protect the foot from injury and infection. The skin is comprised of epidermis and dermis layers, mostly made of collagen and elastin fibers intertwined in a matrix. The average total plantar skin thickness is 1.82±0.67 mm and the mean epidermis and dermis layers are 1.13±0.61 mm and 0.67±0.32 mm, respectively (Wang et al., 2011).

2.2 Diabetes and the foot

2.2.1 Prevalence and cost of diabetic foot ulceration

Diabetes is one of the leading causes of non-traumatic LLA in the US. According to 2009-2012 data, approximately 9.3% of the US population suffer from diabetes. The projected prevalence is 33% by 2050 (Boyle et al., 2010). Approximately 15% of the people with diabetes are expected to have a foot ulcer at least once in their life time (Singh et al., 2005). About 84% of all diabetic foot ulcers may ultimately require amputation (Pecoraro et al., 1990). In 2010, about 73,000 non-traumatic LLA were performed in people diagnosed with diabetes.

The annual cost of diabetes in the US was more than $245 billion in 2012 (CDCP, 2014). At least 33% of the direct costs were associated with the treatment of foot ulcers, totaling $39 billion in 2010 (Driver et al., 2010). Better care and education can be effective strategies in preventing foot ulcer and lower the amputation rate (Apelqvist and Larsson, 2000). Data from 1996-2008 suggests that the frequency of LLA in the diabetic population declined by 3-fold (Li et al., 2012); however, this rate is still 8 times higher than the non-diabetic population.

2.2.2 Pathway to diabetic foot ulcer

Diabetic foot ulcer is caused by multiple factors, but one of the most common pathways is neuropathy resulting in minor trauma that develops into ulceration and, in some cases, leads to amputation (Dinh and Veves, 2005; Pecoraro et al., 1990). People with diabetes frequently suffer from neuropathy which impairs sensation of the feet (Guyton and Saltzman, 2001) and causes foot deformities (Dinh and Veves, 2005). Furthermore, this population also has poor blood supply to the foot (ischemia) due to peripheral vascular disease. The combination of insensate feet, abnormal plantar pressure and joint deformities leads to calluses and soft tissue break down (ulcer), especially at bony prominences. Restricted blood flow further complicates and slows wound healing. If the tissue oxygenation is inadequate, injured tissue can become necrotic and infected, preventing further ulcers from healing (Guyton and Saltzman, 2001).

2.2.3 Effect of diabetes on soft tissue and plantar pressure

Diabetic plantar soft tissue differs from normal tissue at both micro and macro levels (Cheung et al., 2006b; Gefen et al., 2001a; Hsu et al., 2009; Pai, 2011; Pai and Ledoux, 2011; Pai and Ledoux, 2010, 2012; Wang et al., 2011; Zheng et al., 2000). Studies have shown that diabetic soft tissue has damaged collagen fibrils (Hsu et al., 2002) and thicker elastic septae and dermis (Wang et al., 2011). Further, diabetic tissue suffers from increased stiffness (Cheung et al., 2006b; Hsu et al., 2009; Pai and Ledoux, 2010, 2012), especially under the first metatarsal head (Gefen et al., 2001a; Zheng et al., 2000), and reduced thickness (Zheng et al., 2000); and greater hardness at the plantar skin (Thomas et al., 2003b). These changes are associated with elevated plantar pressure in the diabetic neuropathic population (Bus et al., 2004; Bus et al., 2005).

Previous FE foot simulations confirmed that an increase in soft tissue stiffness (to emulate diabetic tissue) results in elevated plantar pressure (Cheung et al., 2005; Thomas et al., 2003a). These highly simplified simulations suggested that internal stresses are also higher in models with increased plantar soft tissue stiffness (Gefen, 2003; Thomas et al., 2003a).

2.3 Finite element foot models

Finite element models of the human foot have been used in a wide range of applications such as predicting surgery outcomes (Cheung et al., 2004; Gefen, 2002; Iaquinto and Wayne, 2011), designing pressure relieving insoles (Budhabhatti et al., 2009; Chen et al., 2003; Cheung and Zhang, 2005; Cheung and Zhang, 2008; Erdemir et al., 2005; Goske et al., 2006; Spears et al., 2007) and investigating internal soft tissue stresses (Chen et al., 2010; Gefen, 2003; Lin et al., 2014). The model complexity ranges from two-dimensional (2D) (Gefen, 2003; Halloran et al., 2010; Qian et al., 2013; Wu, 2007), three dimensional (3D) rigid body (Iaquinto and Wayne, 2011; Xu et al., 2011) to 3D deformable simulations (Camacho et al., 2002; Chen et al., 2001; Chen et al., 2010; Cheng et al., 2008; Cheung and Zhang, 2008; Dengler, 2008; Garcia-Aznar et al., 2009; Guiotto et al., 2014; Isvilanonda et al., 2012; Qiu et al., 2011; Spyrou and Aravas, 2011; Sun et al., 2011).

The majority of the models obtained foot anatomy from computed tomography (CT) and/or magnetic resonance (MR) imaging scans and utilized linear tetrahedral elements to model the component geometry (Chen et al., 2012; Chen et al., 2001; Cheng et al., 2008; Cheung and Zhang, 2008; Dengler, 2008; Garcia-Aznar et al., 2009; Guiotto et al., 2014; Iaquinto and Wayne, 2011; Isvilanonda et al., 2012; Qiu et al., 2011; Spyrou and Aravas, 2011; Sun et al., 2011; Xu et al., 2011). Soft tissue is often represented by a nearly incompressible hyperelastic material (Chen et al., 2001; Chen et al., 2010; Cheng et al., 2008; Cheung and Zhang, 2008; Dengler, 2008; Guiotto et al., 2014; Qiu et al., 2011; Spyrou and Aravas, 2011).

In order to reduce model complexity and improve stability, the material properties and anatomy of the plantar soft tissue have often been simplified by grouping skin, fat and muscle into a homogeneous generic soft tissue (Chen et al., 2012; Chen et al., 2001; Cheng et al., 2008; Cheung and Zhang, 2008; Guiotto et al., 2014; Qiu et al., 2011; Spyrou and Aravas, 2011). Joint contacts are often replaced by fused bones (i.e., no contact) or a single cartilage plug (Chen et al., 2012; Chen et al., 2001; Chen et al., 2014b; Cheng et al., 2008; Cheung and Zhang, 2008; Guiotto et al., 2014; Qiu et al., 2011; Spyrou and Aravas, 2011). Foot ligaments are frequently represented by tension-only truss elements (Chen et al., 2001; Chen et al., 2014b; Guiotto et al., 2014; Lin et al., 2014) and the stiffness is assumed to be similar in all locations. Plantar aponeurosis is simplified to either tension-only truss elements connecting the hindfoot to each of the metatarsal heads (Chen et al., 2010; Cheung and Zhang, 2008) or shell/solid elements with constant thickness (Chen et al., 2012; Chen et al., 2014b). Extrinsic muscle forces, with the exception of the Achilles tendon force, are commonly ignored (Chen et al., 2010; Chen et al., 2014b; Guiotto et al., 2014) or directly applied to bones at the insertion sites (Cheung and Zhang, 2008).

Most FE foot models are validated by comparing the predicted plantar pressure to experimental measurements. Simulations are performed under quasi-static conditions, such as passive foot compression, quiet stance or fixed gait positions using an implicit FE solver (Camacho et al., 2002; Chen et al., 2001; Chen et al., 2010; Chen et al., 2014b; Cheng et al., 2008; Cheung and Zhang, 2008; Garcia-Aznar et al., 2009; Gefen, 2002; Guiotto et al., 2014; Qiu et al., 2011; Sun et al., 2011; Wu, 2007). A summary of the current state-of-the-art FE foot models is given in Table 2.2a and b.

Table 2.2a: Overview of published highly-detailed finite element foot models: model components.

Author	Scan/ Subject‡	Material Model, Element Type†						Element interaction
		Bone	Cartilage	Soft tissue	Ligament	Tendon	Plantar aponeurosis	
Chen W. P. et al. (2003; , 2001)	CT; Male; age 24	Elastic; tetrahedral	Elastic; tetrahedral	Elastic; tetrahedral	Elastic; 1D tension only (1 ligament, 3 elements)	n/a	Elastic; 1D tension only (5 elements)	Single piece of cartilage without contact at MTPJ and IPJ; Other bones are fused and divided into medial/lateral columns; Frictional foot-ground contact ($\mu = 0.3$)
Cheung et al. (2006a; , 2005; , 2008)	MR; Male; age 26; weight 700N	Elastic; tetrahedral	Elastic; tetrahedral	Hyperelastic^2; tetrahedral	Elastic; 1D tension only (72 ligaments)	n/a	Elastic; 1D tension only (5 elements)	Bone-soft tissue share nodes; Single piece cartilage without contact at MTPJ; Frictionless bone contact for other joints; Frictional foot-ground contact ($\mu = 0.6$)
Cheng et al. (2008)	CT; Male; age 30	Elastic; 10-noded tetrahedral	Elastic; 10-noded tetrahedral	n/a	Elastic; 1D tension only (67 ligaments)	n/a	Hyperelastic^4; 8-noded hexahedral	Frictionless MTPJ and plantar fascia- MTPJ contacts; Single piece of cartilage without contact for other joints
Dengler E. (2008), Isvilanonda et al. (2012)	CT, MR; Cadaver; Male; age 44; weight 823 N	Rigid; tetrahedral	Tetrahedral; Elastic in D.E.; Rigid in I. et al.	Hyperelastic^1 fat and generic soft tissue; tetrahedral	Non-linear; 1D tension only (107 ligaments in D.E., 101 in I. et al.)	Non-linear; 1D seatbelt (7 tendons in D.E., 8 in I. et al.)	Non-linear; 1D spring (6 elements in D.E., 15 in I. et al.)	Bone-soft tissue and fat-soft tissue share nodes; Frictional cartilage-cartilage ($\mu_s = 0.1$, $\mu_k = 0.085$) and foot-ground ($\mu = 0.44$ D.E., 0.6 I. et al.) contacts
Budhabhatti et al. (2009)	MR; Male; weight 945N	Rigid; hexahedral	n/a	Hyperelastic ^{1}; hexahedral	n/a	n/a	n/a	Bone-soft tissues share nodes; MTPJ and IPJ defined by connector elements; Frictional foot-ground contact ($\mu = 0.5$)
Garcia-Aznar, J. M. et al. (2009)	CT; Male; age 36	Elastic; tetrahedral (cortical/trabecular)	Elastic; tetrahedral	n/a	Elastic; 1D tension only (483 elements)	n/a	Elastic; 1D tension only	Single piece of cartilage without contact for every joint. Distinct material for cortical and trabecular bone
Chen W. M. et al. (2012; , 2010)	CT; Male; age 26	Elastic; tetrahedral	n/a	Hyperelastic^1; tetrahedral	Elastic; 1D tension only (134 ligaments)	Elastic; 1D tension only (6 tendons)	Elastic; 1D tension only (5 elements)	Bone-soft tissues share nodes; Bone-bone frictionless contact (i.e. no cartilage); Frictional foot-ground contact ($\mu = 0.5$)

Table 2.2a: (Cont'd) Overview of published highly-detailed finite element foot models: model components.

Author	Scan/ Subject‡	Material Model, Element Type†						Element interaction
		Bone	**Cartilage**	**Soft tissue**	**Ligament**	**Tendon**	**Plantar aponeurosis**	
Chen, Y. N. et al. (2014b)	CT; Male; age 30	Rigid; shell	Elastic; 8-noded hexahedral	n/a	Elastic; shell	n/a	Elastic; hexahedral	Frictionless ankle and MTPJ contacts; Single piece cartilage without contact for other joints
Guiotto A. et al., (2014)	CT, MR; 2 Males; age 27, 61; weight 598, 775 N	Rigid; tetrahedral	Elastic; tetrahedral	Hyperelastic[2]; tetrahedral	Elastic; 1D tension only	Elastic; 1D tension only	Elastic; 1D tension only	Bone-soft tissue share nodes; Single piece of cartilage without contact at hindfoot-midfoot and midfoot-forefoot joints; Other joints are fused; Frictional foot-ground contact ($\mu = 0.6$)
Lin et al. (2014)	MR; Male; age 28; weight 960N	Rigid; hexahedral	Elastic; hexahedral	Hyperelastic [1]; hexahedral	Elastic; 1D tension only (44 elements)	n/a	Hyperelastic [4]; hexahedral	Bone-soft tissue share nodes; Frictionless MTPJ contacts; Single piece cartilage without contact for other joints; Frictional foot-ground contact ($\mu = 0.3$)
Current work	CT, MR; Male (normal); age 43; weight 945 N; Male (diabetic); age ??; weight 688N	Rigid; tetrahedral	n/a	Hyperelastic[1] subject-specific skin, fat, muscle and generic soft tissue; tetrahedral	Non-linear; 1D tension only (102 ligaments, 165 elements)	Non-linear; 1D seatbelt (9 tendons)	Non-linear; 1D spring (15 elements); cadaveric test data	Bone-soft tissue and soft tissue interfaces share nodes; Frictional bone-bone rigid contact with offset ($\mu_s = 0.1$, $\mu_k = 0.085$); Foot-ground contact ($\mu = 0.3$)

[†] Unless otherwise indicated, elastic refers to linear elastic material property, tetrahedral and hexahedral refer to 4-noded tetrahedral and 8-noded hexahedral elements, respectively.

[‡] Age in years

[1] Ogden rubber, [2] Second-order polynomial strain energy potential,[3] Neo-Hookean hyperelastic, [4] Mooney–Rivlin hyperelastic

Table 2.2b: Overview of published highly-detailed finite element foot models: Boundary condition and model validation.

Author	Simulation	Boundary conditions	Load	Model validation
Chen W. P. et al. (2003; , 2001)	Quasi-static mid stance to push off (2001); Parametric study of insole design (2003)	Fix proximal nodes of tibia	Prescribe linear and angular velocity of the ground (from motion capture) toward the foot	Compare plantar pressure prediction to literature
Cheung et al. (2006a; , 2005; , 2008)	Quiet stance; Parametric study of plantar fascia stiffness (2004), Achilles tendon force (2006a) and soft tissue material (2005)	Fix distal tibia, fibula and trans-tibial cut surface; Ground translates in vertical direction	For quiet stance, 350N vertical upward GRF and 175N vertical Achilles tendon force	Compare plantar pressure, contact area and arch deformation predictions to F-scan, foot measurement, literature and clinical observations
Cheng et al. (2008)	Quiet stance; Parametric study of toe dorsiflexion angle and Achilles tendon force	Fix medial cuneiform and cuboid; Talus translates in vertical direction	Prescribe toe angular displacement; 100-500N Achilles tendon force	Compare plantar fascia stress, strain and arch deformation predictions to literature and X-ray measurements
†Dengler E. (2008), Isvilanonda et al. (2012)	Quiet stance and clawed hallux	Fix ground; Tibia and fibula translate in vertical direction	400N tibia compression, 200N Achilles tendon (standing); Apply specific tendon forces to simulate clawed hallux	Compare plantar pressure, contact area and bone rotation to cadaver experiment and literature
Budhabhatti et al. (2009)	Push-off to toe-off; Investigate Hallux limitus, first ray arthrodesis and parametric study of foot insole materials	Prescribe positions and orientations of the first metatarsal bone at each static step	Apply force and moment at the MTPJ and IPJ for orientation.	Compare peak plantar pressure to experimental measurements
Garcia-Aznar, J. M. et al. (2009)	Parametric study of bone geometries and configurations	Fix base of the calcaneus; Allow horizontal translation at metatarsal heads	300N body force vector (10deg superoanterior to inferoposterior) at talus and 150N Achilles tendon force in the opposite direction	Qualitative validation with computational model in literature
Chen W. M. et al. (2012)	Heel rise; Parametric study of Achilles tendon force	Fix ground, distal tibia, fibula and superior soft tissue surface	Apply muscle forces to achieve plantar flexion and target GRF	Compare plantar pressure to experimental measurement and soft tissue deformation to literature
Chen, Y. N. et al. (2014b)	Quasi-static gait; divided stance phase into 12 increments	Prescribe sagittal displacement at distal tibia and fibula; Fix inferior surfaces of the proximal phalanges	Apply specific Achilles tendon force	Compare GRF and plantar aponeurosis tension to literature
Guiotto A. et al., (2014)	Quasi-static gait; divided stance phase into 4 increments	Prescribe foot orientation from motion capture; Fix distal tibia	Apply specific GRF and Achilles tendon forces	Compare peak plantar pressure to experimental measurement
†Lin et al. (2014)	Dynamic gait	Prescribe hindfoot, midfoot and phalangeal bone kinematics	n/a	Compare GRF and contact area to experiment and plantar aponeurosis tension to literature
Current work†	Passive compression, quiet stance and dynamic gait	Prescribed time series of tibia translation and orientation	Prescribed muscle force-time series, gravitational force	Compare bone orientation, GRF, plantar pressure, contact force and area to experimental data; Compare force in the Achilles tendon, plantar fascia and ankle joint to literature

† Simulations were carried out using an explicit FE solver in contrast to an implicit solver.

2.4 Subject-specific plantar soft tissue material characterization

The success of FE model prediction is based primarily on accurate anatomy, boundary conditions, and material representation. While accurate subject-specific anatomy can be acquired from CT and MR imaging and boundary conditions may be directly estimated from experiments (e.g., bone kinematics), identifying the subject-specific material properties requires special equipment and complex analysis.

The soft tissue material characterization process typically begins by selecting a constitutive equation (i.e., material model) to represent the tissue. A compression or an indentation test is then conducted to obtain a target experimental force-deformation response of the tissue. The force-deformation data can also be computed for any given set of material properties based on its constitutive equation, specimen shape and boundary condition. The material properties can then be inferred by minimizing the difference between the experimental and the computed force-deformation data.

Typical material models commonly used to represent soft tissue are nonlinear elastic (e.g., hyperelastic, including: Ogden, Second-order polynomial, Neo-Hookean and Mooney–Rivlin), time-dependent linear elastic (e.g., linear viscoelastic) and time-dependent nonlinear elastic (e.g., hyperviscoelastic). Additional material assumptions such as homogeneity, isotropy and nearly incompressibility are often used to reduce the number of material coefficients and simplify the analysis.

In this study, a nearly incompressible Ogden hyperelastic (or Ogden rubber) model is selected based on its flexibility (e.g., it can be reduced to Neo-Hookean or Mooney-Rivlin material if necessary), simplicity, and its ability to capture large nonlinear deformations in soft tissue. The Ogden material strain energy formulation (*W*) is given by equation 2.1.

$$W(\lambda_1, \lambda_2, \lambda_3) = \sum_{m=1}^{n} \frac{\mu_m}{\alpha_m}\left(\tilde{\lambda}_1^{\alpha_m} + \tilde{\lambda}_2^{\alpha_m} + \tilde{\lambda}_3^{\alpha_m} - 3\right) + \frac{1}{2}K(J-1)^2 \tag{2.1}$$

$$J = \lambda_1\lambda_2\lambda_3 \tag{2.2}$$

$$\tilde{\lambda}_i = J^{-1/3}\lambda_i \tag{2.3}$$

$$\mu = \sum_{m=1}^{n} \frac{\mu_m \alpha_m}{2} \tag{2.4}$$

$$\mu_m \alpha_m > 0 \qquad \text{(for each } m = 1,\ldots, n) \tag{2.5}$$

$$K = \frac{2\mu(1+v)}{3(1-2v)} \tag{2.6}$$

Where $\lambda_1, \lambda_2, \lambda_3$ are the three principal stretches, the Jacobian, J, denotes the relative volume change (equation 2.2), and $\tilde{\lambda}_i$ are the deviatoric principal stretches (equation 2.3). Poisson's ratio (v) and hyperelastic coefficients (μ_m and α_m) are the material properties. The coefficient μ_m is related to initial shear modulus μ and strain hardening coefficient (α_m) by equation 2.4. The product of μ_m and α_m is constrained according to equation 2.5 to ensure physiologic response and material stability (Ogden et al., 2004), i.e., this product must be positive. Bulk modulus, K, can be derived from equation 2.6.

Different techniques have been used to determine soft tissue material properties. The following subsections and Table 2.3 review publications which investigate plantar soft tissue material characterization.

2.4.1 *In vitro* plantar soft tissue material characterization

In vitro testing is commonly used to obtain force-deformation responses of the soft tissue when the procedure is too invasive to perform *in vivo* (e.g., destructive testing or mechanically isolated specimens). This type of testing allows specimen geometry, applied strain, and boundary conditions to be precisely controlled. However, reproducing physiologic conditions during testing can be challenging. Furthermore, factors such as tissue degradation, freeze/thaw cycling, temperature, humidity, and boundary conditions may potentially alter the experiment outcomes.

Isolated plantar soft tissue responses under compression and/or shear loading have been previously studied (Ledoux and Blevins, 2007; Miller-Young et al., 2002; Pai and Ledoux, 2010, 2012). Cylindrical or rectangular samples are excised from the plantar soft tissue and subjected to mechanically realistic deformations. If the boundary condition is simple [e.g., frictionless (Ledoux and Blevins, 2007; Miller-Young et al., 2002)], the material properties can be solved using closed-form solutions from the constitutive equation. In contrast, if the boundary condition is complicated (e.g., frictional interface, non-uniform deformation), the closed-form solution may be difficult or impossible to obtained. In this case, the material properties must be determined from inverse FE analysis (Pai and Ledoux, 2010).

Cadaveric hindfoot indentation tests have also been used to characterize the plantar soft tissue material properties (Chokhandre et al., 2012). This type of experiment mitigates the issues related to tissue hydration, but the problems of tissue degradation and the aforementioned external factors still remain. The complicated anatomy and boundary condition also require that the material properties be identified using inverse FE analysis.

2.4.2 *In vivo* subject-specific plantar soft tissue characterization

In vivo compression or indentation tests at the forefoot or hindfoot are typically used to replicate physiologic plantar deformation (Erdemir et al., 2006; Luo et al., 2011; Petre et al., 2013; Stebbins, 2012; Tong et al., 2003) and rely on inverse FE analysis to determine the material properties. The basic experimental set up consists of a load cell connected serially to a linear actuator (Luo et al., 2011). Indentation force is measured via the load cell while deformation (the sum of skin, fat deformations and bone translation) is output from (typically) a linear variable differential transformer (LVDT). In order to account for bone translation, an ultrasound probe is serially connected to the indenter (Erdemir et al., 2006). This type of set up is simple, but the utility of ultrasound imaging is limited by depth, bone shadowing and poor soft tissue contrast (Petre et al., 2008).

Using gated MRI while applying foot compression allows tracking of the internal soft tissue and bone kinematics in 3D. Petre et al. (2008) developed an MRI compatible loading device specifically for the forefoot by utilizing a non-metallic actuator driven by a hydraulic system. Most recent, our group developed a device capable of dynamic loading (0.2 Hz sine wave, peak force 1500 N, peak displacement 25mm) at the forefoot and hindfoot (Stebbins, 2012; Williams, 2015; Williams et al., 2015). Further detail about the construction and operation of the MRI compatible foot loading devices can be found elsewhere (Petre et al., 2008; Stebbins, 2012; Williams, 2015; Williams et al., 2015).

2.4.3 Inverse finite element analysis

Inverse FE analysis is a numerical technique which combines an optimization algorithm with the FE method to identify optimal model parameters to fit a set of target data. The best model parameters are determined by minimizing a user defined objective function that typically describes error between the model-predicted response and a target response determined from experiment. The optimization variables can be physical values such as material properties for material parameter identification or structural dimensions for topology optimization. In classical or direct FE analysis, the deformation of a body is computed from its known initial shape, material properties, and boundary conditions. In contrast, inverse FE analysis simulated a set of input parameters using direct FE then compared to experiment, and the model parameters adjusted iteratively to best match the experimental data (Figure 2.3).

In this study, a metamodel based optimization approach is used to approximate the global behavior of the model responses (i.e., objective value) as a function of material coefficients at each iteration (Lind et al., 2005; Roux et al., 1998; Stander et al., 2010). A Hybrid Adaptive Simulated Annealing (Hybrid ASA) optimization algorithm is used to determine the optimal material parameters (Stander et al., 2010). This algorithm has proven effective and efficient for global optimization (Stander et al., 2010). A detail review of metamodel-based optimization techniques is provided in Appendix I.

Table 2.3: Summary of plantar soft tissue mechanical testing and non-linear elastic material characterization.

Author	Study	Experiment protocol	Material model and properties	Material characterization method
			Isolated soft tissue testing	
Miller-Young et al. (2002) and Spears et al. (2007)	Material properties of the cadaveric calcaneal fat pad	Fast (175 and 350mm/s) unconfined compression tests; Two cylindrical plantar fat specimens (hind and forefoot, peak strain 50%)	Incompressible second-order polynomial hyperelastic[1] with additional time dependent terms ; C_{100}=0.01, C_{010}=0.01, C_{200}=0.10, C_{110}=0, C_{020}=0.10; Units: C_{ij} Pa	The calculated stress-strain curves were fit to the hyperelastic and viscoelastic theories using least squares regression with correlation > 0.9.
Pai and Ledoux (2010; , 2012)	Compressive and shear mechanical properties of the plantar fat (normal and diabetic)	Cylindrical specimens (19.05mm diameter compression and 10.37mm diameter shear, fixed ends) from 4 normal and 4 diabetic cadaveric feet, six specimens from each foot; For compression, displacement control (1-10Hz triangle wave), peak force 20% body weight. For shear, static compression to 36% strain, then applied shear displacement 85% of the initial thickness (1Hz triangle wave)	n/a	Reported the peak stress, peak strain, tangent modulus, energy loss instead of fitting to a material model
Pai and Ledoux (2011)	Quasi-linear viscoelastic properties of the plantar fat (non-diabetic, diabetic)	Cylindrical specimens (19.05mm diameter, fixed ends) from eight cadaveric feet, six specimens from each foot; Displacement control (1-10Hz triangle wave), peak force 20% body weight.	Fit the stress relaxation data to the quasi-linear viscoelastic (QLV) theory. Elastic function[3] described the hyperelastic response. Normal, A=1.72Pa, B=22.8 Diabetic, A=1.05Pa, B=25.7	Normalized (force/peak force) relaxation curves were fit to the QLV theory using least squares regression.
			In vivo/intact foot testing	
Lemmon et al. (1997)[†]	Finite element simulation of the insoles in therapeutic footwear	Measure *in vivo* hindfoot force-deformation data (n = 5) using ultrasound experiment; Mean stress-strain curve is corrected for the boundary effects by a simplified 2D hindfoot FE model.	Second-order polynomial hyperelastic[1] ; C_{10}=85.55, C_{01}=-58.40, C_{20}=38.92, C_{11}=-23.10, C_{02}=8.48, D_1=4.37 D_2=0.68 Units: $C_{ij,}$ kPa and D_i MPa^{-1}	Material properties calculated from an adjusted stress-strain curve in ABAQUS

Table 2.3: (Cont'd) Summary of plantar soft tissue mechanical testing and non-linear elastic material characterization.

Author	Study	Experiment protocol	Material model and properties	Material characterization method
Erdemir et al. (2006)	Inverse FE analysis of the heel pad indentation (non-diabetic, diabetic)	Heel pad force-deformation data 80 feet (40 diabetic and 40 non-diabetic) using ultrasound indentation (0.15mm resolution); Preload 2N, speed 5.7mm/s, peak strain 50%	First order incompressible Ogden hyperelastic[2]; Non-diabetic: μ=16.45 kPa, α=6.82; diabetic: μ=16.88 kPa, α=7.02;	Assumed axisymmetric 2D plane strain hindfoot model, rigid indenter and calcaneus; Optimize μ and α; Objective function was RMSE between predicted and actual force-displacement response
Gu et al. (2010)	Three dimensional inverse FE analysis of the *in vivo* hindfoot	28 year-old, male subject; Hindfoot compression test measured force and actuator displacement	First order incompressible Ogden hyperelastic[2]; Skin: μ=122 kPa, α=18	3D hindfoot FE model with calcaneus bone, plantar skin and fat; Assumed fat material properties from literature; Optimize skin μ and α; Objective function was RMSE between predicted and actual force-displacement response
Chokhandre et al. (2012)	Three dimensional inverse FE analysis of the cadaveric hindfoot	58 year-old, male specimen; Spherical indenter (25.4mm diameter), translation speed 0.04mm/s; Fixed calcaneus and talus; Peak load 220N. Two additional tests (spherical indenter compress-shear and elevated platform compression) used for validation of the optimal results	First order Ogden hyperelastic[2]; μ=1.084 kPa, α=9.78, ν=0.475	3D hindfoot FE model; Lumped skin and fat into a generic soft tissue; Assumed rigid, fixed calcaneus and talus; Rigid indenter driven by a spring. See (Erdemir et al., 2006) for inverse FE detail
Petre et al. (2013)	Three dimensional inverse FE analysis of the *in vivo* forefoot	21 year-old, male subject; Static compression at 4 loads (75N-300N in 75N increment) using MRI compatible forefoot loading device; Captured static MR images at each load	First order Ogden hyperelastic[2]; ν=0.475; Generic soft tissue: μ=26.6 kPa, α=17.7; Skin: μ=40.6 kPa, α=22.7; Fat: μ=16.5 kPa, α=-0.77; Muscle: μ=57.4 kPa, α=28.8	3D forefoot FE model with bones and skin, fat and muscle; Exclude toes; Optimize μ and α of each tissue; Objective function was RMSE between predicted and actual model deformation

[†] Hyperelastic material properties by Lemmon et al. were used in majority of the FE foot models: Cheung et al. (2005), Chen et al. (2010), Spyrou and Aravas (2011), Qui et al. (2011), and Dengler (2008).

[1] Strain energy function (U) as a function of material coefficients C_{ij} and D_{ij} for the second-order polynomial hyperelastic model

$$U = \sum_{i+j=1}^{2} C_{ij} (\bar{I}_1 - 3)^i (\bar{I}_2 - 3)^j + \sum_{i=1}^{2} \frac{1}{D_i} (J_{el} - 1)^{2i} \tag{2.1}$$

[2] Strain energy function (U) as a function of material coefficients μ, α and D for the first-order Ogden hyperelastic model (ABAQUS)

$$U = \left(\frac{2\mu}{\alpha^2} \right) \left(\lambda_1^\alpha + \lambda_2^\alpha + \lambda_3^\alpha - 3 \right) + \frac{1}{D} \left(J - 1 \right)^2 \tag{2.2}$$

[3] Elastic function ($\sigma^{(e)}$) where A and B are material coefficients

$$\sigma^{(e)}(\varepsilon) = A\left(e^{B\varepsilon} - 1\right) \tag{2.3}$$

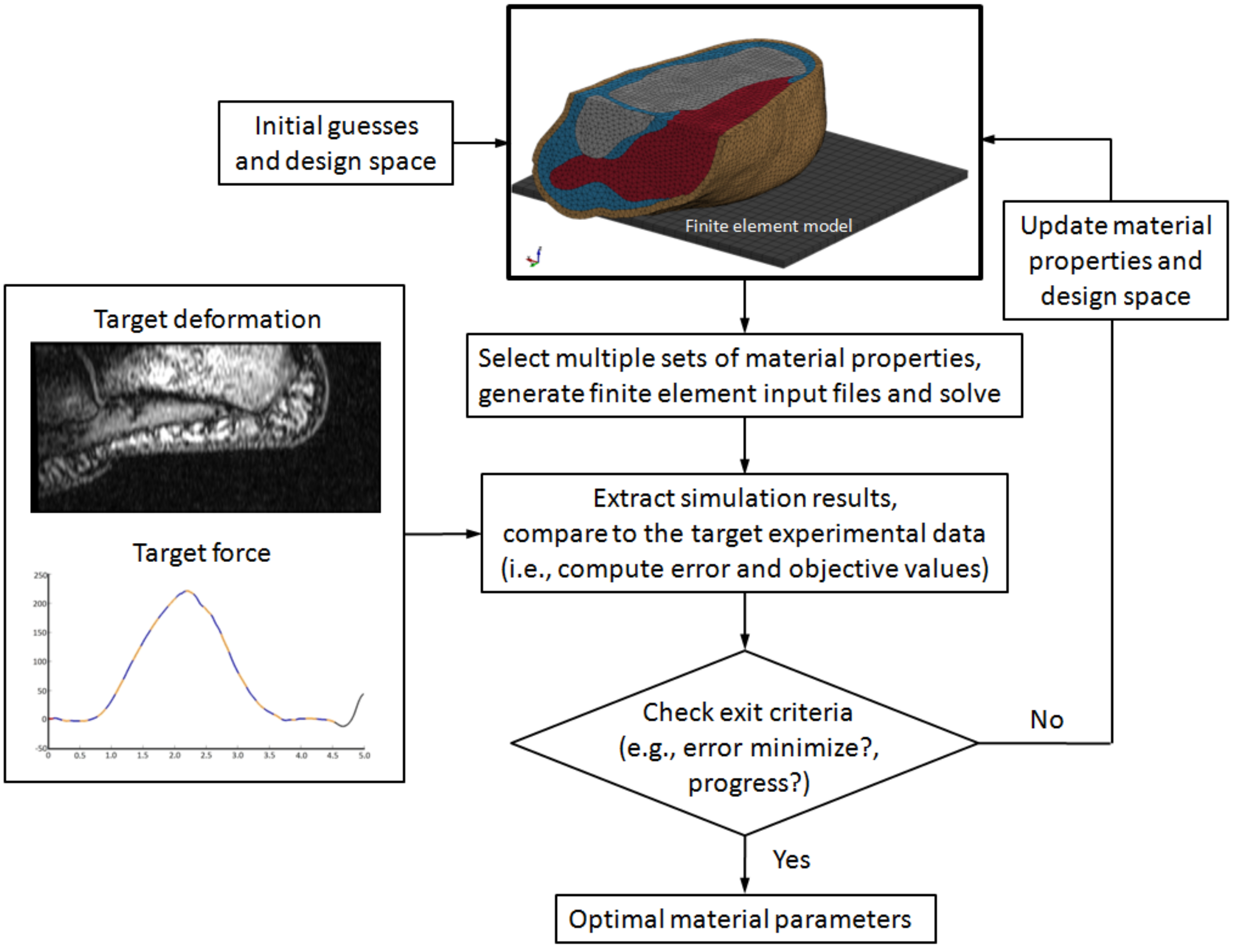

Figure 2.3: Inverse finite element analysis flow chart.

2.5 *In vitro* plantar aponeurosis characterization

The plantar aponeurosis is one of the longest and strongest ligaments in the body. However, the majority of foot models oversimplify this structure, frequently by modeling it as linear elastic, with uniform cross-sectional area and using tension-only spring elements (Cheung and Zhang, 2008; Garcia-Gonzalez et al., 2009; Spyrou and Aravas, 2011; Tao et al., 2010). The plantar aponeurosis has been shown to have a non-linear elastic response (Kitaoka et al., 1994; Wright and Rennels, 1964). While the longitudinal anatomy of the plantar aponeurosis has been previously explored (Chen et al., 2014a; Hedrick, 1996; Moraes Do Carmo et al., 2008), the cross-sectional area of the structure, however, has never been accurately measured.

2.5.1 Mechanical testing of the plantar aponeurosis

Tensile responses of the plantar aponeurosis has been explored in cadaveric specimens (Clark et al., 2009; Erdemir et al., 2004; Kitaoka et al., 1994; Pavan et al., 2014; Wright and Rennels, 1964). Wright and Rennels (1964) attached a clip gage to measure deformation in isolated plantar aponeurosis specimens. The tensile force was increased from 111.2N to failure in 111.2N increments. They observed failures at the grip in all specimens (peak force 890-1000N, peak strain 4.6 – 7.1%). Clark et al. (2009) applied a constant inferosuperior force (98.1N) at the forefoot of two intact limbs. Plantar aponeurosis strains were measured using seven strain gages (four uni-axial and one rectangular rosette). A mean strain of 1.89±0.27% was reported at the central component along the fiber direction. A time-dependent response of the plantar aponeurosis was studied by implementing stress relaxation tests (Pavan et al., 2014). A transversally-isotropic viscohyperelastic constitutive model was developed to describe the overall material properties.

Robotic gait simulation was used to estimate the plantar aponeurosis force pattern during gait (Erdemir et al., 2004). The simulations were performed on seven cadaveric feet; each foot was instrumented with a fiber optic cable passing through the proximal central component of the plantar aponeurosis. The recorded loss in fiber optic signal was calibrated to the plantar aponeurosis force by means of post-experiment tensile testing. They found an average peak plantar aponeurosis force of 96±36% of the subject’s body weight (BW) at 80% of the stance phase. The specimens failed at 916 – 1,743N (2.2 – 2.8 times BW).

A video marker system was used to capture the plantar aponeurosis deformation during dynamic uni-axial tensile tests (Kitaoka et al., 1994) (Table 2.4). Specimens were loaded to 445 N at three different loading rates (11.1, 111.2, 1112.0 N/s) then tested to failure (111.2 N/s ramp rate). The deformation was approximately 3 mm at 445 N and the mean failure load was 1189±244 N. The study concluded that the plantar aponeurosis response was non-linear, nearly elastic and insensitive to the loading rates.

Although two previous studies (Kitaoka et al., 1994; Wright and Rennels, 1964) provided the overall plantar aponeurosis force-deformation data, they are insufficient for the level of regional detail included in this study (Specific Aim 4). Several studies have also estimated the cross-sectional area by assuming a rectangular cross-sectional profile (Chen et al., 2014a; Wright and Rennels, 1964). This assumption is potentially inaccurate and can substantially affect the computed stress and modulus. A molding, casting and sectioning technique has been shown to provide better accuracy for obtaining cross-sectional area of complicated shapes (Schmidt and Ledoux, 2010). This technique will be implemented in the present study.

2.5.2 Digital image correlation

Digital image correlation (DIC) is a type of non-contact deformation measurement technique. This technique utilizes digital image processing to measure displacement and strain fields within a region of interest of a material undergoing deformation. A typical set up for 2D in-plane deformation measurement is illustrated in Figure 2.4. A light source is used to uniformly illuminate the surface of a specimen which is placed normal to the camera sensor. The deformation field is measured by detecting and tracking subsets of pixels between two or more images (e.g., reference and deformed images) and extracting a deformation mapping that maximizes the correlation between images (Hild and Roux, 2006; Mccormick and Lord, 2010). This method is robust, accurate and has been used extensively for non-contact deformation measurement in soft tissue (Bummo and Jung, 2010; Lai and Levenston, 2010; Lauret et al., 2009; Nicolella et al., 2006) including the plantar aponeurosis (Kitaoka et al., 1994). Table 2.4 provides a summary of the literature related to digital image correlation and tracking in soft tissue; a detailed review of the DIC technique is given in Appendix II.

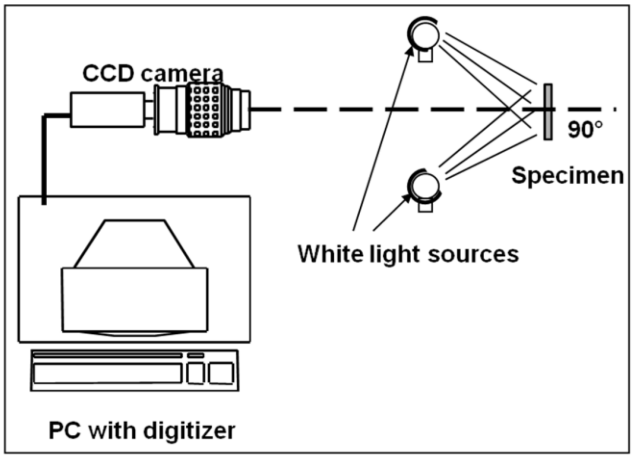

Figure 2.4: Schematic drawing of a 2D in-plane DIC (*adapted from Yao et al., 2008*).

Table 2.4: Summary of two-dimensional digital image correlation techniques in soft tissue testing.

Author	Study and specimen preparation	DIC equipment/parameters	Analysis
Kitaoka et al. (1994)	Dynamic uni-axial tensile properties of the plantar aponeurosis; Bone-specimen-bone samples; loaded to 445N at three rates: 11.1, 111.2, 1112.0N/s; Tested to failure at 111.2N/s; Used six-2mm diameter reflective markers i.e., 2 markers for each of the middle, medial and lateral region	RCA video camera (15, 60fps, 240x 256 pixel)	Commercial DIC code (accuracy of at least 0.25 mm
Elliott and Setton (2001)	Anisotropy in the human anulus fibrosus; Tissue sample (1.37x2.86x 7.73mm) cut and mounted to the grip; Randomly applied black dots	High-resolution digital camera (Kodak 1.4i, 60mm f2.8 lens with 70mm extension tube, resolution 4μm/pixel)	Custom DIC code
Zhang et al. (2002)	Quasi-static mechanical testing of arterial tissue; Rectangular specimens cut from bovine aorta; A quick-drying black enamel paint sprayed on the surface	Digital camera Olympus C-3000Z, 1280x960 pixel, resolution 18μm/pixel; Calibrated the system with a silicone rubber	Custom DIC code (accuracy 1/100 pixel)
Jacquemoud et al. (2007)	Dynamic tensile failure of the planar soft tissue; A cadaveric skin piece was cut into I-shape samples; Surface was covered by random black dots made of mascara	Local displacement by a high-speed video camera (1000fps, 1536x 1024 pixel, 0.1x0.1mm/ pixel); Measured clamp-to-clamp global displacement by the LVDT	Commercial DIC code (accuracy 1/100 pixel)
Manoogian et al. (2008)	Dynamic (strain rate 700%/s) uni-axial tensile properties of the cadaveric placenta; A thin slice was stamped into a dog bone shape; Used optical markers	High-speed video camera (500 fps, 512x512 pixel); Used mirror to access the back surface	Commercial DIC code (accuracy 0.03mm)
Lauret et al. (2009)	Strain fields in a planar section of a brain tissue during acceleration; Sliced porcine brain encapsulated in a rigid cavity; Random speckle (matte black enamel, 0.5mm diameter) applied by an air brush	High-speed video camera (1600fps, 1440x952 pixel)	Commercial DIC code
Gao and Desai (2010)	Estimating zero strain state in porcine liver tissue; Specimen was cut into a rectangular shape and adhered to the loading platen; No surface markings (used tissue texture instead)	Digital camera (Nikon D40X, 18-55mm f3.5-5.6 lens, 3fps, 3872x 2592 pixel); Used polarizing filter to reduce reflection; Determined system error from translation test	Custom DIC code

2.6 Summary

The human foot is constantly subjected to dynamic loading from various activities. The complex system comprised of bone, ligament, tendon, plantar aponeurosis, skin, plantar fat, cartilage and fascia (as well as nonstructural tissues such as nerves and blood vessels) functions to maintain stability of the foot while soft tissue absorbs shock, dissipates stress and cushions the underlying bony prominences. Diabetes has been shown to negatively affect the soft tissue structure and alter the material properties, which leads to an increased risk of developing foot ulcer.

Finite element models provide an ideal tool for exploring the effect of these soft tissue changes on the mechanical responses of the foot. The accuracy and robustness of FE model predictions are based primarily on accurate anatomy, boundary conditions, and material representation. The current state-of-the-art FE foot models incorporate subject-specific anatomy, but lack accurate soft tissue material properties.

Subject-specific plantar soft tissue material properties have been determined at the forefoot and hindfoot using inverse FE analysis. The protocols in these studies can serve as guidelines for determining *in vivo* subject-specific hindfoot soft tissue material properties in this study.

The plantar aponeurosis is another important model component that is often over simplified due to lack of anatomy and material properties. The plantar aponeurosis force during gait and overall force-deformation responses has been reported previously. More accurate cross-sectional geometry and deformation responses can be determined using the molding, casting and sectioning method combined with a digital image correlation approach. These experimental techniques can be used to obtain more accurate material properties of the plantar aponeurosis for input into FE models.

Chapter 3. Finite element analysis of the foot: Model validation and comparison between two common treatments of the clawed hallux deformity

This work is previously published: Isvilanonda, V., Dengler, E., Iaquinto, J.M., Sangeorzan, B.J., Ledoux, W.R., 2012. Finite element analysis of the foot: Model validation and comparison between two common treatments of the clawed hallux deformity. Clinical Biomechanics ***27****, 837-844.*

3.1 Abstract

Background: Clawed hallux is defined by first metatarsophalangeal joint extension and first interphalangeal joint flexion. This deformity can lead to increased plantar pressure and risk of ulceration. We investigated two surgical techniques, the modified Jones and flexor hallucis longus tendon transfer, for correcting this deformity.

Methods: A finite element foot model was modified to generate muscle overpulls, including extensor hallucis longus, flexor hallucis longus and peroneus longus. Both corrective procedures were simulated, predicting joint angle and plantar pressure changes.

Findings: The clawed hallux deformity was generated by four combinations of overpulls: 1) extensor hallucis longus, 2) peroneus longus + extensor hallucis longus, 3) extensor hallucis longus + flexor hallucis longus and 4) all three muscles together. The modified Jones reduced metatarsophalangeal joint angle deformities, but only the two overpulls without the flexor hallucis longus had acceptable hallux pressure. The flexor hallucis longus tendon transfer reduced deformity at the metatarsophalangeal and interphalangeal joints but the hallux was still extended when there is lack of flexion force to counter balance the extension force from the extensor hallucis longus. After the flexor hallucis longus tendon transfer, there was also an increase in metatarsal head pressure for the extensor hallucis longus + flexor hallucis longus overpull, and the all three muscles together overpull.

Interpretation: The modified Jones was effective in correcting clawed hallux deformity involving extensor hallucis longus overpull without flexor hallucis longus overpull. The flexor hallucis longus tendon transfer was effective in correcting clawed hallux deformity resulting from the combined overpull of both extensor hallucis longus and flexor hallucis longus, but not with isolated extensor hallucis longus overpull. An additional procedure to reduce the metatarsal head pressure may be required concomitant to the flexor hallucis longus tendon transfer. However this procedure avoids interphalangeal joint fusion seen with the modified Jones

3.2 Introduction

Clawed hallux is a foot deformity characterized by extension at the first metatarsophalangeal joint (MTPJ) and flexion at the first interphalangeal joint (IPJ) (Kadel et al., 2005; Olson et al., 2003). The deformity is caused by an imbalance of the forces from the extensor hallucis longus (EHL), flexor hallucis longus (FHL) and/or peroneus longus (PL) muscles (Olson et al., 2003). In patients with clawed lesser toes, a deformity with a prevalence of 8.7 percent in an older population (Dunn et at., 2004), symptoms of the deformity include increase in metatarsal head pressure (Bus et al., 2005) and repetitive rubbing of the dorsal surface of the toes against footwear (Dinh and Veves, 2005). Similar symptoms are usually present at the first ray in patients with a clawed hallux, which had a prevalence of 0.7 percent in an older adult population (Dunn et al., 2004). Most clinically troubling, higher peak pressures found on the plantar aspect of the foot can lead to an increased propensity for ulcer formation (Veves et al., 1992) – which risks future lower extremity amputation in diabetic populations (Pecoraro et al., 1990).

Several treatments have been used to correct this deformity and restore normal plantar pressure. Early cases were treated with a night splint and metatarsal bar (Mills, 1924). For moderate cases in which the deformity is still flexible, two surgical corrective techniques, the modified Jones procedure or the FHL tendon transfer, are commonly used (Döderlein et al., 2000; Kadel et al., 2005; Palma et al., 1997; Steensma et al., 2006).

The modified Jones procedure involves transecting the EHL tendon distally and passing the free end through an oblique hole drilled from the inferomedial to dorsolateral aspect of the metatarsal neck (Elias et al., 2007). The tendon is sutured to itself under slight tension which exerts an upward pull on the metatarsal and relieves the hyperextension of the phalanx. An IPJ arthrodesis is performed to eliminate flexion from an unopposed FHL force (Döderlein et al., 2000). The extensor hallucis brevis (EHB) is then attached to the free distal part of the EHL.

With the FHL tendon transfer procedure, the FHL tendon is transected distally and passed through a hole drilled through the metaphysis of the proximal phalanx (Elias et al., 2007) and sutured to itself on the medial side of the hallux. No IPJ arthrodesis is required.

Positive patient satisfaction of 79% to 91% was reported after undergoing the modified Jones procedure (Döderlein et al., 2000; Palma et al., 1997). In one study, all patients were satisfied with FHL tendon transfer (Kadel et al., 2005). However, inter-procedure satisfaction is difficult to ascertain since other procedures were performed concomitant in most patients.

Cadaveric study allows for exploration into how muscle overpulls can give rise this deformity. Olson et al. (2003) successfully reproduced clawed hallux by combination of EHL, FHL and PL muscle overpulls. Elias et al. (2007) compared the ability of the modified Jones and FHL tendon transfer procedures to correct the clawed hallux deformity. However, loading frame capability and specimen frailty limited this study to partial weight bearing.

Finite element (FE) models of the human foot have been developed to overcome the limitations of clinical and cadaveric studies (Chen et al., 2010; Cheng et al., 2008; Cheung and Zhang, 2008; Garcia-Aznar et al., 2009; Qiu et al., 2011; Spyrou and Aravas, 2011; Sun et al., 2011; Wu, 2007). Although FE foot modeling has become sophisticated, the majority of these models have some geometric and/or material limitations such as: two dimensional analysis (Wu, 2007), no encapsulated soft tissue (Cheng et al., 2008; Garcia-Aznar et al., 2009), linear elastic soft tissue mechanical properties (Sun et al., 2011), or cartilage and ligament simplification (Chen et al., 2010; Cheung and Zhang, 2008; Qiu et al., 2011;

Spyrou and Aravas, 2011). These simplifications can potentially affect the prediction of internal soft tissue stress and strain, plantar pressure and bone kinematics.

We have developed an FE foot model with a focus on improved anatomical detail. Once validated, the model was used to study the effect of muscle overpull on the formation of the clawed hallux deformity. The surgical treatments (modified Jones procedure and FHL tendon transfer) were simulated and the joint angle correction and plantar pressures were compared.

3.3 Methods

A fresh frozen left foot from a 44-year-old male donor (823N bodyweight) with no reported prior pathology was used to create the FE model. Prior to testing, the foot was thawed and secured in a custom made acrylic frame, which applied a 70N compressive force on the tibia to maintain a neutral foot orientation during scanning. The frame/foot was scanned using both computed tomography (CT) and magnetic resonance (MR) imaging to obtain detailed anatomical datasets. The CT scans of the foot were performed using a Philips CT MX8000IDT scanner (Philips Healthcare, Best, the Netherlands) at the Veterans Affairs (VA) Puget Sound Health Care System (pixel spacing 0.797 mm, voxel depth 0.3 mm, slice spacing 0.3 mm, slice thickness 0.6 mm). All MRI imaging was performed on a 3.0T Philips Achieva MRI system at the Bio-Molecular Imaging Center at the University of Washington. Two scans were conducted - the first was used for most soft tissue (pixel spacing 0.586 mm, voxel depth 0.6 mm, slice spacing 0.6 mm, slice thickness 0.6 mm, scan options PDW [proton density water]) and a second for cartilage (pixel spacing 0.586 mm, voxel depth 0.6 mm, slice spacing 0.6 mm, slice thickness 0.6 mm, scan options PDW [proton density water], FS [fat saturation], TSE [turbo spin echo]).

Custom software, *MultiRigid*, was used to segment the foot bones from the CT images (Hu et al., 2011). The segmented bones were then registered to the corresponding MR images to assist with manual segmentation of the soft tissue, plantar fat and cartilage at several joints using ImageJ (NIH, Bethesda, USA). A total of 48 parts were exported in stereo lithography (.stl) file format, including: 27 bones (the intermediate and distal phalange of the 5th ray were fused), 6 fat volumes, 14 anatomically derived cartilage geometries (pairs from 7 joints), and 1 encapsulated soft tissue (representing muscle and skin). The geometries were meshed with linear tetrahedral elements using ANSYS ICEM CFD (ANSYS Inc, Canonsburg, USA). An optimized element size (4mm) was found using a mesh convergence analysis. Ligaments, tendons, contacts, constraints, material properties and nodal forces were defined in LS-Prepost (Livermore Software, Livermore, USA). The final model included 101 ligaments, 8 tendons, the plantar fascia and 19 joint contacts (Figure 3.1a and b).

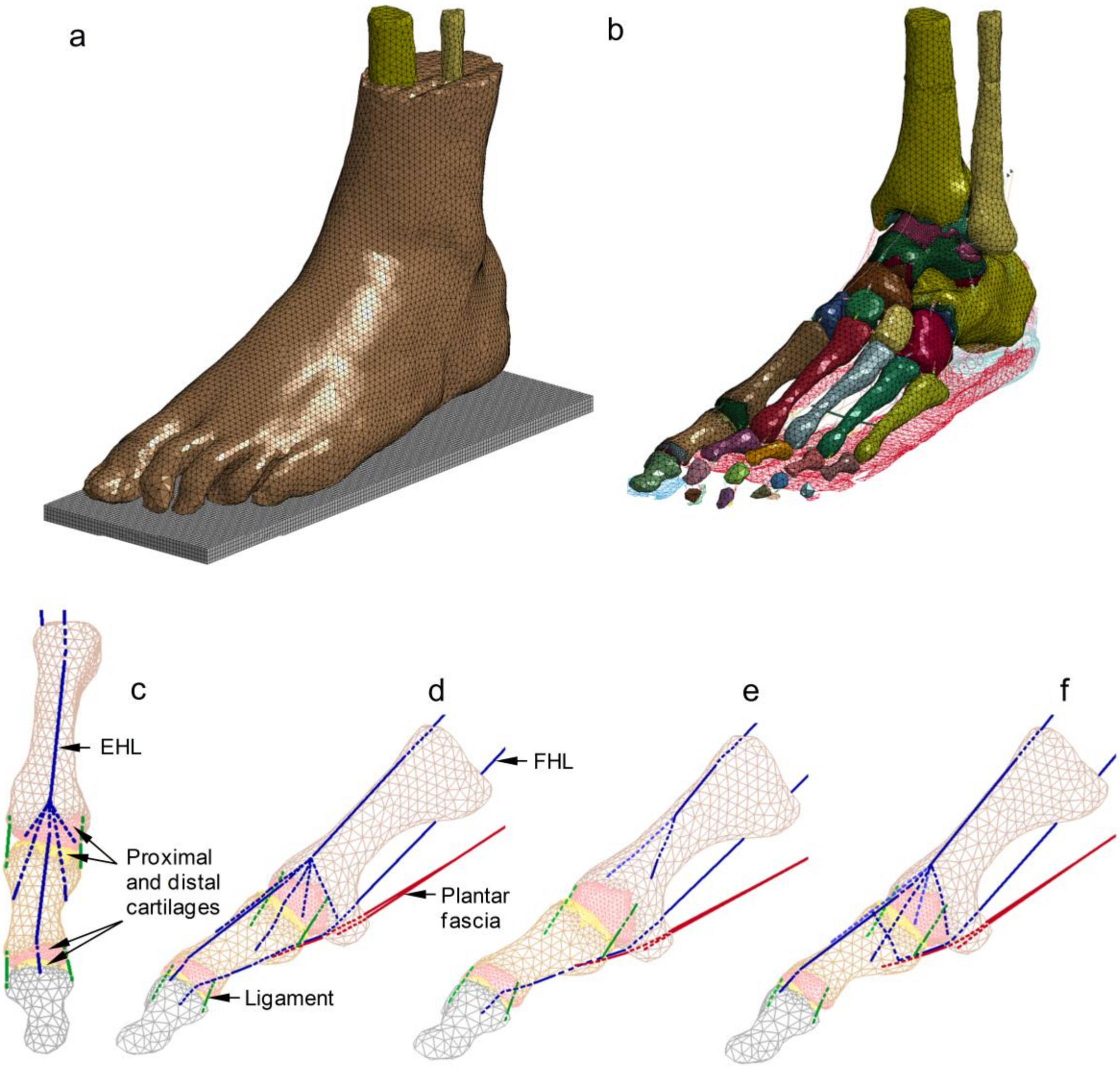

Figure 3.1: (a) Complete finite element model, (b) Structure inside an encapsulated soft tissue showing bone, cartilage, fat, plantar fascia, ligament and tendon, (c) Extensor apparatus of the first ray pre-surgery, (d) First ray pre-surgery, (e) First ray post-surgery modified Jones procedure, (f) First ray post-surgery flexor hallucis longus (FHL) tendon transfer. For (c, d, e and f), tendon and extensor apparatus (blue), ligament (green), digital slips of the plantar fascia (red) and proximal (pink) and distal (yellow) cartilage are shown. Dash line indicates element passing inside or behind the bone surface.

Bone was assumed rigid due to its relatively high stiffness in comparison to soft tissue (Table 3.1). Cartilage was assumed rigid as well because the deformation was relatively small. Non-linear, tension-only discrete elements with individual force-displacement characteristics were specified for each ligament and tendon. To simulate wrapping around bone, tendon and tendon sheaths were modeled with LS-DYNA seatbelt and slipring elements. Improving upon a prior technique, the plantar fascia was created from 15 discrete elements (Iaquinto and Wayne, 2010). The central band (5 elements) connected between the medial calcaneal tuberosity and a rigid shell at the level of the mid-shaft of the metatarsals. The proximal band (5 elements) originated from the rigid shell and progressed to each metatarsal head. Digital slips (5 elements) originated from the rigid shell and attached distally at the base of the proximal phalanges to capture the windlass effect (Hicks, 1954). Tensile properties for each discrete element in the plantar fascia were scaled from a non-linear force displacement curve (Kitaoka et al., 1994). The extensor apparatus of the hallux (Figure 3.1c and d) was modeled by 4 discrete elements connecting the main EHL tendon to the metatarsal head (2 elements) and to the base of the proximal phalanx (2 elements) (Sarrafian and Topouzian, 1969).

The encapsulated soft tissue and the plantar fat were governed by a hyperelastic model with the following strain energy function: (Hallquist, 2006)

$$W(\lambda_1, \lambda_2, \lambda_3) = \sum_{m=1}^{n} \frac{\mu_m}{\alpha_m}\left(\tilde{\lambda}_1^{\alpha_m} + \tilde{\lambda}_2^{\alpha_m} + \tilde{\lambda}_3^{\alpha_m} - 3\right) + \frac{1}{2}K(J-1)^2 \tag{3.1}$$

$$\tilde{\lambda}_i = \frac{\lambda_i}{J^{1/3}} \tag{3.2}$$

where K is the bulk modulus and J is the relative volume change given by the product of three principal stretches (λ_i). The three volumetric independent principal stretches ($\tilde{\lambda}_i$) are related to λ_i by Equation 3.2. Values μ_m and α_m are material parameters calculated from the input stress-strain curve (Lemmon et al., 1997; Pai and Ledoux, 2010) in LS-DYNA. For this study, n=2 (encapsulated soft tissue) and 3 (plantar fat) were used which resulted in material constants for encapsulated soft tissue (μ_1 = -0.964 MPa, α_1 = -

0.055, μ_2 = -0.00034 MPa, α_2 = -7.15) and plantar fat (μ_1 = 0.0000011 MPa, α_1 = 30.9, μ_2 = 0.28 MPa, α_2 = 0.467, μ_3 = -0.90 MPa, α_3 = 0.14).

Table 3.1: Material properties and element types used in the finite element foot model.

Material	Material Model	Element Type	Young's Modulus (MPa)	Poisson's Ratio	Mass Density (10^{-6}kg/mm^3)	Reference
Ground	Rigid	Hexahedral	68,900	0.35	2.7	(Hibbeler, 1997)
Bone	Rigid	tetrahedral	20,100	0.30	0.449	(Muehleman et al., 2002; Zysset et al., 1999)
Cartilage	Rigid	tetrahedral	0.97	0.07	1.0	(Athanasiou et al., 1998)
Fat	Hyperelastic	tetrahedral	[a]	0.49	1.0	(Pai and Ledoux, 2010)
Fat[b]	Linear elastic	tetrahedral	1.04	0.49	1.0	(Pai and Ledoux, 2010)
Soft tissue	Hyperelastic	tetrahedral	[a]	0.49	1.0	(Lemmon et al., 1997)
Soft tissue[b]	Linear elastic	tetrahedral	2.49	0.49	1.0	(Lemmon et al., 1997)
Ligament	Nonlinear	Discrete Spring	[a]	-	-	(Dengler, 2008; Felton, 1996; Luo et al., 1997; Mkandawire et al., 2005; Netter, 2005; Sarrafian, 1993; Schmidt, 2009) [c]
Tendon	Nonlinear	Discrete Seatbelt	[a]	-	-	(Blanton and Biggs, 1970; Maganaris and Paul, 1999; Schechtman and Bader, 1994) [d]
Plantar fascia	Nonlinear	Discrete Spring and Seatbelt	[a]	-	-	(Kitaoka et al., 1994)

[a] Stress-strain (hyperelastic), force-deformation (discrete spring) and force-strain (discrete seatbelt) curves were specified.

[b] Modified material properties at the subcalcaneal region to account for the 70N preload during scanning.

[c] Force-deformation response for the short plantar, inferior calcaneonavicular, interosseous second cuneiform-third cuneiform and interosseous fourth metatarsal-fifth metatarsal ligament were tested in house (Schmidt, 2009). Force-deformation response for other ligaments were extrapolated based on an individual ligament length (Felton, 1996; Luo et al., 1997; Mkandawire et al., 2005; Sarrafian, 1993) and an empirical equation.

[d] Force-strain curve for TA tendon was digitized and calculated from Maganaris and Paul (1999). Force-strain curve for TP tendon was calculated from TA stress-strain curve (Maganaris and Paul, 1999) and TP tendon cross-section area (Blanton and Biggs, 1970). Force-strain curve of the other five tendons were extrapolated from the digitized EDL stress-strain curves (Schechtman and Bader, 1994) and cross-section area of each tendon (Blanton and Biggs, 1970).

As previously mentioned, the foot was scanned under 70N compressive load, resulting in the compression of the plantar soft tissue prior to scanning, leading to an under-representation of the subcalcaneal soft tissue thickness. We estimated 47% tissue strain (Prichasuk, 1994). To account for this, the subcalcaneal soft tissue and fat were given modified pre-loaded linear elastic material properties, determined from the final slope of the corresponding stress strain curve (R^2 = 0.94 for fat and 0.99 for soft tissue). Elsewhere in the foot, the previously determined hyperelastic model was used.

The static and dynamic coefficients of friction for cartilage pairs (tibiotalar, anterior/middle and posterior talocalcaneal, talonavicular, calcaneocuboid, the first MTPJ and the first IPJ) were 0.102 and

0.085, respectively (Merkher et al., 2006). For other joints, a contact interface with the offset distance equivalent to half of the specified minimum gap distance between unloaded bones was used, except for the lesser toes (which were constrained just by the soft tissue). Friction was defined as in joints with cartilage. The coefficient of friction between the foot and the ground was set to 0.6 (estimated from the palm of the hand) (Zhang and Mak, 1999). No relative nodal motion was permitted between material meshes of bone and soft tissue. The proximal ends of the tibia and fibula were restricted to one degree of freedom (vertical translation). A tibia-ground angle was prescribed at 90˚ in both the frontal and sagittal planes for all simulations which approximated its position at early (22%) stance phase (Perry, 1992). Gravitational acceleration of 9.8 m/s^2 was included.

Two model validations were applied, the first being at quiet stance position. To maintain static equilibrium between the applied Achilles tendon force of 200 N and ground reaction force (GRF) target of 400 N, it was necessary to apply a 600N vertical compressive force acting on the transtibial surface. Both loads were linearly ramped from zero to maximum in 0.05 s and held until the model reached equilibrium, defined as when the GRF reached steady state and total kinetic energy was minimal. The footprint was divided into 10 regions to calculate regional loading. Load ratio, peak plantar pressure (averaged over 10x10 mm^2 area, i.e., the average sensor size in Cavanagh et al. (1987)) bone alignments were compared to literature.

The second validation explored the model’s response to extrinsic muscle force imbalances that create the clawed hallux. The partial weight clawed hallux loading protocol from Elias et al. (2007) was prescribed to the model. Peak pressure at the metatarsal head and hallux (averaged over 14x14 mm^2 area (i.e., the average size in Elias et al. (2007) was 14.7x14.7 mm^2) and over 0.05s simulation time) and change in MTPJ and IPJ angle from no-overpull were compared to the reported data.

Full body weight clawed hallux muscle forces for all but the Achilles were calculated from physiologic cross-sectional area, maximum specific tension and the electromyographic activity during gait (Brand et al., 1986; Fukunaga et al., 1996; Perry, 1992; Pierrynowski, 1982; Wickiewicz et al., 1983; Zhou et al., 1995)(Table 3.2). Achilles tendon forces were measured directly (Ishikawa et al., 2005).

Biomechanically realistic forces were applied to the Achilles tendon and proximal end of 7 other extrinsic tendons: PL, EHL, FHL, flexor digitorum longus (FDL), tibialis anterior (TA), tibialis posterior (TP) and peroneus brevis (PB). Target GRF was determined from the cadaver body weight and previous motion analysis data (Aubin et al., 2012). The GRF was maintained at 844N by adjusting compressive force at the transtibial surface to account for muscle forces (Table 3.2). FHL (104N) and PL (96N) overpull forces corresponded to their peak forces found in normal gait (Aubin et al., 2012). Due to low EHL activity in gait, a tendon sub-failure load (200N) (Blanton and Biggs, 1970; Schechtman and Bader, 1994) was chosen for EHL overpull.

Table 3.2: Muscle forces for clawed hallux simulation at full body weight during early stance phase of the gait.

Force (N)	**Overpull Cases**							
	No overpull	**EHL**	**FHL**	**PL**	**PL+EHL**	**PL+FHL**	**EHL+FHL**	**EHL+FHL+PL**
Compression	1303	1499	1403	1395	1591	1495	1599	1691
Achilles	359	359	359	359	359	359	359	359
PL	4	4	4	96	96	96	4	96
PB	5	5	5	5	5	5	5	5
FHL	4	4	104	4	4	104	104	104
EHL	4	200	4	4	200	4	200	200
TA	38	38	38	38	38	38	38	38
TP	39	39	39	39	39	39	39	39
FDL	6	6	6	6	6	6	6	6
Total GRF	844	844	844	844	844	844	844	844

The modified Jones procedure was modeled by removing the extensor apparatus distal to the mid-metatarsal level. Two elements were modeled to connect the end of the EHL to the inferomedial and dorsolateral nodes of the metatarsal neck (Figure 3.1e). (Note that intrinsic muscles, such as EHB, were not included in the foot model, therefore the EHB to EHL transfer could not be simulated.) To simulation fusion, the proximal and distal phalanges were rigidly constrained with a flexion angle equal to their unloaded neutral position. The FHL tendon transfer was modeled by removing the distal FHL tendon at the level of the MTPJ. The proximal remainder of the tendon was attached to the dorsal surface of the base of the proximal phalange (Figure 3.1f).

The models were solved using LS-DYNA explicit analysis (version 971 R5.1, Livermore Software, Livermore, USA). The sagittal MTPJ and IPJ angle measurements employed similar techniques used by Sangeorzan et al (1993).

3.4 Results

3.4.1 FE model validation

In general, the FE foot model was well validated. For quiet stance, the model had higher peak pressures, but similar load ratios when compared to the literature. The model showed peak plantar pressure and load ratio at the hindfoot (290.1 kPa, 60.0% GRF), midfoot (47.6 kPa, 13.6% GRF) and forefoot (51.1 kPa, 26.4% GRF) regions compared to the data from Cavanagh et al. (1987) at the hindfoot (138.9 kPa, 60.5% GRF), midfoot (27.8 kPa, 7.8 % GRF) and forefoot (53.4 kPa, 28.1% GRF) regions (Figure 3.2). The predicted foot contact area, 89.4 cm^2, also agreed with the literature, mean 101.2 cm^2 (SD 18.3) (Cavanagh et al., 1987). Finally, arch deformations and foot bone alignment compared very well with literature (Bandholm et al., 2008; Cavanagh et al., 1997; Williams and Mcclay, 2000) with 15 out of 22 measurements within one SD (Table 3.3).

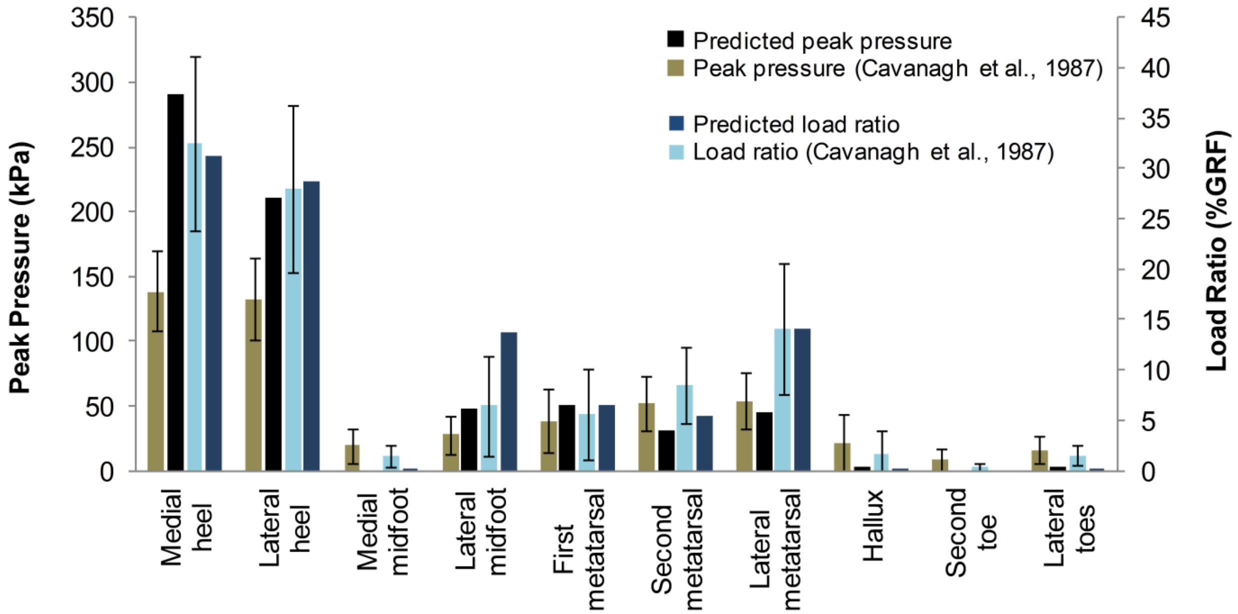

Figure 3.2: Summary of the predicted load ratio and plantar pressure during quiet stance compared to literature. Error bars indicate one SD.

Table 3.3: Finite element predicted foot bone alignments at quiet stance.

Reference	Parameter	FE Predicted	Literature [SD]
(Williams and Mcclay, 2000) n=102 feet	Navicular height (mm)	41.5[a]	34.6 [5.6]
	First ray angle (deg)	19.9 [a]	23.1 [2.9]
(Bandholm et al., 2008) n=15 feet	Navicular height (mm)	41.5	45.0 [8.0]
	Medial longtitudinal arch angle (deg)	156.3	151.5 [12.0]
(Cavanagh et al., 1997) n=50 feet	Navicular height (mm)	41.5	40.2 [8.2]
	Sesamoid height (mm)	6.8	7.6 [2.8]
	5th Metatarsal head height (mm)	8.9[a]	5.1 [1.7]
	5th Metatarsal base height (mm)	11.8	12.4 [3.4]
	Calcaneus height (mm)	7.2[a]	9.8 [2.4]
	Inferior calcaneal inclination (deg)	23.6	22.5 [6.1]
	Superior calcaneal inclination (deg)	18.6	21.3 [6.1]
	Chopart’s angle (deg)	64.2	62.0 [4.9]
	Navicular-medial cuneiform angle (deg)	61.1	62.3 [4.8]
	Lisfranc’s angle (deg)	64.3	63.2 [4.3]
	5th Metatarsal inclination (deg)	8.0	11.0 [3.0]
	1th Metatarsal inclination (deg)	19.9	21.3 [4.6]
	1st Proximal phalanx inclination (deg)	3.9	7.3 [7.7]
	Talar inclination (deg)	16.4 [a]	28.8 [4.5]
	Intermetatarsal 1-5 angle (deg)	18.3 [a]	22.9 [4.3]
	Intermetatarsal 1-2 angle (deg)	9.1	7.8 [2.7]
	1st Metatarsophalangeal angle (deg)	0.1 [a]	14.4 [8.8]
	1st Interphalangeal angle (deg)	14.5	10.4 [4.4]

[a] FE predicted value exceed ± 1SD of the literature.

For the clawed hallux model, the metatarsal head and hallux peak pressure response to the combination of EHL, FHL and PL extrinsic muscle forces compared reasonably well to the literature (Figure 3.3a and b). The model consistently under predicted the metatarsal head pressure (19.2 to 31.2 kPa), but was always within one SD. The model did a better job of predicting the hallux pressure (2.8 to 7.2 kPa under prediction in six cases and 16.5 to 18.0 kPa over prediction in two cases), again within one SD in all instances. The model under predicted MTPJ and IPJ angle changes in all but one of the overpull cases (Figure 3.3c and d). Three out of seven MTPJ predictions fell within one SD, and were within two SDs in all cases. Better prediction was obtained at the IPJ where five out of seven cases fell within one SD. (Including the four cases that the model generated a clawed hallux deformity were in this group.)

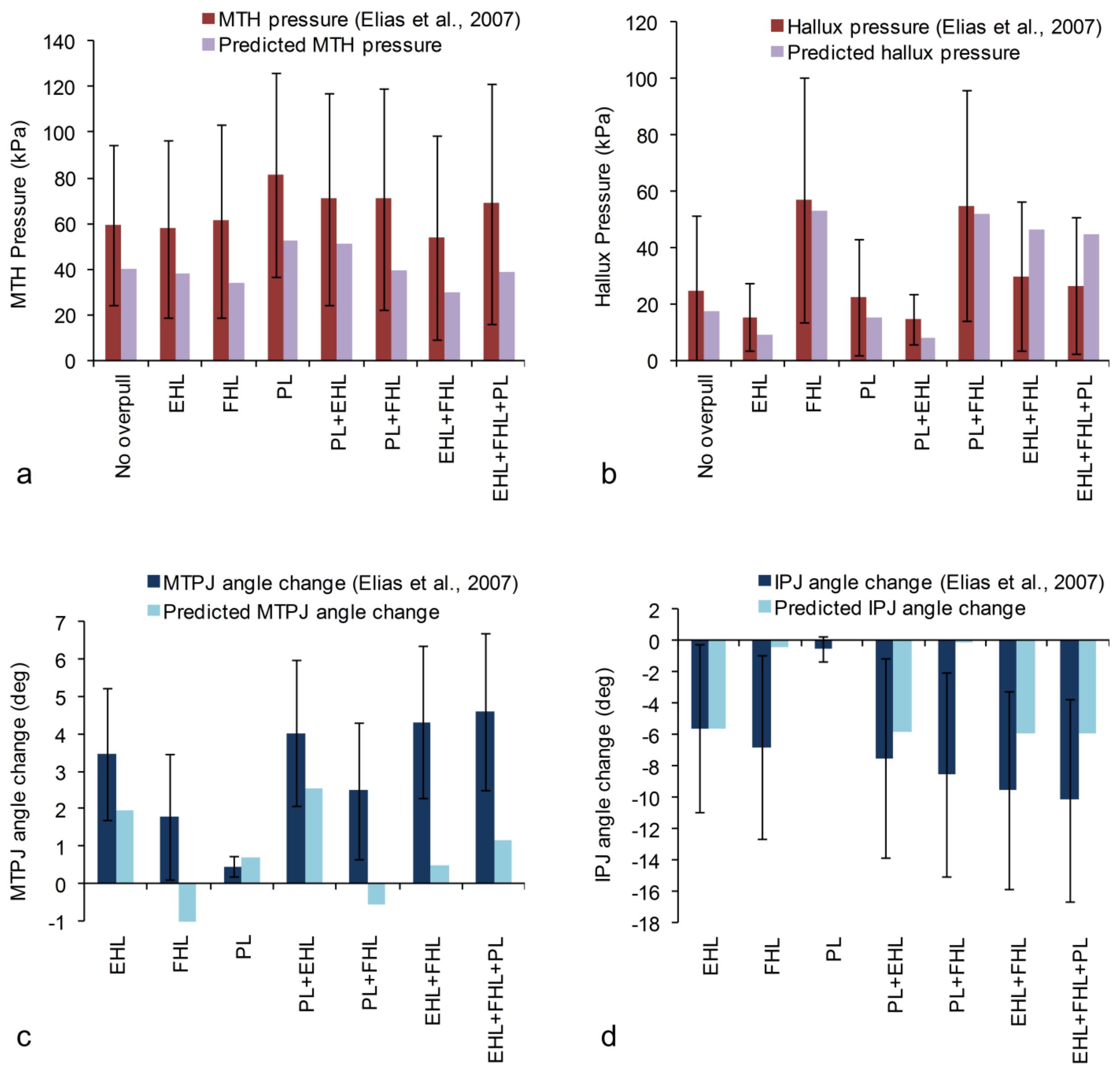

Figure 3.3: Predicted (a) metatarsal head and (b) distal hallux peak plantar pressure and (c) MTPJ and (d) IPJ angle change from extrinsic muscle overpulls compared to literature. Error bars indicate one SD. Positive (extension) and negative (flexion) angle change were measured relative to the bone alignment at no overpull.

3.4.2 Clawed hallux deformity

Of the seven overpull conditions, four (EHL, PL+EHL, EHL+FHL or EHL+FHL+PL) successfully generated a clawed hallux deformity by extending the MTPJ and flexing the IPJ (Table 3.4). The EHL and PL+EHL overpulls also elevated the distal hallux off the ground (Figure 3.4). Three overpull conditions (FHL, PL and PL+FHL) did not result in the angular changes seen with the clawed hallux deformity (Table 3.4) and will not be discussed further.

A very small increase in metatarsal head pressure (0.3 kPa) was found in clawed hallux from PL+EHL overpull. The other three clawed hallux cases (EHL, EHL+FHL and EHL+FHL+PL) showed reduction in metatarsal head pressure compared to the normal foot simulation, with the greatest effect (approximately 30 kPa) with the EHL and EHL+FHL conditions. The distal hallux was completely offloaded in EHL and PL+EHL overpulls, but increased to 26.1 and 29.7 kPa for the EHL+FHL and EHL+FHL+PL conditions, indicating the effect of FHL overpulling.

Table 3.4: Predicted joint angle change and hallux pressure change pre- and post-surgery.

	Overpull Cases	**MTPJ angle change (deg)** [a]	**IPJ angle change (deg)** [a]	**First metatarsal head pressure change (kPa)** [b]	**Distal hallux pressure change (kPa)** [b]
Pre Surgery	No overpull [c]	0.0	0.0	0.0	0.0
	successful clawed hallux				
	EHL	+10.2	-3.5	-28.1	-4.4 [e]
	PL+EHL	+10.6	-2.9	+0.3	-4.4 [e]
	EHL+FHL	+3.2	-15.2	-29.9	+26.1
	EHL+FHL+PL	+3.7	-14.5	-8.0	+29.7
	unsuccessful clawed hallux				
	FHL	-0.9	-2.9	-20.0	+75.3
	PL	+0.5	0.0	+27.8	-1.0
	PL+FHL	-0.7	-2.0	-5.3	+74.2
Post-surgery: Modified Jones [d]	EHL	-3.2	n/a	-39.5	-2.3
	PL+EHL	-2.6	n/a	-22.5	-2.9
	EHL+FHL	-6.0	n/a	-47.4	+66.6
	EHL+FHL+PL	-5.3	n/a	-40.5	+63.7
Post-surgery: FHL Transfer	EHL	+10.0	-1.2	-28.7	-4.4 [e]
	PL+EHL	+10.5	-0.5	+0.5	-4.4 [e]
	EHL+FHL	+0.4	+1.3	-18.8	-4.4 [e]
	EHL+FHL+PL	+0.6	+1.8	+5.4	-4.4 [e]

[a] Positive (extension) and negative (flexion) angle change were measured relative to the foot with no overpull.

[b] Pressures at equilibrium were measured across 14x14 mm^2 area (7x7 elements) then averaged over 0.05s simulation time. Positive (above normal) and negative (below normal) pressure changes were measured relative to the foot with no overpull.

[c] Pre-surgical joint angle (MTPJ 15.5° extension and IPJ 14.9° flexion), average plantar pressure at the metatarsal head (88.3 kPa) and distal hallux (4.4 kPa) were taken from foot with no overpull.

[d] The IPJ was fused at an unloaded neutral configuration.

[e] Distal hallux was lifted off the ground.

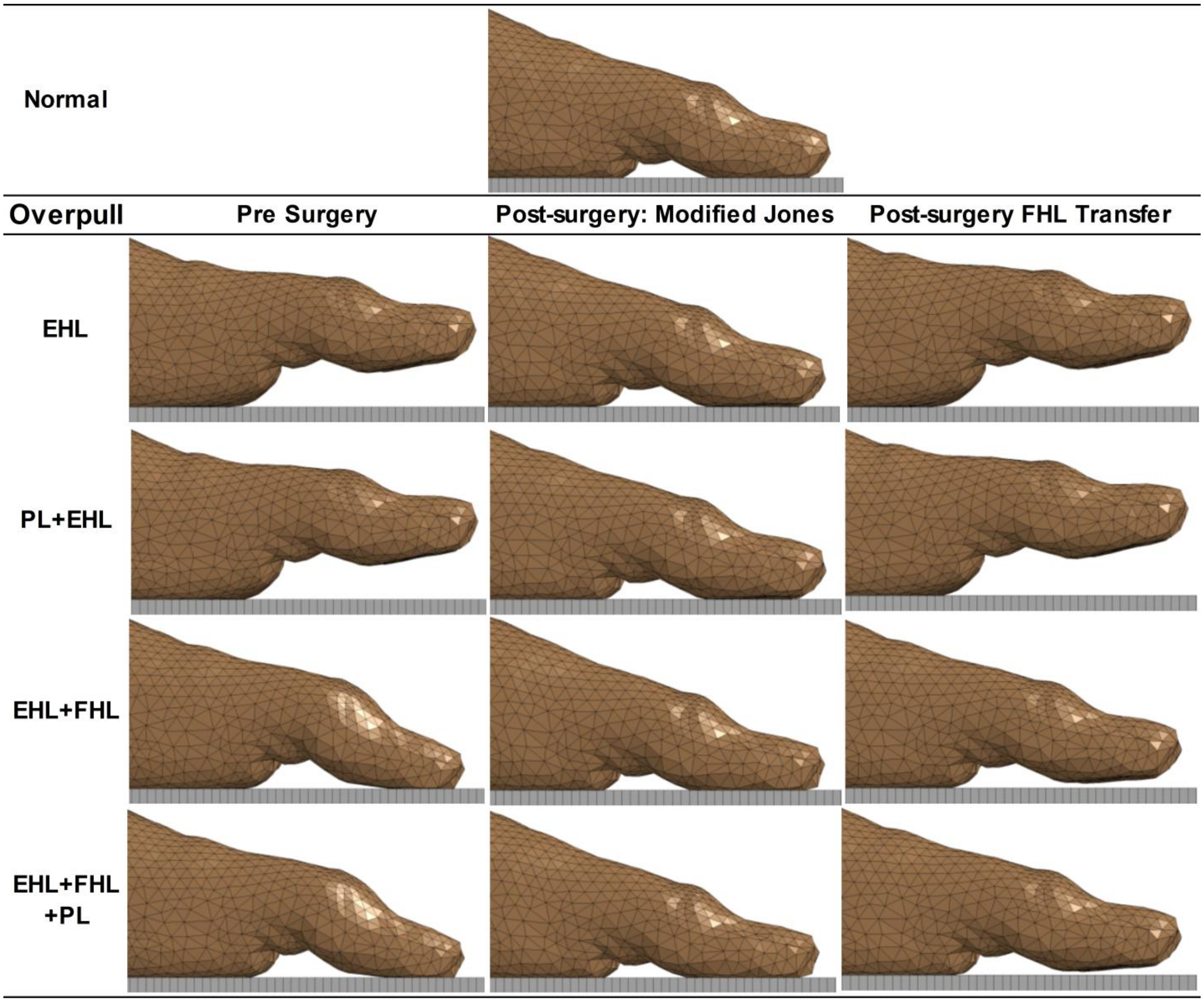

Figure 3.4: Predicted deformity in four clawed hallux cases pre-and post-surgery.

3.4.3 Modified Jones procedure

The modified Jones procedure caused MTPJ flexion in all four clawed hallux simulations and since the IPJ was fused, there was no change in this joint (Table 3.4). The procedure also reduced pressure under the metatarsal head in every instance, but flexion at the MTPJ brought the distal hallux into contact with the ground and, in two cases, generated a large increase in contact pressure (64 to 67 kPa), probably due to the unopposed FHL.

3.4.4 FHL tendon transfer procedure

The FHL tendon transfer procedure reduced the MTPJ extension to near normal in two clawed hallux cases (EHL+FHL and EHL+FHL+PL), but showed persisted hyperextension in the other two cases (EHL and PL+EHL). The IPJ flexion was reduced to with 1.8˚ from normal alignment in all four conditions. The simulations showed increased metatarsal head pressure from pre-surgery in two clawed hallux cases (EHL+FHL and EHL+FHL+PL), but negligible change for the other two cases (EHL and EHL+PL). All four clawed hallux simulations with the FHL tendon transfer had the distal hallux elevated off the ground which resulted in zero contact pressure.

3.5 Discussion

Our FE model incorporates several potential improvements, including: detailed cartilage, plantar fascia and plantar fat anatomy, nonlinear ligament properties, and inclusion of extrinsic muscle tendons that are able to wrap around bones. The clawed hallux deformity, caused by extrinsic muscle imbalances, is often associated with ulcer formation. This study generated a non-pathological foot, afflicted it with a clawed hallux deformity using muscle imbalances, then explored the utility of two surgical treatments to correct this deformity.

3.5.1 FE model validation

The validation at quiet stance agreed with plantar loading data observed clinically (Cavanagh et al., 1987); the load ratios of 7 in 10 regions were within one SD (Figure 3.2). Predicted plantar pressures were within one SD in 4 out of 10 regions, while 8 of 10 were within 2 SD. Foot bone alignment showed good correlation (68.2% of the measurements within one SD) with other studies (Bandholm et al., 2008; Cavanagh et al., 1997; Williams and Mcclay, 2000). This demonstrates that our foot model has the correct static alignment and distributing load correctly.

The discrepancy of plantar pressure in quiet stance validation, especially at the hindfoot (109% above average) and the midfoot (71% above average), despite well predicted load ratios, could have resulted from the 70 N preload during scanning and the subsequent modification of the soft tissue by stiffening of the hindfoot plantar fat - this modification was necessary to obtain physiologic strains during our simulations. Ultimately the results were still not ideal and the non-physiologic force distribution caused high peak pressure. Visually, the preload primarily influenced the hindfoot region, while the forefoot region, which is the focus of this study, was minimally affected. Future models will use feet scanned in an unloaded position to eliminate this pre-straining of the plantar tissue.

The validation of extrinsic muscle overpulls involved in generating the clawed hallux showed a good agreement (all 16 comparison were within one SD of the mean) with the reported peak pressure by Elias et al. (2007). Concerning the angular changes, 8 of 14 values were within one SD. In 15 of 16 cases, our model underpredicted the joint rotations. It is likely that this was due to extra generic soft tissue in the joints, leading to less than physiologic motions. Specifically, nothing in the model prevented the generic soft tissue elements from filling all the space between the bones. Greater realism may be achieved by modeling the joint capsules and accounting for synovial fluid within the joint.

3.5.2 Clawed hallux deformity

The clawed hallux deformity was generated either with large extension at the MTPJ (EHL or PL+EHL) or with large IPJ flexion (EHL+FHL or EHL+FHL+PL). The overpull combinations of EHL+FHL and EHL+FHL+PL resulted in the most severe clawed hallux. Comparing the absolute angles, the deformity predicted by the models (18.7˚ or 19.2˚ MTPJ extension, 30.1˚ or 29.4˚ IPJ flexion) was smaller for the MTPJ, but nearly similar for the IPJ compared to actual clawed hallux patients (37.7˚ MTPJ extension, 28.1˚ IPJ flexion) (Kadel et al., 2005). The MTPJ discrepancy is not surprising as the deformity occurs over time *in vivo*. As with the validation studies, extra generic soft tissue in the joint space may have reduced the range of motion.

The pre-surgical clawed hallux simulations showed a decrease in metatarsal head pressure, in contrast to a large peak pressure increase observed in a similar population of clawed toe patients (72%) (Bus et al., 2005). Comparing isolated muscle overpulls (Table 3.4), it appears that EHL is responsible for the decrease in pressure; the exact mechanism is not known.

3.5.3 Modified Jones procedure

The modified Jones procedure successfully reduced joint deformity in all four clawed hallux cases (EHL, PL+EHL, EHL+FHL and EHL+FHL+PL). The procedure restored normal joint alignment by removing extension across the MTPJ and fusing the IPJ. Post-surgically, the EHL tendon acted on the metatarsal neck to elevate the metatarsal head and reduced the plantar pressure. Distal hallux pressure was restored to within 2.9 kPa from normal in EHL and PL+EHL overpulls, but was further exacerbated in the EHL+FHL and EHL+FHL+PL overpulls due to the strong unbalanced FHL force. Tension from the FHL tendon flexed the MTPJ, pressing the distal hallux (with fused proximal and distal phalanges) down, increasing plantar pressures in this region.

Possible complications could result from the modified Jones procedure. Our simulations showed decreased post-surgical plantar pressure at the metatarsal head compared to pre-surgical; which could relieve pain and promoted ulcer healing. However, the redistributed plantar pressure could put higher loads on other plantar regions. Flexion at the MTPJ from the unopposed FHL could prevent normal extension of the hallux (Döderlein et al., 2000). Another potential complication with the modified Jones procedure was IPJ immobility. The current FE model fused the IPJ at the unloaded neutral configuration, clinical recommendations range from 5.0˚ extension (Döderlein et al., 2000) to neutral (Wülker et al., 2005). It is possible that the post-surgery over pressure seen under the distal hallux with the EHL+FHL and EHL+FHL+PL overpulls could have been mitigated by fusing the IPJ in extension. This should be considered with caution, as fusing IPJ in extension poses the risk of over-loading a minimally padded region of the hallux.

3.5.4 FHL tendon transfer procedure

The FHL tendon transfer procedure was found effective in reducing joint deformity and plantar pressure at the hallux in the EHL+FHL and EHL+FHL+PL overpulls. The IPJ rotation was decreased by eliminating flexion force from the FHL tendon distally to the joint. The MTPJ deformity was corrected by moving the FHL to the proximal phalange. We found that plantar pressure under the metatarsal head was increased from pre-surgery in EHL+FHL and EHL+FHL+PL overpull. Pressure was above normal in

EHL+FHL+PL overpull due to a strong PL overpull force depressing the metatarsal head. The FHL tendon transfer failed to correct joint deformity resulting from EHL and PL+EHL overpull due to insufficient FHL force to counter balance the EHL overpull force.

The FHL tendon transfer procedure predicted post-surgical increased metatarsal head pressure in the EHL+FHL and EHL+FHL+PL overpulls, which could lead to complications. Clinically, 2 out of 10 patients that underwent FHL tendon transfer were dissatisfied with the outcome due to significant pain under the metatarsal head during athletic activity (Steensma et al., 2006). Kadel et al. (2005) transferred PL to PB 11 times concomitant to 22 FHL tendon transfers. There was no literature report of uncorrected clawed hallux deformity with the FHL tendon transfer, in contrast to the FE prediction of two uncorrected conditions. This could be a result from the concomitant procedures performed clinically, which we did not investigate.

3.5.5 Model limitations

The analysis was performed at an instance of the gait cycle using a single set of overpull forces. The model uses linear tetrahedral elements, which have been shown to be overly stiff when compared to hexahedral or higher order tetrahedral elements. Skin and muscles were grouped together into a single encapsulated soft tissue volume. Mechanical properties of untested ligaments were extrapolated from our ligament database using ligament length from the FE model as an input. Additionally, intrinsic muscle function was neglected. Finally, we only modeled a single foot.

3.6 Conclusion

Our FE foot model incorporated improvements in cartilage, ligament, tendon, plantar fascia and plantar fat, and was used to explore the clawed hallux deformity and its surgical treatments. This paper represents our group’s ongoing efforts to improve our computational foot model. The combinations of muscle overpulls tested indicated that there could be multiple scenarios that lead to the clawed hallux deformity. The analysis suggested that the modified Jones procedure is more suited to treating the clawed hallux deformity in the absence of FHL overpull. However, this procedure required fusion of the IPJ. The

FHL tendon transfer is well suited when FHL overpull is present. An additional procedure to reduce the metatarsal head pressure may be required concomitant to the FHL tendon transfer procedure.

Chapter 4. Hyperelastic compressive mechanical properties of the subcalcaneal soft tissue: An inverse finite element analysis

4.1 Abstract

Finite element (FE) foot models can provide insight into soft tissue internal stresses and allow researchers to effectively conduct parametric studies. Accurate plantar soft tissue material properties are essential to the development of FE foot models for clinical interventions. The aim of this study was to identify the first-order and second-order Ogden hyperelastic coefficients of the subcalcaneal soft tissue using an inverse FE analysis. The cylindrical soft tissue FE model was developed based on *a priori in vitro* dynamic compression experiment. The model simulated a 1 Hz triangle wave displacement to apply a compressive strain up to 48%. The hyperelastic coefficients were identified by systematically varying the material parameters to minimize the difference between the model predicted force and the target experimental data. Optimal material coefficients were obtained (μ_1 = 0.0235 kPa and α_1 = 12.07 for the first-order Ogden model and μ_1 = -4.629x10^{-6} kPa, α_1 = -16.829; μ_2 = -1.613 kPa and α_2 = -1.043 for the second-order Ogden model). The second-order Ogden model was superior in capturing the highly nonlinear force-deformation response when compared to the first-order model (root mean square error (RMSE) 0.169 N vs 0.570 N). The material sensitivity analysis indicated that the predicted force was strongly affected by the Poisson’s ratio (12-fold increase in RMSE when reducing Poisson’s ratio by 10% from the baseline) and the coefficient α_1 (3.2-fold and 32-fold increase in RMSE for both first-order and second-order Ogden models when increasing α_1 by 10% from the optimal value).

4.2 Introduction

Finite element (FE) analysis of the foot has been used to predict plantar pressure (Budhabhatti et al., 2009; Chen et al., 2012; Cheung and Zhang, 2008; Isvilanonda et al., 2012), visualize internal soft tissue stress distributions (Chen et al., 2010; Gefen, 2003), perform parametric studies (Budhabhatti et al., 2009; Chen et al., 2012; Cheung et al., 2004, 2006a) and design pressure relief insoles and orthoses (Chen et al., 2003; Cheung and Zhang, 2005; Erdemir et al., 2005). The accuracy of the model predictions depends greatly on physiologic material properties and anatomical data.

Hyperelastic material models, e.g., generalized polynomials (Cheung et al., 2006a; Lemmon et al., 1997), Mooney-Rivlin (Miller-Young et al., 2002) and Ogden (Chen et al., 2012; Chokhandre et al., 2012; Erdemir et al., 2006; Isvilanonda et al., 2012; Spears et al., 2007), are widely used to approximate plantar soft tissue materials. The force-deformation response of the plantar soft tissues can be obtained directly from *in vitro* uni-axial compression tests (Ledoux and Blevins, 2007; Miller-Young et al., 2002; Pai and Ledoux, 2010). From this type of testing, hyperelastic coefficients can be identified using non-linear regression of analytical models (Miller-Young et al., 2002; Natali et al., 2010). These analytical models are often developed for simple specimen geometries and loading scenarios, and therefore require input data from specific material testing methods (e.g., frictionless uni-axial tension/compression). Alternatively, researchers have used heel-pad indentation to obtain structural force-deformation responses from intact feet (Erdemir et al., 2006; Lemmon et al., 1997). The complicated anatomy and boundary conditions associated with these tests require identification of hyperelastic coefficients through an inverse FE analysis (Chokhandre et al., 2012; Erdemir et al., 2006; Gu et al., 2010; Halloran and Erdemir, 2011).

Previously, our group investigated the compressive mechanical response of the *in vitro* plantar fat tissue samples (Pai and Ledoux, 2010). Due to the no-slip boundary condition and large deformation imposed in these experiments, the reported stress-strain data are unsuitable for direct application to analytical model regression, therefore we explored the use of inverse FE analysis to quantifying the compressive Ogden hyperelastic coefficients of the subcalcaneal fat.

4.3 Methods

4.3.1 Material testing

The detailed preparation and testing protocol of the plantar soft tissue samples are described elsewhere (Pai and Ledoux, 2010). Briefly, each specimen (cylinder, 19.05 mm diameter) was isolated from the plantar skin and bone. The specimen was constrained between two loading platens using 220 grit sand paper and maintained under physiologic temperature (35 °C) and humidity (near 100%) inside an environmental chamber. Displacement control triangle waves were used to compress the tissue to an average of 48% strain. Of the five tested frequencies (1, 2, 3, 5 and 10Hz), the 1Hz results from the subcalcaneal region of the non-diabetic samples (n=9) were used for the work presented here. Three loading and unloading force-deformation cycles were averaged to yield an estimate of purely elastic force-deformation which was used as the inverse FE analysis target data (Figure 4.1).

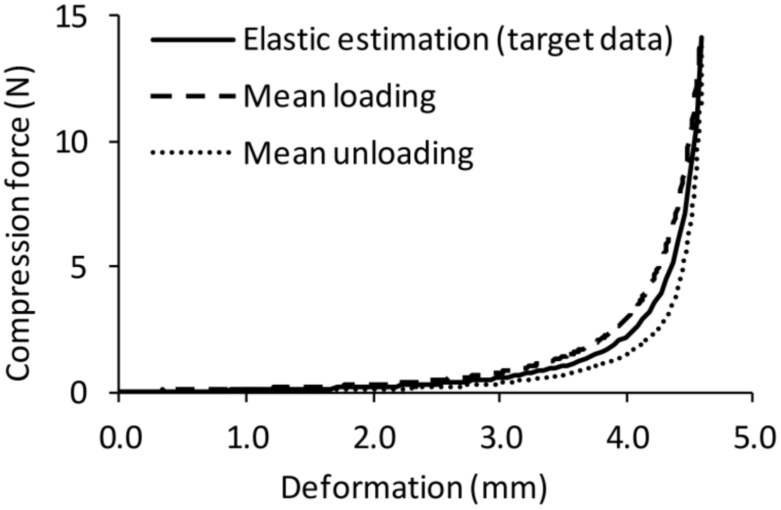

Figure 4.1: The mean elastic compressive force-deformation response (solid line) approximated by averaging the loading (dash line) and unloading (dotted line) cycles of the 1Hz cyclic test of the plantar soft tissue (Pai and Ledoux, 2010). The peak force and displacement were 14.12 N and 4.60 mm, respectively.

4.3.2 Finite element model

A finite element model of the uni-axial compression test (Figure 4.2) was created in LS-Prepost (Livermore Software, Livermore, CA) to simulate the plantar soft tissue specimens. The structure was halved due to symmetry. The model size (from the averaged specimen diameter and thickness of 19.05 mm and 9.54 mm, respectively) was assigned. Mesh refinement analysis was performed on the geometry to obtain convergence of the force-deformation output, i.e., an 8-fold increase in the total number of elements lead to only a 3.0% change in the force-deformation response (data not shown). The final soft tissue model consisted of 2,160 hexahedron elements (constant stress solid element) (Hallquist, 2006).

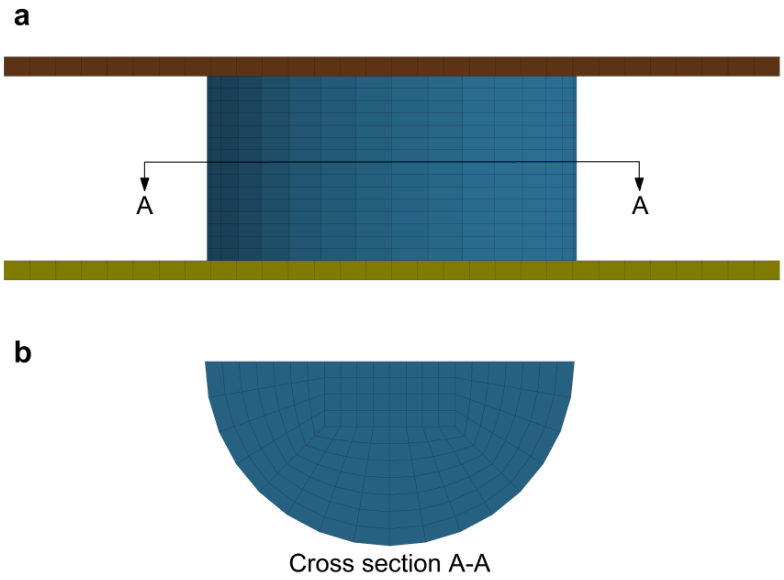

Figure 4.2: Finite element model of the uni-axial compression test of the plantar soft tissue cylinder (halved due to symmetry). Concerning boundary conditions: no slip (fixed) was permit at the soft tissue-platen interfaces to emulate the experimental set up.

The soft tissue was modeled as a homogeneous, isotropic, nearly-incompressible Ogden hyperelastic material (material type 77 in LS-DYNA) (Hallquist, 2006). The strain energy function is represented by equations 4.1-4.5.

$$W(\lambda_1, \lambda_2, \lambda_3) = \sum_{m=1}^{n} \frac{\mu_m}{\alpha_m}\left(\tilde{\lambda}_1^{\alpha_m} + \tilde{\lambda}_2^{\alpha_m} + \tilde{\lambda}_3^{\alpha_m} - 3\right) + \frac{1}{2}K(J-1)^2 \tag{4.1}$$

$$K = \frac{(1+v)}{3(1-2v)}\sum_{m=1}^{n}\mu_m \alpha_m \tag{4.2}$$

$$J = \lambda_1 \lambda_2 \lambda_3 \tag{4.3}$$

$$\tilde{\lambda}_i = J^{-1/3}\lambda_i \tag{4.4}$$

$$\mu_m\alpha_m > 0 \qquad \text{(for each } m = 1,\ldots, n\text{)} \tag{4.5}$$

where $\lambda_1, \lambda_2, \lambda_3$ are the three principal stretches, the Jacobian, *J,* denotes the relative volume change, and $\tilde{\lambda}_i$ are the deviatoric principal stretches. Density (ρ = 1.00 gram/cm^3), Poisson's ratio (v) and hyperelastic coefficients (μ_m and α_m) are the material parameters. Bulk modulus, *K*, can be derived from equation 4.2. Coefficients μ_m and α_m are the design variables that will be optimized. The product of μ_m and α_m is constrained according to equation 4.5 to ensure physiologic response and material stability (Ogden et al., 2004), i.e., this product must be positive. The first-order (n = 1) and second-order (n = 2) Ogden hyperelastic models were analyzed. Poisson's ratio (v = 0.4999) was estimated from the longitudinal wave velocity in subcutaneous fat (C_L = 1,476 m/s) (Duck, 1990), density (ρ) and Young's modulus (E = 674 kPa) (Pai and Ledoux, 2010) by solving equation 4.6 (Duck, 1990).

$$C_L = \left[\frac{E(1-v)}{\rho(1-2v)(1+v)}\right]^{\frac{1}{2}} \tag{4.6}$$

The sand paper-soft tissue interface was reproduced in the FE model by rigidly constraining the superior and inferior soft tissue surfaces to the rigid loading platens, i.e., a no-slip boundary condition. Nodes along the plane of symmetry were constrained to prevent movement in the normal direction. Potential model instabilities include non-physiologic deformation and high hourglass energy larger than 10% of the internal energy (Miller, 2011). To avoid such instabilities, we implemented the following LS-DYNA parameters: global damping (damping constant, 35; i.e., 10% of the lowest natural frequency), hourglass controlling (IHQ = 4; QM = 0.002 to 0.025) and automatic time stepping. Compression was applied by translating the inferior platen toward the fixed superior platen using a linear ramp from 0 to 4.60 mm (48% strain) in 0.5 s (comparable to a 1hz triangle wave). The reaction force on the upper platen from the half symmetric model was doubled to represent the full geometry. The model deformation and force-deformation response were validated with analytical solutions (i.e., mathematical equations that describe force and deformation of a fixed-end cylinder under axial compressive strain) up to 30% strain (Klingbeil and Shield, 1966; Miller, 2005).

4.3.3 Material parameter identification

The Ogden hyperelastic material coefficients (μ_m and α_m) were identified by minimizing the difference between the model predicted force and the target experimental data in LS-OPT (Livermore Software, Livermore, CA). A sequential response surface method (SRSM) optimization technique (Stander et al., 2010) was used. The design space ($0 < | \mu_m | < 0.05$ MPa, $0.1 < | \alpha_m | < 70$) was estimated based on prior literature (Erdemir et al., 2006; Gu et al., 2010; Spears et al., 2007) and pilot simulations. The inverse analysis began by randomly selecting initial guesses for the material parameters (Table 4.1a and b) in MATLAB (MathWorks, Natick, MA). For the first-order model, five random positive μ_m and α_m initial values were chosen, and then the negatives of the same values were calculated, resulting in ten initial guesses. Similarly, for the second-order model, five random positive μ_m and α_m initial values were chosen, and then the corresponding double positive and double negative combinations were used, resulting in 20 initial values. For each initial guess, a D-optimal point selection algorithm (Stander et al., 2010) in LS-OPT chose a subset of μ_m and α_m from the region of interest; the number of experiments (i.e., the number of unique μ_m and α_m pairs) in each subset ranged from 8 to 42. In the first iteration, the region of interest was defined as the entire design space. Next, a series of FE models were generated and solved in LS-DYNA (version 971d R5.1.1 explicit analysis). The computations were performed on two Dell PowerEdge R610 rack servers (each has two-six core 3.46GHz Intel® Xeon® processors). The optimization objective function was defined as a normalized mean square error (nMSE) between the predicted platen reaction forces and the target data (i.e., MSE per peak target force squared). A response surface (i.e., nMSE as a function of design variables) was generated from the simulation results using a linear regression. The optimal parameter set for each iteration was identified from the response surface using a hybrid adaptive simulated annealing optimization algorithm (Stander et al., 2010). In subsequent iterations, a new region of interest was defined and centered about the optimal point from the previous iteration. Iteration progress was made by moving the center of the region of interest and reducing its size (shrink factor = 0.6 to 1). The optimization continued until termination criteria, equations 4.7 and 4.8, both became active.

$$\left| \frac{f^{(k)} - f^{(k-1)}}{f^{(k-1)}} \right| < \varepsilon_f \tag{4.7}$$

$$\frac{\left\| x^{(k)} - x^{(k-1)} \right\|}{\left\| d \right\|} < \varepsilon_x \tag{4.8}$$

where ε_f denotes the objective function accuracy, ε_x refers to the design accuracy, *f* is the nMSE, *x* refers to the vector of design variables, *d* denotes the size of the design space, and *(k)* and *(k-1)* refer to two successive iteration numbers. In this study, $\varepsilon_f = \varepsilon_x = 0.00001$ were used.

Table 4.1a: The initial and optimal first-order Ogden hyperelastic coefficients (μ_1 and α_1) from the inverse finite element analyses.

	Initial coefficients[†]		Initial RMSE (N)	Optimal coefficients[††]		Optimal RMSE (N)
	μ_1 (MPa)	α_1		μ_1 (MPa)	α_1	
1	2.254e-5	1.089	2.524	2.369e-5	12.052	0.570
2	6.896e-3	12.479	870.478	2.333e-5	12.083	0.570
3	6.508e-4	1.999	2.161	2.371e-5	12.050	0.570
4	2.933e-2	0.318	2.416	2.326e-5	12.090	0.570
5	7.664e-4	4.623	1.333	2.367e-5	12.055	0.570
6	-2.254e-5	-1.089	2.518	-1.649e-5	-8.216	0.585
7	-6.896e-3	-12.479	8736.321	-1.633e-5	-8.230	0.585
8	-6.508e-4	-1.999	1.776	-1.630e-5	-8.234	0.585
9	-2.933e-2	-0.318	3.859	-1.631e-5	-8.232	0.585
10	-7.664e-4	-4.623	5.472	-1.638e-5	-8.227	0.585

[†] Five sets of the first-order material coefficients were randomly generated. Both positive and negative coefficients (μ_1 and α_1) were used resulting in 10 initial guesses.

[††] Due to small differences in RMSE from initial guesses 1 to 5, the final optimal coefficients (μ_1 = 2.353e-5 MPa and α_1 = 12.066) were calculated by averaging the optimal coefficients from initial guesses 1 to 5.

Note that LS-OPT evaluates optimizations using normalized mean square error (nMSE), which was converted to root mean square error (RMSE) for ease of understanding.

Table 4.1b: The initial and optimal second-order Ogden hyperelastic coefficients (μ_1, α_1 , μ_2 and α_2) from the inverse FE analyses.

	Initial coefficients[†]				Initial RMSE (N)	Optimal coefficients				Optimal RMSE (N)
	μ_1 (MPa)	α_1	μ_2 (kPa)	α_2		μ_1 (MPa)	α_1	μ_2 (MPa)	α_2	
1	1.666e-6	53.788	0.112	1.771	n/a[*]	9.685e-9	24.326	1.004e-3	2.001	0.189
2	7.817e-8	48.041	1.556	2.282	501.683	1.215e-8	23.981	3.066e-3	0.630	0.193
3	1.143e-5	26.798	0.633	0.618	73.763	1.231e-8	23.962	2.112e-3	0.927	0.193
4	4.615e-7	30.506	0.587	0.543	25.472	1.158e-8	24.056	1.635e-3	1.217	0.193
5	5.671e-8	28.629	2.815	9.462	163.316	1.151e-8	24.070	2.923e-3	0.662	0.193
6	1.666e-6	53.788	-0.112	-1.771	501.954	4.844e-9	25.419	-3.164e-3	-0.563	0.186
7	7.817e-8	48.041	-1.556	-2.282	501.962	4.734e-9	25.451	-2.902e-3	-0.612	0.185
8	1.143e-5	26.798	-0.633	-0.618	73.767	5.114e-9	25.336	-3.279e-3	-0.543	0.186
9	4.615e-7	30.506	-0.587	-0.543	25.476	2.422e-9	26.498	-1.550e-3	-1.081	0.178
10	5.671e-8	28.629	-2.815	-9.462	453.376	4.777e-9	25.439	-3.034e-3	-0.587	0.186
11	-1.666e-6	-53.788	0.112	1.771	125.514	-3.796e-9	-17.025	7.464e-4	2.696	0.171
12	-7.817e-8	-48.041	1.556	2.282	115.811	-1.020e-8	-16.002	1.694e-3	1.176	0.184
13	-1.143e-5	-26.798	0.633	0.618	21.875	-6.361e-9	-16.489	9.104e-4	2.215	0.177
14	-4.615e-7	-30.506	0.587	0.543	7.200	-6.252e-9	-16.510	9.023e-4	2.223	0.177
15	-5.671e-8	-28.629	2.815	9.462	426.134	-9.693e-9	-16.055	1.566e-3	1.277	0.184
16	-1.666e-6	-53.788	-0.112	-1.771	130.265	-7.482e-9	-16.326	-3.139e-3	-0.561	0.176
17	-7.817e-8	-48.041	-1.556	-2.282	118.279	-4.894e-9	-16.772	-2.152e-3	-0.817	0.173
18	-1.143e-5	-26.798	-0.633	-0.618	22.788	-7.487e-9	-16.325	-4.470e-3	-0.406	0.178
19	-4.615e-7	-30.506	-0.587	-0.543	8.043	-2.602e-9	-17.457	-3.806e-3	-0.504	0.181
20[‡]	-5.671e-8	-28.629	-2.815	-9.462	297.001	**-4.629e-9**	**-16.829**	**-1.613e-3**	**-1.043**	0.169

[†] Five sets of the second-order material coefficients were randomly generated. Both positive and negative coefficients (μ_1, α_1 , μ_2 and α_2) were used resulting in 20 initial guesses.
[‡] The final optimal coefficients which resulted in the minimum RMSE are shown in bold.
[*] Initial material coefficients resulted in an unstable simulation.
Note that LS-OPT evaluates optimizations using normalized mean square error (nMSE), which was converted to root mean square error (RMSE) for ease of understanding.

After the optimal Ogden hyperelastic coefficients were identified, parametric analyses were performed to evaluate the model's sensitivity to the material coefficients μ_m and α_m (perturbing each parameter by ± 10% from the optimum) and Poisson's ratio (varying from 0.45 to 0.49999).

4.4 Results

At 30% compression, both the first-order and second-order FE models reproduced deformation that was within 3.6% of the peak deformation of the analytical solution. The predicted force-deformation response (Figure 4.3) was between the analytical solutions of the two hyperelastic material model extremes (root mean square error (RMSE) = 0.05 N and 0.1 N compared to the neo-Hookean material and 0.06 N and 0.02 N compared to the extreme-Mooney material).

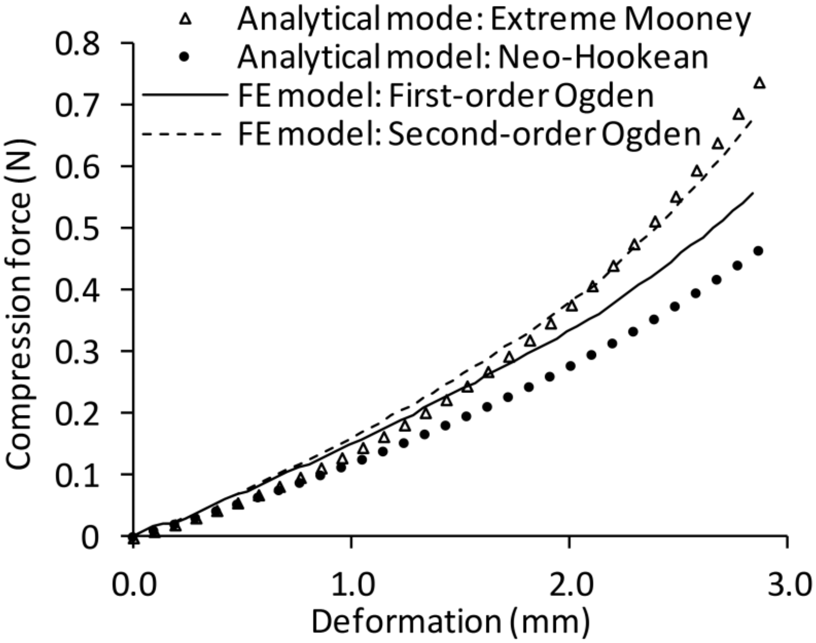

Figure 4.3: The first-order (μ_1 = 1 kPa and α_1 = 2) and second-order (μ_1 = 0.5 kPa, α_1 = 2, μ_2 = -0.5 kPa and α_2 = -2) finite element (FE) analysis showed root mean square error of 0.05 N and 0.1 N compared to the analytical solution of the neo-Hookean material and 0.06 N and 0.02 N compared to the Extreme-Mooney material (Klingbeil and Shield, 1966). An initial shear modulus of 1kPa was arbitrarily chosen for verification.

The optimal hyperelastic coefficients of the subcalcaneal fat were identified from the inverse FE analyses (Tables 4.1a and b, and Figure 4.4). The first-order Ogden model (analysis time 42 hours) fits the target data with 0.570 N RMSE (4.0% of the peak target force), while the second-order Ogden model (analysis time 58 hours) fits the target data with 0.169 N RMSE (1.2% of the peak target force). Variations in the second-order optimal material coefficients were observed (Table 4.1b) while the RMSE remained approximately unchanged (i.e., compare the ninth and eighteenth analysis results in Table 4.1b).

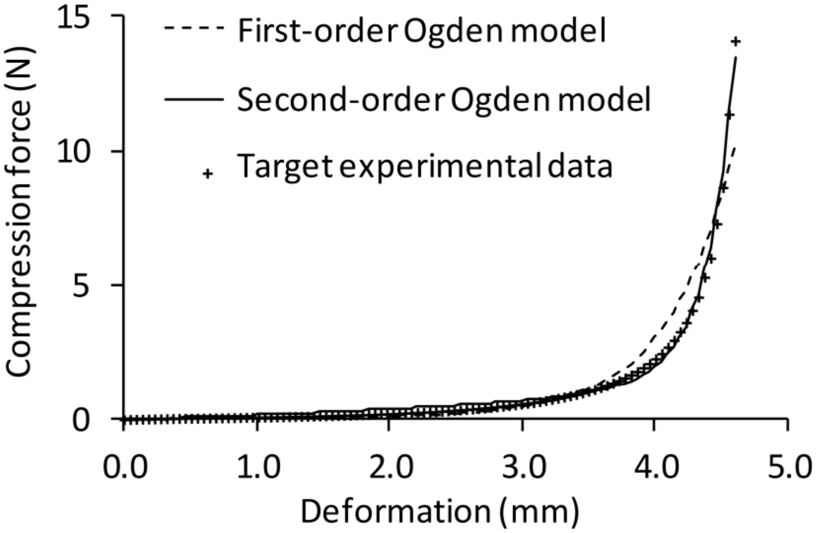

Figure 4.4: Optimized force-deformation response of the first-order Ogden model (dash line) fits the target experimental data (+) with a 0.570 N RMSE, while the second-order Ogden model (solid line) fits the experimental data with 0.169 N RMSE. The optimal coefficients were μ_1 = 2.353e-5 MPa, α_1 = 12.066 for the first-order Ogden model and $\mu_1 = -4.629\text{x}10^{-9}$ MPa, α_1 = -16.829, $\mu_2 = -1.613\ \text{x}10^{-3}$ MPa, α_2 = -1.043 for the second-order Ogden model.

The material sensitivity analysis indicated that coefficient α_1 and Poisson's ratio have substantial influence on the predicted force (Figure 4.5). A ten percent increase in coefficient α_1 resulted in 3.2-fold and 32-fold increase in RMSE from the baseline values for the first-order and second-order Ogden model, respectively. (Note RMSE just quantifies difference, not direction; Figure 4.5 relates whether the force vs. deformation curves became stiffer or less stiff.) Perturbing other material coefficients (μ_1, μ_2 and α_2) resulted in relatively smaller changes (9% to 48% RMSE increase at 10% change of the parameters). Decreasing Poisson's ratio from 0.4999 to 0.45 resulted in a 12-fold increase in RMSE and a less stiff force-deformation curve. Conversely, increasing Poisson's ratio from the baseline to 0.49999 stiffened the material and caused a 94% increase in RMSE.

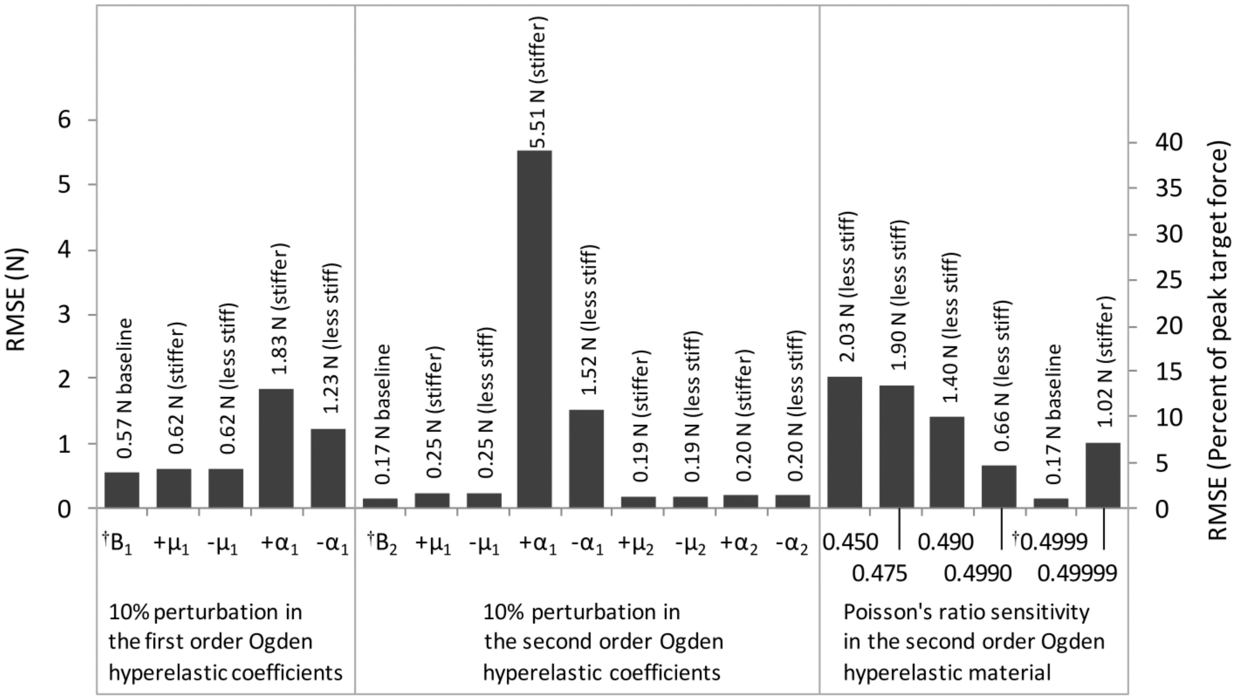

Figure 4.5: Root mean square error (RMSE) increased 3.2 fold or 32 fold when coefficient α_1 was perturbed 10% from the baseline values for the first and second Ogden models, respectively. A 10% decreased Poisson's ratio resulted in a 12-fold increase in RMSE. RMSE was calculated between model predictions and the target experimental data, while "(stiffer)" and "(less stiff)" refers to whether the force vs. deformation curve was above or below the baseline curve. †Baseline simulations were generated using optimal material parameters.

4.5 Discussion

The subcalcaneal fat material parameters were successfully characterized from previously obtained experimental data via an inverse FE analysis. Both first-order and second-order FE models used in this study predicted force and deformation that were in good agreement with the analytical solutions. The optimization results indicated that the second-order Ogden model is superior in capturing the non-linear force-deformation response compared to the first-order model, but requires approximately 38% longer computation time. The models were highly sensitive to α_1 and Poisson's ratio, but less sensitive to the other coefficients (μ_1, μ_2 and α_2).

The Poisson's ratio sensitivity analysis suggests that the selection of a near incompressible Poisson's ratio is highly critical. The chosen Poisson's ratio in this study (v = 0.4999) is greater than previously assumed in the plantar soft tissue literature, e.g., $v = 0.452$ (Chen et al., 2010; Cheung and Zhang, 2008), 0.475 (Chokhandre et al., 2012; Petre et al., 2013) and 0.49 (Isvilanonda et al., 2012) and potentially resulted in a stiffer model behavior.

To compare to the literature, our optimal second-order Ogden coefficients were input into a one-element model of unit size and unconfined nodal constraints. Compared to the unconfined compression data from Miller-Young et al. (2002), our model has a similar final slope, but a longer toe region (Figure 4.6); however, direct comparison of coefficients is difficult since the previous work employed a different material model (i.e., Mooney-Rivlin). Further, there were differences in boundary conditions and testing protocol (e.g., temperature during testing, only using constant strain data, etc.) that further made comparison difficult. Our material model was also less stiff than the stress-strain computed from the heel pad soft tissue properties ($\mu_1 = 1.084$ kPa and $\alpha_1 = 9.78$) of another inverse FE study (Chokhandre et al., 2012). (Note Chokhandre et al. employed a different Ogden strain energy formulation from this paper. This required converting μ_1 to be comparable with our results, as described in detail in the Ogden Equation Comparison section.) The less stiff stress-strain behavior observed in our study is likely due to differences in the mechanical testing protocols (e.g., material vs. structural, boundary conditions, testing rates, temperature during testing, etc.). Also, the inverse analysis of the heel pad indentation lumped skin and fat into a single homogenized material as in Chokhandre et al. (2012) could potentially overestimated plantar fat stiffness and underestimated plantar skin stiffness.

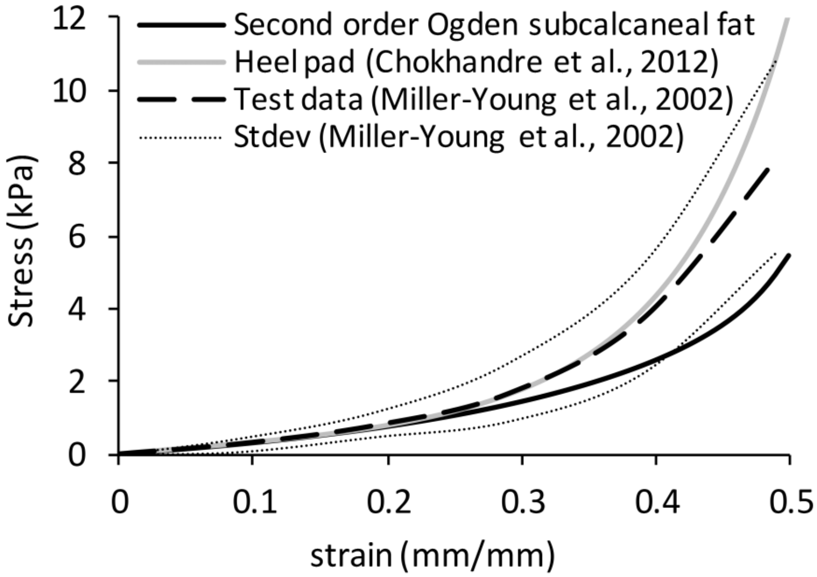

Figure 4.6: The compressive stress-strain response from the optimal second order Ogden material (solid black line) and literature stress-strain data (mechanical testing; dash line and inverse FE analysis; solid grey line).

The bulk modulus (calculated from equation 4.2 by substituting Poisson's ratio of 0.4999 and optimal coefficients, μ and α) of both first-order (K = 0.71 MPa) and second-order (K = 4.21 MPa) materials were substantially lower than the value of water (2.24 GPa) or breast fat (1.86 GPa) (Duck, 1990). However, this estimation was an improvement from the previous study (K = 0.021 MPa) (Chokhandre et al., 2012). Future research should include Poisson's ratio into the design variables and incorporate bulk modulus into the optimization function.

There were several limitations in this study. The friction coefficient at the sand paper-soft tissue interface was undetermined and no-slip boundary condition was assumed. From pilot simulations, this assumption valid when friction coefficient is greater than 0.7. The FE model was validated up to 30% strain due to geometric constraints in the analytical solution, however we observed physiologic model deformation up to the peak deformation (i.e., 48% strain). Several optimal solutions converged to a similar RMSE value, indicating that inverse analysis can generate non-unique solutions for this particular problem and these solutions could be local optima. This non-unique optimization often occurs and has been previously documented (Ogden et al., 2004). In addition, we omitted the time dependent mechanical behavior of the soft tissue and considered only the elastic response to maintain a reasonable number of design variables and analysis time. Furthermore, extremely high Poisson's ratios ($v > 0.49999$) were excluded from this study due to model instabilities. Finally, the target force-deformation response was obtained from cadaveric specimens, rather than living subjects.

In conclusion, the optimal Ogden hyperelastic coefficients of the subcalcaneal fat were identified from previous compression test data using an inverse FE method. The second-order Ogden model was superior in matching the experimentally observed force vs. deformation data. The material parametric study suggested that the model’s force-deformation response was highly sensitive to Poisson’s ratio and the coefficient α_1. These data suggested that a near incompressible Poisson’s ratio should be accurately identified for such models.

4.6 Ogden Equation Comparison

The Ogden strain energy formulation in finite element software LS-DYNA is different from the formulation find in Abaqus. Conversion of hyperelastic coefficients (equation 4.12) is necessary when comparing parameters from the two software packages. For LS-DYNA, the strain energy function (Hallquist, 2006) is given by equation 4.1-4.5 under Methods section. On the other hand, ABAQUS used the following equations (ABAQUS 6.12 theory manual, 2012):

$$U = \sum_{i=1}^{N} \frac{2\mu_i}{\alpha_i^2}\left(\bar{\lambda}_1^{\alpha_i} + \bar{\lambda}_2^{\alpha_i} + \bar{\lambda}_3^{\alpha_i} - 3\right) + \sum_{i=1}^{N} \frac{1}{D_i}\left(J^{el} - 1\right)^{2i} \tag{4.9}$$

$$\bar{\lambda}_i = J^{-1/3}\lambda_i \tag{4.10}$$

$$G = \sum_{i=1}^{N} \mu_i \tag{4.11}$$

Where $\lambda_1, \lambda_2, \lambda_3$ are the three principal stretches, the Jacobian, J^{el}, denotes the elastic volumetric strain and G refers to the initial shear modulus. D_1 is related to the initial bulk modulus by $K = 2/D_1$. Comparing the initial shear modulus of the first order Ogden model from LS-DYNA (Hallquist, 2006) with equation 4.11 leads to the following relationship:

$$\frac{\mu_{LS-DYNA}\alpha_{LS-DYNA}}{2} = \mu_{ABAQUS} \tag{4.12}$$

For the first order Ogden model, substituting μ_{ABAQUS} , D_1 and $\bar{\lambda}_i$ into equation 4.9 and comparing equation 4.9 to equation 4.1 yields:

$$\alpha_{LS-Dyna} = \alpha_{Abaqus} \tag{4.13}$$

Chapter 5. Subject-specific material properties of the heel pad: An inverse finite element analysis

5.1 Abstract

People with diabetes are at a higher risk of developing foot ulcers. Subject-specific finite element (FE) models of the foot can provide useful insights into internal soft tissue loading and the ability of various treatments to modulate this loading. Current FE foot models utilize subject-specific anatomy, but typically lack subject-specific soft tissue material properties. In this study, we determined subject-specific hindfoot soft tissue material properties (generic soft tissue, skin, fat and muscle) from one normal and one diabetic subject using inverse FE analysis techniques. Each subject underwent cyclic MRI experiments which applied a prescribed displacement at 0.2 Hz to the hindfoot. Compressive force and three-dimensional soft tissue imaging data were obtained at 16 phases along the loading-unloading cycles. The FE models consisted of rigid bones and nearly-incompressible first-order Ogden hyperelastic skin, fat, and muscle (resulting in six independent material parameters). The calcaneus and loading platen kinematics were computed from the imaging data and prescribed on the FE model while the inverse FE analysis optimized platen reaction force, muscle vertical displacement and skin mediolateral bulging (i.e., displacement). The inverse FE analysis used an iterative process to search for the material properties which yielded minimum differences between the model predicted and the actual experimental values. Two inverse FE analyses were performed for each subject. First, a generic soft tissue material was modeled, lumping skin, fat, and muscle into a single material (i.e., two material parameters) and optimizing only the platen reaction force. Second, the skin, fat and muscle material properties were individually determined by optimizing the sum of the errors in platen reaction force, muscle vertical displacement and skin mediolateral bulging. We found that the materials ranked from high to low stiffness were: skin, muscle, generic soft tissue and fat. The diabetic soft tissue showed overall stiffer behavior compared to the normal tissue, however, statistical analyses cannot be conducted due to small

sample size. The presented protocols could serve as a guideline for exploring normal and diabetic soft tissue material properties in a larger population.

5.2 Introduction

Plantar soft tissue serves as a shock absorber and provides cushioning to the deeper foot structures. Changes in mechanical responses of the subcalcaneal fat, such as increased stiffness due to age (Hsu et al., 1998) or diabetes (Pai and Ledoux, 2010), can compromise its ability to dissipate stress and thus cause tissue injury (Gefen, 2003). In the diabetic population, elevated plantar pressure can lead to ulceration (Veves et al., 1992) and subsequent lower limb amputation (Pecoraro et al., 1990).

Finite element (FE) models of the foot have been used to explore the biomechanics of diabetic (Cheung et al., 2005; Gefen, 2003) and normal feet (Chen et al., 2012; Cheung et al., 2004, 2006a; Lin et al., 2014). FE models overcome limitations in cadaveric and *in vivo* studies, such as tissue degradation and subject/specimen variation in repeated testing. Clinical applications such as designing custom devices (Budhabhatti et al., 2009; Cheung and Zhang, 2008; Erdemir et al., 2005) and customizing surgical procedures (Isvilanonda et al., 2012) are a few of the many areas where FE foot models can be used to improve treatment outcomes in diabetic patients.

Accurate anatomy and material properties are crucial FE model inputs. Subject-specific foot anatomy is commonly derived from computed tomography (CT) and/or magnetic resonance (MR) imaging. However, obtaining *in vivo* plantar soft tissue material properties requires specialized equipment and complex analyses (Petre et al., 2008; Petre et al., 2013; Stebbins, 2012). For this reason, many FE foot models often simplify skin, fat and muscle into a homogeneous generic soft tissue (Chen et al., 2012; Cheung and Zhang, 2008; Tao et al., 2010; Wang et al., 2014; Yu et al., 2008). An *in vivo* hyperelastic material representing a population average (Lemmon et al., 1997) was commonly used in such models. Assuming generic soft tissue and averaged material properties have been shown to substantially increase peak plantar pressure error (Erdemir et al., 2006; Spears et al., 2007). Improvements in model accuracy can be accomplished by incorporating multi-material soft tissue and subject-specific material properties (Erdemir et al., 2006; Petre et al., 2013; Spears et al., 2007).

Subject-specific soft tissue material properties have previously been indentified from compression or indentation tests using inverse FE analysis techniques (Erdemir et al., 2006; Evans and Holt, 2009; Luo et al., 2011; Petre et al., 2013; Schwenninger et al., 2011; Then et al., 2007). These approaches iteratively search for a set of optimal material properties which minimize a user-defined objective function. The objective function typically describes errors between the model-predicted and the actual experimental values.

Based on the inverse FE analysis technique, *in vivo* hyperelastic material properties of non-diabetic and diabetic hindfeet were identified from an ultrasound indentation experiment (Erdemir et al., 2006). The study assumed two-dimensional (2D) axisymmetric anatomy and hyperelastic generic soft tissue material. Chokhandre et al. (2012) developed a three-dimensional (3D) hindfoot model from a cadaveric specimen. Material properties of generic plantar soft tissue were optimized based on force obtained from indentation experiments. Recently, multiple static compression/indentation experiments experiments of the foot and gluteal region were performed while simultaneously collecting MR images to acquire force and soft tissue deformation (Petre et al., 2013; Then et al., 2007). In a forefoot study by Petre et al. (2013), a multi-material soft tissue FE model, which consisted of multiple soft tissue layers, was generated from unloaded MRI data. The plantar skin, fat and muscle hyperelastic material properties were obtained by optimizing the 3D soft tissue deformation to the target MRI data during static compression. However, a 3D, dynamic loading, multi-material soft tissue model of the foot has yet to be conducted.

The purpose of this study is to characterize the subject-specific hindfoot soft tissue material properties of a healthy normal and a diabetic subject using an inverse FE analysis technique. These material properties are necessary for developing our subject-specific FE foot models. The presented protocols also serve as a guideline for exploring differences between diabetic and non-diabetic soft tissue material properties in a larger population.

5.3 Methods

5.3.1 Hindfoot compression experiment

A healthy control subject (43-year-old male, 945 N body weight (BW)) and a subject with diabetes (31-year-old male, 688 N BW) without prior ulcer history and foot deformity were selected for this IRB approved study. Each subject’s hindfoot was compressed using an MRI compatible loading device (Stebbins, 2012; Williams, 2015; Williams et al., 2015) to emulate the physiologic strain experienced during gait. The experiment provided plantar force and soft tissue deformation for a subsequent inverse FE analysis. The device configuration and experiment protocol are described briefly. Details can be found elsewhere (Stebbins, 2012; Williams, 2015; Williams et al., 2015).

MRI compatible loading device

A master-slave hydraulic cylinder system was used to apply a deformation onto the subject’s hindfoot. Outside the MR scanning room, the master cylinder was driven by a linear servo motor at a prescribed frequency. This in turn drove the (non-metallic) slave actuator inside the MR core, which was attached to an acrylic platen that loaded the plantar surface of the subject’s foot posterior to the calcaneaocuboid joint. To minimize motion superior to the ankle, the subject's leg and body were secured to the MR platform using a metal-free system including ankle-foot orthosis, straps, bars, and padding. To calculate force, a pressure transducer recorded system pressure at 2.5 kHz. The loading device was synchronized to the MRI computer via artificial peripheral pulse unit (PPU) signals.

Imaging modalities

Prior to the MRI compression experiment, a partial weight bearing (10% BW) CT scan was conducted. The CT images were acquired at the Veterans Affairs Puget Sound Health Care System (Phillips CT MX8000IDT, pixel spacing 0.715 mm, voxel depth 0.5 mm, slice spacing 0.5 mm, slice thickness 1.0 mm) to obtain bone anatomy (Figure 5.1).

The MRI compression experiment was performed at the University of Washington Bio-molecular Imaging Center (Phillips Achieva, pixel spacing 0.916 mm, voxel depth 1.0 mm, slice spacing 1.0 mm, slice thickness 2.0 mm). The hindfoot was loaded using a 0.2 Hz, 15-19 mm amplitude displacement-control sine waveform. The plantar soft tissue was preconditioned for 10 cycles before imaging began. A gated MRI technique was used to capture 3D images at 16 phases–each representing a fixed time on the loading-unloading curve (Williams, 2015; Williams et al., 2015).

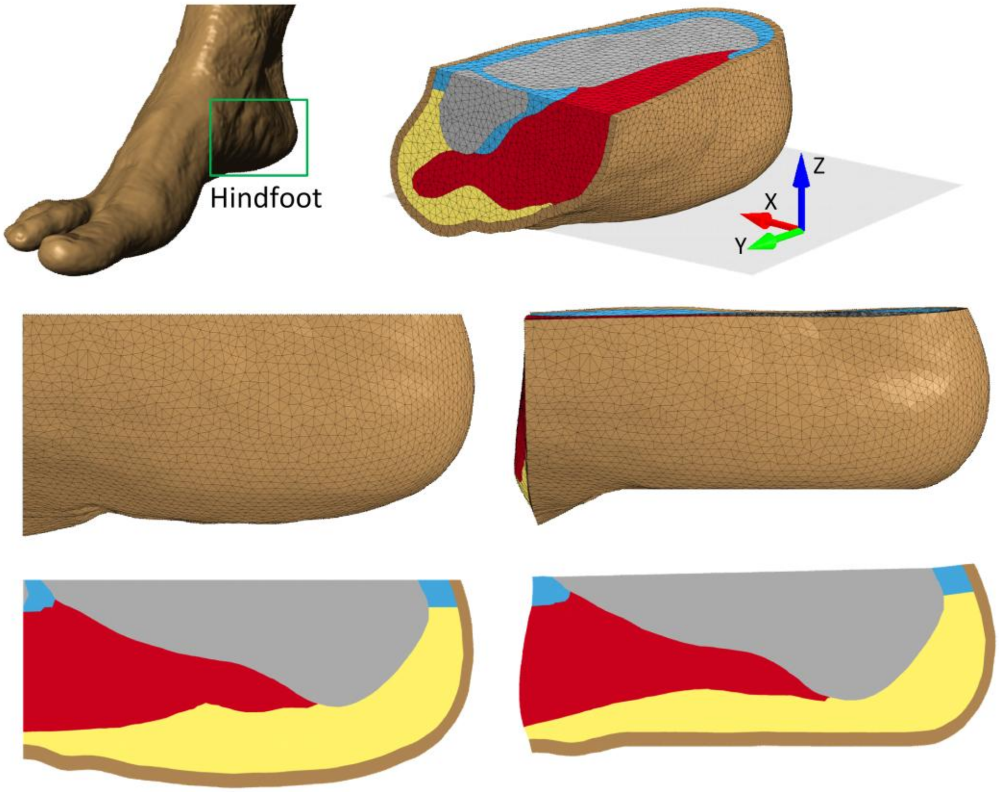

Figure 5.1: Finite element model of the hindfoot illustrating calcaneus bone (gray), skin (brown), fat (yellow) and muscle (red) materials.

Data analysis

The FE model inputs (calcaneus and platen kinematics) and inverse FE target data (platen force, muscle and skin deformations) were extracted from the MRI compression experiment.

(a) Platen force

The platen force was calculated from the hydraulic pressure via a pressure-force calibration curve (Stebbins, 2012; Williams, 2015; Williams et al., 2015). The estimated force-time data were averaged over all cycles (n = ~270) and resampled to 16 points to estimate the target platen force. (Figure 5.2a).

(b) Platen and calcaneus kinematics

The CT and MR data were post-processed using a custom software, *Multi-Rigid* (Hu et al., 2011). The calcaneus, cuboid and second metatarsal bones were segmented from the CT data. The segmented calcaneus was registered to the MR data for each of the 16 phases. (The cuboid and second metatarsal were registered using calcaneus transformation data; the former was used just for illustrative purposes, while that later was used to determine the foot based coordinate system.) Subsequently, fat, muscle (lumped abductor hallucis (AH), flexor digitorum brevis (FDB) and abductor digiti minimi (ADM)), and the outer contour of the skin were segmented. A total of 66 surface models (cuboid and second metatarsal at phase 1; calcaneus, outer skin, fat and muscle at 16 phases) were exported as a triangulated surface mesh.

The platen displacement was estimated from the surface meshes. For the normal subject, a plane was fitted to the planar segment of the skin surface at each phase. The displacement of the plane along the mean direction orthogonal to the plane was defined as the platen displacement. The platen was modified for the diabetic subject experiment by attaching four MRI markers to the bottom surface of the platen. Instead of fitting a plane to skin surface, the plane was defined from the centroids of 3 MRI-opaque markers. The displacements calculation remained unchanged.

A FE model coordinate system (Figure 5.1a) was defined as follows: the global Z-axis (inferosuperior) is a unit vector normal to the loading platen. The dummy axis is defined as a unit vector connecting the most inferior vertex of the calcaneus to the second metatarsal head. The X-axis is the cross product of the dummy and Z-axes. The Y-axis (anteroposterior) is the cross product of the X- and Z-axes. After defining the global coordinate system, the rigid body transformations of the calcaneus relative to phase 1 were determined using finite iterative closest point (ICP) method (Kroon, 2009) in Matlab (MathWorks, Natick, MA).

(c) Muscle and skin displacements

The muscle vertical displacement was determined at eight plantar locations (Figure 5.2b) on the ADM and FDB muscles (four vertices on each muscle). The selected vertices from phase 1 were projected along the Z direction to the plantar surface of the muscle in phases 2 to 16. The mean displacement of all 8 points from each phase was defined as the target muscle vertical displacement.

The mediolateral bulging of the hindfoot was measured along a vector fixed to the calcaneus and provided information about skin deformation (Figure 5.2c). The vector was created for phase 1 by intersecting the frontal plane passing through the lowest calcaneus vertex and the transverse plane passing through the widest mediolateral section of the hindfoot soft tissue. The vector originates from the medial surface and intersected the lateral surface of the skin. A change in length of this vector relative to phase 1 was defined as the target skin bulging displacement.

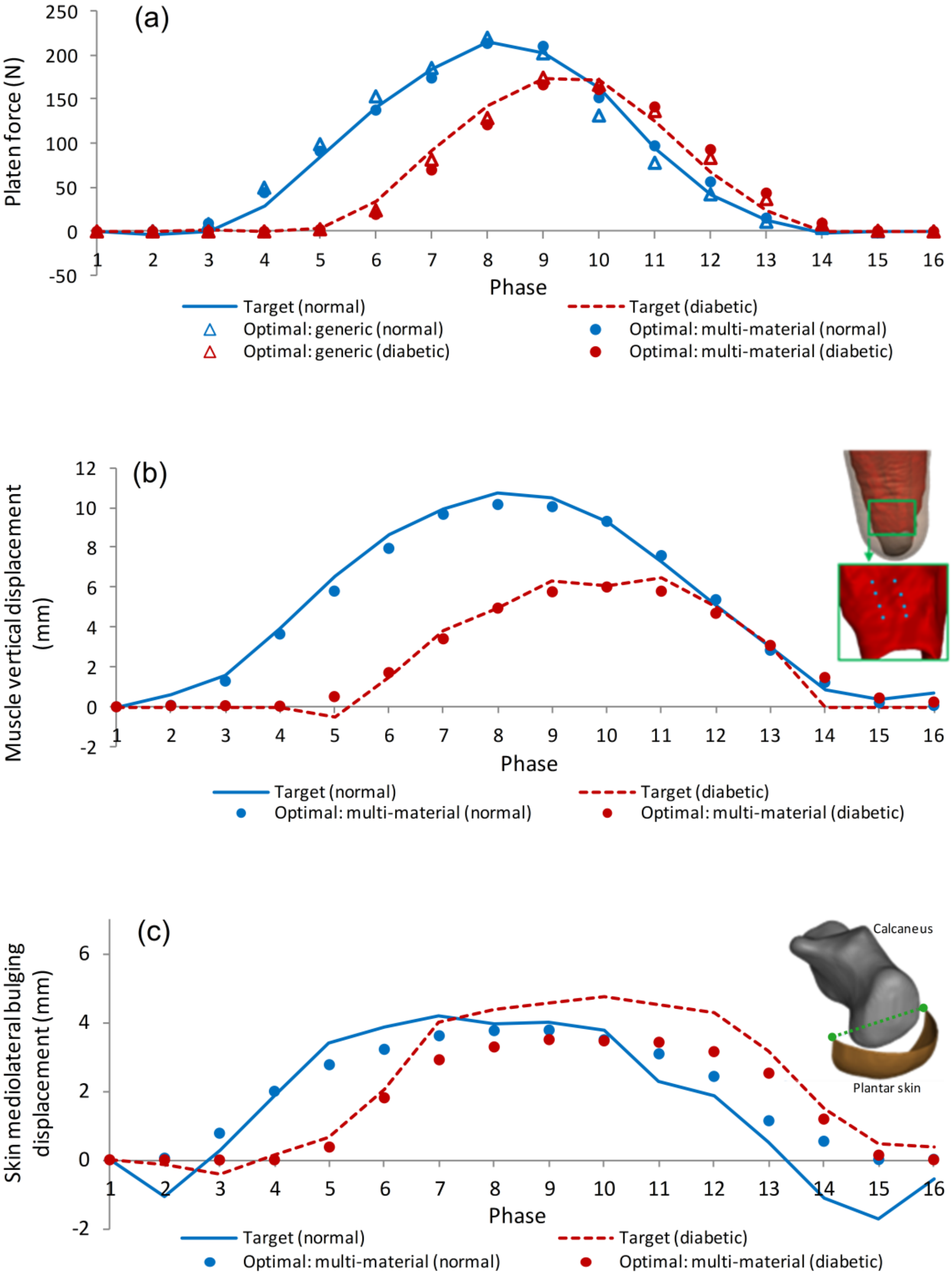

Figure 5.2: Target experimental and predicted optimal (a) force, (b) muscle vertical displacement and (c) skin bulging displacement. The target lines are point-to-point representations of 16 phases.

5.3.2 Finite element model

The FE model of the hindfoot (Figure 5.1) was created from the unloaded anatomy at phase 1. The surface models of the calcaneus, cuboid, outer skin, muscle and fat were post-processed in ScanIP (Simpleware Ltd, Exeter, UK) to generate a constant skin thickness (2.15 mm), remove volume overlaps and smooth surfaces. The model was meshed with linear tetrahedral elements in ANSYS ICEM CFD (ANSYS Inc, Canonsburg, USA) and simulated using LS-DYNA v971s R5.1.1 (Livermore Software, Livermore, CA, USA) explicit solver. Elements along the soft tissue interfaces share nodes such that there was no relative motion. The optimal element settings (size 2.5 mm, element formulation (elform) 13) were determined from a mesh sensitivity analysis to ensure convergence in plantar force and model deformation.

The FE mesh was then preprocessed in LS-Prepost (Livermore Software, Livermore, USA). The calcaneus and cuboid bones and the calcaneocuboid joint were modeled as rigid (Table 5.1) due to their small deformation compared to soft tissue. The skin, fat, muscle and generic soft tissue were governed by a first-order Ogden hyperelastic model with the strain energy function (*W*) as follows:

$$W(\lambda_1,\lambda_2,\lambda_3)=\frac{\mu}{\alpha}\left(\tilde{\lambda}_1^{\alpha}+\tilde{\lambda}_2^{\alpha}+\tilde{\lambda}_3^{\alpha}-3\right)+\frac{1}{2}K(J-1)^2 \tag{5.1}$$

$$J=\lambda_1\lambda_2\lambda_3 \tag{5.2}$$

$$\tilde{\lambda}_i=\frac{\lambda_i}{J^{1/3}} \tag{5.3}$$

The material properties of skin (μ_S and α_S), fat (μ_F and α_F), muscle (μ_M and α_M) and generic soft tissue (μ_G and α_G) were parameterized for inverse FE analyses. The Jacobian *J* is the relative volume change (equation 5.2) given by the product of three principal stretches ($\lambda_1,\lambda_2,\lambda_3$) and *K* denotes bulk modulus. The volumetric independent principal stretches ($\tilde{\lambda}_i$) are related to λ_i by equation 5.3. Near-incompressible Poisson’s ratios (Table 5.1) were estimated from equation 5.4 using ultrasonic wave velocity through the tissue (C_L), mass density (ρ) and modulus (E) from literature (Duck, 1990; Pai and Ledoux, 2010; Song et al., 2007).

$$C_L = \left[\frac{E(1-v)}{\rho(1-2v)(1+v)} \right]^{\frac{1}{2}} \tag{5.4}$$

The calcaneus and platen kinematics at 16 phases were prescribed on the model. Mass and time scaling techniques were used to maintain reasonable computation time (LSTC, 2015). Mass scaling increases the minimum time step size and reduces computation time by imposing artificial masses to small elements. Time scaling shortens simulation time by increasing the loading rate. In this study, a negligible mass increase (< 0.0015%) provided a 1 microsecond constant time step size. The loading rate was increased from 0.2 Hz to 1 Hz, thus reducing the simulation time and computation time by 5-fold. The time scaling resulted in 7.3 N RMS difference in platen force and 0.038 mm and 0.047 mm RMS difference for muscle vertical displacement and skin bulging displacement, respectively (estimated from the normal hindfoot FE model). The effect of time-scaling was negligible due to time-insensitivity of the material model and relatively low kinetic energy in the system.

The predicted platen reaction force, muscle vertical displacement (averaged from eight nodal displacements in the Z direction) and skin bulging displacement (averaged from seven medial and seven lateral nodal displacements in the X direction) were measured from a node set that represented the experimental measurement locations. The data were automatically output from the simulation and resampled to 16 points during inverse FE analysis to match the MR sampling.

Table 5.1: Material model and properties.

	Generic soft tissue	**Skin**	**Fat**	**Muscle**	**Bone**
Material model	Hyperelastic	Hyperelastic	Hyperelastic	Hyperelastic	Rigid
Material property [a]	μ_G and α_G	μ_S and α_S	μ_F and α_F	μ_M and α_M	-
Mass density (10^{-6} kg/mm^3)	1.000	1.142	0.916	1.047	0.449
Modulus (MPa) [b]	-	2.038[c]	0.674	0.699	20,100
Ultrasonic wave velocity through tissue (m/s) [d]	-	1,142	1,476	1,580	-
Poisson's ratio [e]	0.4999	0.4990	0.4999	0.4999	0.3
References	Chapter 4	(Duck, 1990)	(Duck, 1990), (Pai and Ledoux, 2010)	(Duck, 1990), (Song et al., 2007)	(Muehleman et al., 2002; Zysset et al., 1999)

[a] Material properties of skin, fat, muscle and generic soft tissue were parameterized for the inverse FE analysis.

[b] Modulus of skin, fat and muscle were only used for Poisson's ratio estimation.

[c] Unpublished tangent modulus from an in-house subcalcaneal skin compression test.

[d] Values measured at between 1 and 10 MHz, 37°C.

[e] Poisson's ratios of skin, fat and muscle were calculated from equation 5.4. The value for bone was from literature.

5.3.3 Inverse finite element analysis

An inverse FE analysis was performed using a commercial code, LS-OPT 4.1 (Livermore Software, Livermore, CA). The analysis was divided into two steps. First, the generic soft tissue material was assumed by replacing skin, fat and muscle components with a homogeneous soft tissue material (μ_G and α_G). The material properties were determined by optimizing the predicted platen force to the target experimental force. Second, the skin (μ_S and α_S), fat (μ_F and α_F) and muscle (μ_M and α_M) material properties were concurrently optimized using the target platen force, muscle vertical displacement and skin bulging displacement. For both analyses, a sequential response surface method (SRSM) optimization technique (Stander et al., 2010) was used. The design spaces (Table 5.2 and 5.3) were chosen based on pilot simulations and literature (Chokhandre et al., 2012; Erdemir et al., 2006; Petre et al., 2013). The inverse FE analysis began by arbitrarily selecting three initial guesses and including a fourth from the literature (Chokhandre et al., 2012) (Table 5.2 and 5.3). For each initial guess, a subset (n = 12) of material properties were sampled from the region of interest via a D-optimal point selection algorithm (Roux et al., 1998; Stander et al., 2010). During the first iteration, the region of interest includes the entire design space. Twelve FE model inputs, each with different material properties, were generated and solved in LS-DYNA (4 CPUs, shared memory parallel processing). Simulations were run on Dell PowerEdge R610 rack servers (4 units, each has two-six core 3.46GHz Intel® Xeon® processors). After simulation, normalized mean square errors (MSE) between the computed data and the target experimental data were calculated for the platen force, muscle vertical displacement and skin bulging displacement. The optimization objective function was defined as the sum of all three normalized MSE with uniform weighting. Note that for the generic soft tissue analysis, the target muscle and skin deformations were excluded. A response surface describing the objective value as a function of the material properties was created from the simulation results using linear approximation. The optimal material properties from each iteration was identified from the response surface using a hybrid–adaptive-simulated-annealing optimization algorithm (Stander et al., 2010). In subsequent iterations, a new region of interest was defined and centered about the optimal point from the previous iteration. Iteration progress was made by moving the center of the region of interest and reducing its size (shrink factor ~0.6 to 1). The optimization was terminated once the relative function error and relative material parameter error both converged to within 0.001 per iteration.

The stress-strain relationships were derived from the optimal material properties of each tissue for comparison. The sensitivity of the force, muscle vertical displacement and skin bulging displacement to changes in material properties were evaluated by perturbing each material property by ±10% from its optimal value.

5.4 Results

The optimal generic soft tissue material properties were μ_G = 0.790 kPa, α_G = 21.08 for the normal subject and μ_G = 0.415 kPa, α_G = 25.25 for the diabetic subject (Table 5.2 and Figure 5.2a). The root mean square (RMS) errors between the model predicted and the target platen force were 11.5 N (5.3% of the peak target force) and 8.1 N (4.7% of the peak target force) for the normal and diabetic subject, respectively. The peak compressive strains in Z direction, calculated from the platen to calcaneus, were 41% (normal) and 30% (diabetic).

An increase and decrease in μ_G and α_G values resulted in an increase and decrease in the predicted force, respectively (Table 5.3). Across the normal (peak force = 219.8 N) and diabetic (peak force = 174.4 N) subject, perturbing μ_G by ±10% from the optimal values caused a peak force difference of 9% in both subjects. Similarly, varying α_G by ±10% from the optimal values lead to a force difference of 33-50% in the normal subject and 36-56% in the diabetic subject. In general, the peak force was more sensitive to changes in α_G than μ_G, and both model were equally sensitive to μ_G and α_G.

Table 5.2: Optimal generic soft tissue material properties obtained from inverse finite element analysis.

	Initial guess[†]			**Optimal solution**			
Normal	μ_G (kPa)	α_G	Objective value	μ_G (kPa)	α_G	Objective value	Number of iterations
1	0.100	28.00	0.0623	0.789	21.11	0.0029	12
2	0.050	8.00	0.2482	0.790	21.08	0.0029[††]	20
3	0.222	9.78	0.2326	0.773	21.21	0.0029	19
4	1.000	15.00	0.0872	0.795	21.03	0.0029	21
Diabetic							
1	0.100	28.00	0.0802	0.506	24.21	0.0022	28
2	0.050	8.00	0.2268	0.408	25.41	0.0022	25
3	0.222	9.78	0.2124	0.418	25.22	0.0022	11
4	1.000	15.00	0.0861	0.415	25.25	0.0022[††]	27

[†] The design space was $0.020 < \mu_G < 5.000$ kPa and $6 < \alpha_G < 30$. Initial guess 3 was from literature (Chokhandre et al., 2012) and underwent an Abaqus-to-LS-DYNA material properties conversion (Chapter 4).
[††] The minimum objective value from four initial guesses.

Table 5.3: Sensitivity of the predicted force to changes in generic soft tissue material properties.

	Difference from the optimal force	
Normal	Peak (N) [†]	RMS (N)
μ_G + 10%	18.8	9.6
μ_G - 10%	-19.4	9.8
α_G + 10%	109.0	50.4
α_G - 10%	-72.0	34.0
Diabetic		
μ_G + 10%	16.0	7.8
μ_G - 10%	-15.9	8.0
α_G + 10%	97.9	46.1
α_G - 10%	-62.8	29.8

[†] Negative value indicated lower peak force compared to the optimal values. The optimal peak forces were 219.8 N for the normal subject and 174.4 N for the diabetic subject.

The multi-material optimization identified the skin, fat and muscle material properties of the normal subject as: μ_S = 0.156 kPa, α_S = 185.20, μ_F = 1.874 kPa, α_F = 8.29 and μ_M = 0.161 kPa, α_M = 31.95 (Table 5.4). The RMS differences between the predicted data and the target experimental data were 7.4 N, 0.42 mm and 0.80 mm for the platen reaction force, muscle vertical displacement and skin bulging displacement. This constitutes 3%, 4% and 93% of the final objective value, respectively.

The diabetic multi-material optimization experienced difficulty converging. The analyses either terminated prematurely due to unstable materials, or the optimal material properties exhibited overly stiff behaviors (e.g., abnormally high and localized skin-ground contact pressure). To obtain results for this dissertation and proceed with Specific Aim 4, an alternative method was used. The entire design space was explored by performing two optimization iterations at 200 points per iteration. (i.e., a single iteration was run for 200 sets of material parameters). The ten best material properties were identified from the second iteration simulations based on the ten smallest objective values (Table 5.5). Subsequently, ten diabetic FE foot models under quiet stance loading were simulated using these material properties. The set of material properties which resulted in physiologic plantar pressure (e.g., smooth distribution and lowest peak plantar pressure) was selected.

Table 5.4: The optimal skin, fat and muscle material properties of the normal subject.

	Initial guess[†]							Optimal solution							
	Skin		Fat		Muscle		Objective value	Skin		Fat		Muscle		Objective value	Number of iterations
	μ_S (kPa)	α_S	μ_F (kPa)	α_F	μ_M (kPa)	α_M		μ_S (kPa)	α_S	μ_F (kPa)	α_F	μ_M (kPa)	α_M		
1[††]	0.450	73.00	0.600	24.00	0.250	51.20	9.7343	n/a	n/a	n/a	n/a	n/a	n/a	n/a	n/a
2	2.820	185.00	1.500	5.70	0.775	45.50	0.3216	0.195	178.16	2.265	7.80	0.167	31.22	0.0394	25
3	2.020	50.00	0.875	20.95	0.087	38.00	0.8356	0.156	185.20	1.874	8.29	0.161	31.95	0.0393[‡]	34
4	0.222	9.78	0.222	9.78	0.222	9.78	n/a[‡‡]	0.264	169.89	1.920	8.49	0.442	24.76	0.0403	31

[†] The design space was (0.040 < μ_S < 4.000 kPa, 17.00 < α_S < 200.00), (0.450 < μ_F < 3.000 kPa, 5.70 < α_F < 24.00) and (0.020 < μ_M < 0.900 kPa, 17.00 < α_M < 51.20) for skin, fat and muscle tissue, respectively. Initial guess 3 was from literature (Chokhandre et al., 2012) and underwent Abaqus-to-LS-DYNA conversion (Chapter 4). Note that the design space was slightly adjusted for initial guess3.

[††] The optimization failed to converge.

[‡] The minimum objective value from three initial guesses.

[‡‡] Error termination due to model instability.

Table 5.5: Material properties of the diabetic subject identified from the second simulation iteration.

	Material properties						**Normalized MSE**			**Objective value**	**Peak plantar pressure (kPa)** [††]
	μ_S (kPa)	**α_S**	**μ_F (kPa)**	**α_F**	**μ_M (kPa)**	**α_M**	**Force**	**Muscle vertical displacement**	**Skin bulging displacement**		
1	1.348	200.00	0.918	8.22	0.900	29.29	0.0087	0.0089	0.0152	0.0327	206.3
2	1.060	200.00	0.200	16.06	0.321	29.29	0.0057	0.0058	0.0220	0.0335	201.0
3	2.500	192.71	1.636	8.22	0.803	23.45	0.0095	0.0059	0.0181	0.0335	202.4
4	0.772	200.00	0.439	10.18	0.610	35.12	0.0072	0.0105	0.0162	0.0339	192.0
5	2.212	200.00	0.679	12.14	0.321	23.45	0.0084	0.0056	0.0208	0.0348	216.2
6	0.772	192.71	0.200	16.06	0.417	29.29	0.0068	0.0061	0.0244	0.0372	183.5
7	0.772	185.42	0.679	8.22	0.803	38.04	0.0083	0.0134	0.0157	0.0375	176.2
8	2.500	163.56	1.396	10.18	0.514	23.45	0.0079	0.0056	0.0245	0.0381	184.0
9[†]	0.772	163.56	0.200	14.10	0.321	38.04	0.0058	0.0091	0.0240	0.0389	155.8
10	0.772	185.42	1.157	10.18	0.514	26.37	0.0064	0.0059	0.0273	0.0396	176.5

[†] Selected material properties based on low force and muscle vertical displacement error, smooth plantar pressure distribution (not shown) and small peak plantar pressure.

[††] Peak plantar pressure were simulated using a pilot FE foot model of the diabetic subject under a quiet stance loading.

Based on this method, the diabetic skin, fat and muscle material properties were: μ_S = 0.772 kPa, α_S = 163.56, μ_F = 0.200 kPa, α_F = 14.10 and μ_M = 0.321 kPa, α_M = 38.04. The RMS errors between the simulation and the target experimental data were 13.2 N, 0.65 mm and 0.73 mm for platen reaction force, muscle vertical displacement and skin bulging displacement. This constitutes 15%, 23% and 62% of the objective value, respectively.

For both normal and diabetic simulations, the predicted peak compressive strains (superoinferior direction) in each tissue were skin: 7.2% and 8.6%, fat: 49.2% and 34.9%, and muscle: 28.0% and 19.0%, respectively.

The effect of material properties on the predicted force, muscle vertical displacement and skin bulging displacement were studies (Table 5.6). The platen force was most sensitive to the strain hardening coefficient of the plantar fat (α_F). In all cases, stiffer material properties (i.e., higher μ or α) increased the platen force. The muscle and skin displacements were only weakly sensitive to changes in the material properties (less than 0.2mm for a 10% perturbation). Increasing skin stiffness increased muscle vertical displacement and skin bulging displacement. A stiffer plantar fat material decreased skin bulging displacement, but increased muscle vertical displacement. Conversely, stiffer muscle decreased muscle vertical displacement, but increased skin bulging displacement.

Table 5.6: Sensitivity of the predicted platen force, muscle vertical displacement and skin bulging displacement to changes in skin, fat and muscle material properties.

	Peak difference [RMS difference] from optimal		
	Force (N)	**Muscle vertical displacement (mm)**	**Skin bulging displacement (mm)**
Normal skin			
μ_S + 10%	2.9 [1.6]	0.016 [0.010]	0.017 [0.010]
μ_S - 10%	-3.1 [1.6]	-0.013 [0.010]	-0.022 [0.012]
α_S + 10%	15.7 [7.9]	0.067 [0.049]	0.074 [0.051]
α_S - 10%	-17.4 [8.5]	-0.089 [0.061]	-0.090 [0.060]
Normal fat			
μ_F + 10%	11.3 [5.9]	0.017 [0.007]	-0.020 [0.012]
μ_F - 10%	-13.2 [6.7]	-0.019 [0.013]	0.032 [0.017]
α_F + 10%	36.9 [17.4]	0.019 [0.010]	-0.048 [0.035]
α_F - 10%	-33.0 [15.7]	-0.036 [0.021]	0.061 [0.042]
Normal muscle			
μ_M + 10%	4.5 [2.4]	-0.029 [0.020]	0.014 [0.007]
μ_M - 10%	-6.4 [3.2]	0.028 [0.015]	-0.009 [0.005]
α_M + 10%	27.3 [13.0]	-0.131 [0.083]	0.062 [0.035]
α_M - 10%	-26.5 [12.7]	0.124 [0.078]	-0.052 [0.033]
Diabetic skin			
μ_S + 10%	2.3 [1.1]	0.005 [0.003]	0.021 [0.011]
μ_S - 10%	-2.1 [1.1]	-0.006 [0.003]	-0.023 [0.014]
α_S + 10%	10.8 [5.3]	0.015 [0.009]	0.070 [0.043]
α_S - 10%	-10.7 [5.1]	-0.018 [0.010]	-0.099 [0.054]
Diabetic fat			
μ_F + 10%	8.9 [4.3]	0.022 [0.014]	-0.023 [0.013]
μ_F - 10%	-8.8 [4.2]	-0.026 [0.016]	0.020 [0.013]
α_F + 10%	44.7 [20.9]	0.063 [0.040]	-0.101 [0.058]
α_F - 10%	-36.2 [16.9]	-0.075 [0.045]	0.092 [0.055]
Diabetic muscle			
μ_M + 10%	5.3 [2.6]	-0.028 [0.018]	0.007 [0.004]
μ_M - 10%	-5.0 [2.5]	0.029 [0.019]	-0.005 [0.004]
α_M + 10%	25.4 [12.1]	-0.102 [0.061]	0.016 [0.007]
α_M - 10%	-23.4 [11.3]	0.109 [0.067]	-0.019 [0.008]

5.5 Discussion

Physiologic plantar soft tissue material properties are important inputs for developing an accurate FE foot model. In this study, we determined the subject-specific hindfoot soft tissue material properties from cyclic MRI compression data by utilizing an inverse FE analysis technique. Note that due to the small sample size, statistical analysis was not performed. The following comparisons were based on material properties of two individual subjects and literature data.

The generic soft tissue material properties can provide insight into the overall responses of the heel pad. In both normal and diabetic subjects, the generic soft tissue stiffness was stiffer than fat but less stiff compared to muscle (skin is the most stiff). The diabetic material had a lower initial shear modulus ($\mu = 2\mu_G\alpha_G = 20.97$ kPa) but a higher strain hardening coefficient ($\alpha_G = 25.25$) than normal material ($\mu = 33.31$ kPa, $\alpha_G = 21.08$). This resulted in the diabetic tissue experiencing lower stress at small strain, but the stress increasing more rapidly as strain increased. The calculated stress-strain results (Figure 5.3a) suggested that the diabetic subject in this study may have stiffer plantar soft tissue compared to normal.

The initial modulus (0.023 MPa (normal) and 0.014 (diabetic)) and tangent modulus at 30% compressive strain (0.73 MPa (normal) and 0.94 MPa (diabetic)) were calculated from the stress-strain data. (Unless otherwise specified, tangent modulus was calculated at 30% strain for appropriate comparison to literature.) Our initial moduli were less stiff compared to that measured during gait (0.105±0.011 MPa) but our tangent moduli were stiffer than 0.306±0.016 MPa reported (Gefen et al., 2001b). The initial/tangent moduli of the plantar soft tissue from other inverse FE studies were 0.003 MPa/0.015 MPa for a cadaveric hindfoot (Chokhandre et al., 2012), 0.05 MPa/0.15 MPa at the hindfoot (Erdemir et al., 2006) and 0.07 MPa/1.14 MPa at the forefoot (Petre et al., 2013), respectively (Figure 5.3a). Note that initial moduli from Gefen et al. (2001b), Chokhandre et al. (2012) and Erdemir et al. (2006), and tangent moduli from Gefen et al. (2001b) and Chokhandre et al. (2012) were reported in their articles. Other initial and tangent moduli were calculated from the reported material properties.

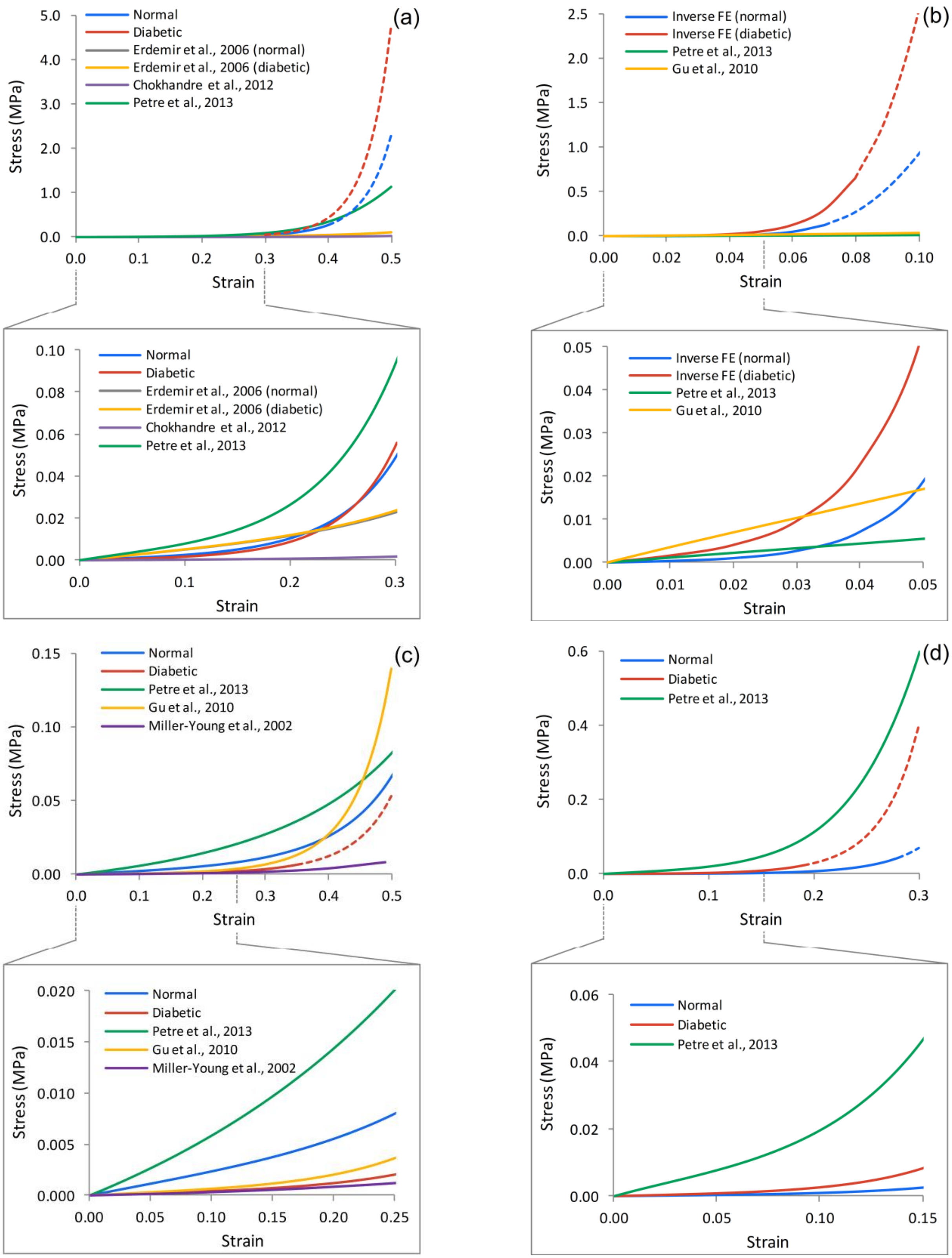

Figure 5.3: Stress-strain results computed from the optimal material properties of the (a) generic soft tissue, (b) skin, (c) fat and (d) muscle. Dash lines indicated extrapolation from the estimated peak strain. Stress-strain results at a finer scale were enlarged.

The skin compressive strain cannot be accurately measured from the MRI data due to limited image resolution and small skin thickness. The FE-predicted skin compression was less than 9%. Stress-strain data were extrapolated to 10% strain in Figure 5.3b and used to calculate the tangent modulus. The plantar skin stress-strain results from the normal subject were substantially stiffer compared to literature (Gu et al., 2010; Petre et al., 2013). The initial/tangent moduli were 0.065 MPa/49.0 MPa compared to 0.11 MPa/0.19 MPa (Petre et al., 2013) and 0.34 MPa/0.49 MPa (Gu et al., 2010) calculated from inverse FE literature. The discrepancies between our results and literature were potentially due to relatively low sensitivity of the skin deformation measurement to changes in material properties. There could be multiple skin material properties while still yielding similar objective values (e.g., Table 5.5 cases 2 and 3). Another potential factor was a higher Poisson's ratio (i.e., low compressibility) used in our study (0.499 compared to 0.475 (Petre et al., 2013)) which may be responsible for the sharp stress increase at high strain.

The plantar fat modulus at 50% strain from the normal subject was greater than previous cadaveric hindfoot (Miller-Young et al., 2002) and *in vivo* forefoot (Petre et al., 2013) studies (Figure 5.3c), but less stiff compared to the hindfoot study (Gu et al., 2010). The initial modulus and tangent modulus at 50% compressive strain were 0.02 MPa and 0.64 MPa, respectively. Miller-Young et al. (2002) reported initial modulus and tangent modulus of 0.003 MPa and 0.04 MPa from quasi static uni-axial unconfined compression test of isolated plantar fat specimens. The lower moduli in these experimental studies was likely due to different boundary and initial conditions compared to the present study. For example, the *in vivo* subcalcaneal fat may be subjected to preloads from the surrounding soft tissue and bone, whereas an isolated cadaveric specimen was constrained between two frictionless rigid platens (0.01N preload) and surrounded by air. A similar study by Pai and Ledoux (2010) obtained the tangent modulus of 0.67 MPa for the subcalcaneal fat. However, similar to the cadaveric skin experiment, their results may be influenced by friction at the soft tissue-platen interfaces. The plantar fat stress-strain responses calculated from other inverse FE studies demonstrated large variations. The initial modulus and tangent modulus at 50% compressive strain were 0.05 MPa/0.44 MPa (Petre et al., 2013) and 0.006 MPa/2.27 MPa (Gu et al., 2010). The discrepancies could be due to subject variation, FE model simplifications, optimization technique (e.g., optimize force vs deformation) and material compressibility assumption.

The predicted initial/tangent moduli of the plantar muscle were 0.007 MPa/1.46 MPa, respectively compared to 0.15 MPa/8.30 MPa computed from the forefoot muscle material properties (Petre et al., 2013) (Figure 5.3d). Similar to skin, the sensitivity of the muscle vertical displacement to change in material properties was small and could result in multiple optimal solutions.

There were potential limitations that need to be acknowledged. This study focused on quantifying the subject-specific plantar soft tissue material properties. These material properties are crucial inputs for our subject-specific FE foot model. However, in order to determine statistically meaningful comparisons, such as differences between normal and diabetic groups, a larger sample size is required.

The MR image resolution used in our study was relatively coarse and could affect the accuracy of the muscle vertical displacement and skin bulging displacement measurements. A segmentation error of one pixel could potentially result in target muscle and skin displacement error up to 14% and 23% of the peak values, respectively. Finer image resolution can be obtained by increasing scan time. However, this may increases the risk of motion artifacts from subject movements. Sensitivity analysis of the optimization solutions to changes in the target experimental data was not conducted due to extensive computation time required.

Linear tetrahedral elements were selected because of their automatic meshing capability. The computation time was approximately 15 hours per simulation. The authors are aware that tetrahedral elements are computationally more expensive compared to hexahedral elements and that hexahedral elements are superior in terms of deformation, stress and contact pressure predictions (Tadepalli et al., 2011). However, the tetrahedral element formulation (LS-DYNA elform 13) used in this study has been shown to performed equally good compared to linear hexahedral elements when simulating large, nearly-incompressible deformations (Bonet and Burton, 1998). Furthermore, discretizing complicated shapes into hexahedral elements can be labor intensive. A trade-off study between model generation time, computation time and prediction accuracy using these two element types should be explored. The model generation time can be further improved by utilizing morphing techniques, which deform the gold standard elements to fit different anatomies (Sigal et al., 2010).

The FE model assumed shared nodes between soft tissue layers as well as bone-soft tissue interface whereas in the actual hindfoot, soft tissue layers can slide relative to each other. This assumption may explain low sensitivity of the skin bulging displacement to change in material properties and together with inadequate MR image resolution may potentially lead to large error between the optimal skin bulging displacement and the *in vivo* deformation (Figure 5.2c).

Soft tissue in this study was modeled as a nearly incompressible hyperelastic material. The non subject-specific Poisson's ratios (v = 0.499, 0.4999) were calculated from literature and were larger than values commonly used, e.g., v = 0.452 (Chen et al., 2010; Cheung and Zhang, 2008), 0.475 (Chokhandre et al., 2012; Petre et al., 2013) and 0.49 (Isvilanonda et al., 2012). Note that typical Poisson's ratios of an elastomeric rubber ranges between 0.49 to 0.49995 (Hibbit D. et al., 2007). Bulk moduli were estimated from the optimal material properties for generic soft tissue (41.5 MPa normal, 27.3 MPa diabetic), skin (7.2 MPa normal, 31.6 MPa diabetic), fat (38.8 MPa normal, 7.0 MPa diabetic) and muscle (12.9 MPa normal, 30.5 MPa diabetic). These values were lower than the bulk moduli of water (2.24 GPa) or breast fat (1.86 GPa) (Duck, 1990), but was an improvement from the previous studies, e.g., K = 0.02 MPa (Chokhandre et al., 2012) and 0.52 MPa (Petre et al., 2013) for the generic soft tissue and 0.80 MPa, 0.33 MPa and 1.13 MPa for the forefoot skin, fat and muscle, respectively (Petre et al., 2013).

The sensitivity of the predicted muscle vertical displacement and skin bulging displacement to changes in the material properties were relatively small compared to the platen force. This could result in non-unique optimal material properties. The sensitivity of the objective function can be improved by computing deformation from the entire surface of the tissue instead using several nodes.

The alternative optimization method was used in the diabetic material analysis due to convergence issues. This method was less time intensive, but may have only yielded suboptimal solutions. A more direct approach is to adjust the design space (e.g., smaller regions of interest that yielded stable simulations) and weighting ratio of the objective function such that the analysis can progress and terminate normally. This direct approach will be fine tuned and used to compute the final results for the publication.

5.6 Conclusion

The present study determined subject-specific plantar soft tissue material properties for a healthy normal subject and a subject with diabetes using data from a MR compression experiment and utilizing the inverse FE analysis technique. These material properties are crucial inputs for the development of subject-specific FE models which are aimed at performing parametric analyses, predicting outcomes and designing custom devices for individual person. The proposed protocol demonstrated the ability to combine optimization algorithms, numerical simulation, and structural testing to estimate material properties of complicated shapes. A larger sample size is required in order to analyze the differences in material properties between the normal and the diabetic population.

Chapter 6. Regional differences of the mechanical properties of the plantar aponeurosis

6.1 Abstract

The plantar aponeurosis functions to support the arch of the foot during weight bearing. Accurate anatomy and material properties are critical in developing analytical and computational models of this tissue. In this study, we determined the cross-sectional areas and material properties of four regions of the plantar aponeurosis: the proximal and distal portions of the middle bulk of the tissue and the medial (to the first ray) and lateral (to the fifth ray) regions. Bone-plantar aponeurosis-bone specimens were harvested from fifteen cadaveric feet by isolating the calcaneal and metatarsal/phalangeal insertions. Cross-sectional areas were measured using molding, casting and sectioning methods. Mechanical testing was performed using displacement control triangle waves (0.5, 1, 2, 5 and 10 Hz) loaded to physiologic tension by estimating from 96% body weight and scaling by the area ratio of the region. Five specimens were tested for each region. Regional deformations were recorded by a high-speed video camera and analyzed in MATLAB. We found overall differences in cross-sectional areas and biomechanical behavior across regions. The stress-strain responses are non-linear and mainly elastic (energy loss 3.6% to 7.2%). Moduli at the proximal and distal middle regions (400 and 522 kPa) were significantly higher than the medial and lateral regions (225 and 242 kPa). The effect of frequency on biomechanical outcomes was small (e.g., 3.5% change in modulus), except for energy loss (107% increase as frequency increased from 0.5 to 10 Hz). This work demonstrates that cross-sectional area and material properties differ by region of the plantar aponeurosis.

6.2 Introduction

The plantar aponeurosis is located within the plantar aspect of the foot. This strong fibrous tissue originates from the posteromedial calcaneal tuberosity then divides into five longitudinal segments at the mid-metatarsal level (Bojsen-Moller and Flagstad, 1976; Hedrick, 1996; Moraes Do Carmo et al., 2008; Sarrafian, 1993). Towards the forefoot, the fibers blend into the metatarsophalangeal joint complex and the subcutaneus tissue. Tensile force in the plantar aponeurosis is essential in maintaining stability of the foot arch during weight bearing (Arangio et al., 1997; Hicks, 1954). Plantar aponeurosis disorders (e.g., plantar fasciitis) accounted for approximately one million patient visits per year in the United States (Riddle and Schappert, 2004) and costed approximately $192 to $376 million in medical treatment in 2007 (Tong and Furia, 2010). A better understanding of the biomechanical response of the plantar aponeurosis can potentially aid in preventive care and optimize treatment options.

The plantar aponeurosis anatomy and its biomechanical role have been studied utilizing living subjects, cadaveric specimens and predictive models (Arangio et al., 1997; Bojsen-Moller and Flagstad, 1976; Chen et al., 2014a; Cheung et al., 2004; D'ambrogi et al., 2003; Erdemir et al., 2004; Erdemir and Piazza, 2004; Gefen, 2002; Iaquinto and Wayne, 2010; Kim and Voloshin, 1995; Kitaoka et al., 1997; Kitaoka et al., 1994; Kogler et al., 2001; Lin et al., 2014; Moraes Do Carmo et al., 2008; Pavan et al., 2014; Sharkey et al., 1999; Ward et al., 2003; Wright and Rennels, 1964) . The plantar aponeurosis is commonly described by its origin and insertion sites (Bojsen-Moller and Flagstad, 1976; Hedrick, 1996; Moraes Do Carmo et al., 2008; Sarrafian, 1993) and dimensions: width, thickness and length (Chen et al., 2014a; Moraes Do Carmo et al., 2008; Sarrafian, 1993). Due to geometry oversimplifications, an accurate cross-sectional area cannot be computed from these measurements. The lack of cross-sectional area information compromises the ability to estimate stresses and moduli during material characterization.

The tensile response of the plantar aponeurosis was previously investigated (Kitaoka et al., 1994; Pavan et al., 2014; Wright and Rennels, 1964). Wright and Rennels (1964) found that the plantar aponeurosis stress-strain response was non-linear and elastic. The average moduli (344 MPa initial, 827 MPa final) were calculated from force-deformation measurements by assuming a rectangular cross-sectional area. Kitaoka et al. (1994) investigated the force-deformation responses of bone-plantar aponeurosis-bone specimens and found similar non-linear elastic behavior. Digital image correlation (DIC) methods were used to quantify stiffness in the medial, middle and lateral zones. However, their zone demarcation rendered the material differences as a function of zone inconclusive. Further, the cross-sectional area was not quantified; thus, only structural responses (e.g., force-deformation curves and stiffness) were reported.

As the anatomy and function of the plantar aponeurosis are not well understood, in predictive modeling (e.g., finite element and multi-linkage foot models) material properties and anatomy are necessarily simplified. The majority of these models assumed a linear elastic plantar aponeurosis with constant cross-sectional areas (Cheung and Zhang, 2008; Garcia-Gonzalez et al., 2009; Spyrou and Aravas, 2011; Tao et al., 2010).

To improve the plantar aponeurosis representation in numerical foot modeling, Pavan et al., determined the tissue’s transversally isotropic viscohyperelastic constitutive model using stress relaxation tests. Although the specimens were excised from three regions of the plantar aponeurosis, the influence of region on mechanical behavior was not investigated. A simple rectangular specimen geometry also avoided the need for anatomical cross-sectional areas measurement. However, this anatomical information is extremely important for developing plantar aponeurosis models.

Understanding the regional anatomy and material properties of the plantar aponeurosis will offer crucial information that can be integrated with predictive models to investigate the plantar aponeurosis functionality. The purpose and novelty of this study is to characterize the cross-sectional areas and mechanical properties of the plantar aponeurosis at four regions (i.e., proximal and distal middle, medial and lateral). This knowledge is important in developing analytical and computational models of the plantar aponeurosis to gain insight into the biomechanical functions, effect of disorders and treatment options of this tissue.

6.3 Methods

6.3.1 Specimen preparation

Fifteen plantar aponeurosis specimens were harvested from fresh-frozen cadaveric feet (mean±SD; age: 70±7 years old, weight: 773±178 N and body mass index (BMI): 25.7±5.9; Table 6.1). Each foot was fully thawed and soft tissues surrounding the plantar aponeurosis were removed. The bone-plantar aponeurosis-bone specimen was isolated from the foot by performing osteotomies at the calcaneus, metatarsal neck and the base of the proximal phalanges (Figure 6.1). The proximal and distal middle, medial and lateral regions were visually identified based on fiber orientation (Figure 6.1). The tissue proximal to the junction where the plantar aponeurosis divides into the distal slips was defined as the proximal middle region. The medial, distal middle and lateral regions extended from the proximal-distal junction towards the first, the second through fourth and the fifth metatarsophalangeal joint complexes, respectively.

Table 6.1: Donor information.

	Biomechanical test region, Mean±SD			***p*-value**[a]
	Proximal and distal middle	**Medial**	**Lateral**	
Age (yr)	65±2	74±6	70±8	0.13
Weight (N)	805±179	696±204	818±162	0.53
BMI (kg/m^2)	27±6	24±7	26±6	0.79
Gender (M,F)	4,1	4,1	4,1	-

[a] Significance level; $p < 0.05$.

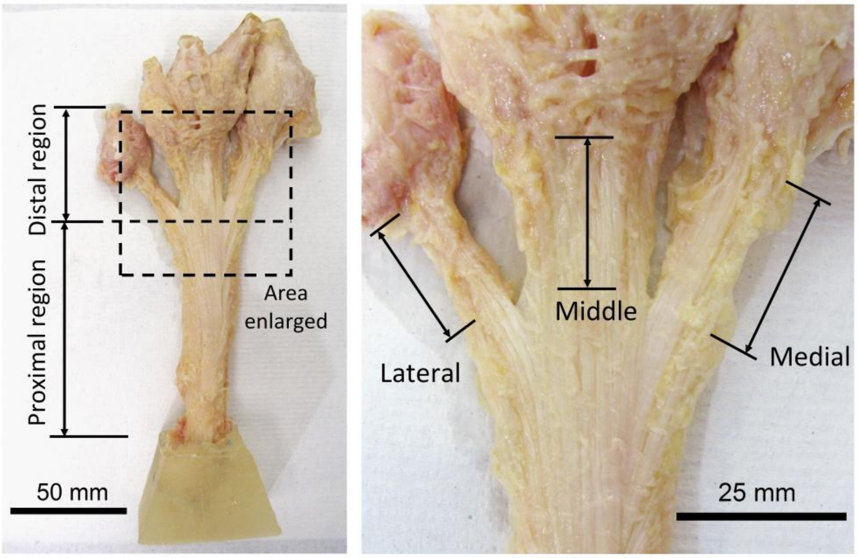

Figure 6.1: Plantar view of an isolated bone-plantar aponeurosis-bone specimen from a right foot. Calcaneus (seen left) was embedded in a polymethylmethacrylate (PMMA) block.

6.3.2 Cross-sectional area measurement

The cross-sectional areas of the four regions were quantified using a previously published technique which involves molding, casting and sectioning (Schmidt and Ledoux, 2010). In brief, a silicone polymer (OOMOO25, Smooth-On Inc, PA) was used to create a mold of each specimen. Specimens were hung vertically with 0.7 N applied at the proximal end to maintain tension in the tissue. After carefully removing the specimen, a liquid plastic polymer (Smooth-Cast 305, Smooth-On Inc, PA) was poured into the mold to make a positive replica of each specimen. These positive replicas were sectioned perpendicular to the fiber direction using Dremel 4000 electric tool equipped with a fiberglass reinforced cut-off wheel (Robert Bosch Tool Corporation, IL). Spacing between sections was 10mm in the proximal middle region and 2mm for all distal regions (Figure 6.2). The cut face of each cross-section was painted black (the positive itself is white) and photographed perpendicular to the cut face, with a metric ruler in the cut plane and within the field of view. Custom MATLAB (MathWorks, Natick, MA) code was used to quantify the area of the painted cut face.

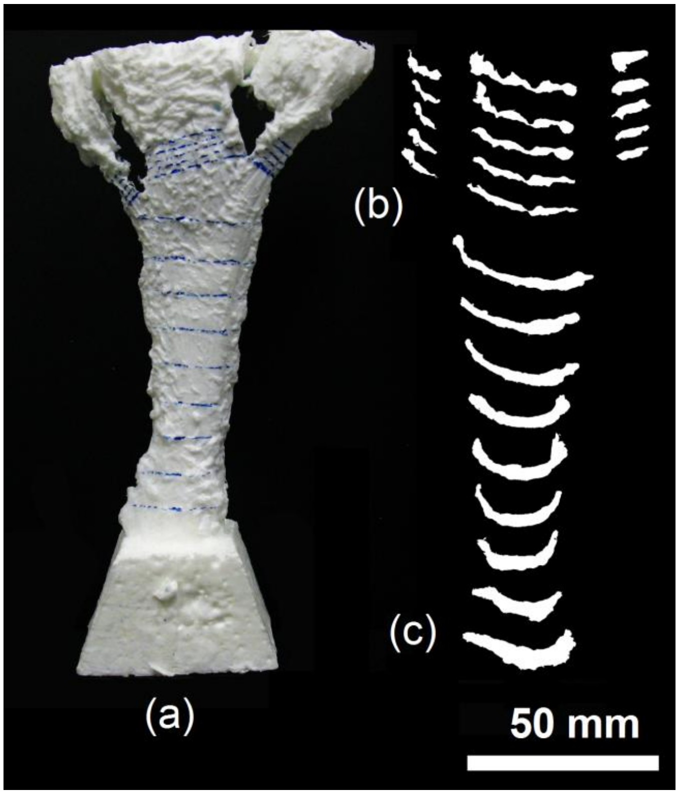

Figure 6.2: (a) Positive replica of the plantar aponeurosis, (b) examples of cross-sectional areas distal and (c) proximal. Note that the cross-sections were painted black, but were inverted during analysis.

6.3.3 Biomechanical testing

Five specimens were randomly chosen and tested for each region (proximal and middle distal regions were tested from the same specimen). Portions of the tissue which would not be loaded (e.g., the medial and lateral regions when testing the proximal and distal middle regions) were resected (Figure 6.3a) to minimize artifacts. The motion of the unloaded portions of the tissue during testing generated both inertial errors and occluded the loaded tissues). For each region tested, the borders were chosen to maximized gage length. Those gage areas were manually marked on the plantar side of the specimen using black enamel paint to create a speckled field. The remaining forefoot bones were potted in polymethylmethacrylate (PMMA) using a custom designed mold to ensure a rigid specimen-clamp interface.

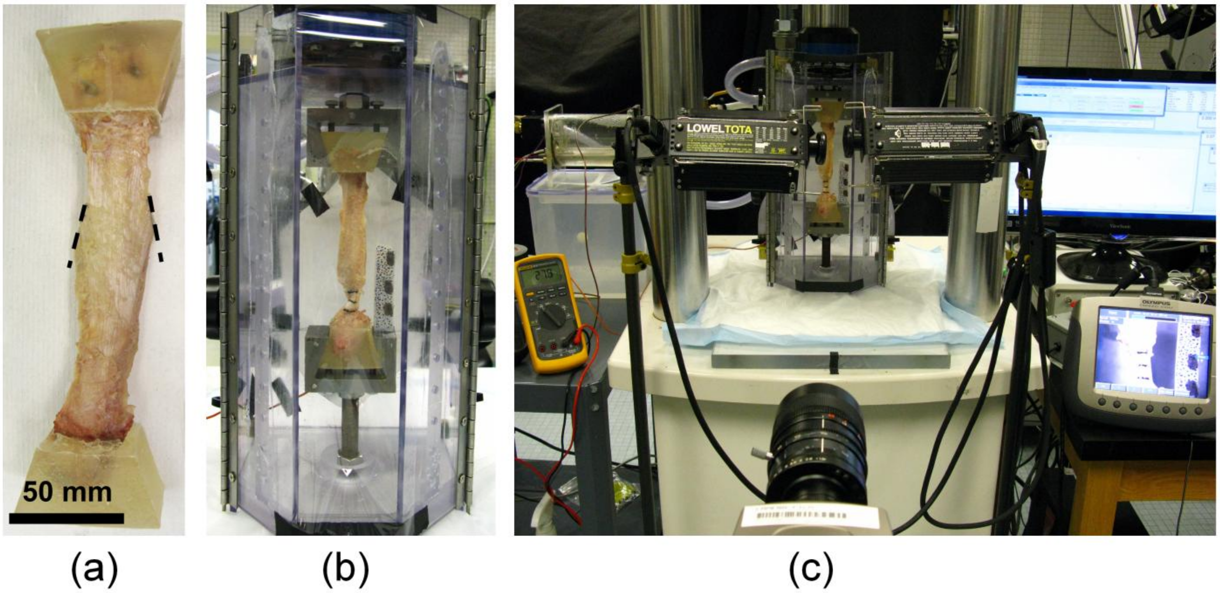

Figure 6.3: (a) A specimen prepared for the middle region tests by resecting (dash line) the medial and lateral bands then (b) securing to titanium clamps in an environmental chamber. (c) The experimental set up consisted of three systems: the materials testing machine, environmental chamber and high-speed video camera.

Mechanical testing was performed using an ElectroForce 3400 material testing machine (Bose Corporation, Minnetonka, MN) equipped with a custom designed environmental chamber (Figure 6.3b). The chamber maintained physiologic temperature (32 ±2 °C) and humidity (near 100%) while allowing an unobstructed view of the specimen during video recording. The specimen was secured to the loading frame via two custom designed titanium clamps. The target peak load during testing was derived by using 96% body weight (a peak plantar aponeurosis force during gait (Erdemir et al., 2004)) and scaling by the area ratio of the region tested. A preload of 2% of the target peak load was used.

The test sequence for each specimen was as follows: two load control trials were performed at 1 Hz using a triangle wave cycling between preload and target peak load for 30 cycles, with a 10-minute unloaded recovery period and crosshead adjustment between trials. The first load control trial and crosshead adjustment removed slack in the system and ensured that actuator translation was within the displacement range (25.0 mm) of the linear motor. The second trial determined the displacement targets for that specimen. The mechanical testing was then carried out using displacement control. Five frequencies (0.5, 1, 2, 5, 10 Hz) were tested in a randomized order, using a triangle waveform to load the tissue between displacement targets. For each frequency, a total of 30 cycles were applied (cycles 1-26 preconditioned the tissue, while cycles 27-29 were used for analysis). Specimens recovered for 10 minutes between tests. Force and actuator position were recorded at 1000 Hz (5000 Hz for a 10 Hz test).

6.3.4 Optical deformation measurement

To record the deformation of the gage length during mechanical testing, an *i*-SPEED 1GB high-speed video camera (Olympus Corporation, Waltham, MA) equipped with a Fujinon 10-110 mm f1.6 lens (Fujifilm, Edison, NJ) and two-1 kW strobe lights (Figure 6.3c) sampled 600 x 800 pixel images at a frame rate of 100 times the loading frequency. Prior to testing, alignment between the camera sensor and the deformation plane was confirmed using a double-mirror system (zig-align, Menlo Park, CA). A rigid calibration plate with printed patterns (0.5mm diameter dots, 2.5mm grid spacing) was imaged and custom MATLAB code was used to estimate pixel size and compute a distortion correction map. The videos were post-processed to remove image distortion; then two-dimensional (2D) in-plane deformations were analyzed using digital image correlation and tracking code written in MATLAB (Eberl et al., 2010).

6.3.5 Analysis

Force measurements were synchronized with the optical deformation data by aligning the actuator displacements, which were simultaneously recorded by the high-speed camera, and the linear variable displacement transducer (LVDT). A speckle-patterned target was attached to the specimen clamp during every test and two comparisons were made. An ideal situation (i.e., slow (5 mm/s) ramp, optimal alignment and adequate lighting) was first tested, then during tissue tests an overall comparison was conducted. Peak stress (maximum force divided by the original cross-sectional area), peak strain (maximum axial deformation divided by the gage length at preload), modulus (slope of the loading stress-strain curve at the final 25% deformation) and energy loss (area between the loading and unloading stress-strain curves) were calculated for each frequency and each region. Linear mixed effects regression was used to test for association between specimen region or frequency and biomechanical outcomes (peak strain, peak stress, final modulus and energy loss). Biomechanical outcome was the dependent variable, frequency (modeled as 4 indicator variables with 0.5 Hz as the reference group) and region were independent fixed effects, and age was included as a model covariate. Random effects were not modeled for differences in outcomes by frequency across specimen, as there was very little within subject/within region/within frequency level variability. Analysis of the association between region and outcomes were adjusted for frequency and age, and analysis of the association between frequency and outcomes were adjusted for region and age. If significant associations were found, pair-wise analyses were carried out using simultaneous inference (Hothorn et al., 2008).

Linear mixed effects regression was also used to determine if cross-sectional area (the dependent variable) differed by region (the independent fixed effect) with random effects as previously mentioned for the model looking at differences in those specimens undergoing biomechanical testing. For models including all area measurements, random effects were modeled for the mean differences in region across specimen (as all specimens had area measurements for each of the 4 regions). Pair-wise comparisons were carried out as above. Separate linear mixed effects regressions for each region were carried out to determine if cross-sectional areas (the dependent variable) differed for those specimens undergoing biomechanical testing compared to those who did not (the independent fixed effect) with random effects for the differences in overall mean area across specimen. Analyses were carried out using R 2.15.3 (R Core Team, 2013), the lme4 (Bates et al., 2012) and nlme (Pinheiro et al., 2013) packages to conduct the linear mixed effects models, and the *multcomp* (Hothorn et al., 2008) package to conduct the pair-wise comparisons.

6.4 Results

The plantar aponeurosis had irregular cross-sectional anatomy (Figure 6.2). No cross-sectional area differences were found between mechanically tested and non tested regions ($p > 0.05$ for all 4 regions). Across regions, cross-sectional areas were different ($p < 0.05$) except between the medial and distal middle regions (Figure 6.4).

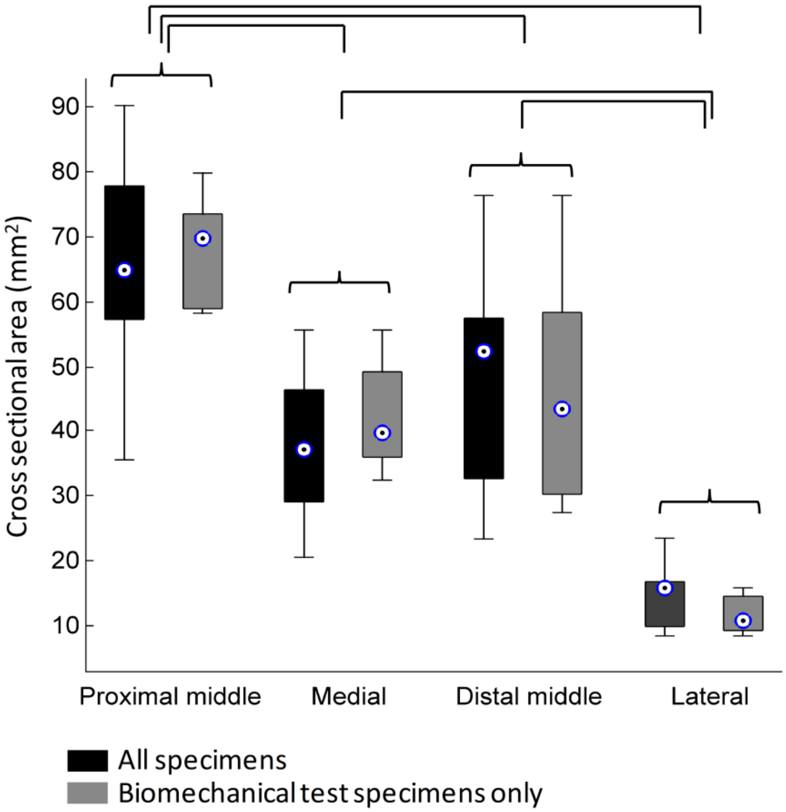

Figure 6.4: Cross-sectional areas of the plantar aponeurosis among regions. Significance level $p < 0.05$ from linear mixed effects regression of area on region. No cross-sectional area difference ($p > 0.05$) was found between biomechanical test and all specimens groups at all four regions.

The optical deformation measurement system could reliably tracked displacement of 5 mm at 100 fps with 18.8 μm accuracy in an ideal set up condition when the DIC was compared to the LVDT data. During biomechanical testing, the accuracy was 35±16 μm (0.55% of the mean actuator displacement) between the DIC tracking of the clamp and the LVDT measurement.

The stress-strain relationship from biomechanical testing indicated that the tensile responses were non-linear, with an increasing modulus at higher strains (Figure 6.5). The medial and lateral regions had significantly higher peak strains and lower modulus ($p < 0.05$) as compared to the proximal and middle distal regions (Table 6.2) There was no difference between the medial vs. lateral and proximal vs. distal middle regions. Peak stresses were similar in all regions except between medial and lateral . Energy loss at the lateral region was significantly higher ($p < 0.05$) compared to the other three regions (no differences within the three regions).

The plantar aponeurosis exhibited very little strain rate dependence (Table 6.3). Although several pair-wise comparisons indicated statistically significant differences, the magnitudes were small (e.g., a 3.5% modulus increase as the frequency increased 20 fold from 0.5 to 10 Hz), except for energy loss, which increased by 107% as the frequency increased from 0.5 to 10 Hz.

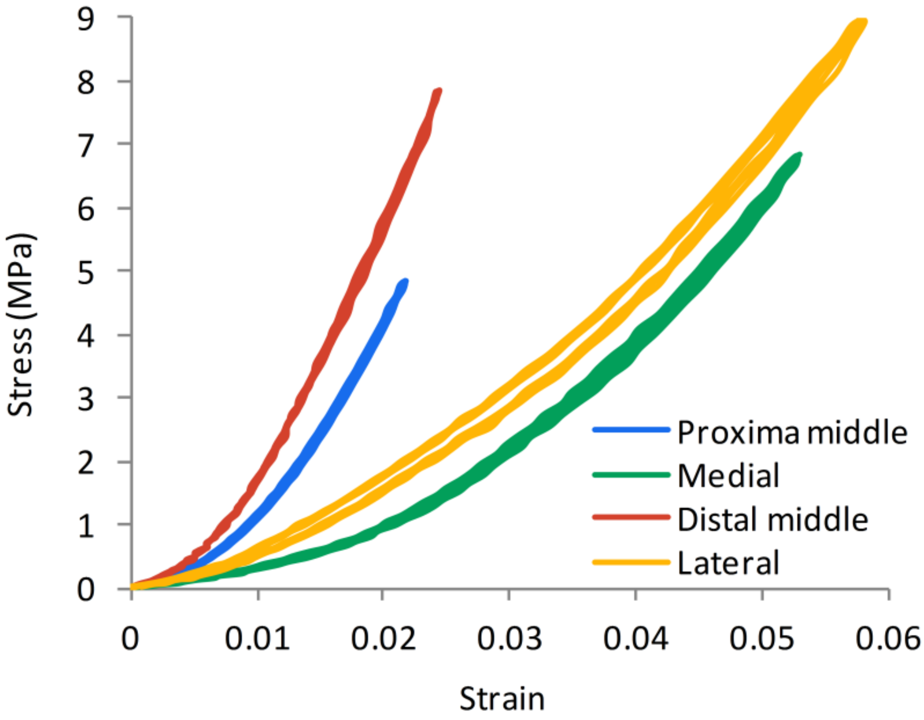

Figure 6.5: Representative stress-strain responses showed different moduli and peak strains across regions. Energy losses were relatively small indicating nearly elastic behavior.

Table 6.2: Estimated mean±SE of biomechanical outcome by region[*].

	Biomechanical test region				p-value[a]
	Proximal middle	**Medial**	**Distal middle**	**Lateral**	
Peak stress (MPa)	6.09±1.42	5.39±0.62	7.75±0.93	8.29±0.58	0.010[b]
Peak strain (%)	2.30±0.57	4.39±0.51	2.11±0.54	5.10±0.48	0.0023[c]
Final modulus (MPa)	400±59	225±66	522±62	242±24	0.0045[c]
Energy loss (%)	3.6±0.6	4.1±0.6	2.4±1.2	7.2±0.6	0.003[d]

[*] Values estimated at 0.5 Hz and age 70 yr from linear mixed effects regression of biomechanical outcome on region adjusting for frequency and age.

[a] Significance level; $p < 0.05$.

[b] Pair-wise comparisons; $p < 0.05$ for lateral vs. medial.

[c] Pair-wise comparisons; $p < 0.05$ for proximal and distal middle vs. medial and lateral.

[d] Pair-wise comparisons; $p < 0.05$ for lateral vs. proximal middle, medial and distal middle.

Table 6.3: Estimated mean±SE of biomechanical outcome by frequency[*].

	Frequency (Hz)					p-value[a]
	0.5	**1**	**2**	**5**	**10**	
Peak stress (MPa)	6.09±1.42	6.30±1.42	6.34±1.42	6.53±1.42	6.60±1.42	<0.001[b]
Peak strain (%)	2.30±0.57	2.30±0.57	2.35±0.57	2.34±0.57	2.38±0.57	<0.001[c]
Final modulus (MPa)	401±57	406±57	407±57	416±57	415±57	<0.001[d]
Energy loss (%)	3.6±0.6	3.8±0.6	4.4±0.6	5.5±0.6	7.3±0.6	<0.001[e]

[*] Values estimated at 0.5 Hz and age 70 yr from linear mixed effects regression of biomechanical outcome on region adjusting for region and age.

[a] Significance level; $p < 0.05$.

[b] All pair-wise comparisons $p < 0.001$ except for 2Hz vs. 1Hz and 10Hz vs. 5Hz.

[c] Pair-wise comparisons; $p < 0.001$ for 10Hz vs. 0.5Hz or 1Hz; $p < 0.05$ for 2Hz or 5Hz vs. 0.5Hz or 1Hz.

[d] Pair-wise comparisons; $p < 0.001$ for 5Hz or 10Hz vs. 0.5Hz; $p < 0.05$ for 5Hz or 10Hz vs. 1Hz or 2Hz.

[e] All pair-wise comparisons $p < 0.001$ except for 0.5Hz vs. 1Hz.

6.5 Discussion

The regional cross-sectional areas and material properties of the plantar aponeurosis are crucial for developing physiologic predictive models and understanding its functionality. This study explored the anatomy and biomechanical properties of the plantar aponeurosis at four regions: the proximal and distal middle, medial and lateral.

There are differences in both the geometric and mechanical properties of the plantar aponeurosis across regions. By utilizing the molding, casting and sectioning technique, complete cross-sectional areas of the plantar aponeurosis can be accurately and non-destructively quantified – allowing both geometric and mechanical measures to be performed on the same tissue. The cross-sectional areas from this study (Figure 6.4) were substantially larger than areas computed from the literature (rectangular assumption, width and thickness measured with vernier caliper); 36.3 mm^2 overall cross-sectional area (Wright and Rennels, 1964); 43.1 mm^2, 9.0 mm^2, 16.7 mm^2 and 3.3 mm^2 for the proximal, the distal first, second to fourth and fifth bundles, respectively (Chen et al., 2014a). The discrepancies are likely due to oversimplification of the shape, different dissection protocols and tissue compression from vernier caliper. In this study, the mean proximal cross-sectional area was 33% smaller than the sum of three distal regions, suggesting that the potential injury site (i.e., mechanical overload) could be located at the smallest cross-sectional area on the proximal region (average 41 mm or approximately 32 % of the total plantar aponeurosis length from the calcaneal insertion). However, several studies have shown plantar aponeurosis failures (Kitaoka et al., 1994) or plantar fasciitis symptoms (Thomas et al., 2010) occurred near the calcaneal attachment, suggesting that minimal area is not the only factor.

The biomechanical results of this study indicate that the material properties of the plantar aponeurosis are nonlinear, differ by region and are primarily elastic. Similar nonlinear, elastic behavior had been reported in previous studies (Kitaoka et al., 1994; Wright and Rennels, 1964). The stiffness, peak stresses, peak strains and moduli from the current study are difficult to compare to literature due to differences in experimental set up including: preloading, target peak force, peak deformation and measurement location. Kitaoka et al. (1994) found an overall stiffness (mean±SD) of approximately 209±51.9 N/mm compared to our study with 442±104.3 N/mm, 576±89.4 N/mm, 1,207±328.6 N/mm and 166±35.0 N/mm at the proximal middle, medial, distal middle and lateral regions, respectively. The computed moduli from our study (225-522 MPa) were lower than 827 MPa previously reported (Wright and Rennels, 1964). It is worth noting that stiffness is a structural property rather than material property. Computing modulus from stiffness requires very accurate gage length and cross-sectional area measurements.

There were statistically significant differences in biomechanical outcome across frequency. However, except for energy loss, the magnitude of these differences are small compared to those from regional comparisons (maximum differences of less than 8% across frequency compared to 54% or higher across regions) and may not be clinically meaningful. Comparable to our findings, Kitaoka et al. (1994) concluded that the plantar aponeurosis stiffness was insensitive to loading rate. We found that energy loss, on the other hand, demonstrates positive correlation with loading rate. A similar trend had been observed in foot ligaments (energy loss: 12.5% - 17.0%) (Schmidt, 2009) and plantar fat (energy loss: 61.9% - 74.9%) (Pai and Ledoux, 2010) with a higher magnitude compared to plantar aponeurosis (energy loss: 3.6% - 7.3%). This nearly elastic response agreed with observations that plantar aponeurosis functioned as an energy storage component during weight bearing (Ker et al., 1987; Kim and Voloshin, 1995).

This study has some potential limitations. Although physiologic force distribution in different plantar aponeurosis regions is unknown, we assumed equal stresses across three distal regions. A computational modeling study reported similar trends (Lin et al., 2014). Despite this assumption, we found peak stresses at the medial and lateral regions were significantly different. This is likely due to a relatively large difference in body weight between the medial and lateral groups. Another limitation was that the proximal and distal middle regions were tested from the same specimen due to anatomical and mechanical testing constraints (i.e., we required bone-plantar aponeurosis-bone samples). As a result, the proximal region was not loaded to the target force (96% body weight) due to a force limitation at the distal middle region. Last, the specimen thickness was small compared to the length and width dimensions, thus, we only quantify axial deformation for the 2D plantar aspect of the tissue.

This study demonstrates that cross-sectional areas and mechanical properties of the plantar aponeurosis differs across regions. The mechanical responses are non-linear and nearly elastic. We measured a minor effect of loading rate on the biomechanical behavior, except for energy loss which was significantly higher as loading rate increases. The cross-sectional areas and mechanical properties presented here could be used to develop a material constitutive model or directly applied to biomechanical analysis, with implications for better understanding of the etiology of plantar aponeurosis disorders and to improve preventive care and treatment options.

Chapter 7. Predicting plantar pressure and internal stress in the foot during quiet stance and gait using subject-specific finite element analysis

7.1 Abstract

Diabetic foot ulceration has been hypothesized to initiate deep inside the plantar soft tissue and is thought to be influenced by mechanical factors, such as foot deformities, abnormal foot loading, and changes in soft tissue material properties. Finite element (FE) models can provide insight into the effect of these mechanical changes on internal stresses of the foot. However, many of previous FE foot models were quasi-static and imposed major simplifications on anatomy and material properties which could compromise their usefulness in certain applications. The purpose of this study was to develop and validate two subject-specific FE foot models (normal and diabetic), to explore the plantar pressure and internal soft tissue stress during quiet stance and the stance phase of gait, and to investigate the effect of soft tissue simplifications. The model included subject-specific bone, skin, muscle and fat anatomy obtained from CT and MR imaging data. Subject-specific hyperelastic material properties were assigned for each soft tissue. Ligaments and tendons were modeled by non-linear spring and seatbelt elements, respectively. Four regions of the plantar aponeurosis were modeled with non-linear material properties. The models were validated with *in vivo* experimental data collected in-house and with literature data under three loading conditions: passive compression, quiet stance, and the stance phase of gait, by analyzing bony kinematics, ground reaction forces (GRFs), plantar pressure, plantar aponeurosis force and ankle joint force. The model results suggested that the hydrostatic stress in the soft tissue was substantially higher than the von Mises stress. The location and time of the peak forefoot internal stresses (von Mises and hydrostatic) may not always coincide with the peak plantar pressure or vertical GRF, but frequently did. The forefoot and hallux had a greater risk of injury due to higher peak von Mises and hydrostatic stresses and longer loading duration compared to the hindfoot. Parametric analysis at quiet stance suggested that stiffer plantar fat increased plantar pressure and internal stress. In this study, modeling soft tissue as

multi-material layers is necessary to simulate physiologic plantar pressure. However, non-subject-specific material properties may be used for plantar pressure prediction. Generic soft tissue simplification should be avoided.

7.2 Introduction

Diabetic foot ulceration is one of the leading causes of non-traumatic lower-limb amputations in the United States (CDCP, 2014). The primary causes of diabetic foot ulceration are peripheral neuropathy and peripheral vascular disease which often result in foot deformities, elevated plantar pressure, and soft tissue injury (Bus et al., 2005; James A. Birke, 1991; Singh et al., 2005). After a prolonged exposure to high plantar pressure, the tissue will eventually develop calluses, an important indication of pre-ulcerative lesion in the neuropathic foot (Edmonds and Foster, 2006; Murray et al., 1996). It is believed that this thick callused region injures the deeper soft tissue and causes ulceration (Edmonds and Foster, 2006; Murray et al., 1996).

Changes in soft tissue mechanical properties also contribute to diabetic foot ulceration. Diabetic plantar soft tissue suffers from increased stiffness (Cheung et al., 2006b; Hsu et al., 2009; Klaesner et al., 2002; Pai and Ledoux, 2010, 2012), especially under the first metatarsal head (Gefen et al., 2001; Zheng et al., 2000), greater hardness at the plantar skin (Piaggesi et al., 1999; Thomas et al., 2003), and soft tissue atrophy (Zheng et al., 2000).

Finite element (FE) models of the foot have been used to gain insights into the biomechanics of healthy, normal (Chen et al., 2010; Cheung et al., 2004, 2006a) and diabetic feet (Cheung et al., 2005; Gefen, 2003; Thomas et al., 2004), predict surgery outcomes (Cheung et al., 2004; Gefen, 2002; Iaquinto and Wayne, 2011; Isvilanonda et al., 2012), design pressure relieving insoles (Budhabhatti et al., 2009; Chen et al., 2003; Cheung and Zhang, 2005; Cheung and Zhang, 2008; Erdemir et al., 2005; Goske et al., 2006; Spears et al., 2007) and investigate internal soft tissue stresses (Chen et al., 2010; Gefen, 2003; Lin et al., 2014; Petre et al., 2013). The model complexity ranges from two-dimensional (2D) (Gefen, 2003; Halloran et al., 2010; Qian et al., 2013; Wu, 2007), three dimensional (3D) rigid body (Iaquinto and Wayne, 2011; Xu et al., 2011) to 3D deformable simulations (Camacho et al., 2002; Chen et al., 2012; Chen et al., 2001; Cheng et al., 2008; Cheung and Zhang, 2008; Dengler, 2008; Garcia-Aznar et al., 2009; Guiotto et al., 2014; Isvilanonda et al., 2012; Qiu et al., 2011; Spyrou and Aravas, 2011; Sun et al., 2011).

The majority of the models obtained foot anatomy from computed tomography (CT) and/or magnetic resonance (MR) images and utilized linear tetrahedral elements to model the geometry (Chen et al., 2012; Chen et al., 2001; Cheng et al., 2008; Cheung and Zhang, 2008; Dengler, 2008; Garcia-Aznar et al., 2009; Guiotto et al., 2014; Iaquinto and Wayne, 2011; Isvilanonda et al., 2012; Qiu et al., 2011; Spyrou and Aravas, 2011; Sun et al., 2011; Xu et al., 2011). Soft tissue is often represented by a nearly incompressible hyperelastic material (Chen et al., 2001; Chen et al., 2010; Cheng et al., 2008; Cheung and Zhang, 2008; Dengler, 2008; Guiotto et al., 2014; Isvilanonda et al., 2012; Qiu et al., 2011; Spyrou and Aravas, 2011).

In order to reduce model complexity and improve stability, the material properties and anatomy of the plantar soft tissue have often been simplified by grouping skin, fat and muscle into a homogeneous generic soft tissue (Chen et al., 2012; Chen et al., 2001; Cheng et al., 2008; Cheung and Zhang, 2008; Guiotto et al., 2014; Qiu et al., 2011; Spyrou and Aravas, 2011). Further, these models tend to use *in vivo* generic soft tissue material properties that represented population average. These simplifications (i.e., generic soft tissue, non subject-specific material) can lead to substantial errors in the predicted plantar pressures (Erdemir et al., 2006; Guiotto et al., 2014; Spears et al., 2007; Spirka et al., 2014).

Furthermore, joint contacts are sometimes replaced by fused bones (i.e., no contact) or a single cartilage plug (Chen et al., 2012; Chen et al., 2001; Chen et al., 2014; Cheng et al., 2008; Cheung and Zhang, 2008; Guiotto et al., 2014; Qiu et al., 2011; Spyrou and Aravas, 2011). Foot ligaments are often represented by tension-only truss elements (Chen et al., 2012; Chen et al., 2001; Chen et al., 2014;

Guiotto et al., 2014; Lin et al., 2014) and the stiffness is assumed to be similar in all locations. The plantar aponeurosis is simplified to either tension-only truss elements connecting the hindfoot to each of the metatarsal heads (Chen et al., 2010; Cheung and Zhang, 2008) or shell/solid elements with constant thickness (Chen et al., 2012; Chen et al., 2014). Extrinsic muscle forces, with the exception of the Achilles tendon force, are commonly ignored (Chen et al., 2010; Chen et al., 2014; Guiotto et al., 2014) or are directly applied to bones at the tendon insertion sites instead of via tendon actuation (Cheung and Zhang, 2008). These oversimplifications in joint contacts, ligament and muscle forces can potentially cause non-physiologic bone kinematics and force distributions (Actis et al., 2006; Guiotto et al., 2014).

Most FE foot models are validated by comparing the predicted plantar pressure to experimental measurements and the literature. Simulations are typically performed under quasi-static conditions, such as passive foot compression, quiet stance, or fixed gait positions using an implicit FE solver (Chen et al., 2001; Chen et al., 2010; Chen et al., 2014; Cheng et al., 2008; Cheung and Zhang, 2008; Garcia-Aznar et al., 2009; Gefen, 2002; Guiotto et al., 2014; Qiu et al., 2011; Sun et al., 2011; Wu, 2007). These types of (implicit) quasi-static analyses require that the model satisfies an equilibrium condition at every solver iteration. This requirement that the model is always in equilibrium substantially limits the model’s utility and accuracy, as the foot is more likely to experience higher loads and deformations during dynamic activities compared to the quasi-static condition.

In this study we developed and validated two subject-specific FE foot models – one of a healthy, normal subject and one of a diabetic subject. This model includes several improvements over prior work such as: the use of subject-specific input (anatomy, soft tissue material properties, tibial kinematics), modeling techniques (plantar aponeurosis, ligament, tendon and joint cavity/contact) and validation protocols (static and dynamic conditions, experimental and literature data). The models were used to determine plantar pressure and internal stress estimations during quiet stance and gait. A parametric analysis at the quiet stance condition was performed to estimate the effect of plantar soft tissue assumptions on these pressure and stress results.

7.3 Method

7.3.1 Finite element model development

A healthy normal subject (43-year-old male, 945 N body-weight (BW)) and a subject with diabetes (31-year-old male, 688 N BW) without prior ulcer history and without foot deformity participated in this IRB-approved study. Partial weight bearing (10% BW) CT images of each subject's right foot in the neutral position (i.e., tibia normal to ground) were acquired at the Veterans Affairs Puget Sound Health Care System (Phillips CT MX8000IDT, pixel spacing 0.715 mm, voxel depth 0.5 mm, slice spacing 0.5 mm, slice thickness 1.0 mm). Unloaded soft tissue anatomy was obtained using an MRI scan at the Bio-Molecular Imaging Center at the University of Washington (3.0T Phillips Achieva MRI system, pixel spacing 0.6 mm, voxel depth 0.6 mm, slice spacing 0.6 mm, slice thickness 1.2 mm, proton density water). The 28 bones of each scanned foot, including length of ~10cm of distal tibia and fibula, were segmented from the CT images using custom software, *MultiRigid* (Hu et al., 2011). The segmented bones were then registered to the MR images to generate a dummy MR data set in which all bones were masked. Subsequently, fat, muscle (lumping all visible intrinsic muscles into one component) and the outer skin contour were segmented. A total of 31 surface models (28 registered bones, fat, intrinsic muscle and skin surface) were exported as a triangulated surface mesh (Figure 7.1a and b). The surface mesh was post-processed in ScanIP (Simpleware Ltd, Exeter, UK) to remove gaps, overlaps and surface irregularities. Skin thickness (3 or 2 pixels, i.e., 2.15 mm plantar and 1.43 mm dorsum), joint cavities/capsules and generic soft tissue (dorsum region of the foot that is not occupied by other materials) were generated using a series of Boolean operations (Figure 7.1a, b). The surface models were meshed with linear tetrahedral elements in ANSYS ICEM CFD (ANSYS Inc, Canonsburg, USA) (Figure 7.1c, d). The optimal element size (2.5 mm) and formulation (elform 13) were determined from a mesh sensitivity analysis (Appendix IV). The floor consisted of 5mm x 5mm x 5mm hexahedral elements and modeled as a rigid body to emulate the emed®-x pressure measurement platform (emed®, novel GmbH, Munich, Germany). Fourteen rigid spherical shells (three 14-mm and eleven 8.4-mm diameter, Figure 7.1c) were fixed to the skin elements to represent the retro reflective marker set used in experiments (Leardini et al., 2007).

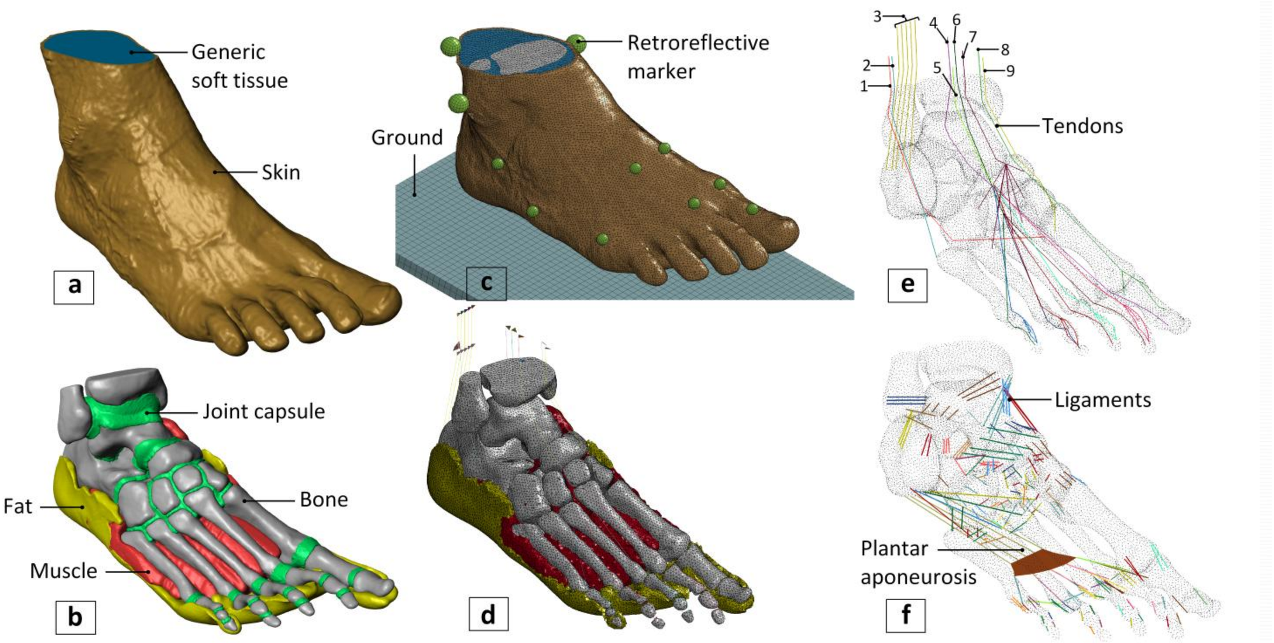

Figure 7.1: (a, b) Surface model of the normal foot generated from CT and MR images showing skin (brown), generic dorsal soft tissue (blue), plantar fat (yellow), intrinsic muscle (red), bones (gray) and joint capsules (green). (c, d) The model was meshed with linear tetrahedral elements. (c) Rigid ground and retro-reflective markers were created. (e) Nine extrinsic muscle tendons, (f) 102 ligaments and the plantar aponeurosis were included in the model. The list of extrinsic muscle tendons are: 1) peroneus longus, 2) peroneus brevis, 3) the Achilles, 4) flexor hallucis longus, 5) extensor digitorum longus, 6) flexor digitorum longus, 7) tibialis posterior, 8) extensor hallucis longus and 9) tibialis anterior.

The FE model of the normal subject was pre-processed in LS-Prepost (Livermore Software, Livermore, USA). The skin, fat, muscle and generic soft tissue were represented by first-order nearly-incompressible Ogden hyperelastic materials (equation 7.1).

$$W(\lambda_1,\lambda_2,\lambda_3)=\frac{\mu}{\alpha}\left(\tilde{\lambda}_1^{\alpha}+\tilde{\lambda}_2^{\alpha}+\tilde{\lambda}_3^{\alpha}-3\right)+\frac{1}{2}K(J-1)^2 \tag{7.1}$$

$$J=\lambda_1\lambda_2\lambda_3 \tag{7.2}$$

$$\tilde{\lambda}_i=\frac{\lambda_i}{J^{1/3}} \tag{7.3}$$

where subject-specific material coefficients (Table 7.1) for the skin (μ_S and α_S), fat (μ_F and α_F), muscle (μ_M and α_M) and generic soft tissue (μ_G and α_G) were obtained from inverse FE analysis (Chapter 5). The Jacobian (J) is the relative volume change (equation 7.2) given by the product of three principal stretches ($\lambda_1, \lambda_2, \lambda_3$) and K denotes bulk modulus. The volumetric independent principal stretches ($\tilde{\lambda}_i$) are related to λ_i by equation 7.3.

Bones were modeled as rigid bodies due to their small deformation compared to the soft tissue. Joint cavities were assumed to have zero stiffness (i.e., elements in the joint cavities were deleted). A total of 102 ligaments (Figure 7.1f) were included in the model using one or more nonlinear spring elements per ligament (total of 165 elements). Nine extrinsic muscle tendons and the plantar aponeurosis were created (Figure 7.1e, f) based on previously established techniques (Isvilanonda et al., 2012). The extrinsic muscle tendons in this model were: peroneus longus, peroneus brevis, the Achilles, flexor hallucis longus, extensor hallucis longus, flexor digitorum longus, extensor digitorum longus, tibialis anterior and tibialis posterior.

The plantar aponeurosis was divided into four bands by region: the proximal and distal middle (central bulk of the tissue), medial to the first ray, and lateral to the fifth ray (Isvilanonda et al., 2012). As an improvement over our previous model, each band was assigned to a unique force-deformation property obtained from cadaveric experiments (Chapter 6). Twenty-six joint articulations (static friction coefficient = 0.1, dynamic = 0.085 (Merkher et al., 2006)) were defined by rigid contacts with static offset distance. Cartilage deformation was accounted for by reducing the contact thickness by 5%, 6% and 7.5% during partial weight bearing, quiet stance and gait simulations, respectively (Bischof et al., 2010; Li et al., 2008; Wan et al., 2008). This joint modeling technique eliminated small deformable cartilage elements, therefore improving model stability and solving time. The coefficients of friction for skin-ground and skin-skin (toes 2, 4 to toes 1,3,5) contacts interfaces were assigned to 0.3 (Buczek and Banks, 1996).

Table 7.1: Material properties and element types used for each FE model component.

Material	Material Model	Element Type	Material Coefficient	Mass Density (10^{-6}kg/mm^3)	Reference
Ground	Rigid	Hexahedral	E=68.9 GPa [a], v=0.35	2.7	(Hibbeler, 1997)
Bone	Rigid	Tetrahedral	E=20.1 GPa [a] v=0.30	0.449	(Muehleman et al., 2002; Zysset et al., 1999)
Skin	Hyperelastic	Tetrahedral	Normal [b]: μ = 0.158 kPa, α = 185.20 Diabetic [b]: μ = 0.772 kPa, α = 163.56 v=0.4990	1.142	Chapter 5
Muscle	Hyperelastic	Tetrahedral	Normal [b]: μ = 0.161 kPa, α = 31.95 Diabetic [b]: μ = 0.321 kPa, α = 38.04 v=0.4999	1.047	Chapter 5
Fat	Hyperelastic	Tetrahedral	Normal [b]: μ = 1.874 kPa, α = 8.29 Diabetic [b]: μ = 0.200 kPa, α = 14.10 v=0.4999	0.916	Chapter 5
Generic soft tissue	Hyperelastic	Tetrahedral	Normal [b]: μ = 0.787 kPa, α = 21.11 Diabetic [b]: μ = 0.415 kPa, α = 25.25 v=0.4999	1.0	Chapter 5
Ligament	Nonlinear	Discrete Spring	[c]	n/.a	(Dengler, 2008; Felton, 1996; Luo et al., 1997; Mkandawire et al., 2005; Netter, 2005; Sarrafian, 1993; Schmidt, 2009) [d]
Tendon	Nonlinear	Discrete Seatbelt	[c]	n/a	(Blanton and Biggs, 1970; Maganaris and Paul, 1999; Maganaris and Paul, 2002; Schechtman and Bader, 1994) [e]
Plantar fascia	Nonlinear	Discrete Spring and Seatbelt	[c]	n/a	Chapter 6

[a] E denotes Young's modulus.

[b] μ, α denote the first order Ogden hyperelastic coefficients; v denotes Poisson's ratio.

[c] Force-deformation (discrete spring) and force-strain (discrete seatbelt) relationships were specified.

[d] Force-deformation response for the short plantar, inferior calcaneonavicular, interosseous second cuneiform-third cuneiform and interosseous fourth metatarsal-fifth metatarsal ligaments were tested in house (Schmidt, 2009). Force-deformation response for other ligaments were extrapolated based on an individual ligament length (Felton, 1996; Luo et al., 1997; Mkandawire et al., 2005; Sarrafian, 1993) and an empirical equation.

[e] TA and the Achilles tendon force-strain curves were digitized from Maganaris and Paul (1999) and (2002), respectively. TP tendon force-strain relationship was estimated from TA stress-strain data (Maganaris and Paul, 1999) and TP tendon cross-sectional area (Blanton and Biggs, 1970). Force-strain relationships for the other five tendons were extrapolated from the EDL stress-strain data (Schechtman and Bader, 1994) and cross-sectional area of each tendon (Blanton and Biggs, 1970).

The finite element model was customized for the diabetic subject by incorporating subject-specific anatomy and soft tissue material properties (Table 7.1). Ligament and plantar aponeurosis force-deformation curves, tendon paths and joint contact offsets were customized based on the subject's specific bone anatomy. Note that the unloaded MRI scans resulted in a slightly plantar flexed foot model for both subjects. In order to realign the ankle to the neutral orientation, an inferosuperior force was applied to the first and fifth metatarsal heads and the head of the talus. Bones distal to the talus were temporarily grouped to preserve their unloaded positions relative to each other. The stress generated in the soft tissue as well as all temporary constraints were removed in the adjusted model.

7.3.2 *In-vivo* experiments

Four barefoot experiments were conducted: 1) passive foot compression, 2) quiet stance on a pressure platform, 3) gait over a force plate and 4) gait over a pressure platform. The partial weight bearing CT images acquired for the bone anatomy were reused for the passive foot compression validation. Quiet stance and gait experiments were conducted at the motion analysis laboratory at the Veterans Affairs Puget Sound Health Care System. Trajectories of 11 foot markers (Leardini et al., 2007), 3 ankle markers and 3 proximal tibia markers (Figure 7.2) were collected at 120 Hz using a 12-camera motion analysis system (Vicon, Oxford, UK). Ground reaction force (GRF) and pressure were recorded at 1200 Hz using a series of five force plates (AMTI, Watertown, MA), while plantar pressure was recorded at 100 Hz via a pressure platform (emed®-x, novel GbmH, Munich Germany).. The quiet stance trial was conducted with the right foot on the pressure sensor while the left foot rested on the laboratory floor. The data were collected for five seconds and then averaged over the final two seconds. Gait data were collected from seven force plate trials and seven pressure platform trials, all with a right foot strike at a self selected speed (1.31 ±0.02 m/s normal, 1.43 ±0.05 m/s diabetic). The mean tibial kinematics calculated across seven trials were described by a time series of 4x4 transformation arrays computed about the lateral malleolus marker.

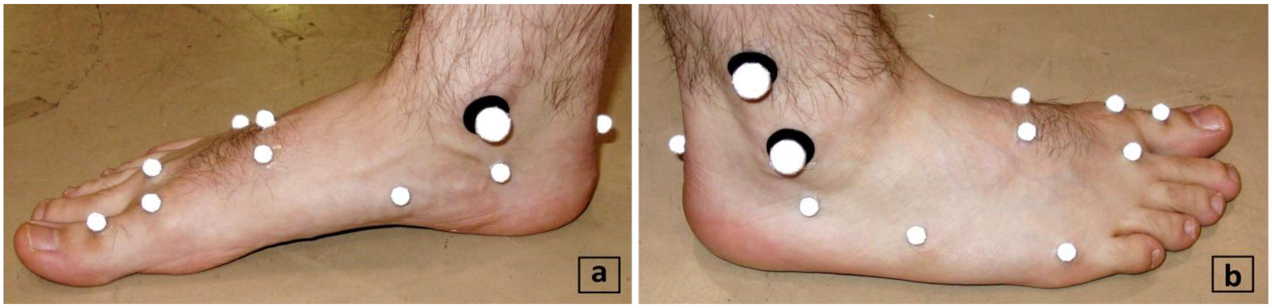

Figure 7.2: (a) Medial and (b) lateral views of the foot and the retro reflective marker set.

7.3.3 Finite element simulations

The passive foot compression test was simulated by constraining the tibia in a neutral orientation relative to ground while allowing all three translation degrees of freedom (DOF). A trans-tibial axial force and Achilles tendon force were applied to hold the ground reaction force at 10% BW. Since the in vivo Achilles tendon force was unknown, two extreme cases (i.e., zero force and near heel lift [20% BW]) were simulated. Ten bony alignments were measured and compared to the segmented CT data based on a 2D radiographic measurement protocol (Cavanagh et al., 1997).

Quiet stance position was simulated by prescribing the tibia orientation based on the motion analysis data while allowing all three translation DOF. All extrinsic muscle tendons except the Achilles were given a negligible load (0.5 N) to maintain seatbelt element stability. The Achilles tendon force was estimated by aligning the anteroposterior location of the center of pressure (COP) to the pressure platform data. The mediolateral COP location was fine tuned by applying a small adjustment (< 3.0 degrees) to the initial tibia orientation. Note that the COP position was measured relative to the posterioromedial corner of the foot print. The transtibial compression force was applied such that once all tendon forces and gravitational acceleration (9.81 m/s^2) were accounted for, the equilibrium GRF was 50% BW (473 N normal, 344 N diabetic). The simulated peak pressure, mean pressure, contact force and contact area at 11 plantar regions were compared to the pressure platform measurements based on mask regions provided by the emed software. The following mask regions were analyzed: medial and lateral hindfoot, midfoot, first through fifth metatarsals, hallux, second toe, and combined third to fifth toes.

The dynamic force plate and pressure platform gait experiments yielded different stance times, tibial kinematics and contact force; thus each ground surface condition required a separate simulation. The simulation began (0.0s) by establishing the initial foot position prior to heel strike (which occurred at 0.2s). During this period, initial tendon forces (Figure 7.3, adapted from (Aubin et al., 2012)) and gravitational acceleration were applied while the tibia was fixed in heel strike position and orientation, but the foot was just off the ground. The tendon forces generated ankle dorsiflexion from 0 to 0.15 seconds before reaching equilibrium at 0.2 seconds. Immediately after, the tibia constraints were replaced with prescribed translation and orientation boundary conditions. An initial translation velocity, estimated from the lateral malleolus at heel strike, was imposed onto the soft tissue components. During the entire stance phase of gait (0.215 seconds to toe off), the mean tibial kinematics-time series (from motion analysis) and extrinsic muscle tendon force-time series (Figure 7.3) were prescribed. The first and second peaks of the simulated vertical GRF were manually tuned to match the experimental data by adjusting the initial ground position and the Achilles tendon force, respectively. A similar tuning concept has been previously used in cadaveric gait simulation (Aubin et al., 2012) to achieve a target vertical GRF. Vertical and shear components of the GRF as well as COP progression were compared between the gait force plate simulation and the experimental data. Bone kinematics were compared to experimental measurements and literature based on protocols provided by Leardini et al. (2007) and Lundgren et al. (2008), respectively. The vertical GRF, COP progression and predicted plantar pressure at 11 regions from the pressure platform simulation were compared to the experimental data. In addition to primary validation with the experimental measurements, the predicted plantar aponeurosis force, tibiotalar joint reaction force and the optimal Achilles tendon force were also compared to literature (Erdemir et al., 2004; Sanford et al., 2014) as a secondary validation.

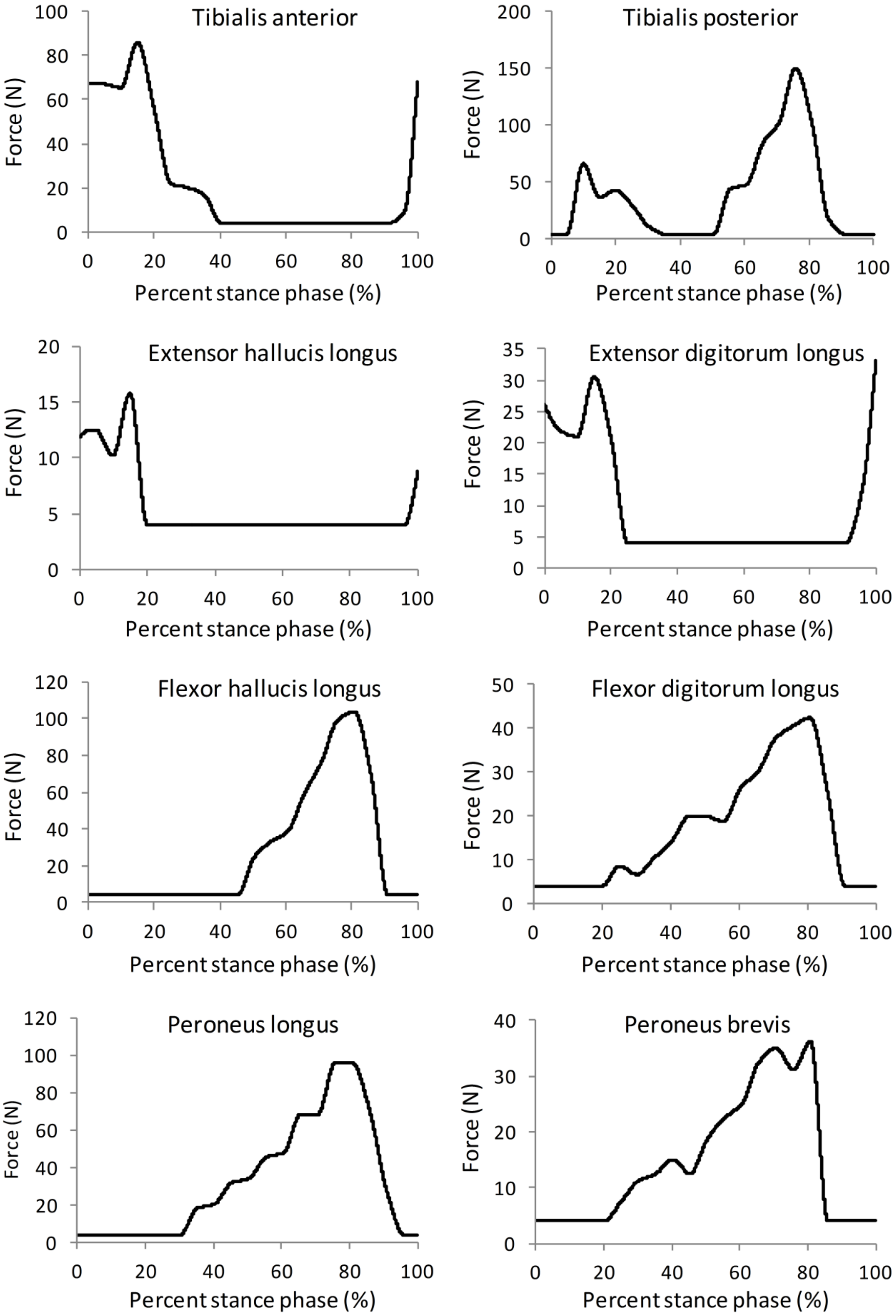

Figure 7.3: Estimated *in vivo* extrinsic muscle tendon forces during stance phase of gait adapted from Aubin et al. (2012).

After the simulations were complete, the predicted plantar pressure and internal soft tissue stresses during quiet stance and gait were analyzed. The plantar pressure was estimated from the ground surface model for a fair comparison with the pressure platform measurement. The internal stress in the plantar fat was determined at eight regions of interest (ROI) located inferior to the following bony prominences: calcaneal tuberosity, fifth metatarsal base, first through fifth metatarsal heads and hallux. Von Mises stress, which has been previously associated with soft tissue injury (Gefen, 2003), was calculated. In addition, hydrostatic stress was analyzed to assess risk of restricted blood flow (Mithraratne et al., 2012) and cell damage (Mahara et al., 2014). For each ROI, the mean von Mises and hydrostatic stresses were computed by averaging across 1,000 elements (3,000 elements for the subcalcaneal tissue as the calcaneal tuberosity has larger curvature compare to metatarsal heads) along the plantar fat pad thickness. A similar approach has been used in the literature (Gefen, 2003).

The quiet stance FE model of the normal foot was also used to perform parametric analysis to explore the effects of increasing plantar fat stiffness on plantar pressure and internal stress, assuming generic soft tissue and using non-subject-specific soft tissue material properties.

7.4 Results

7.4.1 Model validation

The predicted bone angles matched closely to *in vivo* measurements from the passive foot compression condition (Table 7.2). The differences between the simulated and experimental data ranges from 0.4% to 52.3% in the normal foot and 0.8% to 23.0% in the diabetic foot. Several simulated bone angles were closer to the experimental data when the Achilles tendon was in tension (e.g., calcaneal inclination in the normal foot).

Table 7.2: Bone angles measured from passive foot compression experiments and finite element simulations based on 2D radiographic views.

Angles[†] (deg)	Normal *In vivo*	Normal FE simulated data (Achilles 0% BW)	Normal FE simulated data (Achilles 20% BW)	Diabetic *In vivo*	Diabetic FE simulated data (Achilles 0% BW)	Diabetic FE simulated data (Achilles 20% BW)
Inf calc	17.89	25.13	19.83	15.34	19.52	15.91
Sup calc	21.08	27.42	22.70	20.70	25.26	21.59
Chop	62.42	70.52	68.44	60.41	63.26	60.89
Nav-Cun	57.80	61.04	59.85	57.42	58.38	58.10
Lisfranc	59.88	59.66	57.88	66.42	67.35	65.92
M1	25.45	25.69	26.07	23.17	21.32	23.34
M5	5.41	7.21	8.24	9.32	12.09	11.47
Talus	22.49	17.59	21.09	22.77	20.36	23.54
1-2 angle	6.23	5.71	6.13	8.00	7.78	7.70
1-5 angle	20.79	15.66	16.49	25.57	21.26	20.78

[†] Lateral view angle terminology: Inf calc = inferior calcaneal inclination; Sup calc = superior calcaneal inclination; Chop = Chopart's joint angle; Nav-Cun = navicular to first cuneiform angle; Lisfranc = Lisfranc's angle; M1 = first metatarsal inclination and M5 = fifth metatarsal inclination.

Anteroposterior view angle terminology: 1-2 angle = first to second intermetatarsal angle; 1-5 angle = first to fifth intermetatarsal angle. A full description of these terms can be found elsewhere (Cavanagh et al., 1997).

The experimental and simulated plantar pressure distribution are similar, but not exactly matched (Figure 7.4). The quiet stance simulation required an Achilles tendon force of 515N (54.5% BW) in the normal subject and 361N (52.5% BW) in the diabetic subject to reproduce the physiologic COP location. The *in vivo* peak plantar pressures were measured from the normal (100 kPa medial hindfoot / 110 kPa forefoot at the third and fourth metatarsals) and diabetic (85 kPa medial and lateral hindfoot / 70 kPa forefoot at the third metatarsal) subjects. The simulated peak plantar pressures were 118 kPa hindfoot / 136 kPa forefoot in the normal subject and 136 kPa hindfoot / 140 kPa forefoot in the diabetic subject. Eleven regional peak plantar pressure, mean plantar pressure, contact force and contact area measurements are given (Figure 7.5). Note that the simulated peak plantar pressure may include numerical artifacts. The mean pressure, contact force and contact area showed smaller errors and were within 25% of the experimental data in 17 out of 27 comparisons (excluding the second to fifth toes).

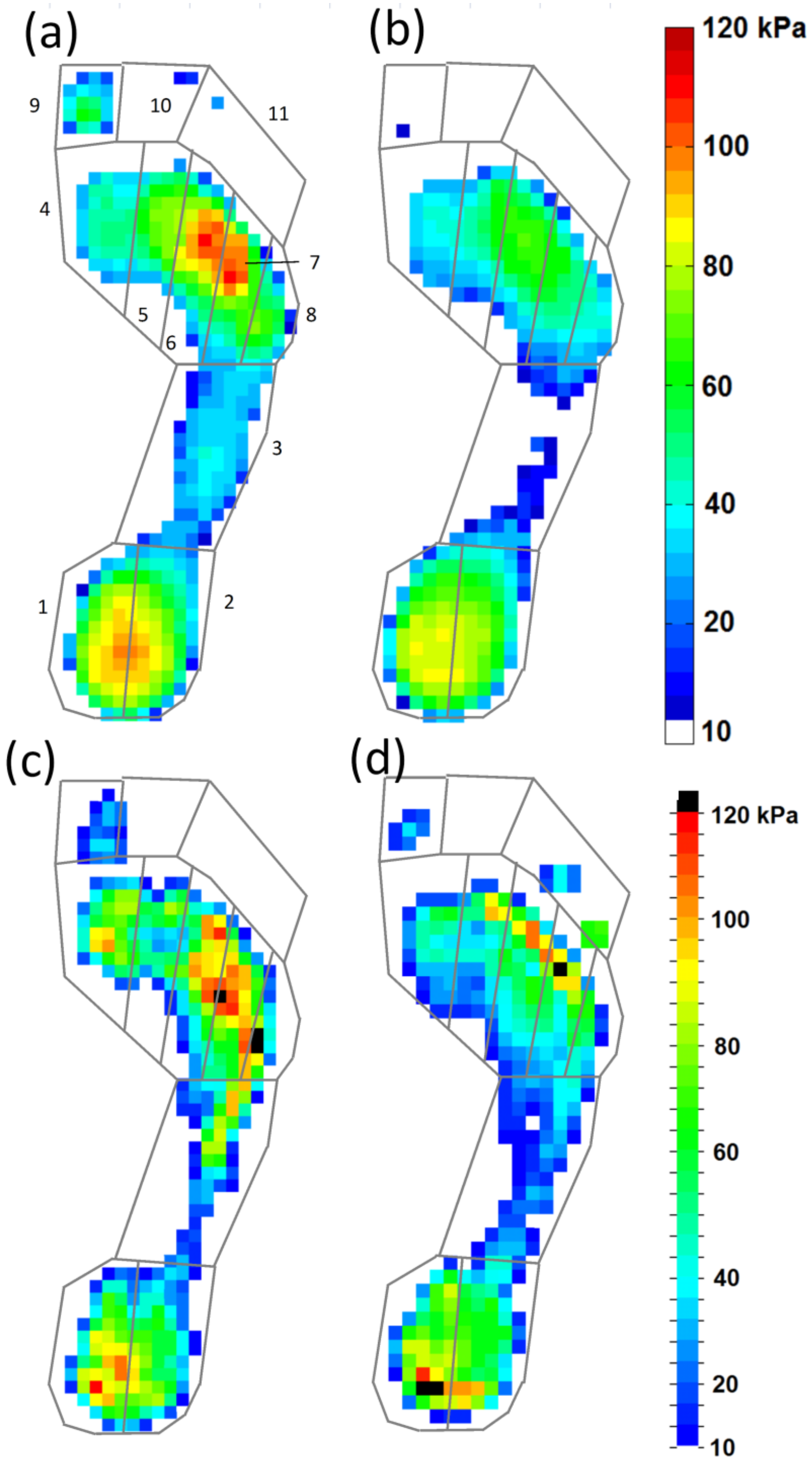

Figure 7.4: Quiet stance plantar pressure from experimental measurements; (a) normal subject and (b) diabetic subject, and finite element simulated results: (c) normal subject and (d) diabetic subject. Gray outlines indicate the 11 mask regions. The mask regions from 1-11 were: 1) medial hindfoot, 2) lateral hindfoot, 3) midfoot, 4) first metatarsal, 5) second metatarsal, 6) third metatarsal, 7) fourth metatarsal, 8) fifth metatarsal, 9) hallux, 10) second toe and 11) third to fifth toes.

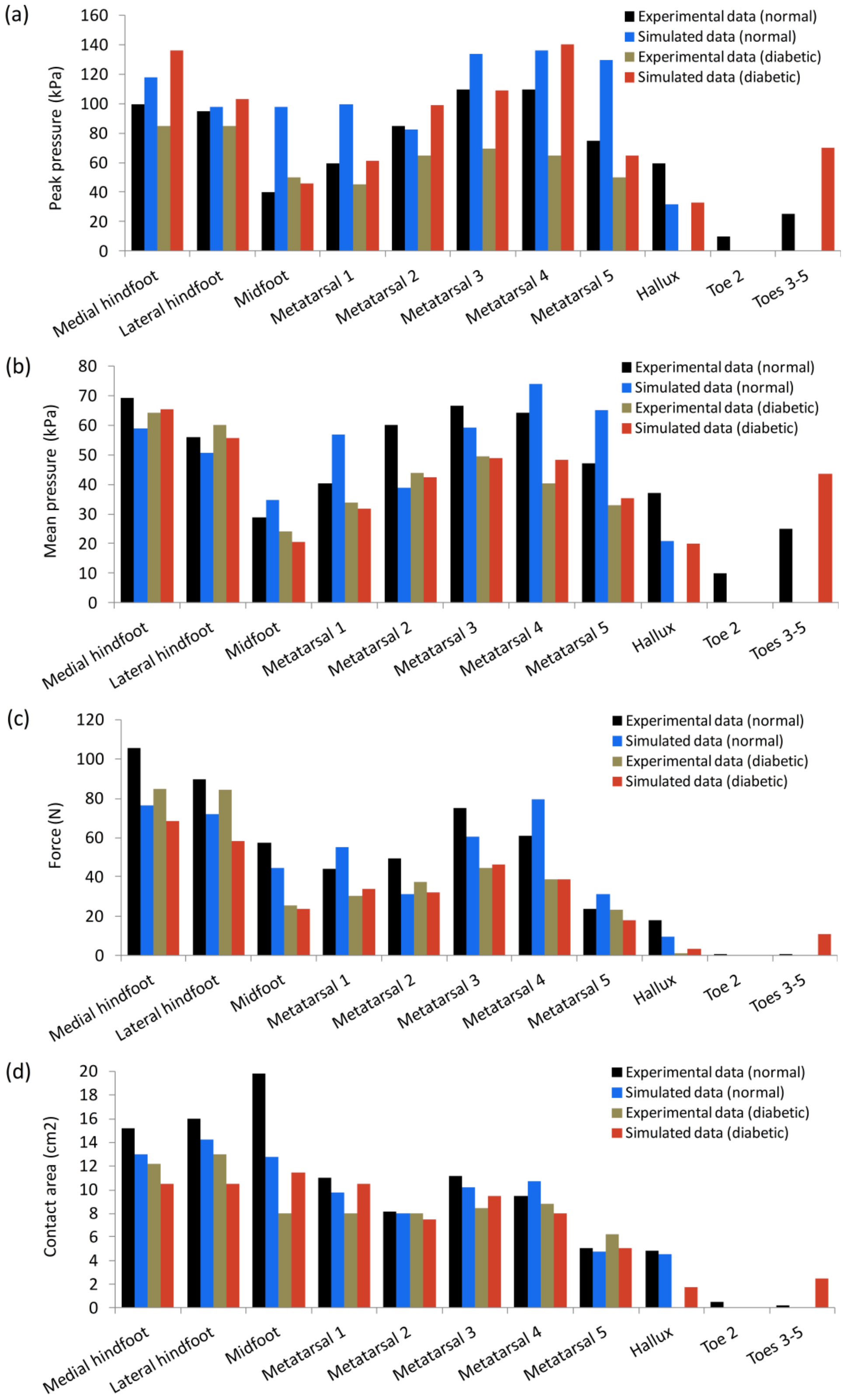

Figure 7.5: Regional measurements of the experimental and simulated (a) peak plantar pressure, (b) mean plantar pressure, (c) contact force and (d) contact area during quiet stance in the normal and diabetic subjects.

The normalized peak vertical GRF was similar in both subjects (110-120% BW) (Figure 7.6), but the mean stance time differed (0.68s and 0.60s for the normal and diabetic subjects, respectively). The impact force at heel strike in the diabetic subject was considerably higher compared to the normal subject which lead to a considerable skin artifact at the ankle retro reflective marker and required additional signal filtering before prescribing to the FE model. The *in vivo* peak plantar pressure was below the second and third metatarsal heads (431 kPa-454 kPa) at 78%-81% stance phase for the normal subject and under the hallux (766 kPa at 78% stance phase) for the diabetic subject (Figure 7.7).

The simulated vertical GRF-time series agreed with our experimental data (RMS error of 13% (normal) and 16% (diabetic) of the peak vertical GRF from both the force plate and the pressure platform data) (Figure 7.6a, b). In order to correctly match the first vertical GRF, the initial ground vertical position was adjusted by 1mm-7mm (e.g., to accounted for an imperfect measure of floor level). The predicted posteroanterior shear GRF showed overall desirable characteristics (e.g., braking and propelling action at proper phases of gait), but the magnitude could not be correctly predicted (RMS error of 49% (normal) and 46% (diabetic) of the peak posteroanterior shear GRF) (Figure 7.6c). The mediolateral shear GRF was small in both experimental and simulated data (RMS error of 97% (normal) and 60% (diabetic) of the peak mediolateral shear GRF), and there was noise in the simulated force (Figure 7.6d). Note that unlike for the vertical GRF data, no attempt was made to adjust the simulations to improve the shear forces. The predicted anteroposterior and mediolateral progression of the center of pressure were within the ranges measured *in vivo* (Figure 7.7). Foot deformation and simulated/experimental plantar pressure at four instances of gait (first peak force, minimum force, second peak force and 90% stance phase push off) are illustrated (Figure 7.8).

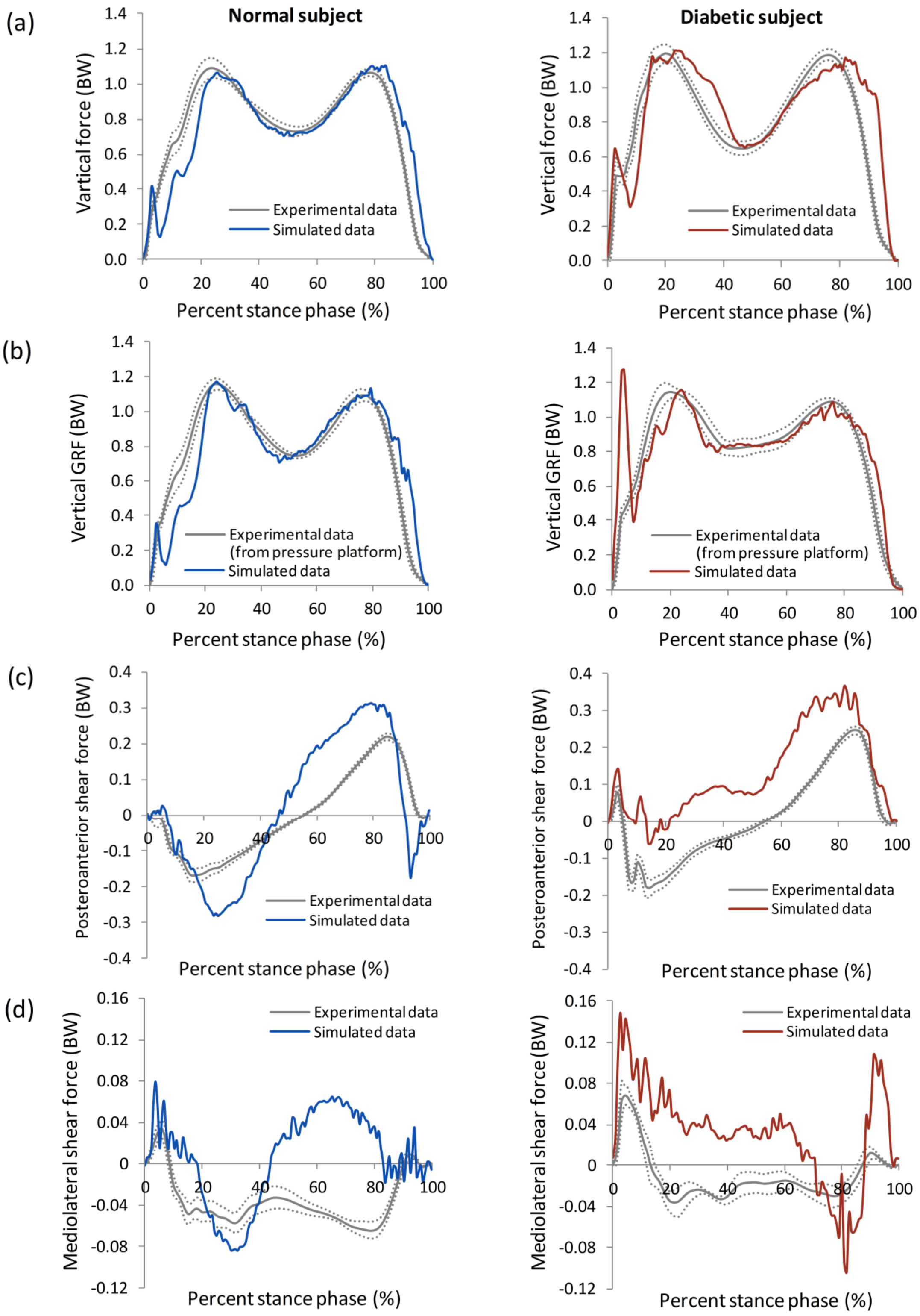

Figure 7.6: Vertical (positive superior) ground reaction forces measured from (a) gait force plate and (b) gait pressure platform experiments. (c) Posteroanterior (positive anterior) and (d) mediolateral (positive lateral) shear ground reaction forces measured from gait force plate experiment only. Experimental data are represented by solid gray line (mean) and dotted line (standard deviation). Finite element simulated data were plotted in solid blue line (normal) and solid red line (diabetic).

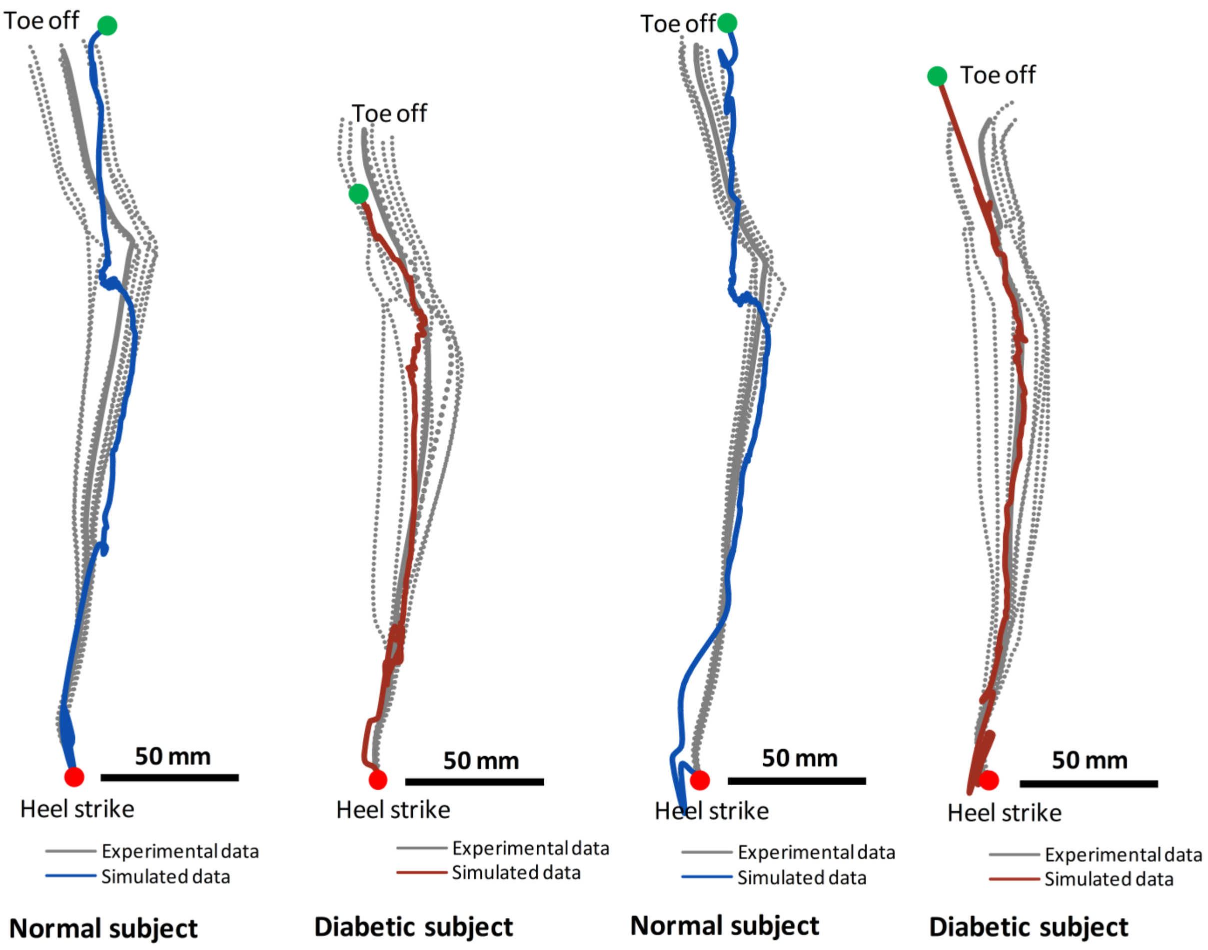

(a) (b)

Figure 7.7: Center of pressure progression from heel strike (red dot) to toe off (green dot) measured from (a) force plate and (b) pressure platform trials. Experimental data are represented by solid gray line (mean) and dotted gray lines (individual trial). Finite element simulated data are plotted in solid blue line (normal) and solid red line (diabetic).

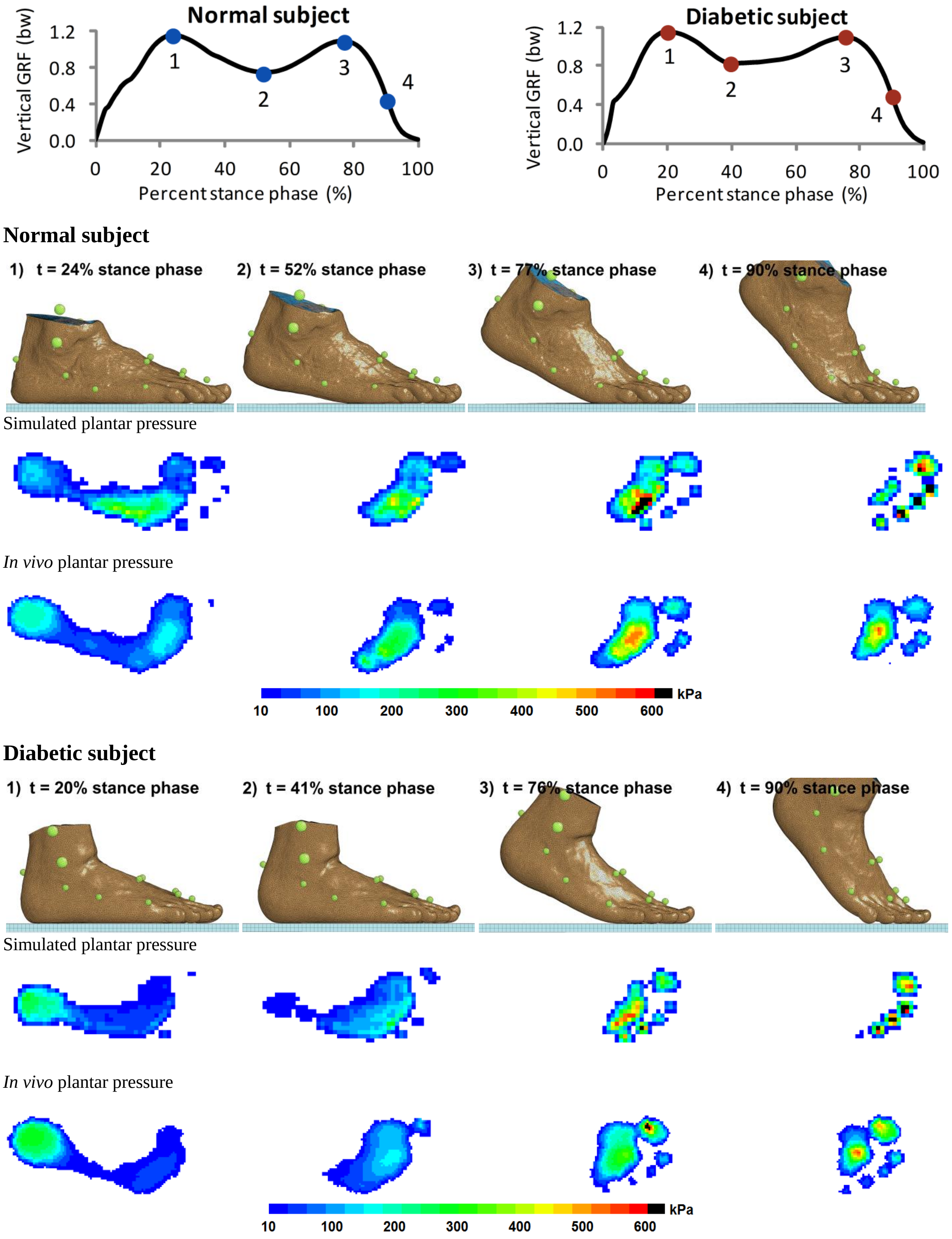

Figure 7.8: Predicted foot deformation and plantar pressure distribution compared to the corresponding *in vivo* plantar pressure measurement at four instances of gait.

The simulated peak plantar pressure was below the third metatarsal head (1097 kPa) at 80% stance phase for the normal subject and under the fourth metatarsal head (624 kPa at 66% stance phase) and hallux (627 kPa at 91% stance phase) for the diabetic subject. The contact area of the both subjects is predicted well by the model (RMS error of 9% of the peak total contact area for both subjects), but peak pressure is over estimated (RMS error of 89% (normal) and 38% (diabetic) of the peak pressure) (Figure 7.9, Supplementary Section D). The time history of the experimental and the simulated plantar pressures, contact force, and contact area at 11 regions are given in Supplementary Section A.

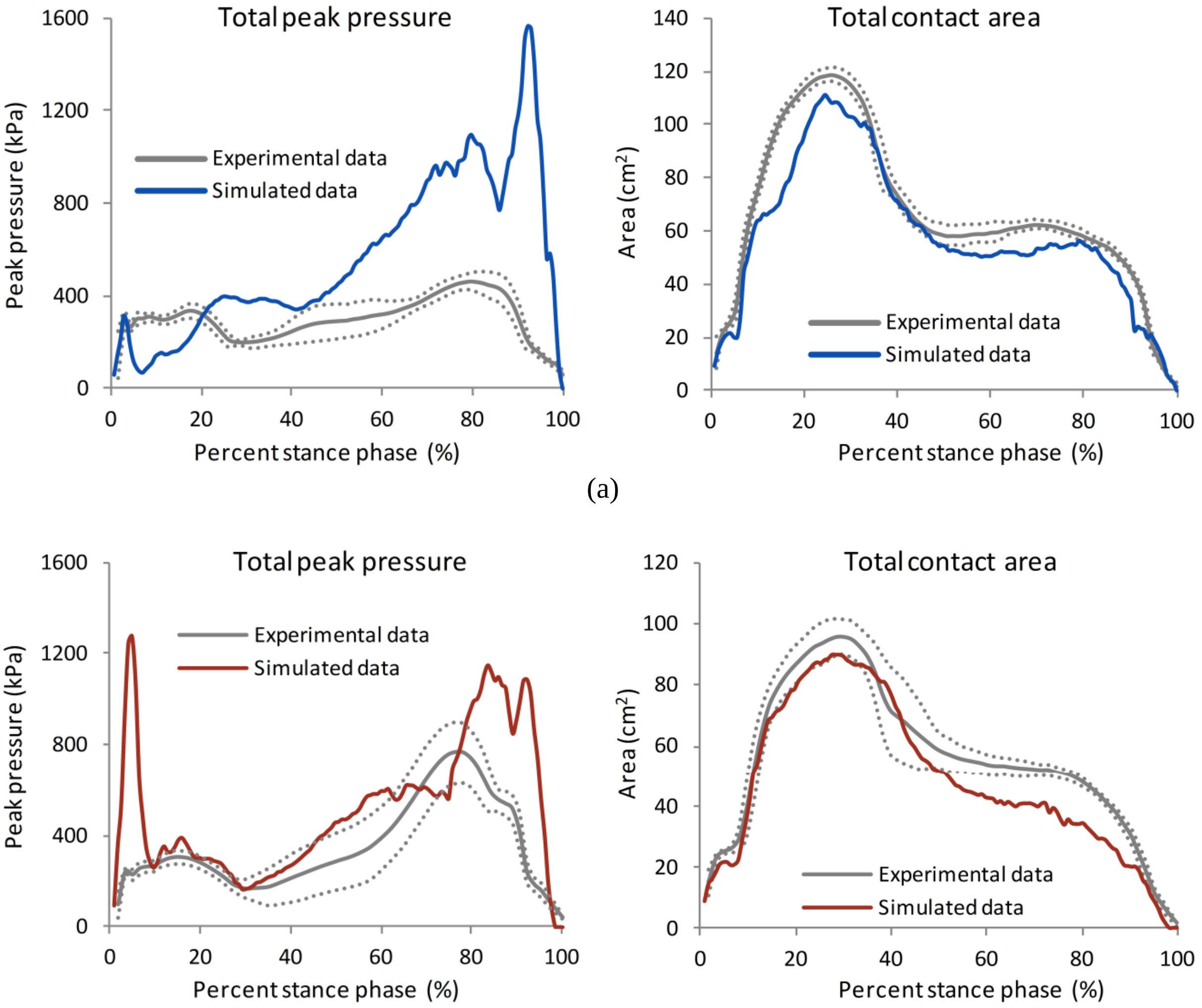

(a)

(b)

Figure 7.9: Time series of the total peak pressure and total contact area in (a) normal foot and (b) diabetic foot from experimental measurements (mean: solid gray line, SD: dotted line) and finite element simulations (normal: solid blue line, diabetic: solid red line).

The bone-to-ground and segment-to-segment angles from the force plate simulation (Figure 7.10) showed physiologic movements in sagittal plane (e.g., small RMS error in metatarsals to ground angles) but implied an overly stiff transverse metatarsal arch (e.g., fifth metatarsal to second metatarsal angle). A complete list of experimental and simulated bone-to-ground and segment-to-segment comparisons are given in Supplementary Section B. Note that bone kinematics were not analyzed from the pressure platform simulation due to incomplete experimental data.

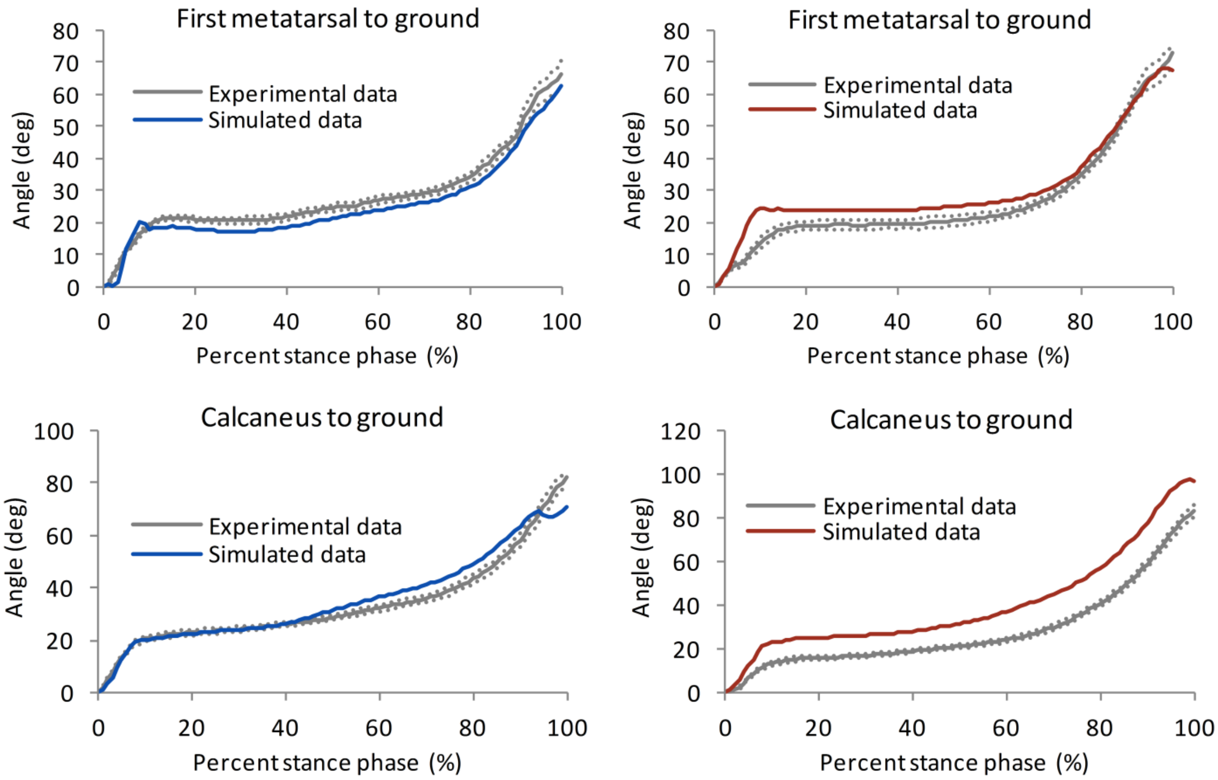

\

Figure 7.10: Bone-to-ground and segment-to-segment angles of the normal (left column) and diabetic (right column) subjects. Experimental (mean: solid gray line, SD: dotted line) and simulated data (blue and red lines) are plotted. First metatarsal to ground, calcaneus to ground and medial longitudinal arch are all sagittal plane angles, while fifth metatarsal to the second metatarsal is a transverse plane angle. The angles relative to ground are normalize to contact position and a positive change indicates the anterior part of the bone is rotating below the posterior part. Positive change for the medial longitudinal arch indicates plantar flexion of the first metatarsal relative to the calcaneus. Positive change for the fifth metatarsal to the second metatarsal indicates abduction of the fifth metatarsal relative to the second metatarsal.

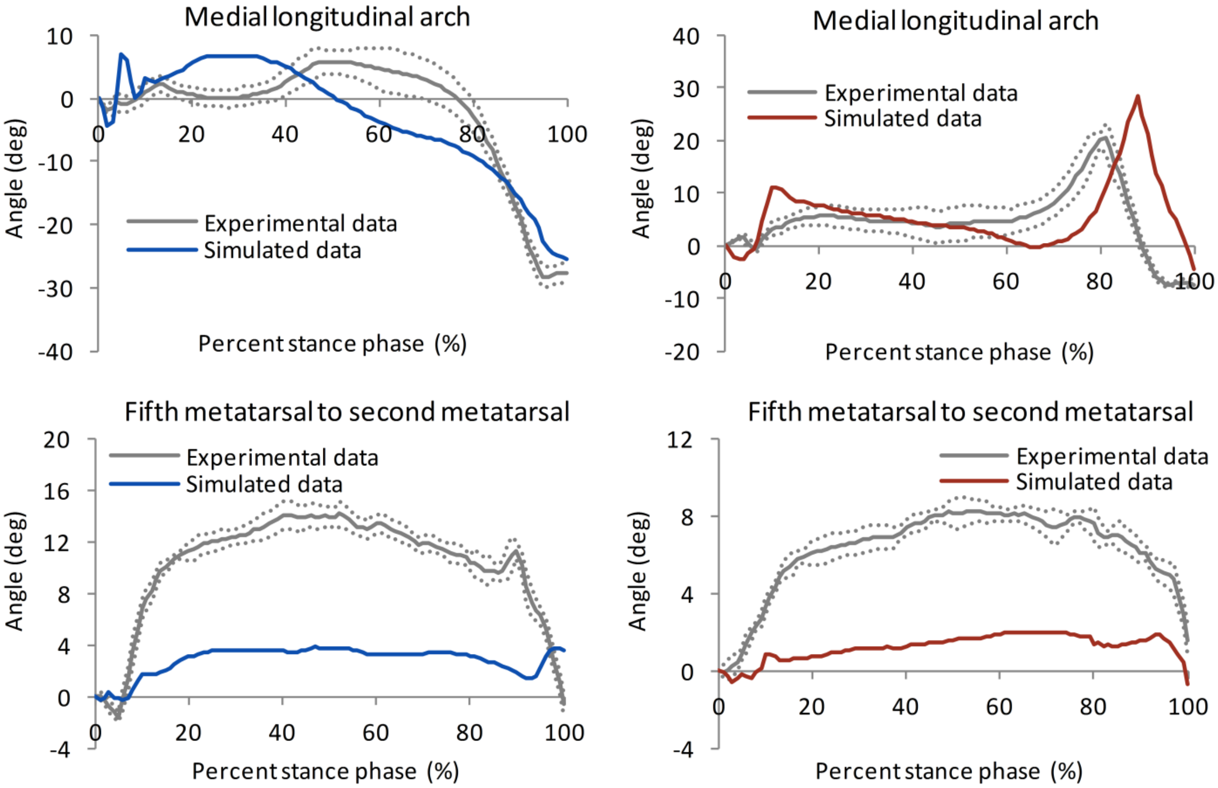

Figure 7.10: (Cont'd) Bone-to-ground and segment-to-segment angles of the normal (left column) and diabetic (right column) subjects. Experimental (mean: solid gray line, SD: dotted line) and simulated data (blue and red lines) are plotted. First metatarsal to ground, calcaneus to ground and medial longitudinal arch are all sagittal plane angles, while fifth metatarsal to the second metatarsal is a transverse plane angle. The angles relative to ground are normalize to contact position and a positive change indicates the anterior part of the bone is rotating below the posterior part. Positive change for the medial longitudinal arch indicates plantar flexion of the first metatarsal relative to the calcaneus. Positive change for the fifth metatarsal to the second metatarsal indicates abduction of the fifth metatarsal relative to the second metatarsal.

The pattern and magnitude of the simulated peak Achilles tendon force, peak plantar aponeurosis force and ankle joint resultant force were comparable to the literature (Erdemir et al., 2004; Sanford et al., 2014) (Figure 7.11). Overall bone-to-bone kinematics were within the ranges reported from invasive *in vivo* experiments (Lundgren et al., 2008) (Supplementary Section C). The differences between the simulated results and the experimental/literature data in terms of RMS error were quantified (Supplementary Section D). The following dynamic gait measurements were compared: ground reaction force, plantar pressure, contact force, contact area, bone kinematics, Achilles tendon force, plantar aponeurosis force and ankle joint resultant force.

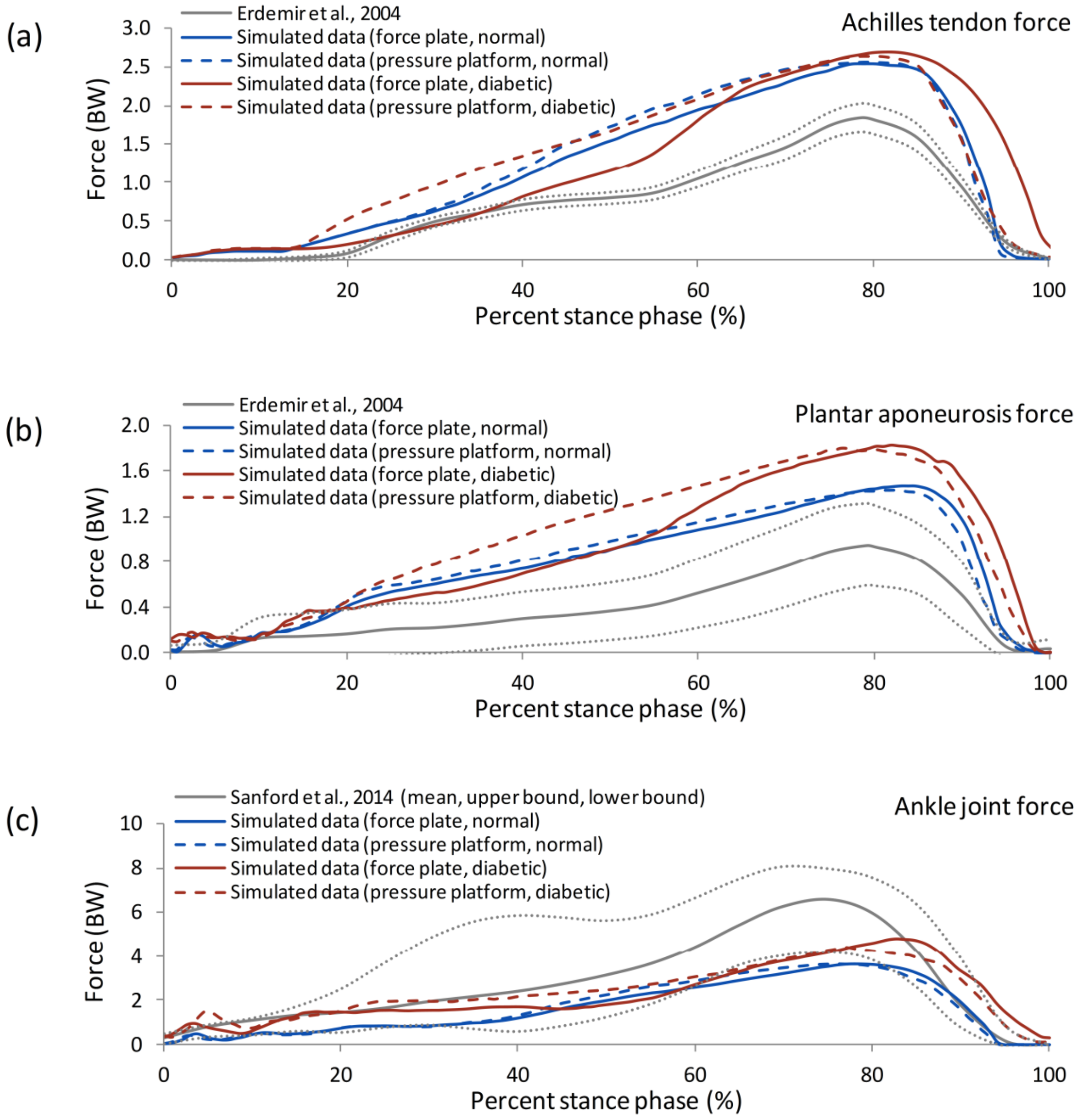

Figure 7.11: (a) The estimated Achilles tendon force (i.e., after model tuning) and (b) simulated plantar aponeurosis force and (c) ankle joint resultant force compared to the *in vitro* (Erdemir et al., 2004) and *in vivo* (Sanford et al., 2014) data.

7.4.2 Model prediction

For this study, the internal stress state was described by the mean von Mises and hydrostatic stresses across the thickness of the plantar fat at eight ROI (Figure 7.12). From the quiet stance simulation (Table 7.3), the hydrostatic stress was 2.1 to 5.7-fold higher than the von Mises stress. The peak von Mises and hydrostatic stresses were 41.4 kPa and 95.5 kPa under the fourth metatarsal head for the normal subject, and 32.3 kPa (von Mises) under the calcaneal tuberosity and 69.8 kPa (hydrostatic) under the third metatarsal head for the diabetic subject. We observed internal von Mises stress concentrated in small regions under the bony prominences while hydrostatic pressure affected a larger area of the soft tissue (Figure 7.13, Supplementary Section E). The locations of peak von Mises and hydrostatic stresses agreed with the simulated/measured peak plantar pressure regions, except for the hydrostatic stress in the diabetic subject.

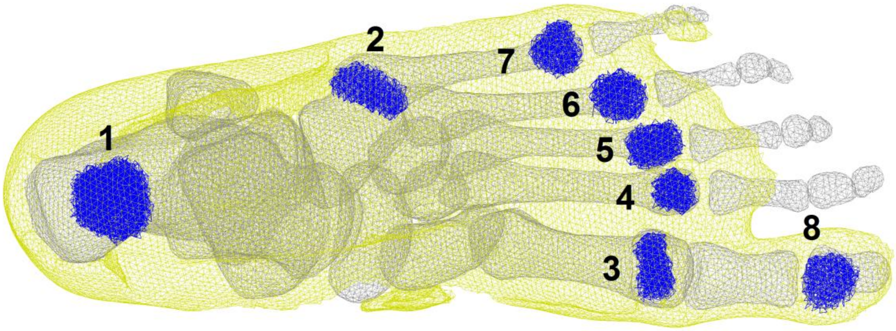

Figure 7.12: (a) An example of eight regions of interest in the plantar fat of the normal subject indentified for the internal stress analysis (highlighted in blue). The regions are 1) subcalcaneal, 2) fifth metatarsal base, 3) first metatarsal head, 4) second metatarsal head, 5) third metatarsal head, 6) fourth metatarsal head, 7) fifth metatarsal head and 8) hallux.

Table 7.3: Estimated internal von Mises and hydrostatic stresses in the plantar fat during quiet stance.

Region of interest	**Mean von Mises stress (kPa)**		**Mean hydrostatic stress (kPa)**	
	Normal	**Diabetic**	**Normal**	**Diabetic**
Subcalcaneal	29.7	32.3	75.8	67.9
Fifth metatarsal base	14.0	2.7	32.0	15.7
First metatarsal head	26.0	10.7	64.1	35.3
Second metatarsal head	15.3	10.9	56.9	55.6
Third metatarsal head	25.6	15.2	75.6	69.8
Fourth metatarsal head	41.4	16.3	95.5	65.9
Fifth metatarsal head	20.5	7.5	67.5	33.0
Hallux	5.7	1.6	14.5	5.5

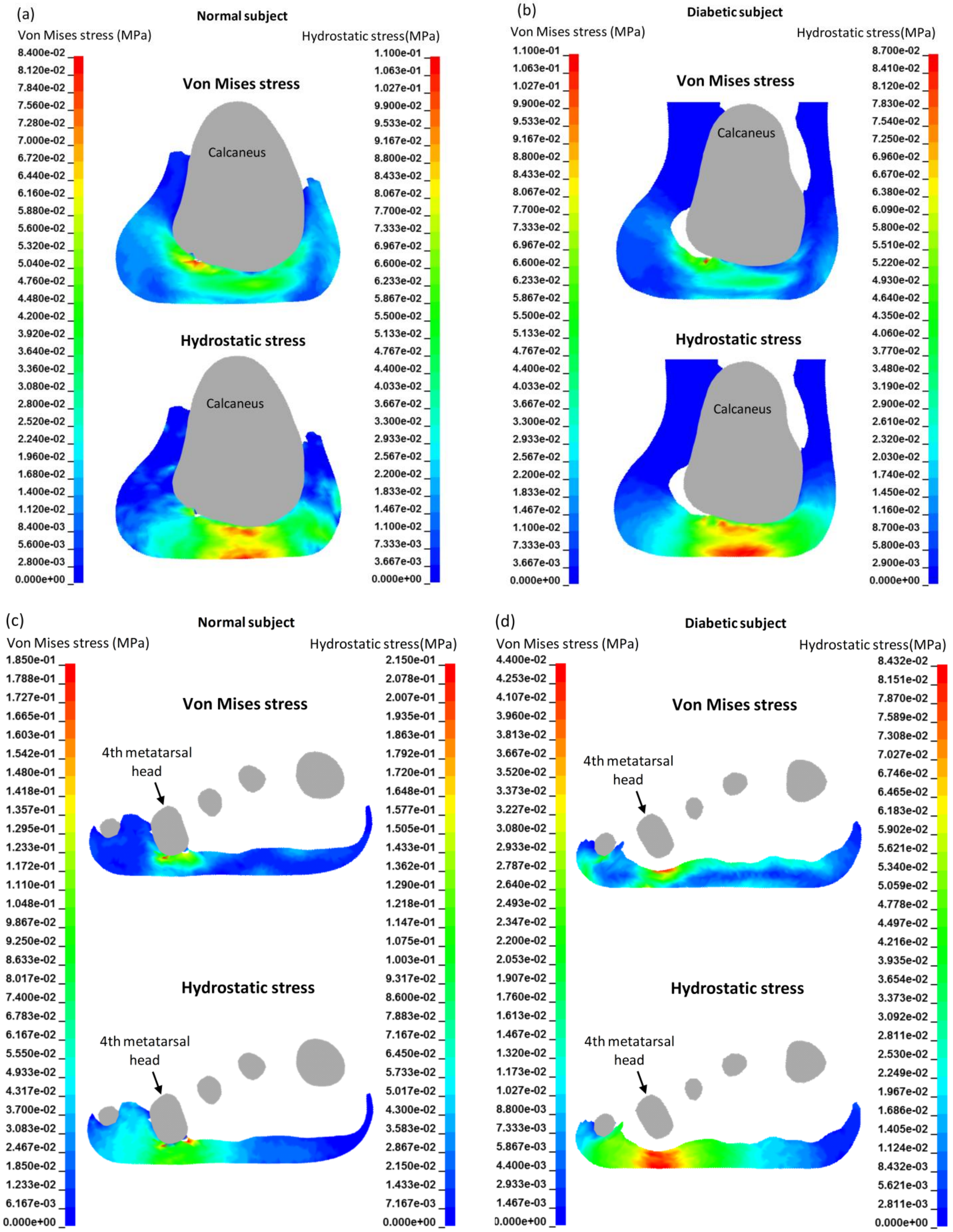

Figure 7.13: Contour plot of the internal von Mises and hydrostatic stresses in the frontal plane at (a) subcalcaneal and (b) fourth metatarsal head regions during quiet stance.

The estimated internal stresses during gait indicated load transfer from hindfoot (at heel strike) to lateral midfoot/forefoot, forefoot, and hallux (at toe off). The hydrostatic stress was consistently higher than the von Mises stress throughout the stance phase of gait (Figure 7.14). Two of the highest hindfoot stresses occurred during heel strike and towards the end of loading response phase (15-20% stance phase). The time at maximum hindfoot stress (excluding hindfoot impact) agreed with the first vertical GRF peak (Figure 7.5). During this period, the estimated maximum hindfoot von Mises/hydrostatic stresses (from force plate and pressure platform simulations) were 79.5-81.7 kPa/160.0-163.7 kPa in the normal subject and 178.0-208.8 kPa/280.4-328.3 kPa in the diabetic subject. As the COP progressed forward, the load was shifted briefly to the midfoot (measured at the base of the fifth metatarsal) and resulted in peak von Mises/hydrostatic stress of 73.8-83.9 kPa/146.1-166.9 kPa at 32-35%/25-31% stance phase in the normal subject and 18.9-21.1 kPa/77.2-77.7 kPa at 38-48%/27.8-36.2% stance phase in the diabetic subject.

As the COP reached the forefoot, a distinct load transfer was predicted in each subject. In the normal foot, peak von Mises and hydrostatic stresses of 308.8-311.8 kPa and 358.2-363.0 kPa occurred under the fourth metatarsal head at 67-74% stance phase. The stresses then moved to the medial forefoot and resulted in peak von Mises/hydrostatic stresses of 53.0-63.0 kPa/109.0-129.9 kPa (first metatarsal), 101.6-106.9 kPa/190.0-205.5 kPa (second metatarsal) and 192.8-196.8 kPa/337.0-345.0 kPa (third metatarsal), which occurred simultaneously at 75-84% stance phase. Note that the hydrostatic stresses under the third and fourth metatarsal heads were nearly equal. The final push off phase generated a peak hallux von Mises/hydrostatic stresses of 97-121 kPa/267.0-325.5 kPa at 87-91% stance phase. Both peak forefoot von Mises and hydrostatic stresses occurred slightly sooner than the second peak of the vertical GRF which occurred at 80-84% stance phase. The location of peak forefoot stresses were also different from the peak plantar pressure which occurred under the third metatarsal head (1097 kPa) in the simulated data and under the second and third metatarsal regions (454 kPa second metatarsal, 431 kPa third metatarsal) in the experimental measurement.

The diabetic forefoot von Mises/hydrostatic stresses reached the maximum value at 66-74%/58-73% stance phase and was mainly distributed under the second to fourth metatarsal heads (91.8-97.8 kPa/226.1-234.9 kPa (second metatarsal), 106.0-117.6 kPa/255.2-284.4 kPa (third metatarsal) and 102.2-120.3 kPa/200.5-242.7 kPa (fourth metatarsal)). The peak stress then progressed to the hallux (137.5-145.7 kPa (von Mises stress) and 311.8-324.0 kPa (hydrostatic stress)) during push off at 87-90% stance phase. Similar to the normal subject, the peak forefoot von Mises and hydrostatic stresses occurred slightly sooner than the second vertical GRF peak (76-82% stance phase). The maximum stress during push off at the hallux agreed with the simulated/measured peak plantar pressure location during gait (627.8 kPa simulated, 766.0 kPa measured under the hallux at 78-91% stance phase).

Contour plots of the internal stresses (Supplementary Section E) indicated that stress distribution pattern was similar to the quiet stance results – i.e., the von Mises stress was concentrated below bony prominences where as the hydrostatic stress was generally higher and affected a broader area of the soft tissue.

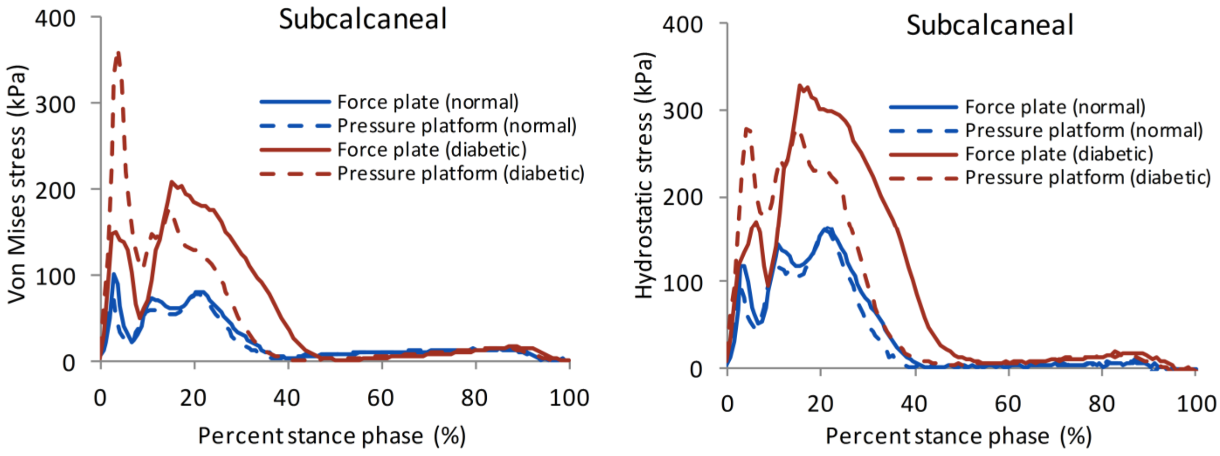

Von Mises stresses

Hydrostatic stresses

Figure 7.14: Mean von Mises and hydrostatic stresses in the plantar fat during stance phase of gait at eight regions of interest.

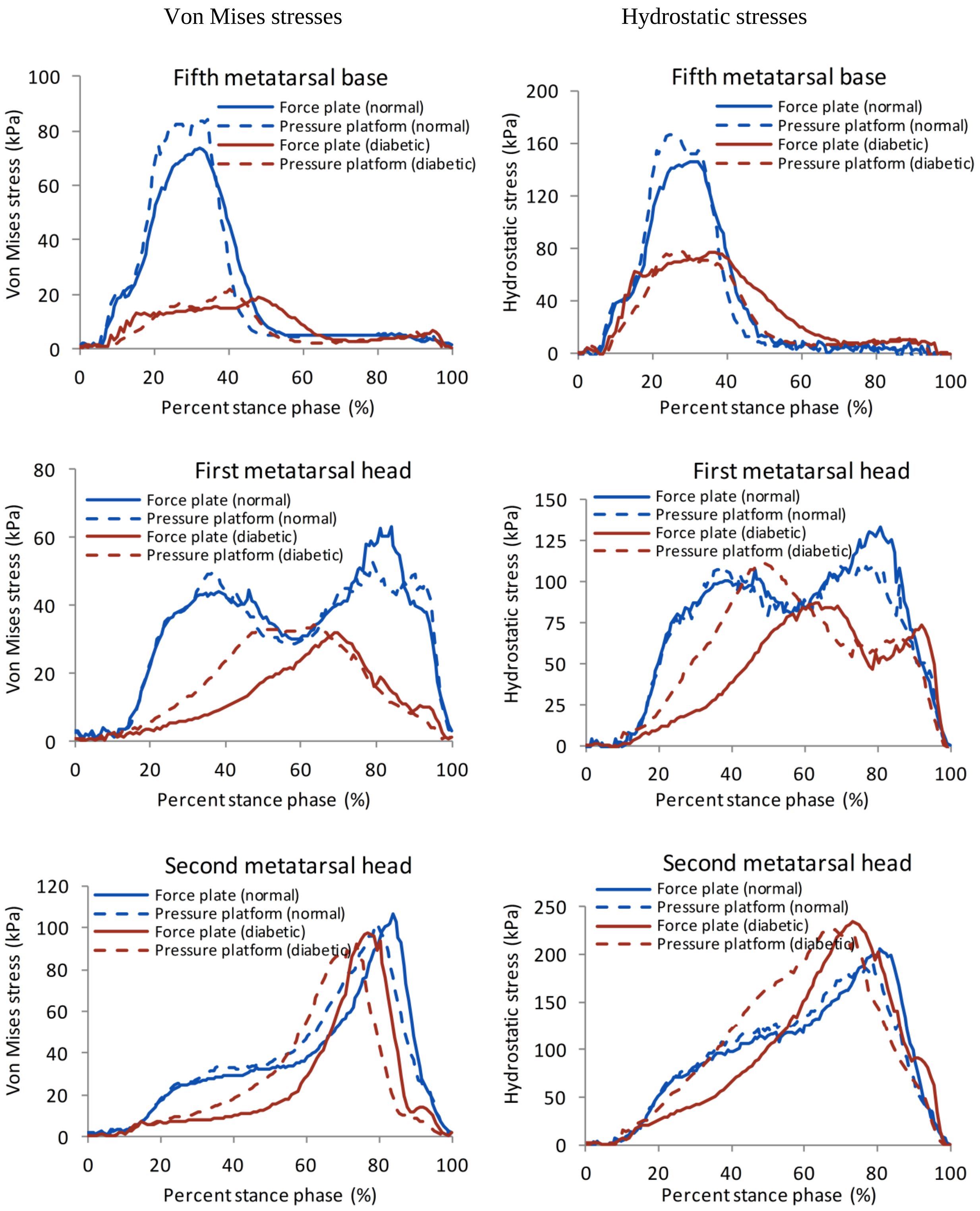

Figure 7.14: (Cont'd) Mean von Mises and hydrostatic stresses in the plantar fat during stance phase of gait at eight regions of interest.

Von Mises stresses Hydrostatic stresses

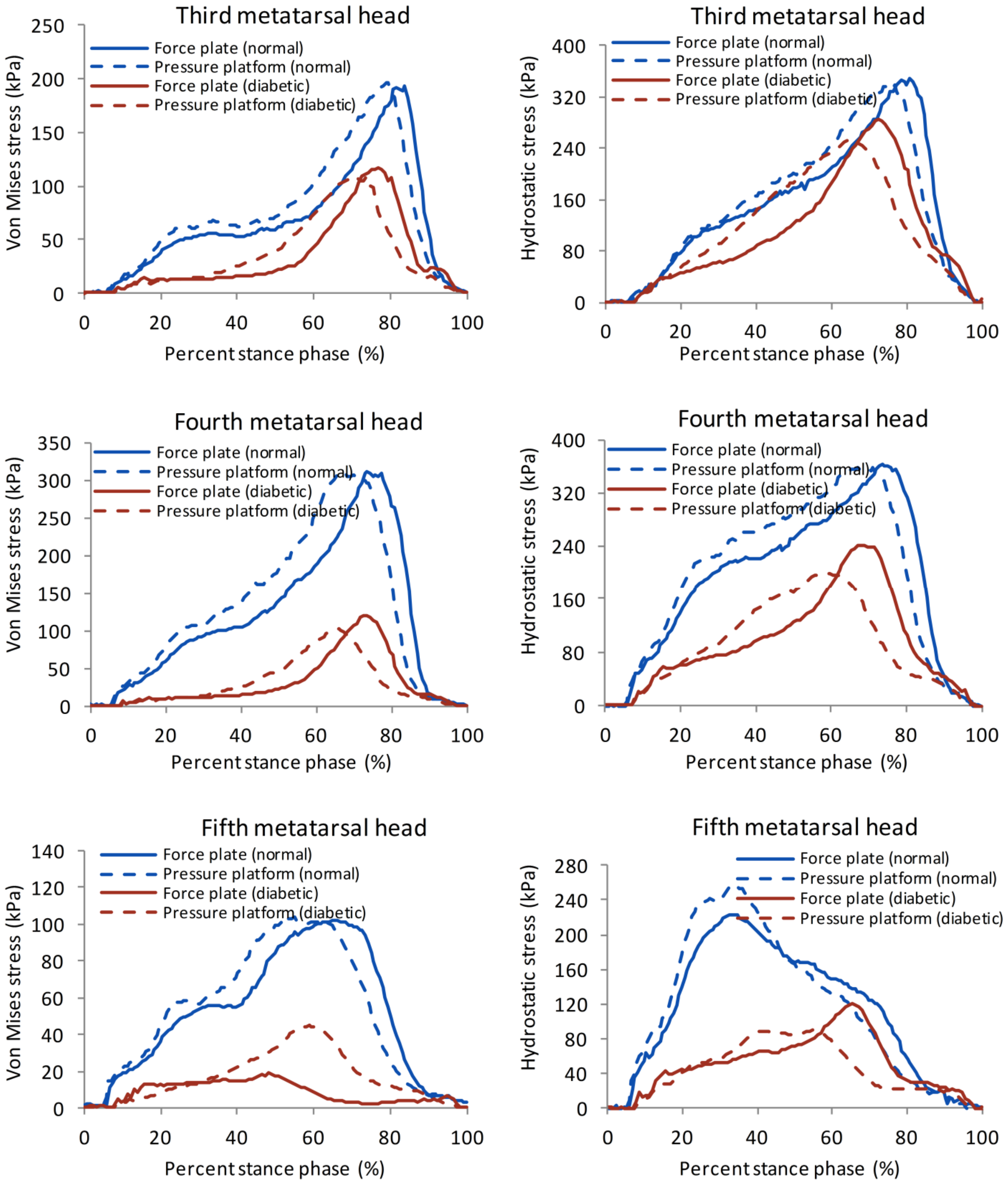

Figure 7.14: (Cont'd) Mean von Mises and hydrostatic stresses in the plantar fat during stance phase of gait at eight regions of interest.

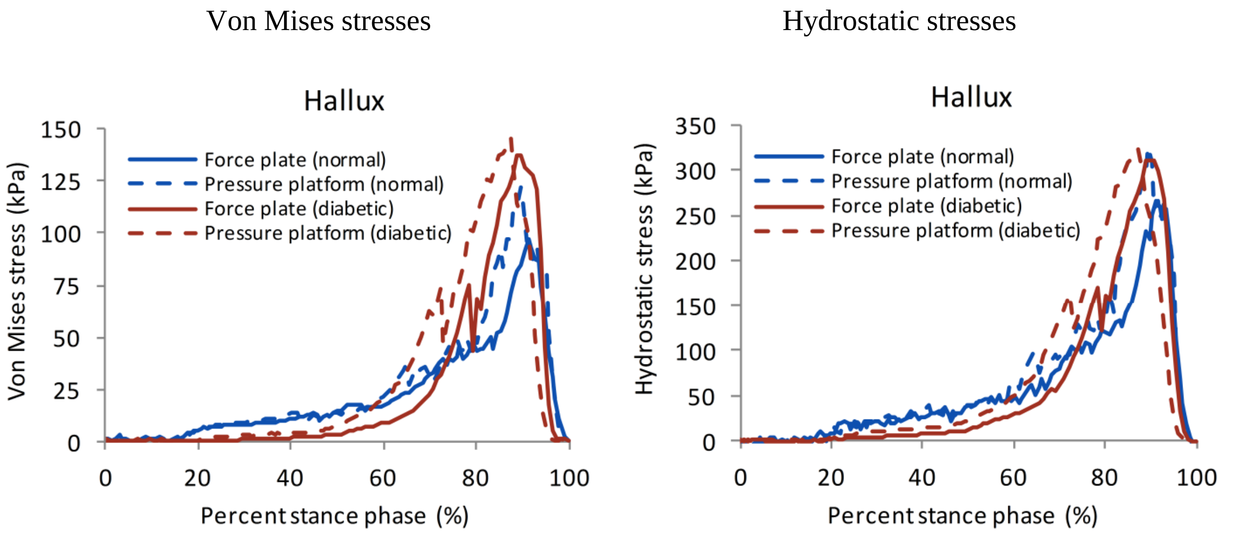

Figure 7.14: (Cont'd) Mean von Mises and hydrostatic stresses in the plantar fat during stance phase of gait at eight regions of interest.

The effect of soft tissue material property assumptions on quiet stance plantar pressure and internal stress were investigated using the normal foot model (Table 7.4, Figure 7.15). Emulating the diabetic condition by doubling the plantar fat stiffness (Cheung et al., 2005; Pai and Ledoux, 2010) lead to an increase in plantar pressure (11% at the hindfoot and 16% at the forefoot), von Mises stress (28% at the hindfoot and 33% at the forefoot) and hydrostatic stress (15% at the hindfoot and 19% at the forefoot), and a reduction of the overall contact area (6%). The effect of assuming subject-specific generic soft tissue material properties increased the peak plantar pressure by 151% at the hindfoot and 62% at the forefoot while also increasing the overall contact area by 12%. When the subject-specific skin, fat and muscle material properties were replaced with data from Petre et al. (2013), we observed increase in contact area (55%), a reduction in peak plantar pressure (20% hindfoot, 6% forefoot), an altered internal stress pattern (63% von Mises stress increase at the hindfoot, 17% von Mises stress decrease at the forefoot, 23% hindfoot hydrostatic stress decrease and peak forefoot hydrostatic stress shifted to the first metatarsal) and an overall less numerical artifacts in the pressure distribution. In all three simulations, the center of pressure location was within 6mm from the baseline model without any adjustment to the tibial orientation or the Achilles tendon force.

Table 7.4: Changes in the contact area, plantar pressure and internal stress due to soft tissue material property assumptions.

	Experimental data	**Simulated data**			
		Subject-specific, multi-material	**Subject-specific, multi-material with stiffer fat**	**Subject- specific, generic soft tissue**	**Non-subject-specific, multi-material**[††]
Posteroanterior COP (mm)[†]	127.5	127.6	127.7	121.6	125.1
Mediolateral COP (mm)[†]	42.5	43.9	44.1	38.2	41.5
Contact area (cm^2)	101.5	80.2	75.7	89.5	124.5
Peak hindfoot plantar pressure (kPa)	100	118	130	294	94
Peak forefoot plantar pressure (kPa)[‡]	110	136	154	215	125
Peak hindfoot von Mises stress (kPa)	n/a	29.7	38.1	154.5	48.4
Peak hindfoot hydrostatic stress (kPa)	n/a	75.8	87.0	124.0	58.7
Peak forefoot von Mises stress (kPa)	n/a	41.4[‡]	55.1[‡]	162.8[‡]	34.5[‡]
Peak forefoot hydrostatic stress (kPa)	n/a	95.5[‡]	113.4[‡]	135.4[‡]	48.5

[†] COP location was measured relative to the lower left corner of the foot print. Note that the sensor size was 5mm x 5mm.

[‡] Peak pressure/internal stress located under the fourth metatarsal head.

[††] Non-subject-specific skin, fat and muscle material properties were from Petre et al. (2013). Material properties were converted from Abaqus to LS-DYNA (Chapter 4, Section 4.6).

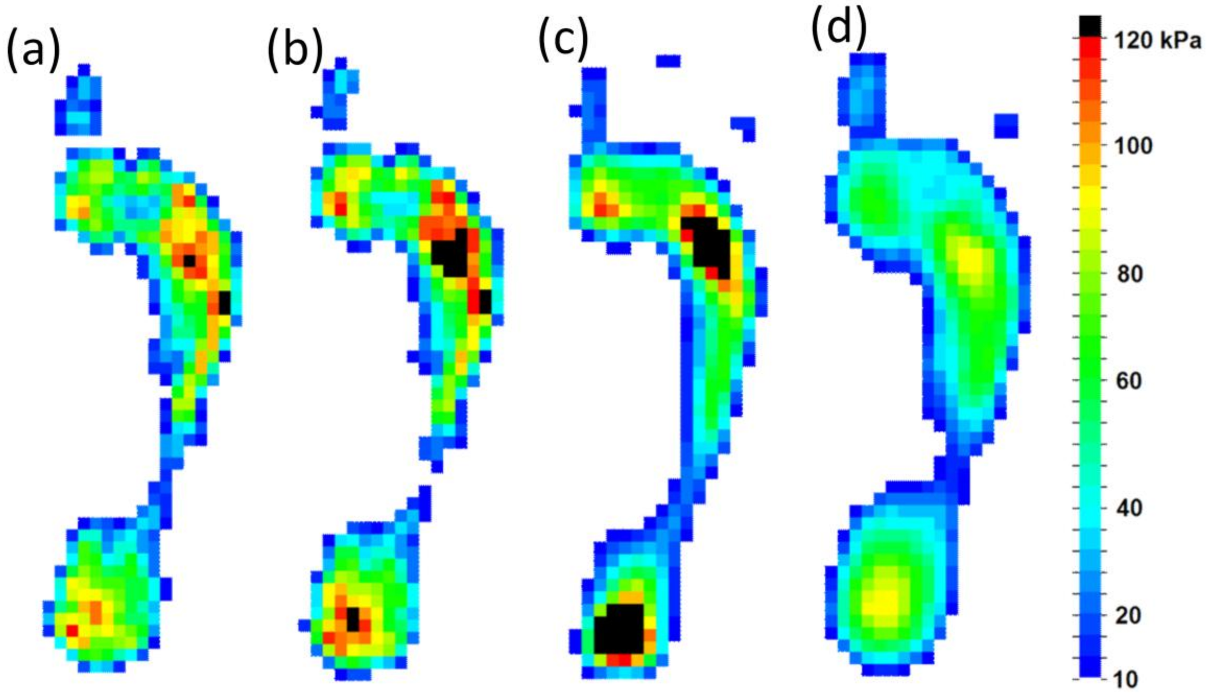

Figure 7.15: Influence of the material property assumptions on quiet stance plantar pressure and contact area. (a) Baseline subject-specific multi-material model, (b) subject-specific multi-material model with doubled fat stiffness, (c) subject-specific generic soft tissue and (d) non-subject-specific multi-material soft tissue.

7.5 Discussion

In this study, we developed and validated two subject-specific FE foot models to explore plantar pressure and internal soft tissue stresses during quiet stance and gait. Each model utilized subject-specific bone and soft tissue anatomy, subject-specific skin, fat, muscle and generic soft tissue material properties, and tibial kinematics extracted from an experiment on that subject. Our model included an improved plantar aponeurosis structure and detailed ligament and tendon components. The model was validated under passive compression, quiet stance and dynamic gait conditions. Note that due to limited sample size, statistical analyses were not conducted. The following comparisons were based on experimental and simulation results from two individual subjects.

7.5.1 Passive foot compression validation

Under 10% BW compression force, the model indicated physiologic bony alignment in the sagittal plane, but an overall stiffer transverse metatarsal arch deformation which may be partly explained by the lack information of unloaded ligament length. More accurate material properties extracted from mechanical testing of foot ligaments may be required to better represent this tissue. The simulation results also suggest that the Achilles tendon may not be completely unloaded during this passive compression test.

7.5.2 Quiet stance validation

The *in vivo* and simulated plantar pressures indicated that the normal subject had higher peak plantar pressure than the diabetic subject. The *in vivo* pressure in this study was lower than 138.9±31.4 kPa reported at the hindfoot, but higher than 53.4±21.8 kPa observed at the forefoot by Cavanagh et al. (1987). Note that our pressure sensor has higher resolution than that study (0.25 cm^2 vs 1 cm^2). Our *in vivo* hindfoot pressures were also lower than subject-specific measurements from other studies using F-scan equipment. Those studies reported hindfoot pressure between 130-210 kPa (Chen et al., 2010; Cheung et al., 2005; Yu et al., 2008). Forefoot pressures (~90 kPa) were comparable to our *in vivo* data.

The diabetic subject in this study was young and healthy despite having the disease for over 25 years, and reported no known foot problems. The normal subject was healthy, but reported plantar callus below the third and fourth metatarsal heads. The callus location coincided with the simulated and the measured peak plantar pressure site. Other studies have reported an association between callus and peak plantar pressure (Pitei et al., 1999; Young et al., 1992).

The quiet stance FE foot simulation estimated the Achilles tendon force of 54.5% BW (109% of one foot GRF) in the normal subject and 52.5% BW (105% of one foot GRF) in the diabetic subject. This Achilles tendon force was twice as high as that commonly applied force in other FE modeling studies (Chen et al., 2010; Cheung et al., 2005; Sun et al., 2011). However, those studies did not confirm the COP location or moment generated at the ground structure (when a point force was applied at the COP) with experimental data. Cheung et al. (2006a) investigated the Achilles tendon force at quiet stance using FE foot model and found that a tendon force of 75% of one foot GRF produced the closest COP location to the experimental data.

The overall plantar pressure distribution and magnitude from quiet stance simulations agreed with the pressure platform measurements. Several ground elements measured abnormally high pressure which influenced the peak pressure results (e.g., Figure 7.4). This was likely numerical artifacts caused by abnormally stiff skin elements (from severe distortion and nearly-incompressible material assumption) contact with the floor elements.

7.5.3 Dynamic gait validation

The *in vivo* peak plantar pressure during gait was higher in the diabetic subject, although this subject had lower quiet stance plantar pressure compared to the normal subject. The location of the peak pressure was also different between quiet stance and gait for the diabetic subject. These results suggested that static plantar pressure alone may be inadequate to assess injury-prone area in patients.

The dynamic gait simulations were able to accurately capture physiologic vertical GRF which was the primary loading in the foot. The impact force at heel strike, which was observed in individual trial but smoothed due to averaging, was captured in the FE simulations. However, the shear GRF provided a poorer match. The predicted shear force could be influenced by the coefficient of friction between skin and ground. We used a coefficient of friction of 0.3 for both subjects and both skin-force plate and skin-pressure platform contacts. This is in range of commonly used coefficients of friction in FE foot models (0.3 to 0.6) (Chen et al., 2012; Guiotto et al., 2014; Tadepalli et al., 2011). The mediolateral shear force in the normal subject showed an opposite trend between 40-90% stance phase (Figure 7.6d). The cause of this opposite trend needs to be further investigated.

Results from the pressure platform validation suggested that the models were able to adequately predict regional contact force, contact area and mean pressure, but frequently over-predicted peak plantar pressure, especially at the toes and at several metatarsal heads (e.g., Figure 7.7). The over-prediction was likely due to aforementioned element quality issues as well as stiff metatarsophalangeal (MTP) joints. Stiff MTP joints are caused by the highly non-linear plantar hindfoot skin material properties (which were used for the entire foot skin), a large joint range of motion and the lack of extra skin around them. Incorporating softer skin material properties around joints may lower joint stiffness and allow larger range of motion.

Our model included plantar fat under the hallux because this location tends to develop ulceration (Mohamed et al., 2010). The hallux pressure and internal stress was particularly of interest in the diabetic subject because abnormal pressure under this region was observed *in vivo* and reproduced in the gait simulation.

The simulated bone kinematics were able to reproduce specific characteristics that were measured *in vivo* (e.g., MLA and bone-to-ground angles). The model showed limited bone movements in the transverse plane (e.g., fifth metatarsal to second metatarsal angle), reconfirming that the ligament material properties may require improvement.

The optimal Achilles tendon force-time behavior resembled the characteristics reported in cadaveric studies (Aubin et al., 2012; Erdemir et al., 2004; Sharkey and Hamel, 1998). The predicted plantar aponeurosis force was comparable to literature (Erdemir et al., 2004). Note that the cadaveric tests were often performed at a slower gait speed and were not performed at full body weight; accordingly the forces were typically lower. The simulated ankle joint resultant force from our study also falls within the *in vivo* range (Sanford et al., 2014).

7.5.4 Internal stress analysis

The internal stress in this study was reported as mean von Mises and hydrostatic stresses computed across the thickness of the plantar fat at eight ulceration-prone areas. These measurements were dependent on the number of selected elements and likely cannot capture the true peak stresses in the tissue. However, systematically identifying the element of maximum stress in our model was difficult due to several highly deformed/stressed elements near the MTP joints.

In our study, the forefoot von Mises stresses from quiet stance simulations were comparable to 2D result (30 kPa) from Gefen et al.(2003), however, the location was different (first-second metatarsal heads versus fourth metatarsal in this study). We were unable to compare our stress results from quiet stance and gait simulations to other 3D FE foot studies (Chen et al., 2010; Fernandez et al., 2012; Gefen et al., 2000; Spears et al., 2005) due to the generic soft tissue material assumption and different/unclear stress measurement techniques (e.g., reported absolute peak stress versus mean stress in this study).

The dynamic gait simulation results suggested that two peak stresses in the hindfoot occurred at heel strike and at the instance of the first peak vertical GRF. The peak internal von Mises and hydrostatic stresses were 2.7 and 2.1 (normal), and 6.0 and 4.5 (diabetic) times the quiet stance hindfoot stress, respectively. As the load progressed to the forefoot, the peak internal stress migrated to under the fourth metatarsal head in the normal foot (15.0 (von Mises) and 3.8 (hydrostatic) times the quiet stance forefoot stress) and under the hallux in the diabetic foot (8.7 (von Mises) and 4.6 (hydrostatic) times the quiet stance forefoot stress). The location of the peak internal stress in the diabetic model agreed with the experimental and simulated peak plantar pressures. However, the peak internal stress in the normal foot model (under the fourth metatarsal head) was located laterally to the experimental (second and third metatarsal) and simulated (third metatarsal) peak plantar pressure. The result suggested that location of peak internal stress may not always coincide with the peak plantar pressure. This similar trend was observed previously (Petre et al., 2013).

We observed higher hydrostatic stresses compared to the von Mises stress in all of our quiet stance and gait simulations. This was because of near-incompressible material assumption, which resembled physiologic soft tissue and resulted in higher tissue resistance to volume change relative to shape change (i.e., deformation). Analysis of von Mises stress and hydrostatic stress implied different modes of tissue damage. Von Mises stresses measured tissue deformation and related to overloading and micro-tearing, where as hydrostatic stresses compressed soft tissue from all directions - thus restricting blood flow (Mithraratne et al., 2012) and potentially inducing cell death (Mahara et al., 2014).

The stress level that indicate tissue injury threshold is difficult to determine. Chen et al. (2010), estimated ulceration risk when internal von Mises stress reach 1,542 to 2,238 kPa. Hydrostatic stress higher than the pressure inside peripheral arteries of the foot (5.0-20.0 kPa) could reduce blood flow (Fernandez et al., 2012; Mithraratne et al., 2012) and stress exceeding 200 MPa may damage cells (Mahara et al., 2014). From our foot simulation, the von Mises stress was well below the injury threshold, but the peak hydrostatic stress generally exceeded foot peripheral artery blood pressure. However, cyclic nature of the hydrostatic stress during gait may allow adequate blood flow.

A substantially higher forefoot von Mises and hydrostatic stresses during gait in the normal subject coincided with the location of the callus tissue (under the third and fourth metatarsal head). Note that although we predicted higher plantar pressure and internal stress in this vicinity, our model did not include the callus tissue. It is possible that this callus tissue develops as a natural strategy to shield abnormal plantar pressure from damaging deeper soft tissue. A parametric analysis of the foot model with and without callus tissue may be an area for further research.

The internal stress-time data also suggested that the forefoot tissue was exposed to a higher internal stress at a longer duration compared to the hindfoot. This resulted in higher stress doses (integral of stress over time) and a higher risk of internal tissue injuries at the forefoot. A similar trend was found clinically where diabetic foot ulcerations frequently occur in the forefoot, especially under the metatarsal heads and the hallux (Boffeli et al., 2002; Mohamed et al., 2010).

In this study, the normal subject had a higher peak forefoot internal stress during quiet stance and gait compared to the diabetic subject, although overall diabetic soft tissue was stiffer (Chapter 5). The trend was opposite from our general hypothesis that stiffer diabetic tissue leads to higher internal stresses. This was likely because there were several other factors that could affect the internal stress prediction. For example, different anatomy between subjects (minor fourth metatarsal head depression in the normal subject), individual standing/gait pattern, and natural variability. A parametric analysis performed in the next section isolated other potential factors and focused only on the effect of soft tissue material properties on plantar pressure and internal stresses.

The parametric analysis of the quiet stance model assumed that the COP location was unchanged after the soft tissue material properties were altered. The parametric analysis was not performed in the dynamic gait model because the effect of altered soft tissue material properties on gait kinematics was unknown. The quiet stance simulation results suggested that stiffer plantar fat, which emulates diabetic tissue, causes elevated plantar pressure and higher von Mises and hydrostatic stresses. Several FE foot studies reported similar findings (Cheung et al., 2005; Gefen, 2003). Elevated plantar stress was also found, clinically, be one of the contributing factors to diabetic foot ulceration (Birke et al., 1991). The simplification of generic soft tissue material properties substantially increased peak plantar pressure and internal stress. Using material properties of a different healthy, normal subject (Petre et al., 2013) in our model underestimated the peak plantar pressure, but still yielded comparable results to the base-line simulation and the *in vivo* data. Improvements in plantar pressure distribution were observed, potentially due to a smaller Poisson's ratio ($v = 0.475$ compared to $v = 0.499$ and 0.4999 used in this study). The predicted internal stresses, however, were considerably different from the base-line results. Findings from the parametric analysis suggested that including multiple soft tissue layers in the model is essential to obtain physiologic plantar pressure. Depending on the application of the model (e.g., predicting plantar pressure or internal soft tissue stress), it may be acceptable to replace the subject-specific multi-layer material properties with non-subject-specific data.

This study has several potential limitations. Linear tetrahedral elements were used because of their automatic meshing capability. The averaged nodal pressure tetrahedral element formulation (Bonet and Burton, 1998) used in our study has been shown to perform equally well compared to hexahedral elements (Appendix IV). The actual cartilage component was not modeled; instead, we assumed bone contacts with a specific offset distance for each joint. This assumption prevented our model from predicting joint contact pressures, although joint contact forces were available. Soft tissue was represented by an Ogden hyperelastic material and lacked time-dependent properties. The interfaces between bone and soft tissue and between tissue layers were defined using node sharing (i.e., no sliding along fascial planes), which resulted in overly stiff behavior. Modeling soft tissue interfaces as contacts may yield more accurate behavior, but could cause model instability and increased computation time. Mechanical properties of the untested ligaments were extrapolated from our database based on estimated ligament length from subject-specific anatomy. Extrinsic muscle forces were estimated from literature and similar values were used for both foot models. Intrinsic muscle volume was included in the model, but intrinsic muscle forces were neglected. Internal stresses were analyzed in the plantar fat layer only because we believed this was the potential foot ulceration site. Finally, our model required approximately

5 hours of computation time to perform 0.1s simulation using 8 cores on a Dell PowerEdge R610 rack server (3.46GHz Intel® Xeon® processors). In order for the model to be clinically useful, the development and computation time needs to be greatly reduced.

7.6 Conclusion

The subject-specific FE foot models developed in this study incorporated subject-specific anatomy, soft tissue material properties and tibial kinematics. Improvements in ligament, tendon, joint cavity and plantar aponeurosis structures were implemented. The model validation protocols in passive compression, quiet stance and gait were presented. These FE foot modeling techniques could serve as a guideline for other studies. The simulation results suggest that internal soft tissue of the foot is subjected to substantially higher hydrostatic stress compared to von M ises stress which could lead to tissue damage from restricted blood flow and potentially cause micro-tearing. During gait the plantar fat could experience up to 15 times higher von Mises stress and 4.6 time higher hydrostatic stress compared to quiet stance. The location and time at the peak forefoot internal stresses may not always coincide with the peak plantar pressure or vertical GRF. Higher internal stresses and longer duration under the forefoot and hallux compared to the hindfoot may explain the incidence of high forefoot and hallux ulceration in the diabetic neuropathic population. Larger sample size is required before any statistical analysis can be conducted to determine differences between normal and diabetic feet. The parametric analysis suggested that including multiple soft tissue layers in the model was necessary to obtain physiologic plantar pressure. A set of non-subject-specific material properties may be used when only plantar pressure is of interest; however, simplifying soft tissue layers to generic material should be avoided.

Supplementary Section A: Regional peak and mean plantar pressure, contact force and contact area from experiment (mean: solid gray line, SD: dotted line) and finite element simulations (normal subject (solid blue line), diabetic subject (solid red line)). Plantar foot contact was divided into 3 regions (hind-, mid- and forefoot) as well as 11 regions (medial hindfoot, lateral hindfoot, midfoot, metatarsal 1 to 5, hallux, toe2 and other toes).

Normal subject (3 regions)

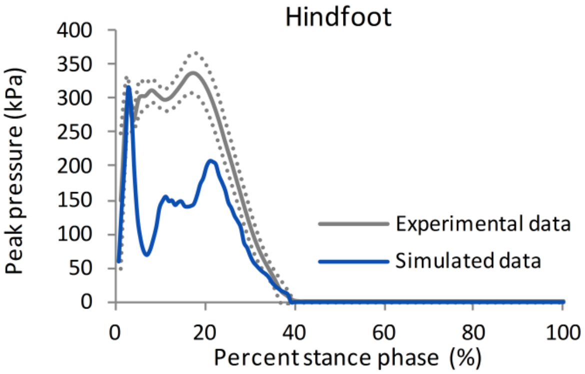

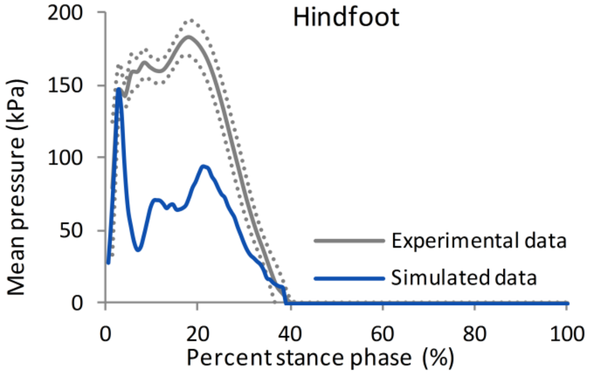

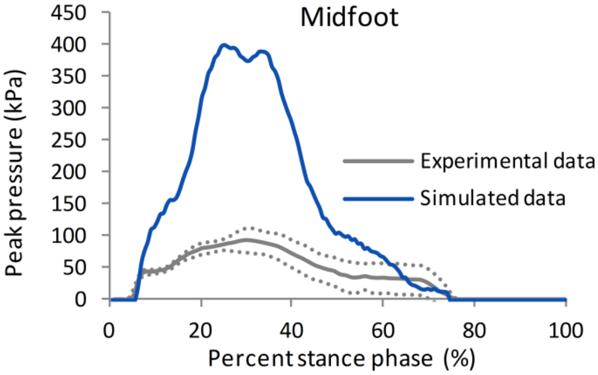

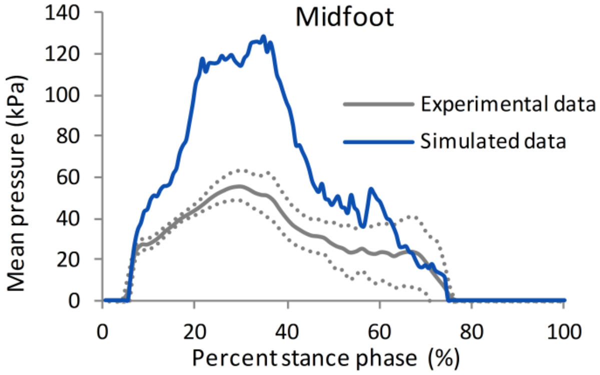

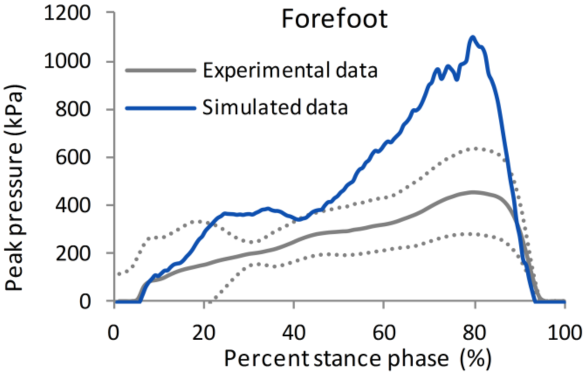

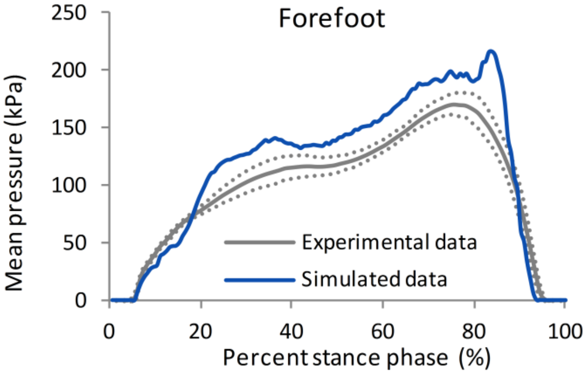

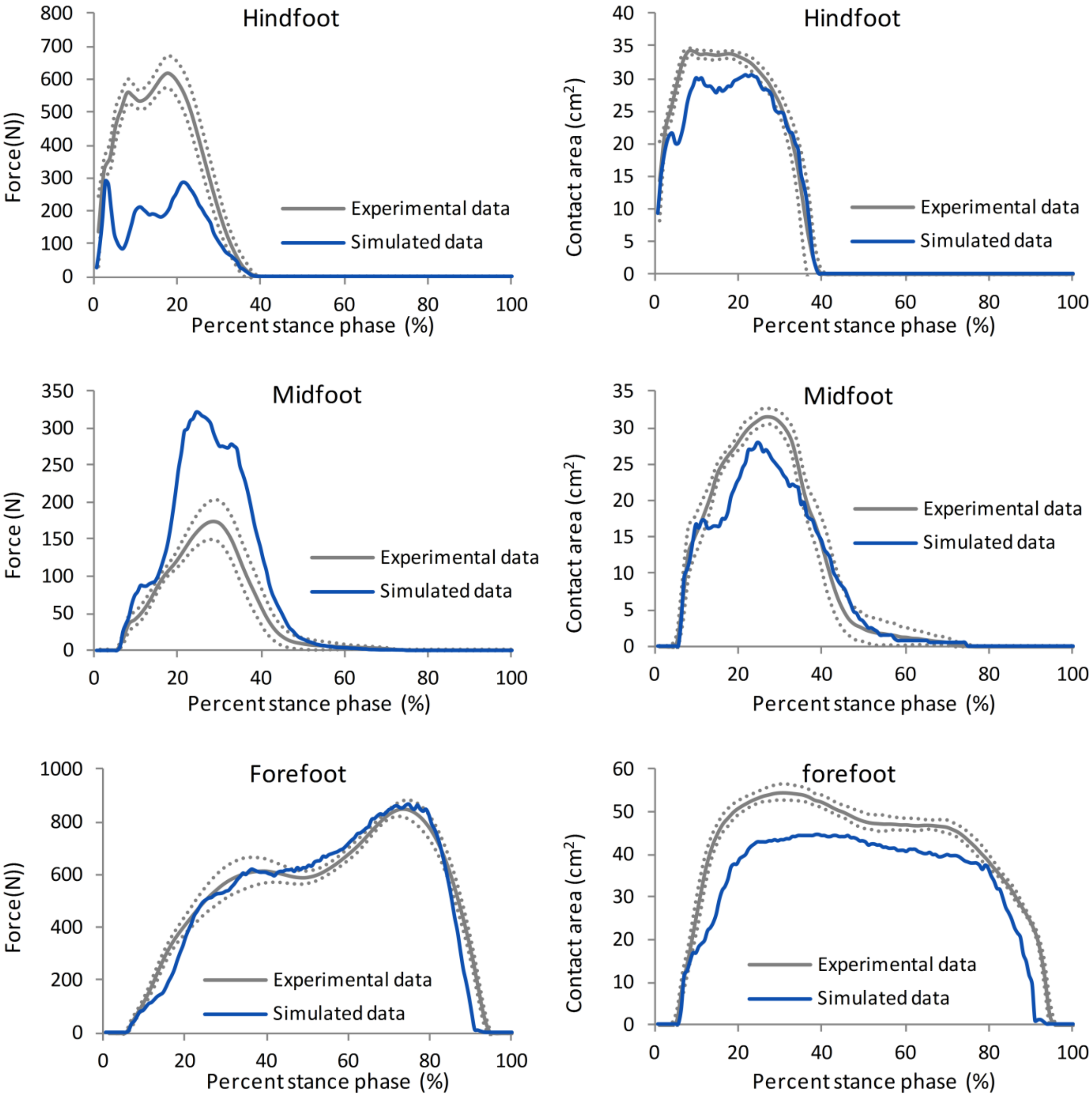

Figure A1: Peak pressure, mean pressure, contact force and contact area at the hindfoot, midfoot and forefoot of the normal subject from experiment (mean: solid gray line, SD: dotted line) and finite element simulation (solid blue line).

Normal subject (11 regions)

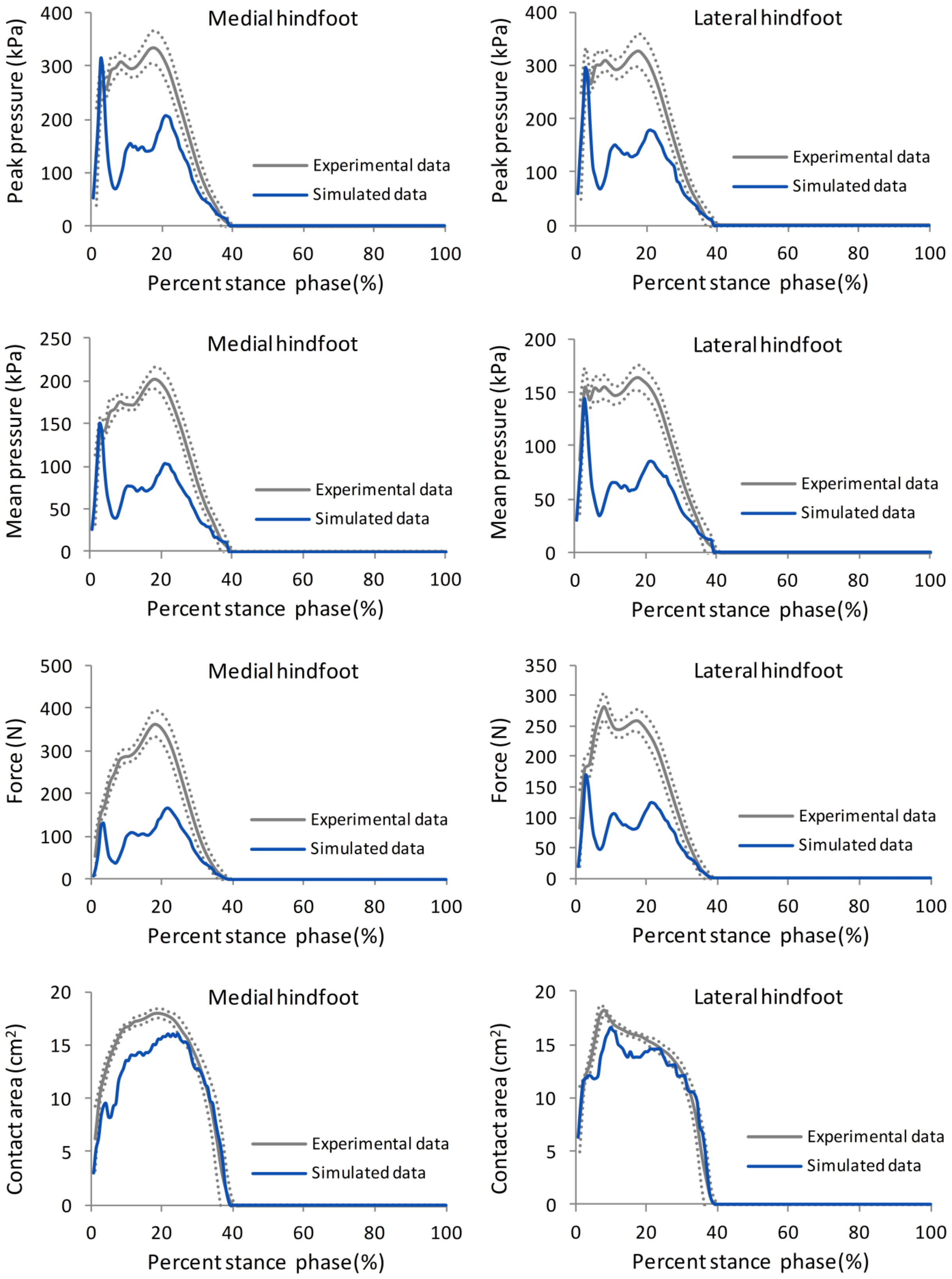

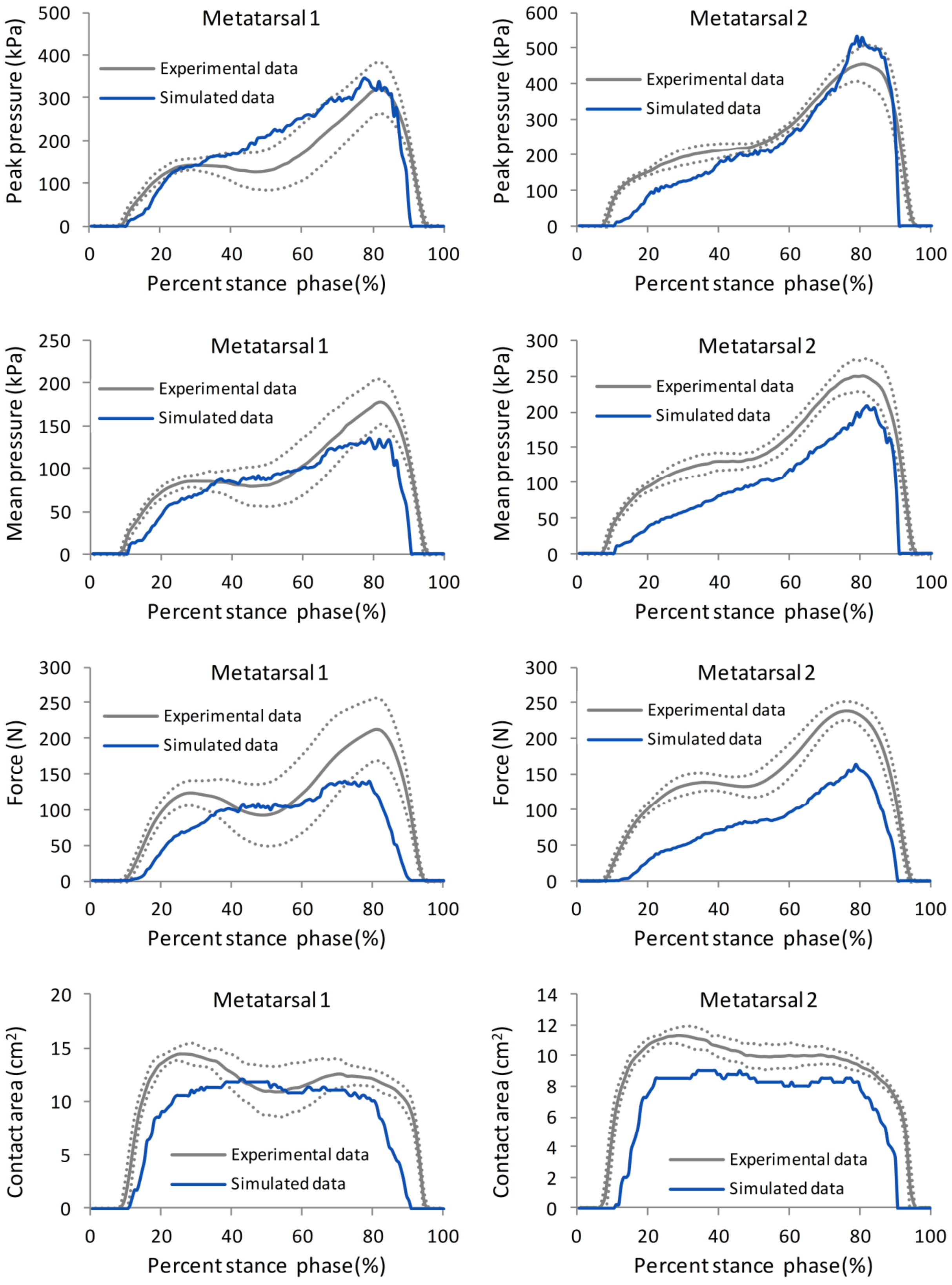
Metatarsal 1
Peak pressure (kPa)
500
400
300
200
100
0
Experimental data
Simulated data
0
20
40
60
80
100
Percent stance phase(%)
Metatarsal 2
Peak pressure (kPa)
600
500
400
300
200
100
0
Experimental data
Simulated data
Percent stance phase(%)
Metatarsal 1
Mean pressure (kPa)
250
200
150
100
50
0
Experimental data
Simulated data
Percent stance phase(%)
Metatarsal 2
Mean pressure (kPa)
300
250
200
150
100
50
0
Experimental data
Simulated data
Percent stance phase(%)
Metatarsal 1
Force (N)
300
250
200
150
100
50
0
Experimental data
Simulated data
Percent stance phase(%)
Metatarsal 2
Force (N)
300
250
200
150
100
50
0
Experimental data
Simulated data
Percent stance phase(%)
Metatarsal 1
Contact area (cm²)
20
15
10
5
0
Experimental data
Simulated data
Percent stance phase(%)
Metatarsal 2
Contact area (cm²)
14
12
10
8
6
4
2
0
Experimental data
Simulated data
Percent stance phase(%)

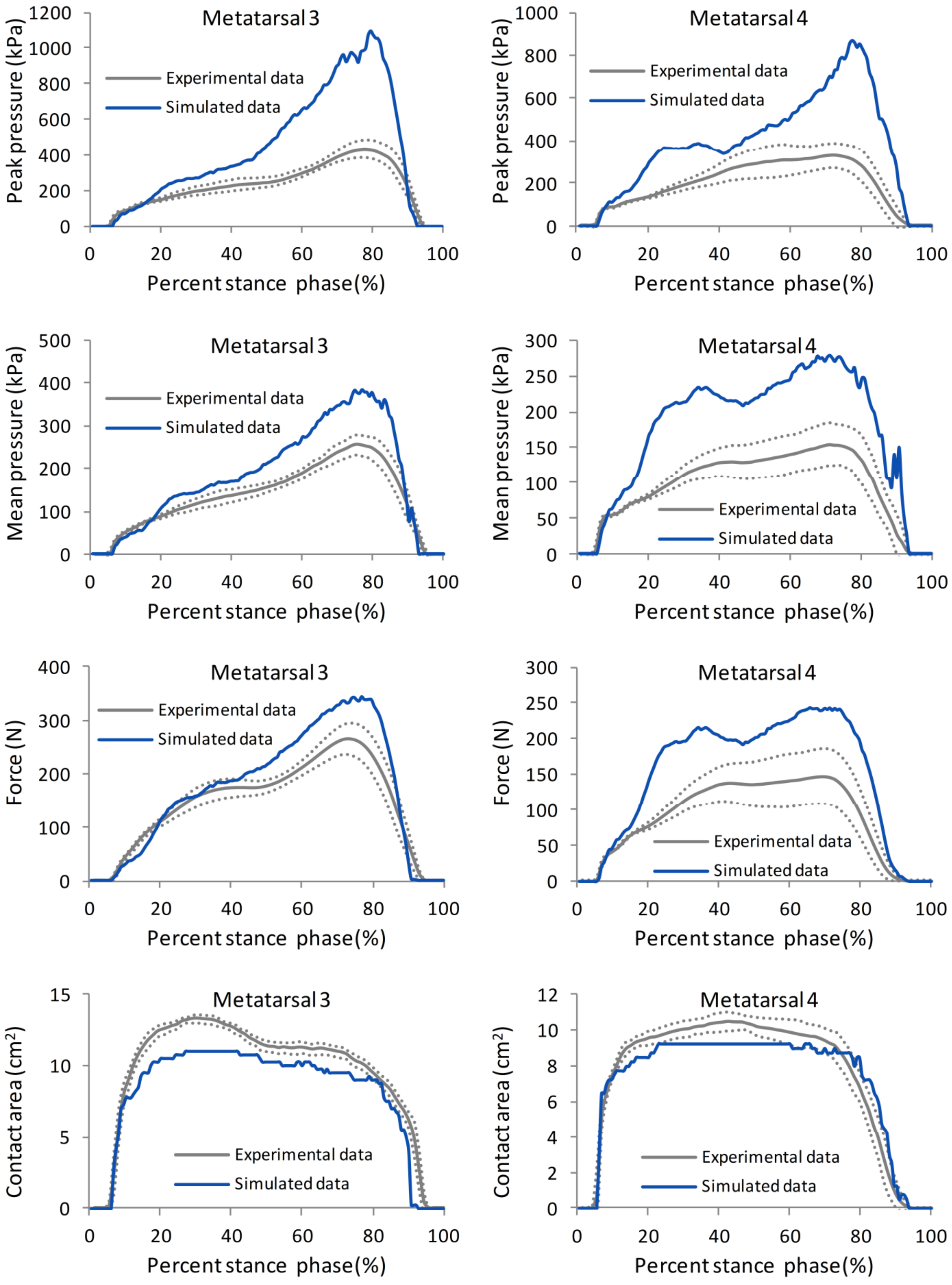
Metatarsal 3
Peak pressure (kPa)
1200
1000
800
600
400
200
0
Experimental data
Simulated data
0
20
40
60
80
100
Percent stance phase(%)
Metatarsal 4
Peak pressure (kPa)
1000
800
600
400
200
0
Experimental data
Simulated data
0
20
40
60
80
100
Percent stance phase(%)
Metatarsal 3
Mean pressure (kPa)
500
400
300
200
100
0
Experimental data
Simulated data
0
20
40
60
80
100
Percent stance phase(%)
Metatarsal 4
Mean pressure (kPa)
300
250
200
150
100
50
0
Experimental data
Simulated data
0
20
40
60
80
100
Percent stance phase(%)
Metatarsal 3
Force (N)
400
300
200
100
0
Experimental data
Simulated data
0
20
40
60
80
100
Percent stance phase(%)
Metatarsal 4
Force (N)
300
250
200
150
100
50
0
Experimental data
Simulated data
0
20
40
60
80
100
Percent stance phase(%)
Metatarsal 3
Contact area (cm²)
15
10
5
0
Experimental data
Simulated data
0
20
40
60
80
100
Percent stance phase(%)
Metatarsal 4
Contact area (cm²)
12
10
8
6
4
2
0
Experimental data
Simulated data
0
20
40
60
80
100
Percent stance phase(%)

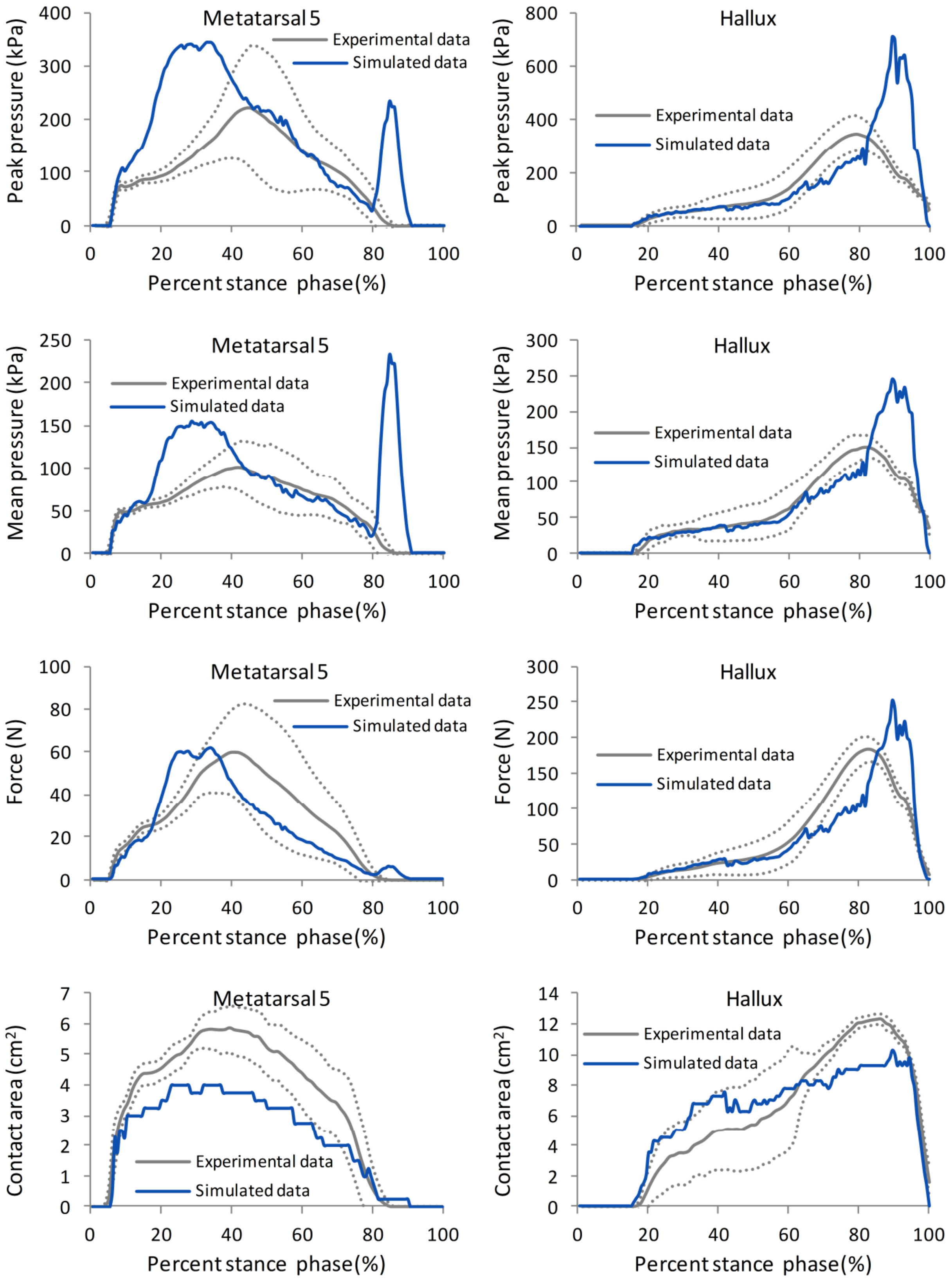
Metatarsal 5
Peak pressure (kPa)
0
100
200
300
400
Experimental data
Simulated data
0
20
40
60
80
100
Percent stance phase (%)
Hallux
Peak pressure (kPa)
0
200
400
600
800
Experimental data
Simulated data
Percent stance phase (%)
Metatarsal 5
Mean pressure (kPa)
0
50
100
150
200
250
Experimental data
Simulated data
Percent stance phase (%)
Hallux
Mean pressure (kPa)
0
50
100
150
200
250
300
Experimental data
Simulated data
Percent stance phase (%)
Metatarsal 5
Force (N)
0
20
40
60
80
100
Experimental data
Simulated data
Percent stance phase (%)
Hallux
Force (N)
0
50
100
150
200
250
300
Experimental data
Simulated data
Percent stance phase (%)
Metatarsal 5
Contact area (cm²)
0
1
2
3
4
5
6
7
Experimental data
Simulated data
Percent stance phase (%)
Hallux
Contact area (cm²)
0
2
4
6
8
10
12
14
Experimental data
Simulated data
Percent stance phase (%)

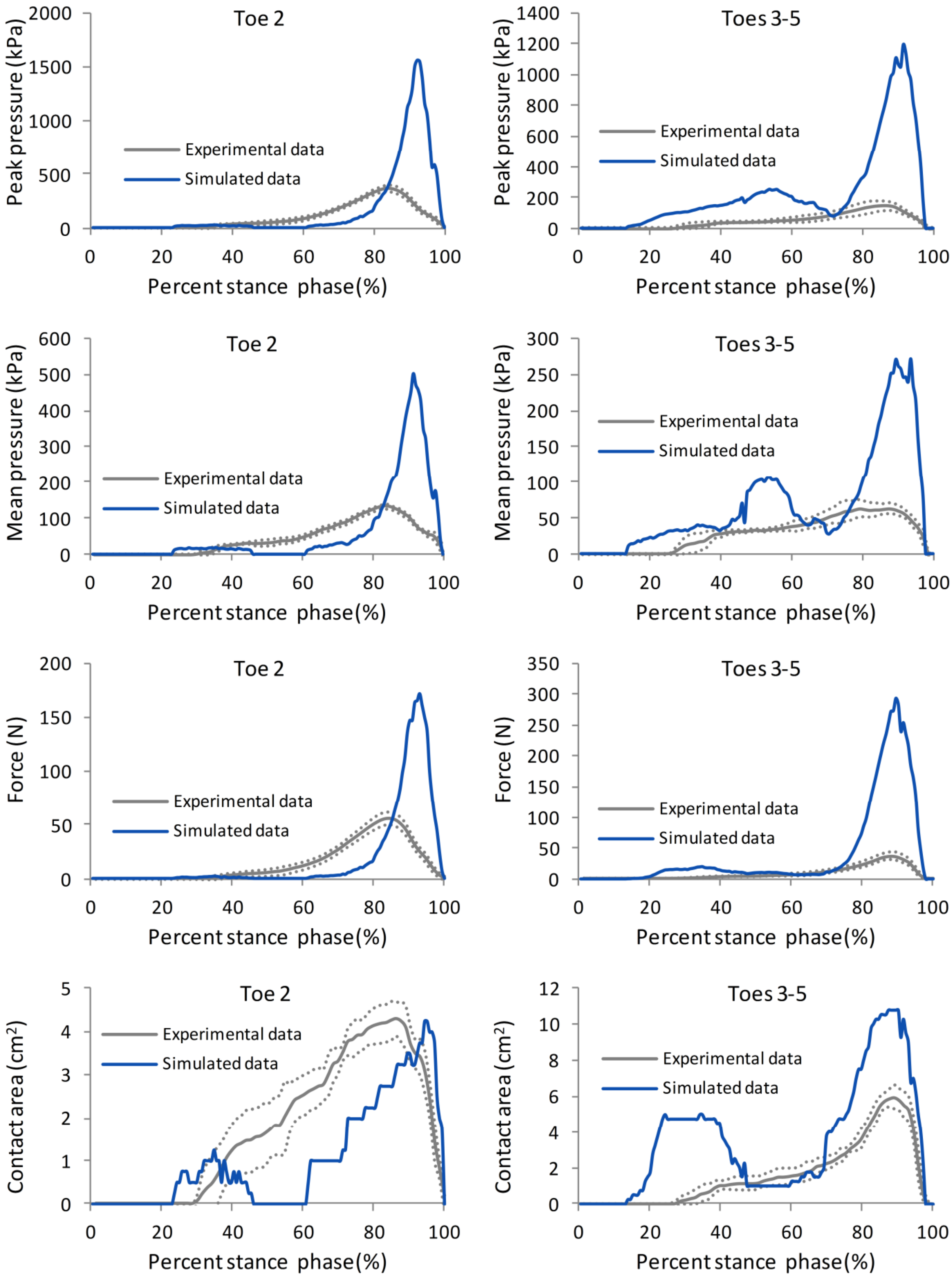

Figure A2: Peak pressure, mean pressure, contact force and contact area of the normal subject at 11 regions from from experiment (mean: solid gray line, SD: dotted line) and finite element simulation (solid blue line). Note that midfoot results are presented in Figure A1.

Diabetic subject (3 regions)

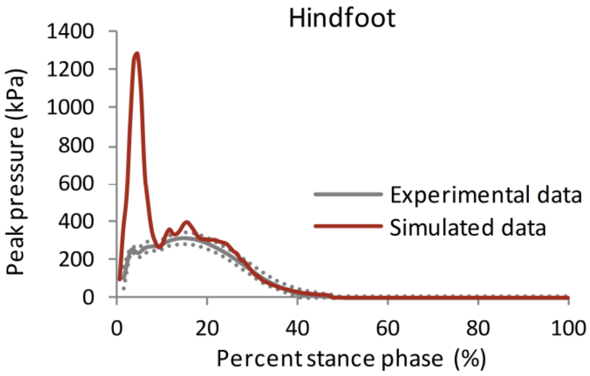

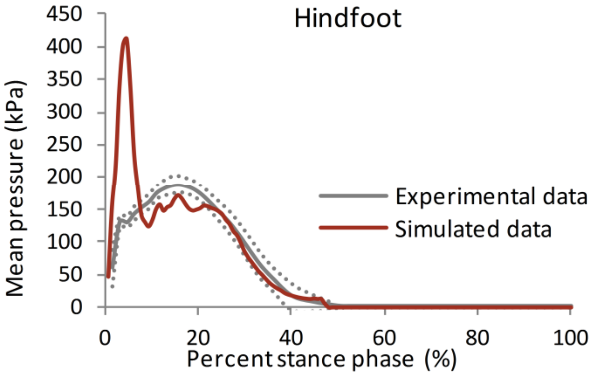

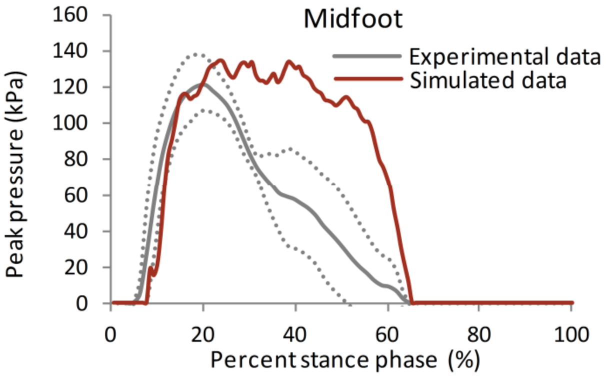

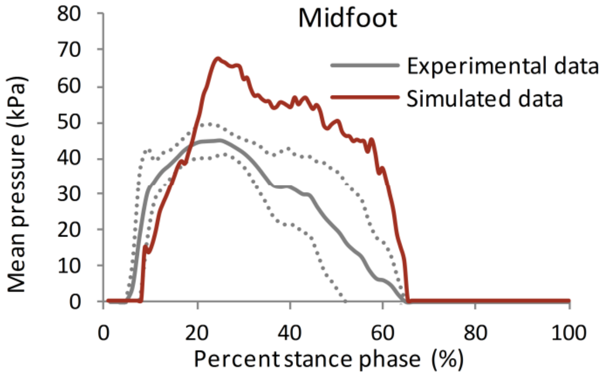

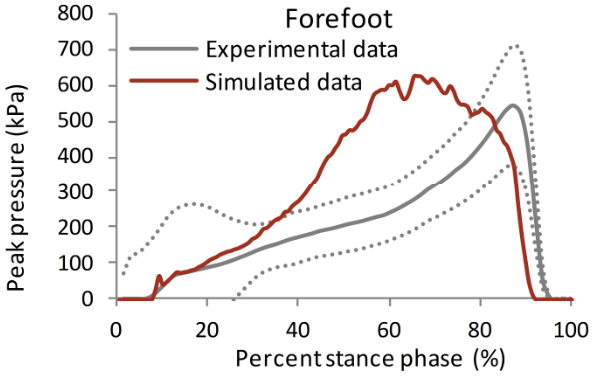

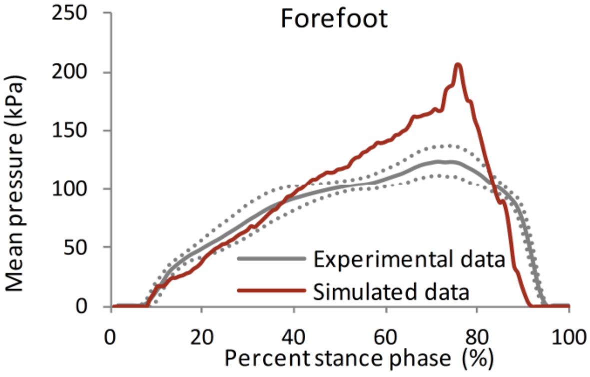

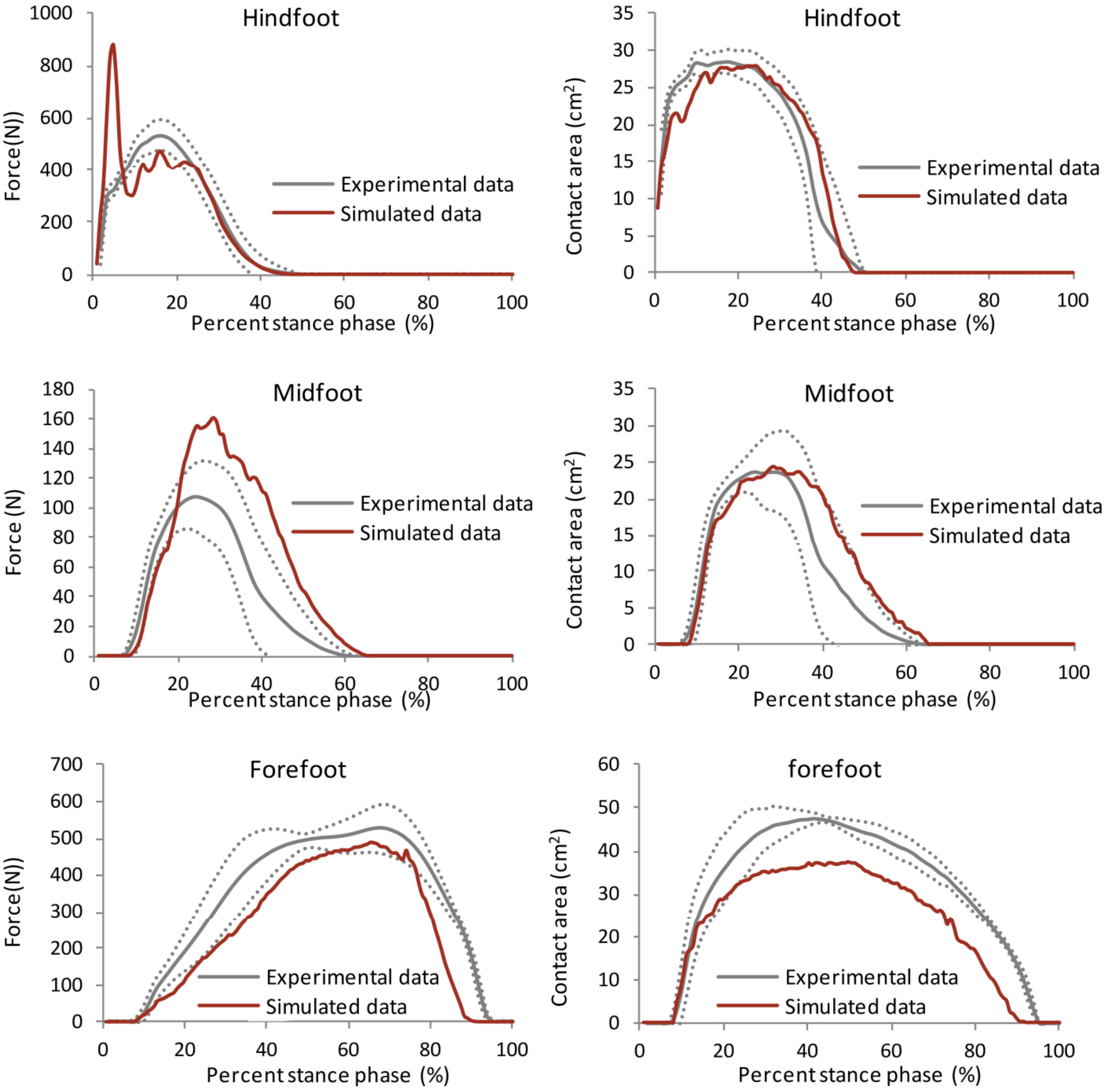

Figure A3: Peak pressure, mean pressure, contact force and contact area at the hindfoot, midfoot and forefoot of the diabetic subject from experiment (mean: solid gray line, SD: dotted line) and finite element simulation (solid red line).

Diabetic subject (11 regions)

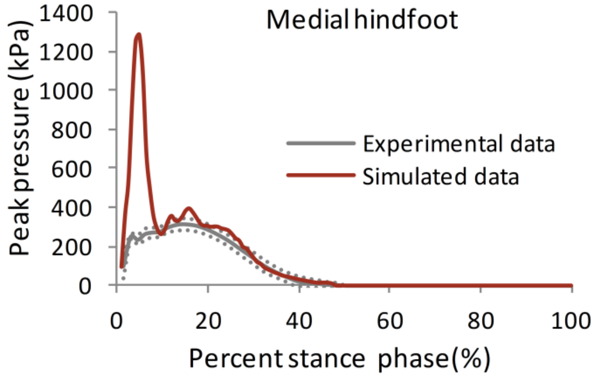

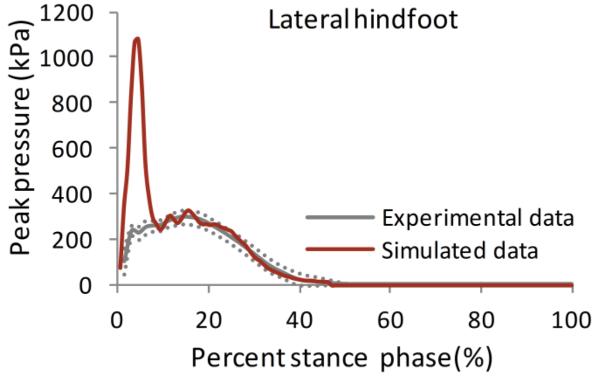

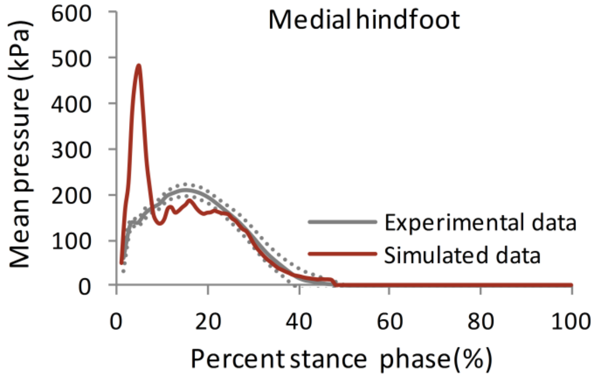

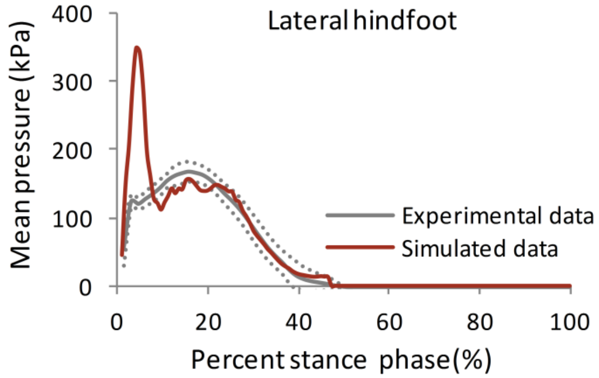

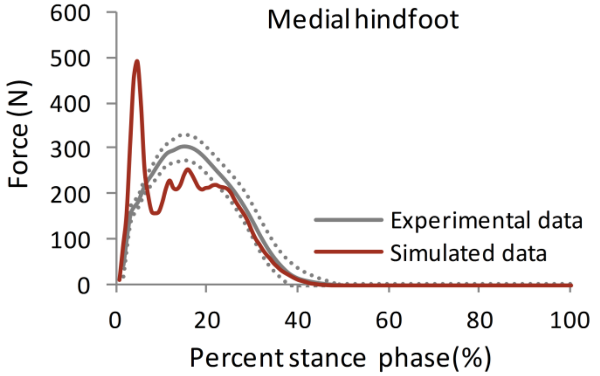

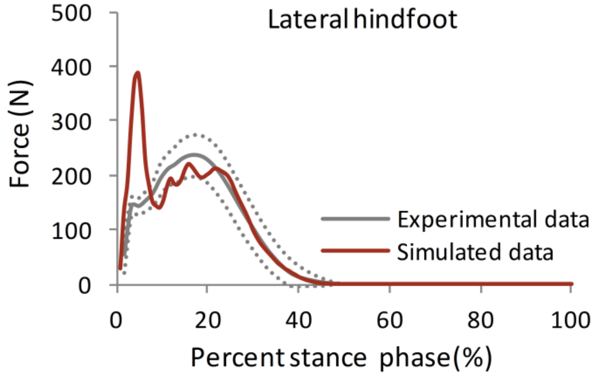

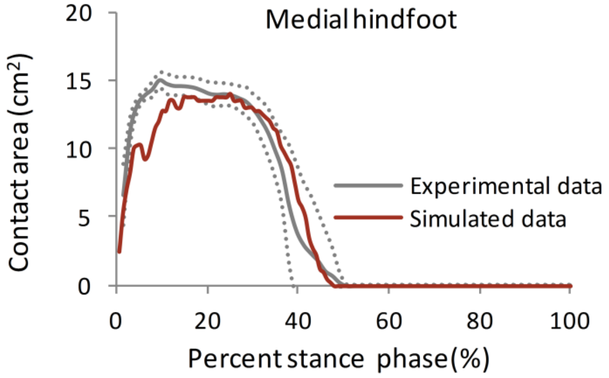

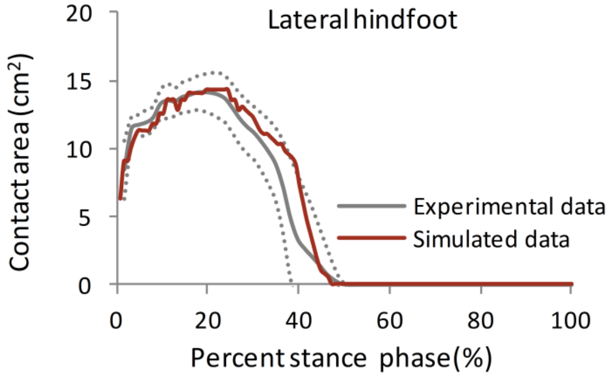

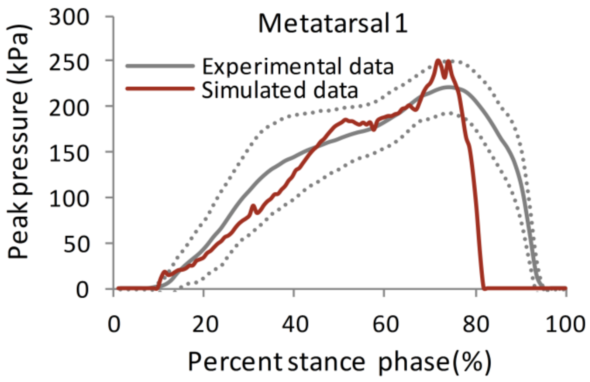
Metatarsal 1
Experimental data
Simulated data
Peak pressure (kPa)
300
250
200
150
100
50
0
0
20
40
60
80
100
Percent stance phase (%)

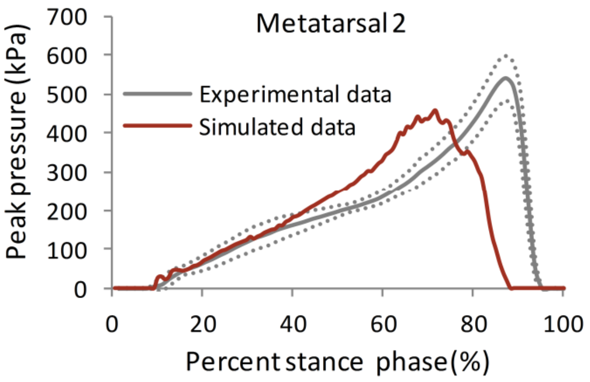
Metatarsal 2
Experimental data
Simulated data
Peak pressure (kPa)
700
600
500
400
300
200
100
0
0
20
40
60
80
100
Percent stance phase (%)

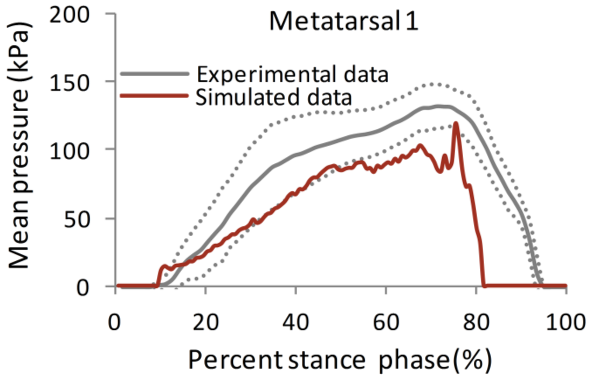
Metatarsal 1
Experimental data
Simulated data
Mean pressure (kPa)
200
150
100
50
0
0
20
40
60
80
100
Percent stance phase (%)

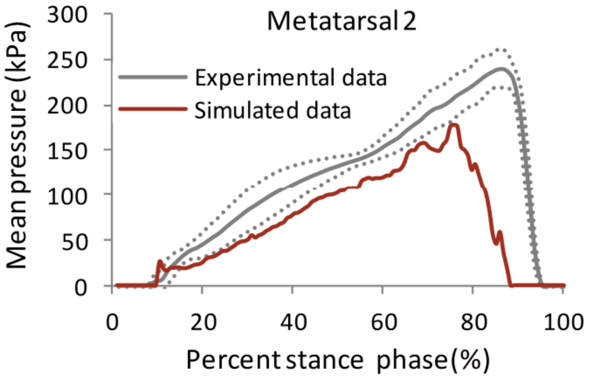
Metatarsal 2
Experimental data
Simulated data
Mean pressure (kPa)
300
250
200
150
100
50
0
0
20
40
60
80
100
Percent stance phase (%)

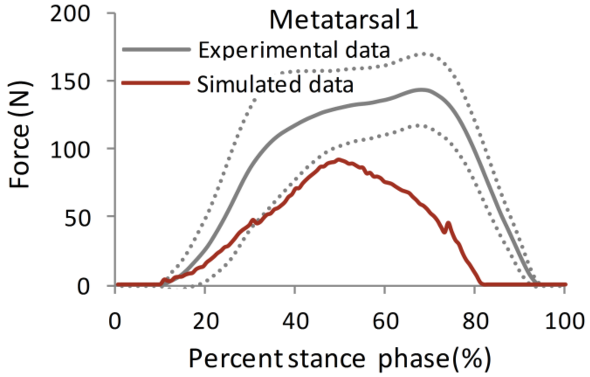
Metatarsal 1
Experimental data
Simulated data
Force (N)
200
150
100
50
0
0
20
40
60
80
100
Percent stance phase (%)

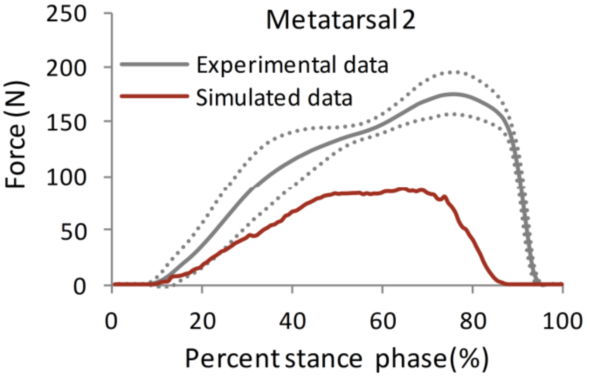
Metatarsal 2
Experimental data
Simulated data
Force (N)
250
200
150
100
50
0
0
20
40
60
80
100
Percent stance phase (%)

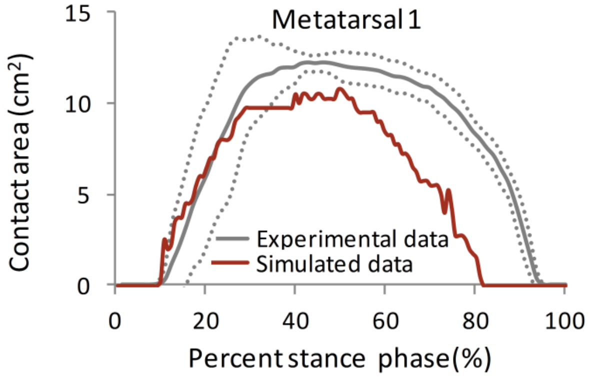
Metatarsal 1
Experimental data
Simulated data
Contact area (cm²)
15
10
5
0
0
20
40
60
80
100
Percent stance phase (%)

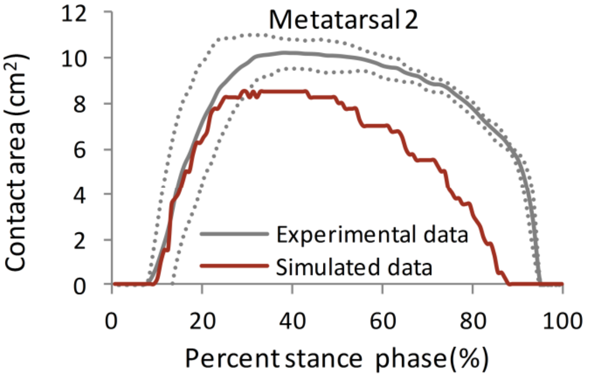
Metatarsal 2
Experimental data
Simulated data
Contact area (cm²)
12
10
8
6
4
2
0
0
20
40
60
80
100
Percent stance phase (%)

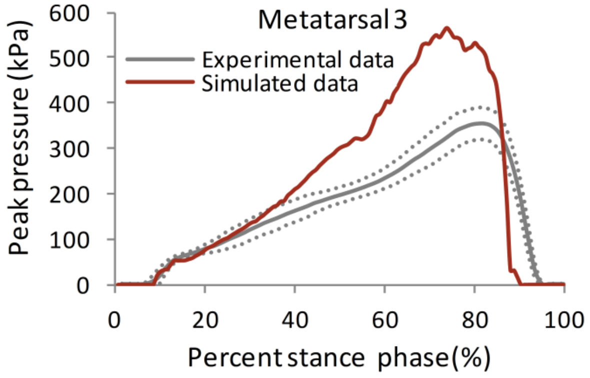
Metatarsal 3
Experimental data
Simulated data
Peak pressure (kPa)
600
500
400
300
200
100
0
0
20
40
60
80
100
Percent stance phase (%)

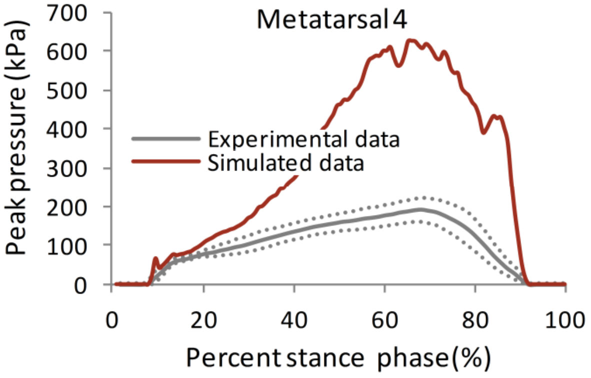
Metatarsal 4
Experimental data
Simulated data
Peak pressure (kPa)
700
600
500
400
300
200
100
0
0
20
40
60
80
100
Percent stance phase (%)

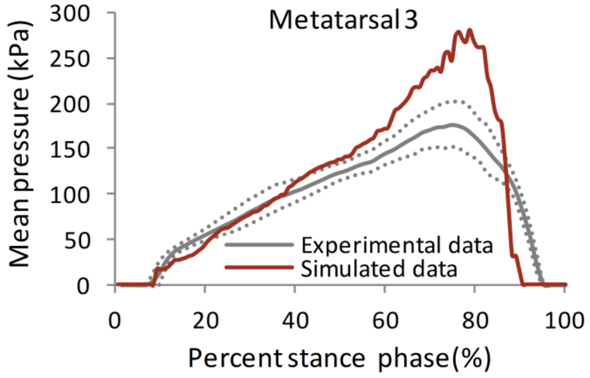
Metatarsal 3
Experimental data
Simulated data
Mean pressure (kPa)
300
250
200
150
100
50
0
0
20
40
60
80
100
Percent stance phase (%)

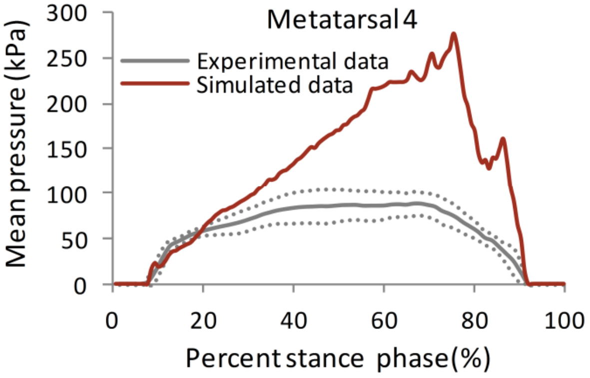
Metatarsal 4
Experimental data
Simulated data
Mean pressure (kPa)
300
250
200
150
100
50
0
0
20
40
60
80
100
Percent stance phase (%)

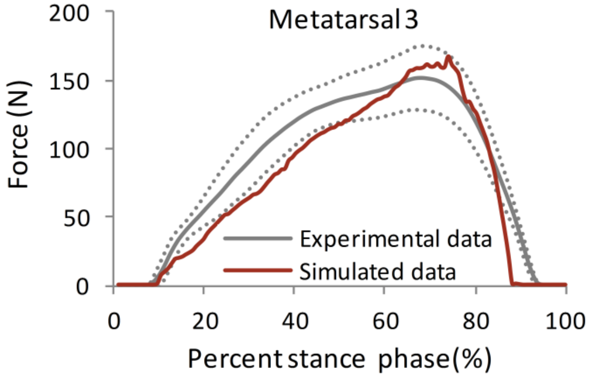
Metatarsal 3
Experimental data
Simulated data
Force (N)
200
150
100
50
0
0
20
40
60
80
100
Percent stance phase (%)

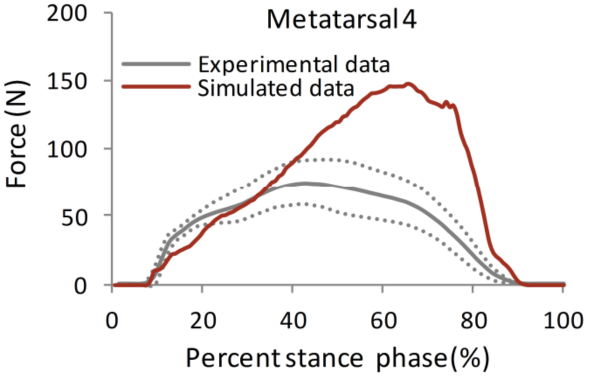
Metatarsal 4
Experimental data
Simulated data
Force (N)
200
150
100
50
0
0
20
40
60
80
100
Percent stance phase (%)

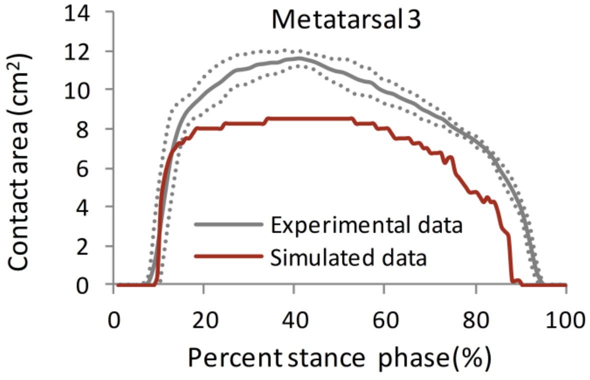
Metatarsal 3
Experimental data
Simulated data
Contact area (cm²)
14
12
10
8
6
4
2
0
0
20
40
60
80
100
Percent stance phase (%)

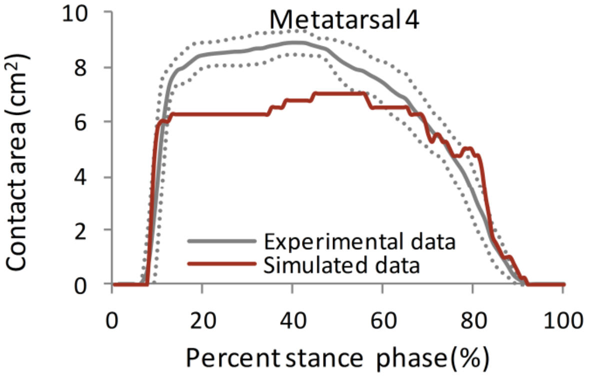
Metatarsal 4
Experimental data
Simulated data
Contact area (cm²)
10
8
6
4
2
0
0
20
40
60
80
100
Percent stance phase (%)

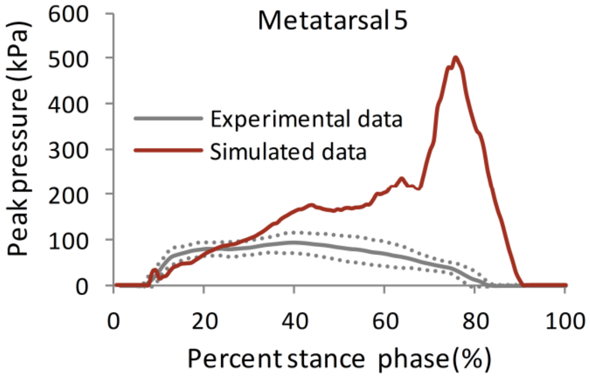
Metatarsal 5
Peak pressure (kPa)
600
500
400
300
200
100
0
Experimental data
Simulated data
0
20
40
60
80
100
Percent stance phase (%)

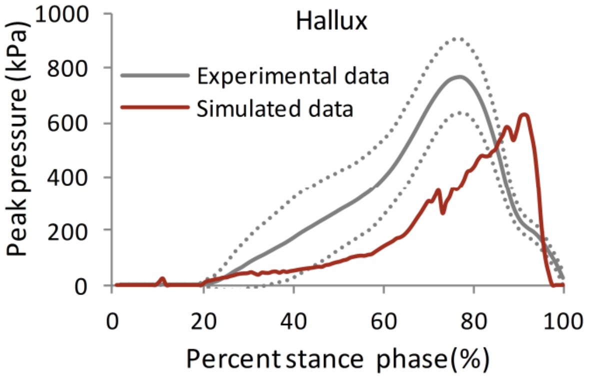
Hallux
Peak pressure (kPa)
1000
800
600
400
200
0
Experimental data
Simulated data
0
20
40
60
80
100
Percent stance phase (%)

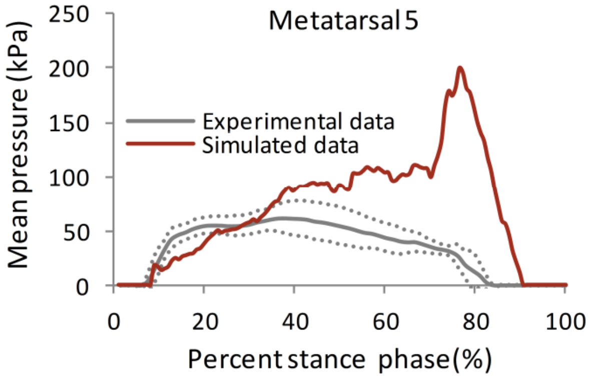
Metatarsal 5
Mean pressure (kPa)
250
200
150
100
50
0
Experimental data
Simulated data
0
20
40
60
80
100
Percent stance phase (%)

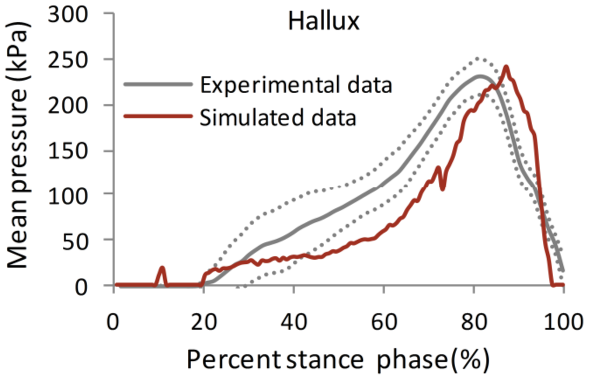
Hallux
Mean pressure (kPa)
300
250
200
150
100
50
0
Experimental data
Simulated data
0
20
40
60
80
100
Percent stance phase (%)

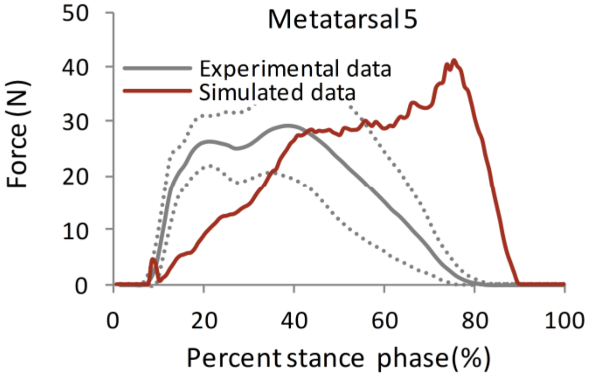
Metatarsal 5
Force (N)
50
40
30
20
10
0
Experimental data
Simulated data
0
20
40
60
80
100
Percent stance phase (%)

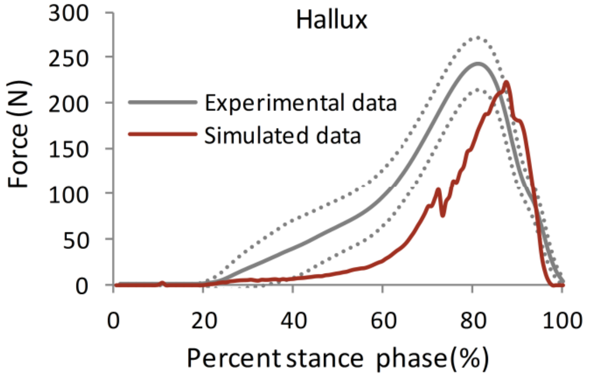
Hallux
Force (N)
300
250
200
150
100
50
0
Experimental data
Simulated data
0
20
40
60
80
100
Percent stance phase (%)

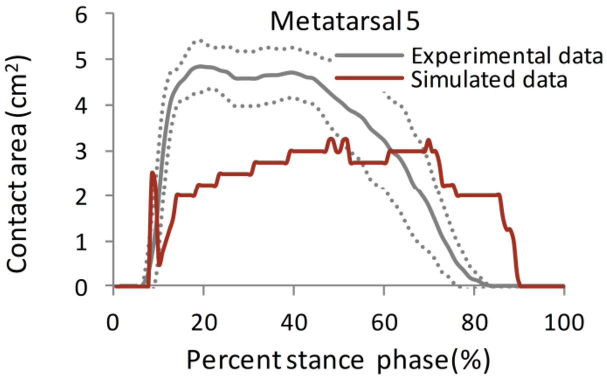
Metatarsal 5
Contact area (cm²)
6
5
4
3
2
1
0
Experimental data
Simulated data
0
20
40
60
80
100
Percent stance phase (%)

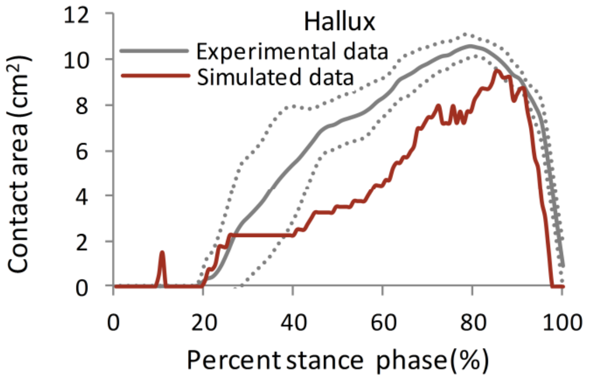
Hallux
Contact area (cm²)
12
10
8
6
4
2
0
Experimental data
Simulated data
0
20
40
60
80
100
Percent stance phase (%)

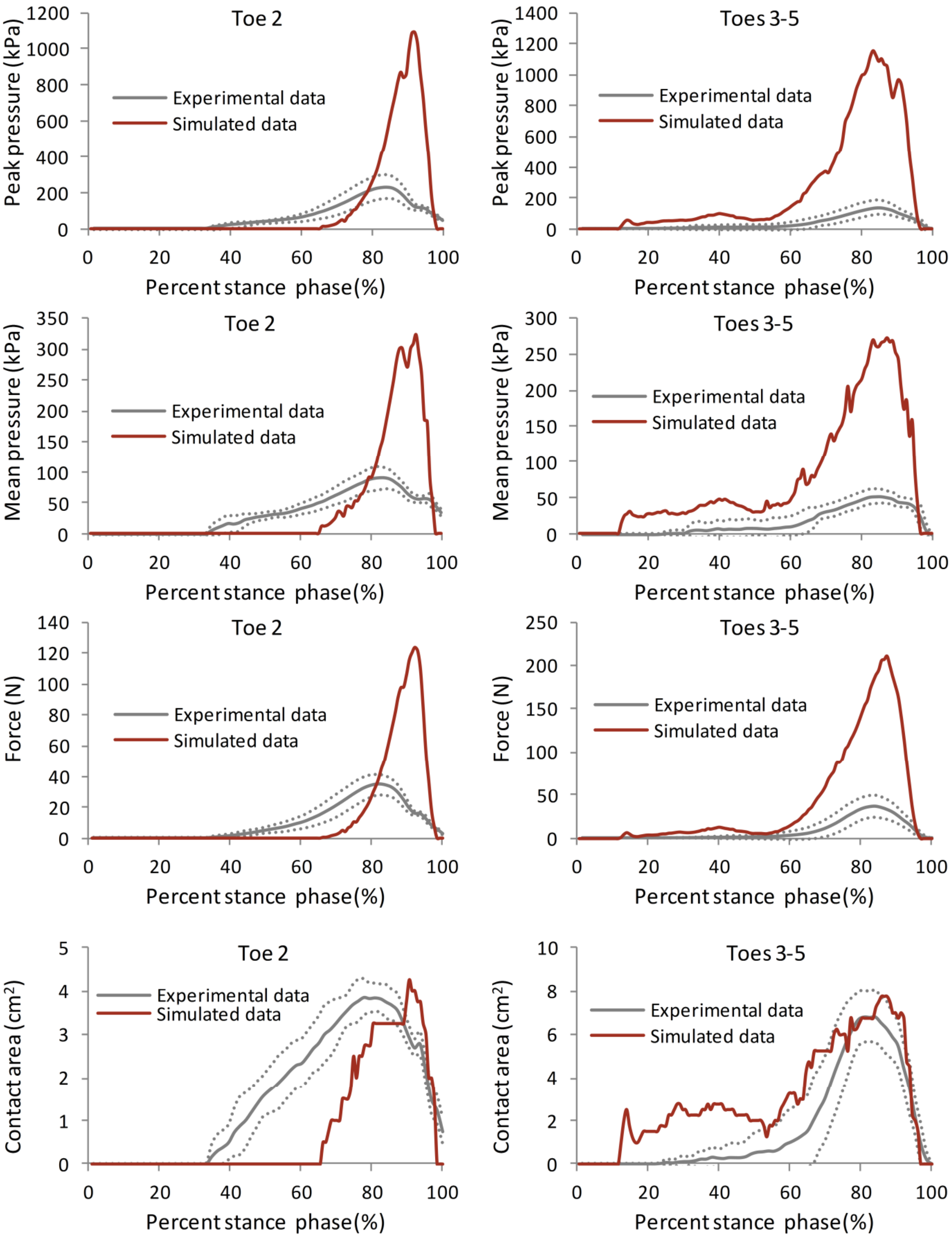

Figure A4: Peak pressure, mean pressure, contact force and contact area of the diabetic subject at 11 regions from experiment (mean: solid gray line, SD: dotted line) and finite element simulation (solid red line). Note that midfoot results are presented in Figure A3.

Supplementary Section B: Bone-to-ground and segment-to-segment angles from gait on force plate trials. Experimental (mean: solid gray line, SD: dotted line) and finite element simulated data are plotted for the normal (solid blue line) and diabetic (solid red line) feet. Angles were expressed as distal bone/segment relative to the proximal bone/segment/ground.

Normal foot

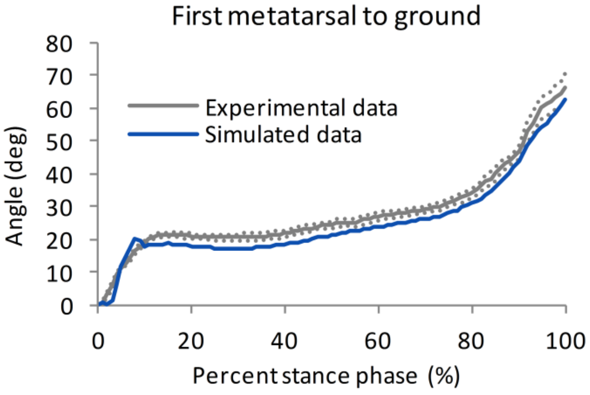

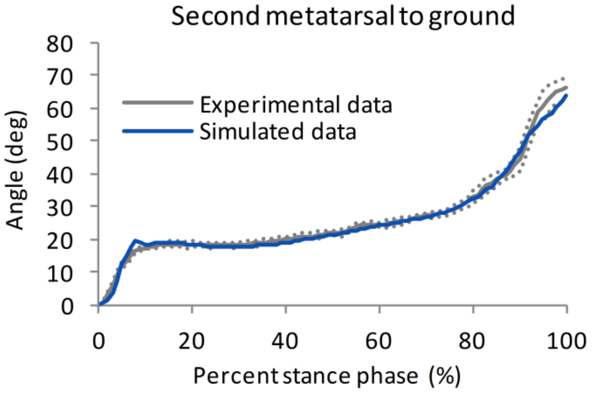

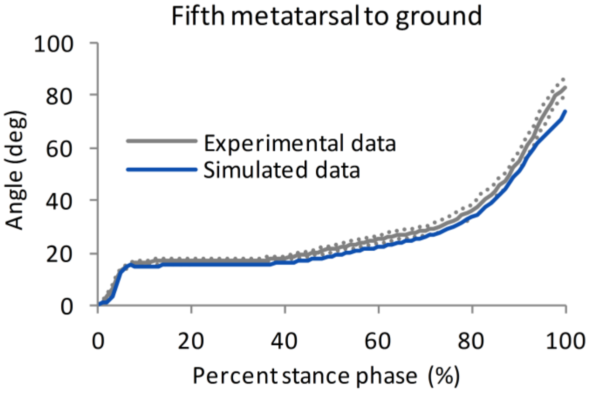

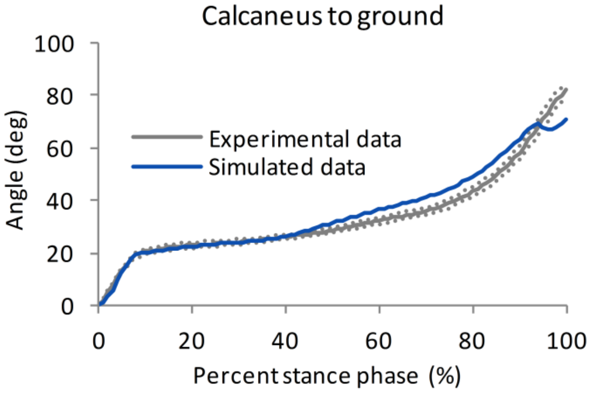

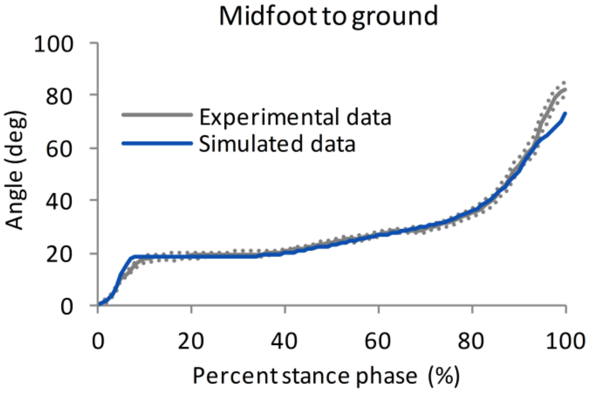

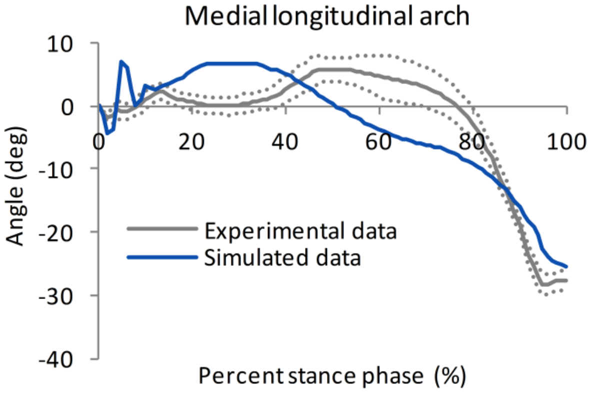

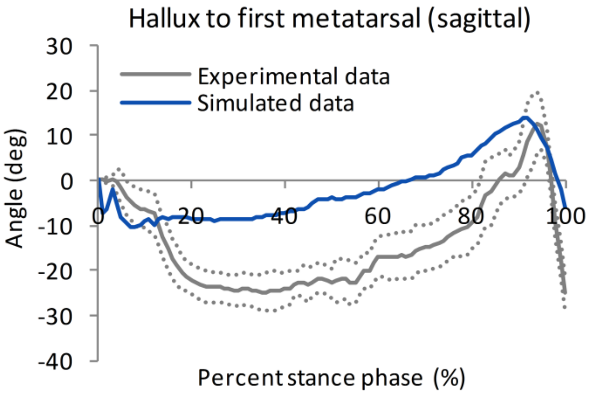
Hallux to first metatarsal (sagittal)
Angle (deg)
30
20
10
0
-10
-20
-30
-40
0
20
40
60
80
100
Experimental data
Simulated data
Percent stance phase (%)

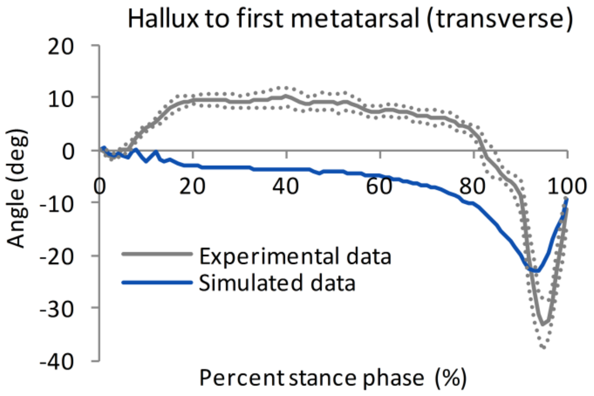
Hallux to first metatarsal (transverse)
Angle (deg)
20
10
0
-10
-20
-30
-40
0
20
40
60
80
100
Experimental data
Simulated data
Percent stance phase (%)

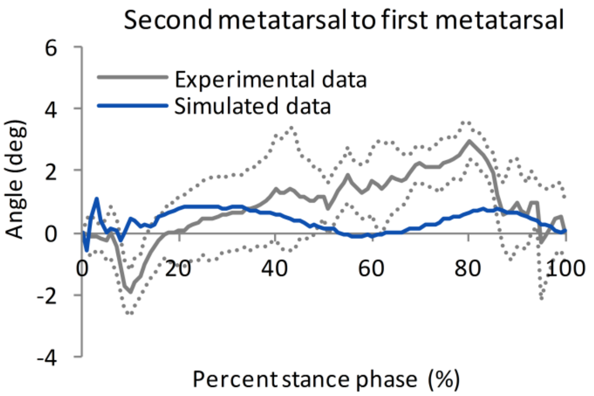
Second metatarsal to first metatarsal
Angle (deg)
6
4
2
0
-2
-4
0
20
40
60
80
100
Experimental data
Simulated data
Percent stance phase (%)

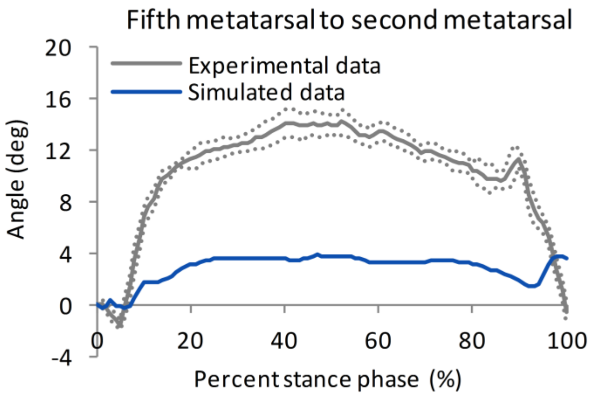
Fifth metatarsal to second metatarsal
Angle (deg)
20
16
12
8
4
0
-4
0
20
40
60
80
100
Experimental data
Simulated data
Percent stance phase (%)

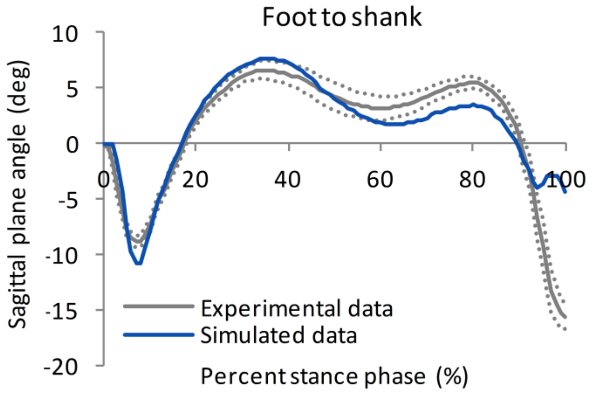
Foot to shank
Sagittal plane angle (deg)
10
5
0
-5
-10
-15
-20
0
20
40
60
80
100
Experimental data
Simulated data
Percent stance phase (%)

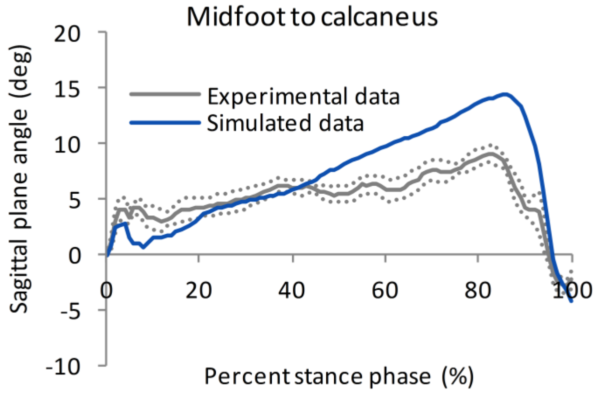
Midfoot to calcaneus
Sagittal plane angle (deg)
20
15
10
5
0
-5
-10
0
20
40
60
80
100
Experimental data
Simulated data
Percent stance phase (%)

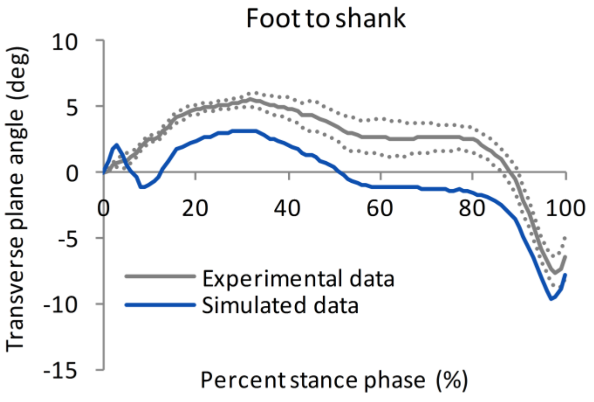
Foot to shank
Transverse plane angle (deg)
10
5
0
-5
-10
-15
0
20
40
60
80
100
Experimental data
Simulated data
Percent stance phase (%)

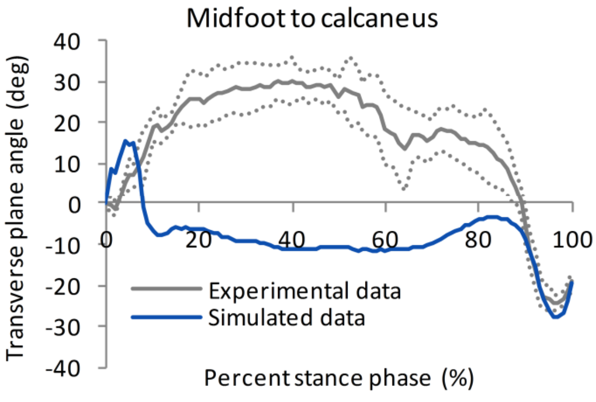
Midfoot to calcaneus
Transverse plane angle (deg)
40
30
20
10
0
-10
-20
-30
-40
0
20
40
60
80
100
Experimental data
Simulated data
Percent stance phase (%)

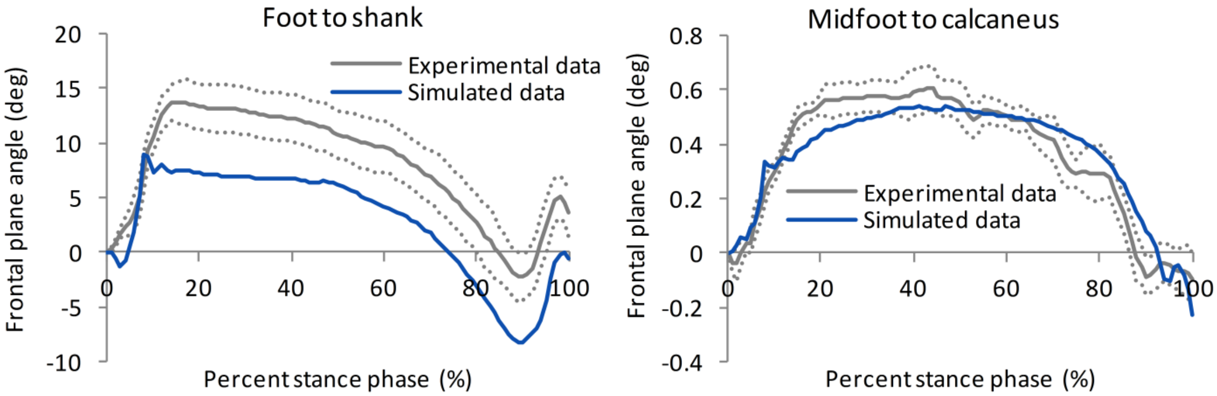

Figure B1: Experimental (mean: solid gray line, SD: dotted line) and simulated (solid blue line) bone-to-ground and segment-to-segment angles in the normal subject. The first, second and fifth metatarsal to ground, calcaneus to ground, midfoot to ground and medial longitudinal arch are all sagittal plane angles, while second metatarsal to the first metatarsal and fifth metatarsal to the second metatarsal are transverse plane angles. The angles relative to ground are normalize to contact position and a positive change indicates the anterior part of the bone is rotating below the posterior part. Positive change for the medial longitudinal arch indicates plantar flexion of the first metatarsal relative to the calcaneus. Positive change for the second metatarsal to the first metatarsal and the fifth metatarsal to the second metatarsal indicates abduction of the second metatarsal relative to the first metatarsal and the fifth metatarsal relative to the second metatarsal, respectively. Positive change in the sagittal foot to shank and midfoot to calcaneus angles indicates dorsiflexion of the distal segment relative to the proximal segment. Likewise, positive change in the transverse plane angle indicates abduction of the distal segment relative to the proximal segment, and positive change in the frontal plane angle indicates eversion of the distal segment relative to the proximal segment.

Diabetic foot

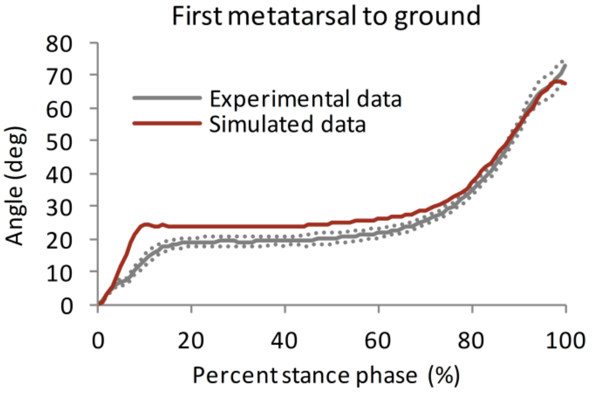

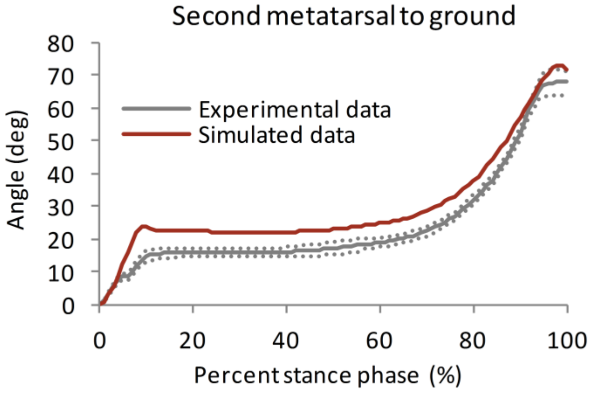

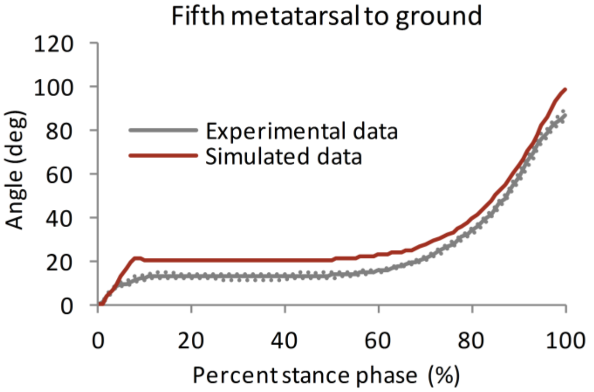

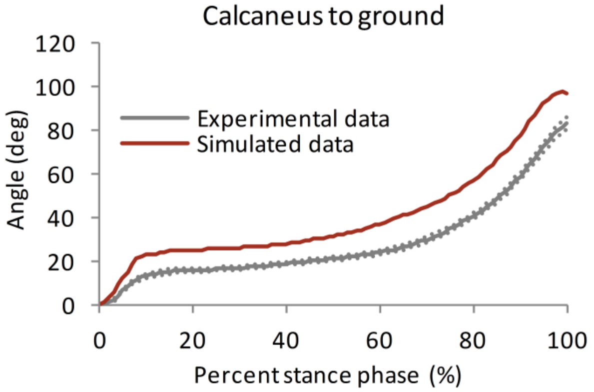

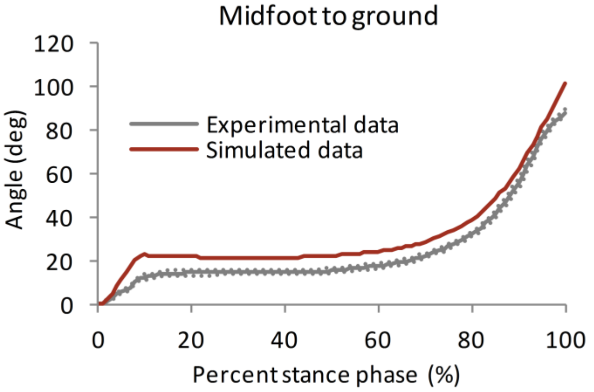

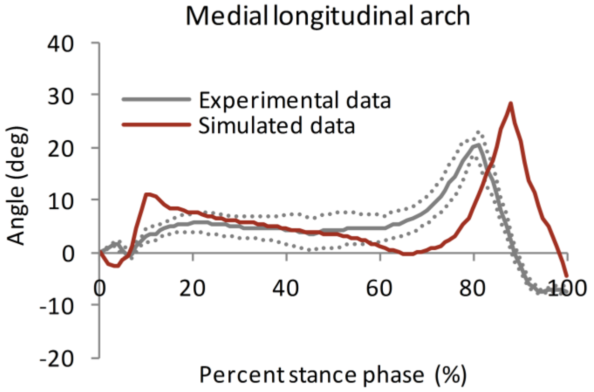

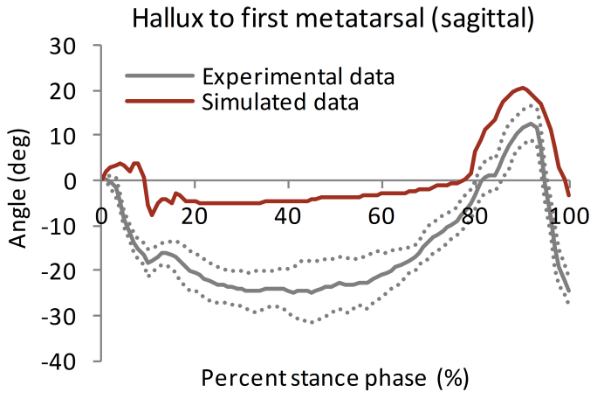
Hallux to first metatarsal (sagittal)

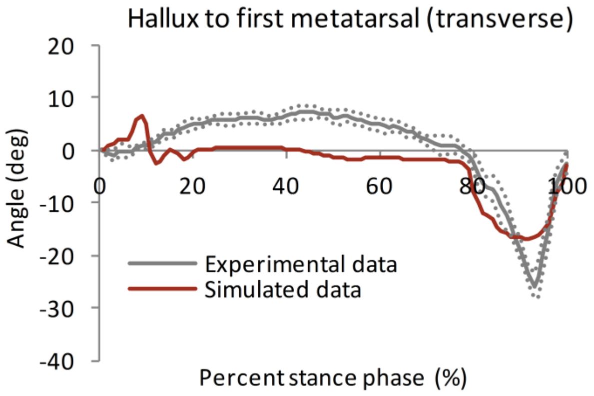
Hallux to first metatarsal (transverse)

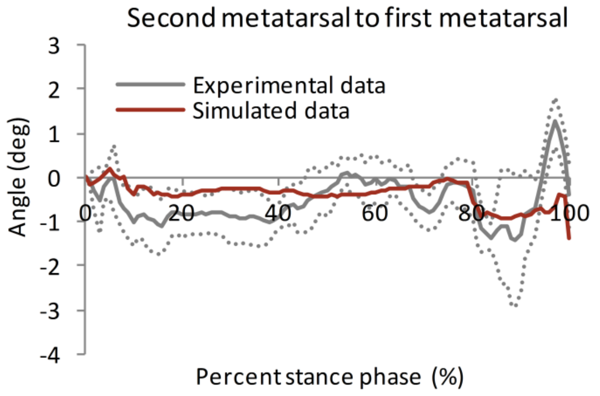
Second metatarsal to first metatarsal

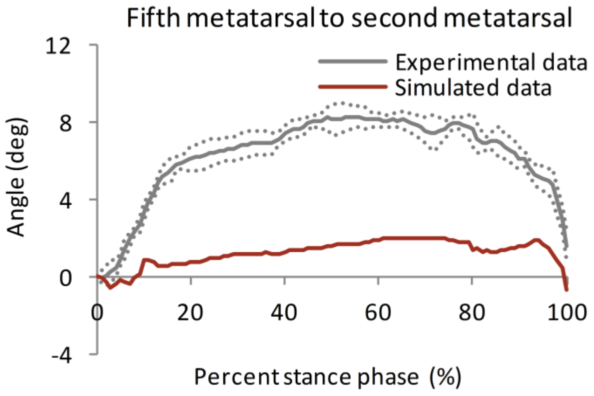
Fifth metatarsal to second metatarsal

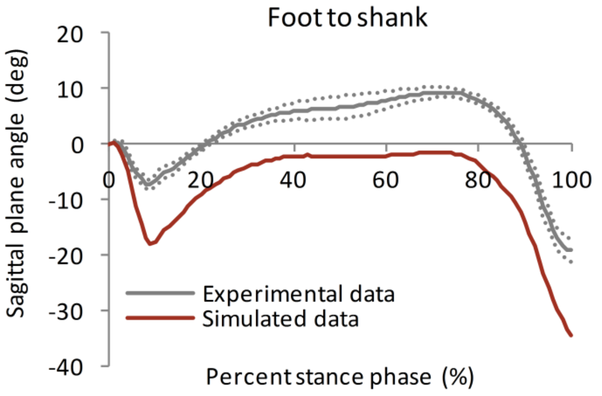
Foot to shank

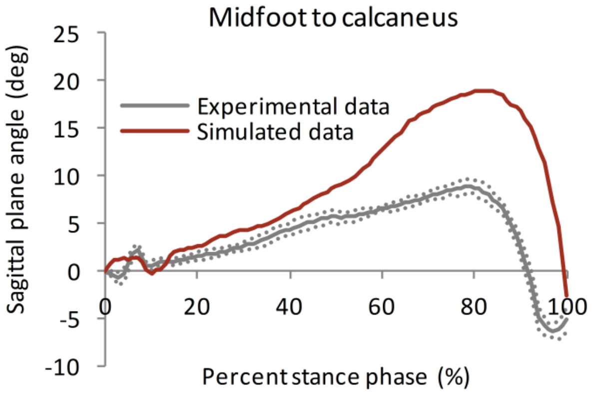
Midfoot to calcaneus

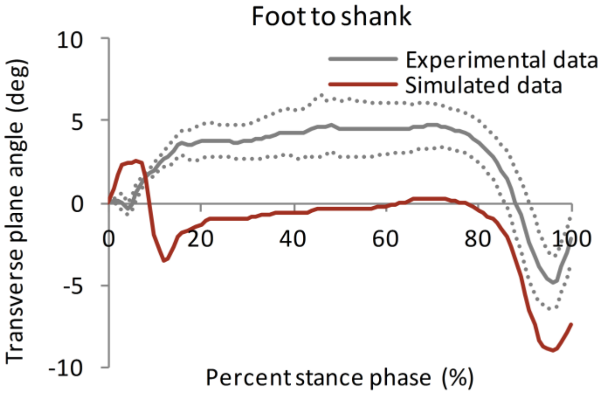
Foot to shank

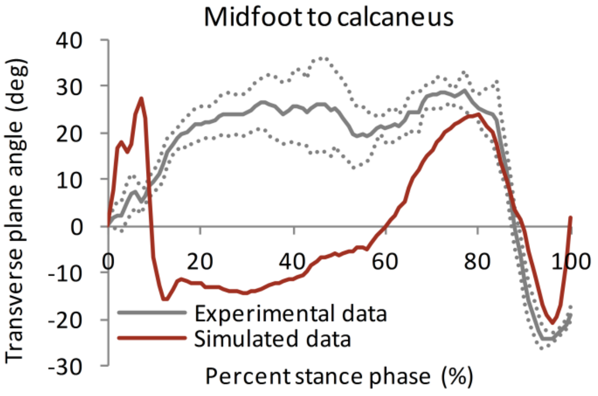
Midfoot to calcaneus

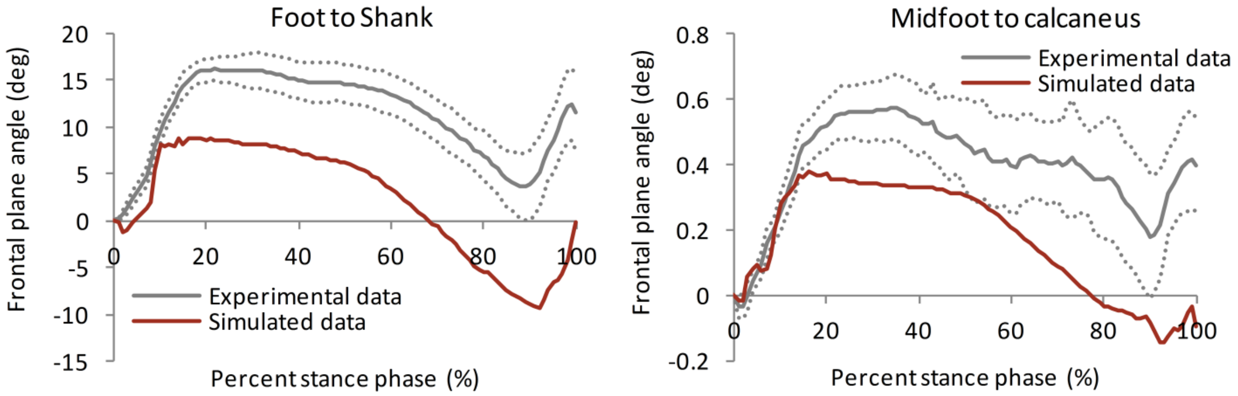

Figure B2: Experimental (mean: solid gray line, SD: dotted line) and simulated (solid red line) bone-to-ground and segment-to-segment angles in the diabetic subject. The first, second and fifth metatarsal to ground, calcaneus to ground, midfoot to ground and medial longitudinal arch are all sagittal plane angles, while second metatarsal to the first metatarsal and fifth metatarsal to the second metatarsal are transverse plane angles. The angles relative to ground are normalize to contact position and a positive change indicates the anterior part of the bone is rotating below the posterior part. Positive change for the medial longitudinal arch indicates plantar flexion of the first metatarsal relative to the calcaneus. Positive change for the second metatarsal to the first metatarsal and the fifth metatarsal to the second metatarsal indicates abduction of the second metatarsal relative to the first metatarsal and the fifth metatarsal relative to the second metatarsal, respectively. Positive change in the sagittal foot to shank and midfoot to calcaneus angles indicates dorsiflexion of the distal segment relative to the proximal segment. Likewise, positive change in the transverse plane angle indicates abduction of the distal segment relative to the proximal segment, and positive change in the frontal plane angle indicates eversion of the distal segment relative to the proximal segment.

Supplementary Section C: Bone-to-bone angle-time series from invasive *in vivo* experiment (Lundgren et al., 2008) (upper and lower bounds in dotted lines) and gait finite element simulations. The force plate and pressure platform results are represented by solid and dash lines, respectively. Results from the normal and diabetic subjects are shown in blue and red lines, respectively.

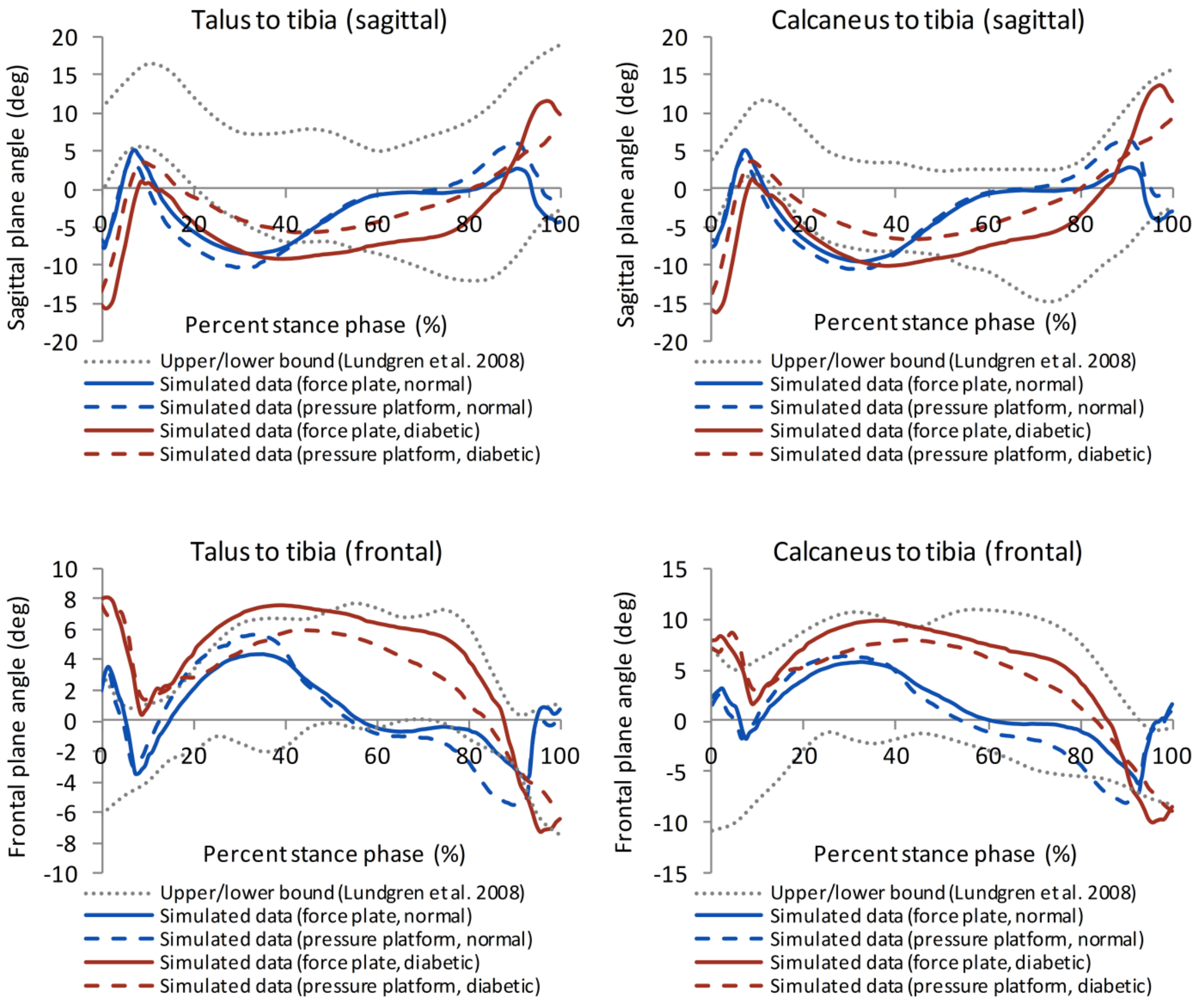

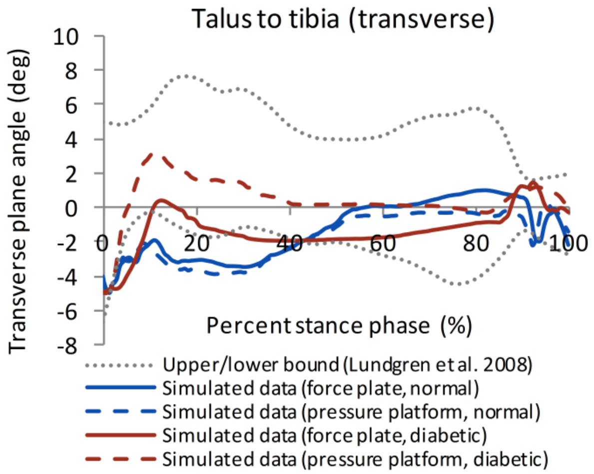
Talus to tibia (transverse)

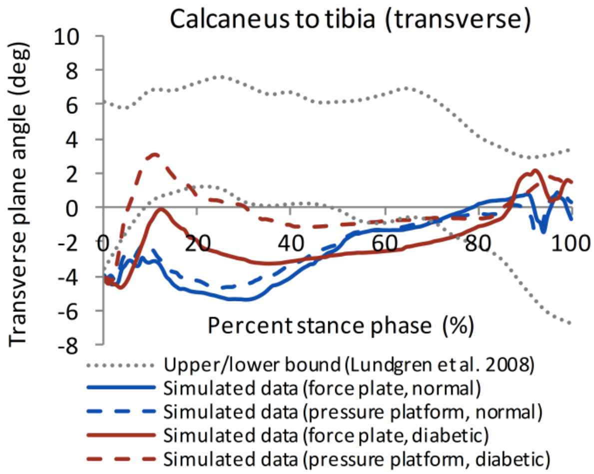
Calcaneus to tibia (transverse)

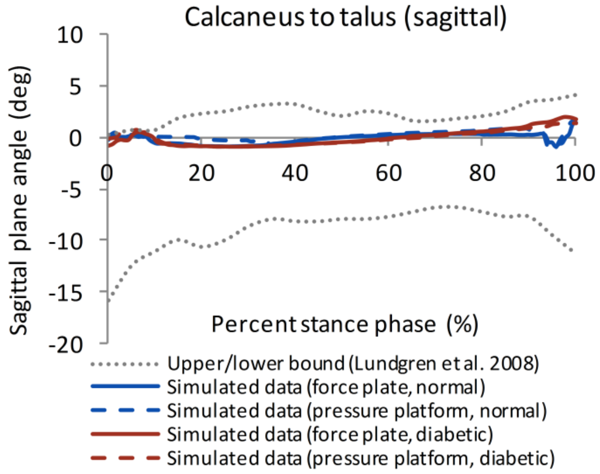
Calcaneus to talus (sagittal)

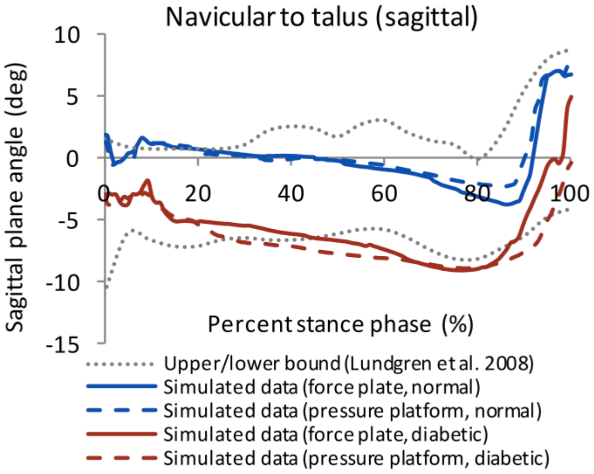
Navicular to talus (sagittal)

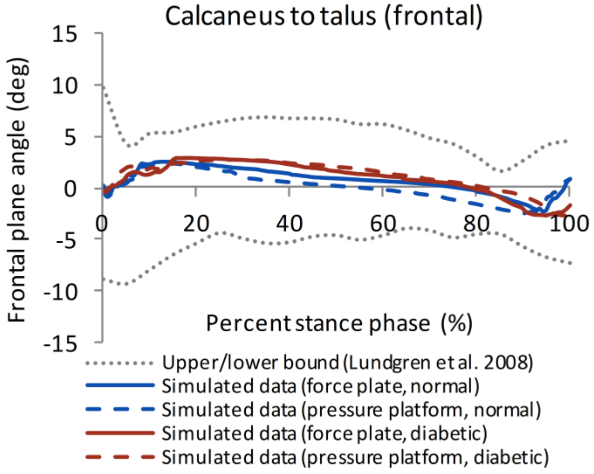
Calcaneus to talus (frontal)

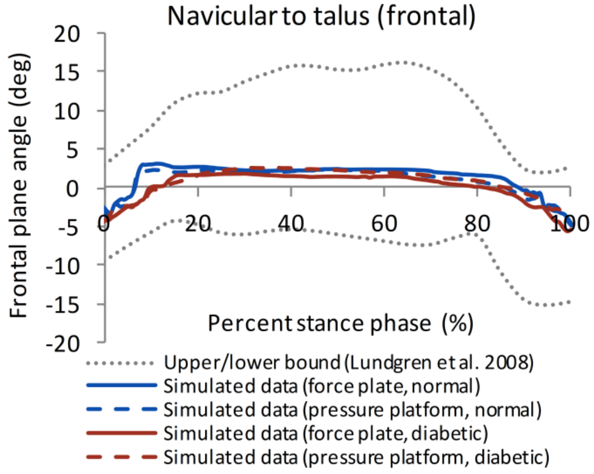
Navicular to talus (frontal)

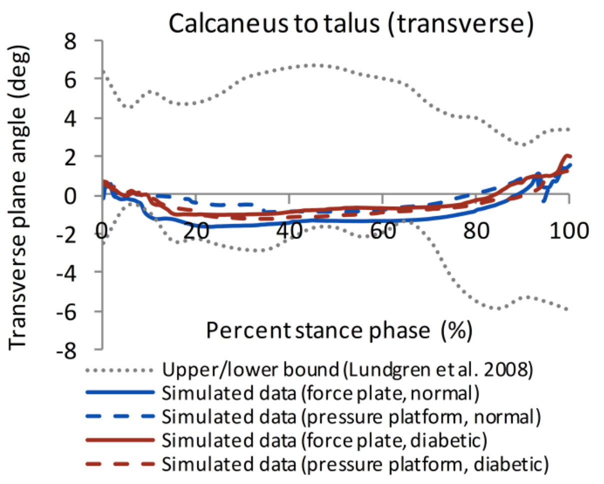
Calcaneus to talus (transverse)
Transverse plane angle (deg)
8
6
4
2
0
-2
-4
-6
-8
0
20
40
60
80
100
Percent stance phase (%)
Upper/lower bound (Lundgren et al. 2008)
Simulated data (force plate, normal)
Simulated data (pressure platform, normal)
Simulated data (force plate, diabetic)
Simulated data (pressure platform, diabetic)

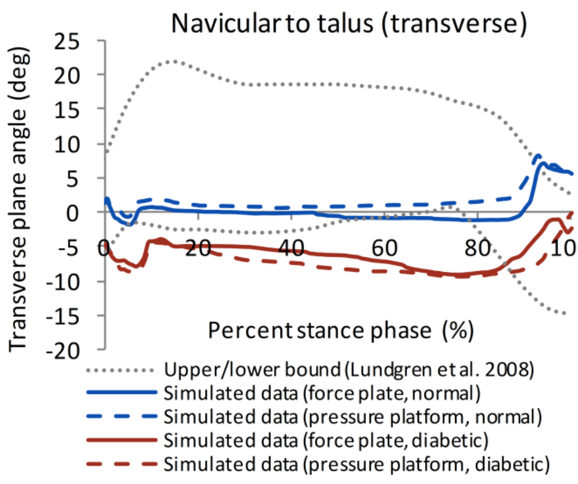
Navicular to talus (transverse)
Transverse plane angle (deg)
25
20
15
10
5
0
-5
-10
-15
-20
0
20
40
60
80
100
Percent stance phase (%)
Upper/lower bound (Lundgren et al. 2008)
Simulated data (force plate, normal)
Simulated data (pressure platform, normal)
Simulated data (force plate, diabetic)
Simulated data (pressure platform, diabetic)

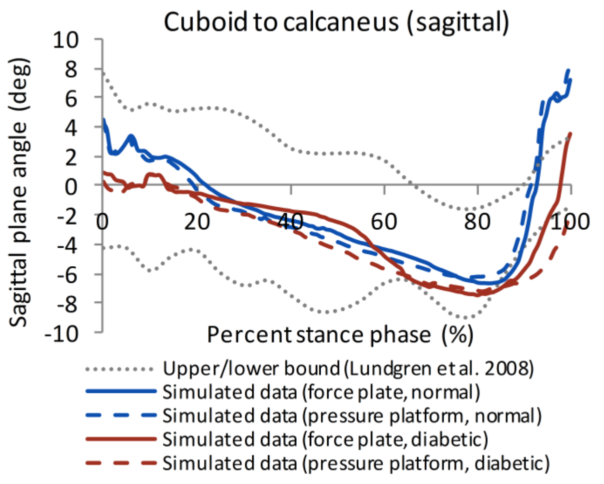
Cuboid to calcaneus (sagittal)
Sagittal plane angle (deg)
10
8
6
4
2
0
-2
-4
-6
-8
-10
0
20
40
60
80
100
Percent stance phase (%)
Upper/lower bound (Lundgren et al. 2008)
Simulated data (force plate, normal)
Simulated data (pressure platform, normal)
Simulated data (force plate, diabetic)
Simulated data (pressure platform, diabetic)

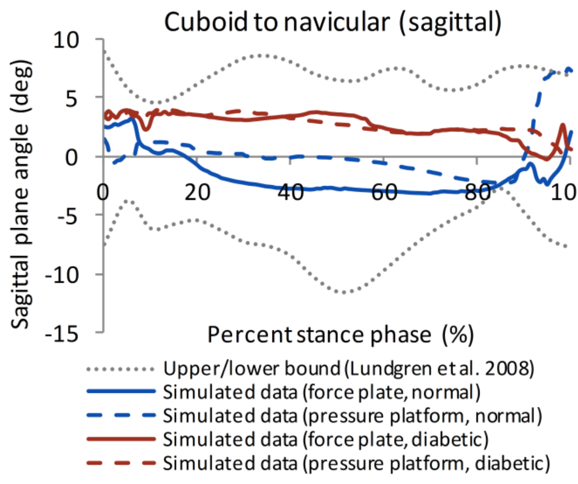
Cuboid to navicular (sagittal)
Sagittal plane angle (deg)
10
5
0
-5
-10
-15
0
20
40
60
80
100
Percent stance phase (%)
Upper/lower bound (Lundgren et al. 2008)
Simulated data (force plate, normal)
Simulated data (pressure platform, normal)
Simulated data (force plate, diabetic)
Simulated data (pressure platform, diabetic)

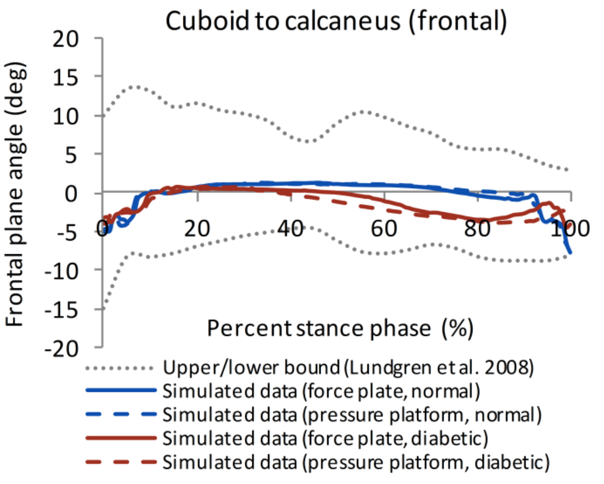
Cuboid to calcaneus (frontal)
Frontal plane angle (deg)
20
15
10
5
0
-5
-10
-15
-20
0
20
40
60
80
100
Percent stance phase (%)
Upper/lower bound (Lundgren et al. 2008)
Simulated data (force plate, normal)
Simulated data (pressure platform, normal)
Simulated data (force plate, diabetic)
Simulated data (pressure platform, diabetic)

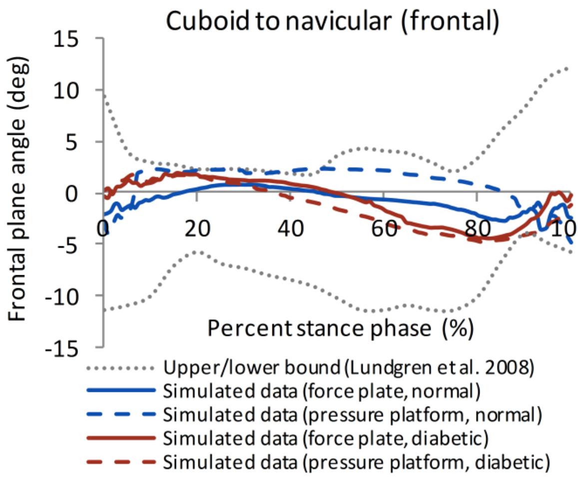
Cuboid to navicular (frontal)
Frontal plane angle (deg)
15
10
5
0
-5
-10
-15
0
20
40
60
80
100
Percent stance phase (%)
Upper/lower bound (Lundgren et al. 2008)
Simulated data (force plate, normal)
Simulated data (pressure platform, normal)
Simulated data (force plate, diabetic)
Simulated data (pressure platform, diabetic)

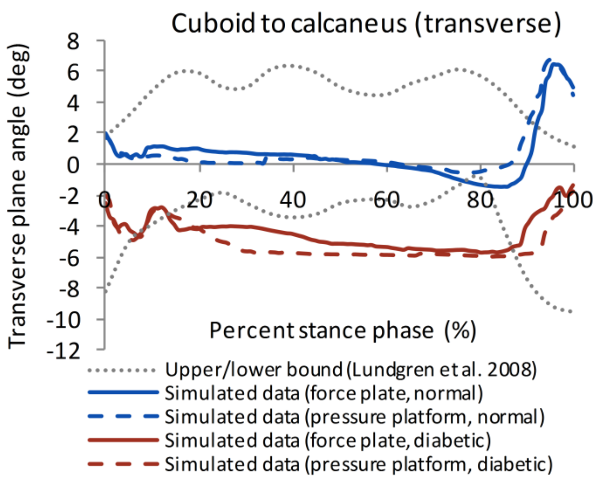
Cuboid to calcaneus (transverse)
Transverse plane angle (deg)
8
6
4
2
0
-2
-4
-6
-8
-10
-12
0
20
40
60
80
100
Percent stance phase (%)
Upper/lower bound (Lundgren et al. 2008)
Simulated data (force plate, normal)
Simulated data (pressure platform, normal)
Simulated data (force plate, diabetic)
Simulated data (pressure platform, diabetic)

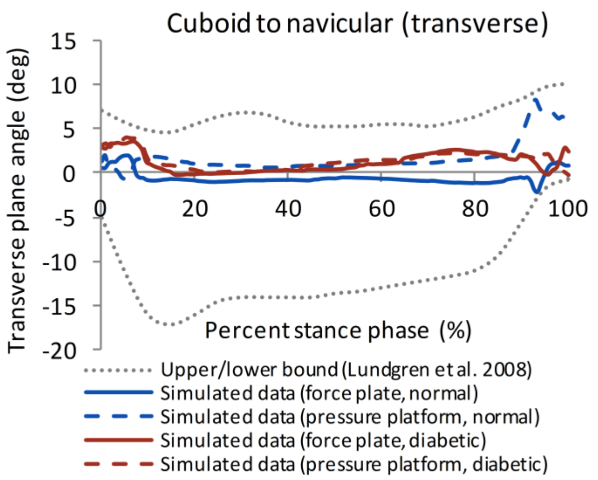
Cuboid to navicular (transverse)
Transverse plane angle (deg)
15
10
5
0
-5
-10
-15
-20
0
20
40
60
80
100
Percent stance phase (%)
Upper/lower bound (Lundgren et al. 2008)
Simulated data (force plate, normal)
Simulated data (pressure platform, normal)
Simulated data (force plate, diabetic)
Simulated data (pressure platform, diabetic)

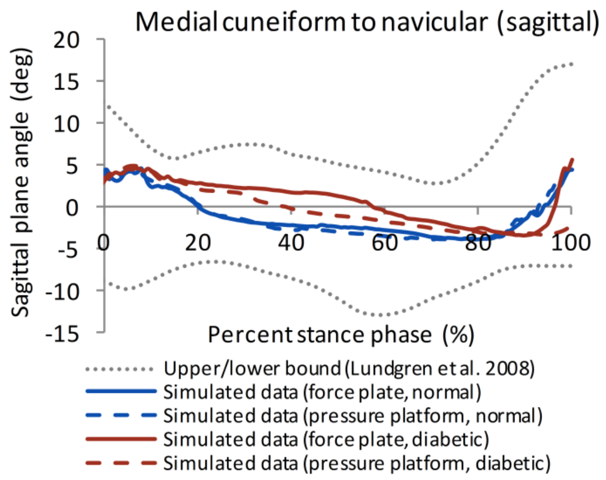
Medial cuneiform to navicular (sagittal)
Sagittal plane angle (deg)
20
15
10
5
0
-5
-10
-15
0
20
40
60
80
100
Percent stance phase (%)
Upper/lower bound (Lundgren et al. 2008)
Simulated data (force plate, normal)
Simulated data (pressure platform, normal)
Simulated data (force plate, diabetic)
Simulated data (pressure platform, diabetic)

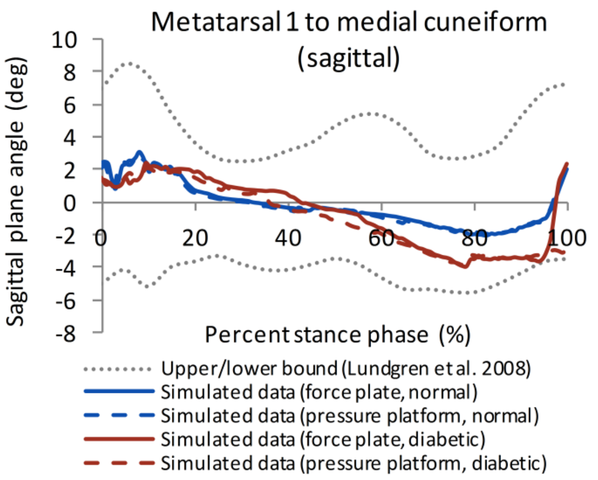
Metatarsal 1 to medial cuneiform (sagittal)
Sagittal plane angle (deg)
10
8
6
4
2
0
-2
-4
-6
-8
0
20
40
60
80
100
Percent stance phase (%)
Upper/lower bound (Lundgren et al. 2008)
Simulated data (force plate, normal)
Simulated data (pressure platform, normal)
Simulated data (force plate, diabetic)
Simulated data (pressure platform, diabetic)

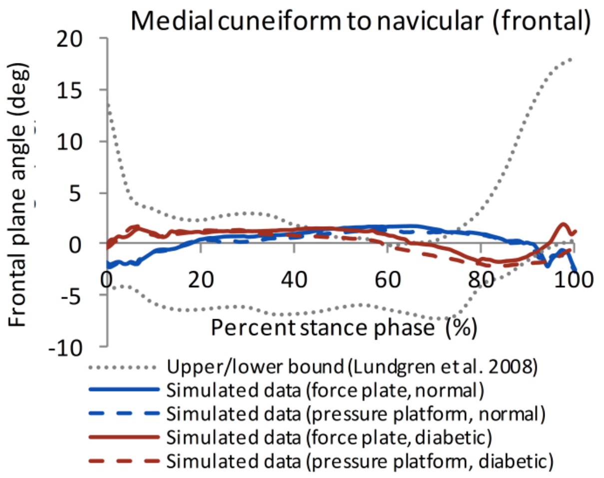
Medial cuneiform to navicular (frontal)
Frontal plane angle (deg)
20
15
10
5
0
-5
-10
0
20
40
60
80
100
Percent stance phase (%)
Upper/lower bound (Lundgren et al. 2008)
Simulated data (force plate, normal)
Simulated data (pressure platform, normal)
Simulated data (force plate, diabetic)
Simulated data (pressure platform, diabetic)

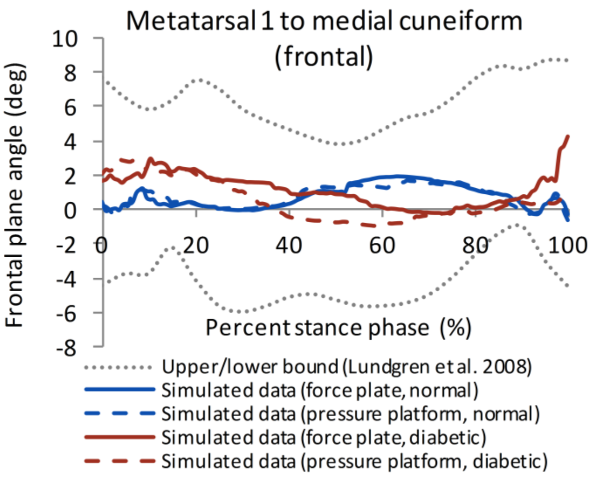
Metatarsal 1 to medial cuneiform (frontal)
Frontal plane angle (deg)
10
8
6
4
2
0
-2
-4
-6
-8
0
20
40
60
80
100
Percent stance phase (%)
Upper/lower bound (Lundgren et al. 2008)
Simulated data (force plate, normal)
Simulated data (pressure platform, normal)
Simulated data (force plate, diabetic)
Simulated data (pressure platform, diabetic)

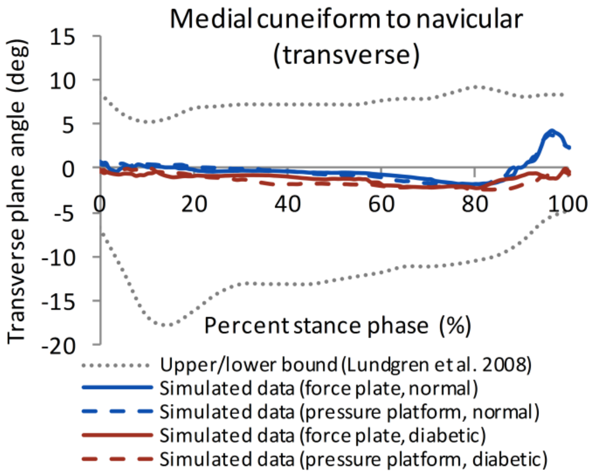
Medial cuneiform to navicular (transverse)
Transverse plane angle (deg)
15
10
5
0
-5
-10
-15
-20
0
20
40
60
80
100
Percent stance phase (%)
Upper/lower bound (Lundgren et al. 2008)
Simulated data (force plate, normal)
Simulated data (pressure platform, normal)
Simulated data (force plate, diabetic)
Simulated data (pressure platform, diabetic)

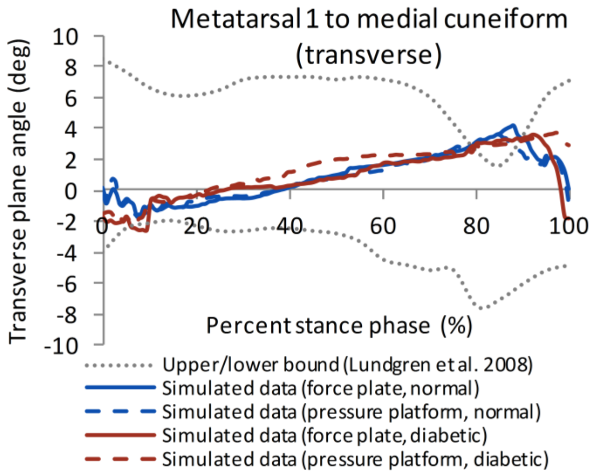
Metatarsal 1 to medial cuneiform (transverse)
Transverse plane angle (deg)
10
8
6
4
2
0
-2
-4
-6
-8
-10
0
20
40
60
80
100
Percent stance phase (%)
Upper/lower bound (Lundgren et al. 2008)
Simulated data (force plate, normal)
Simulated data (pressure platform, normal)
Simulated data (force plate, diabetic)
Simulated data (pressure platform, diabetic)

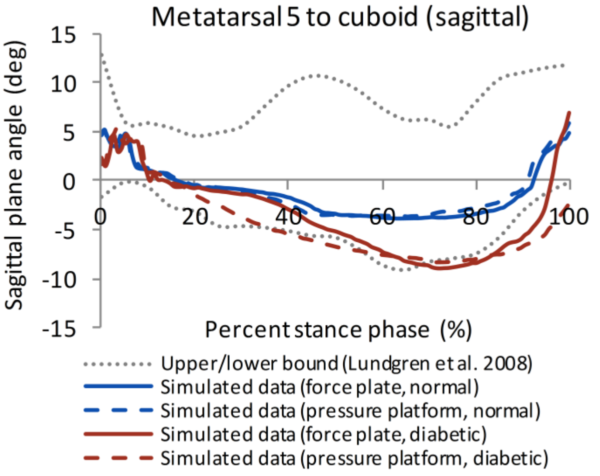
Metatarsal 5 to cuboid (sagittal)
Sagittal plane angle (deg)
15
10
5
0
-5
-10
-15
0
20
40
60
80
100
Percent stance phase (%)
Upper/lower bound (Lundgren et al. 2008)
Simulated data (force plate, normal)
Simulated data (pressure platform, normal)
Simulated data (force plate, diabetic)
Simulated data (pressure platform, diabetic)

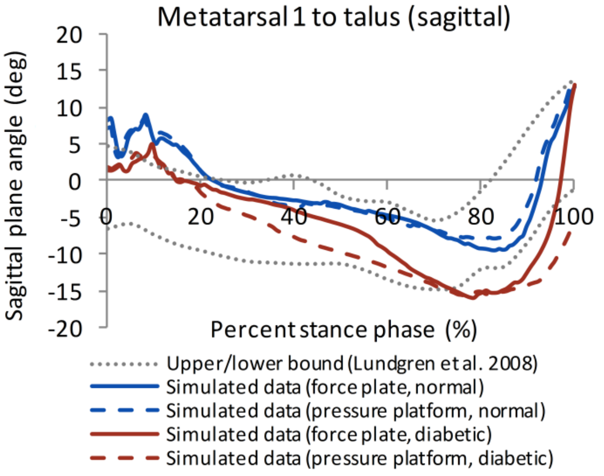
Metatarsal 1 to talus (sagittal)
Sagittal plane angle (deg)
20
15
10
5
0
-5
-10
-15
-20
0
20
40
60
80
100
Percent stance phase (%)
Upper/lower bound (Lundgren et al. 2008)
Simulated data (force plate, normal)
Simulated data (pressure platform, normal)
Simulated data (force plate, diabetic)
Simulated data (pressure platform, diabetic)

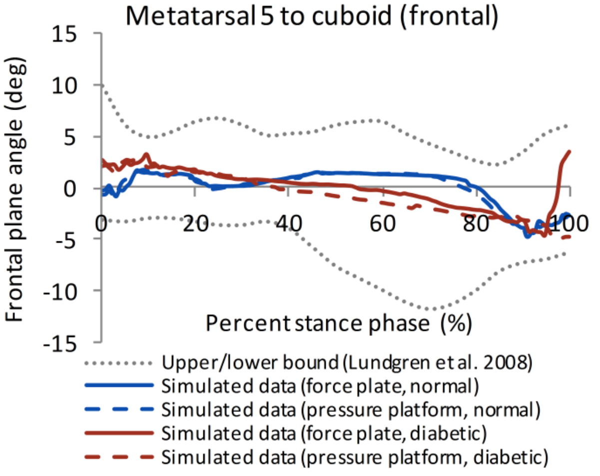
Metatarsal 5 to cuboid (frontal)
Frontal plane angle (deg)
15
10
5
0
-5
-10
-15
0
20
40
60
80
100
Percent stance phase (%)
Upper/lower bound (Lundgren et al. 2008)
Simulated data (force plate, normal)
Simulated data (pressure platform, normal)
Simulated data (force plate, diabetic)
Simulated data (pressure platform, diabetic)

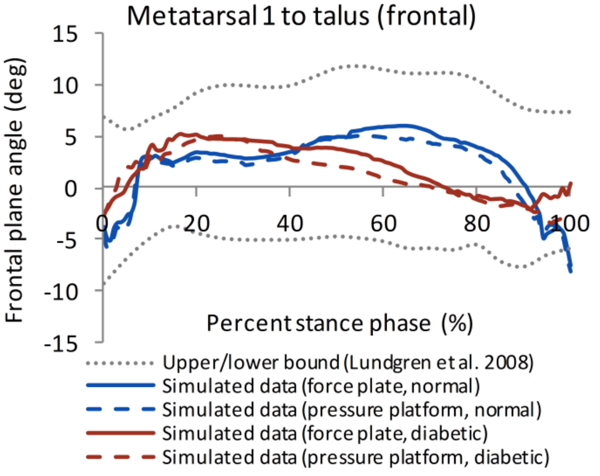
Metatarsal 1 to talus (frontal)
Frontal plane angle (deg)
15
10
5
0
-5
-10
-15
0
20
40
60
80
100
Percent stance phase (%)
Upper/lower bound (Lundgren et al. 2008)
Simulated data (force plate, normal)
Simulated data (pressure platform, normal)
Simulated data (force plate, diabetic)
Simulated data (pressure platform, diabetic)

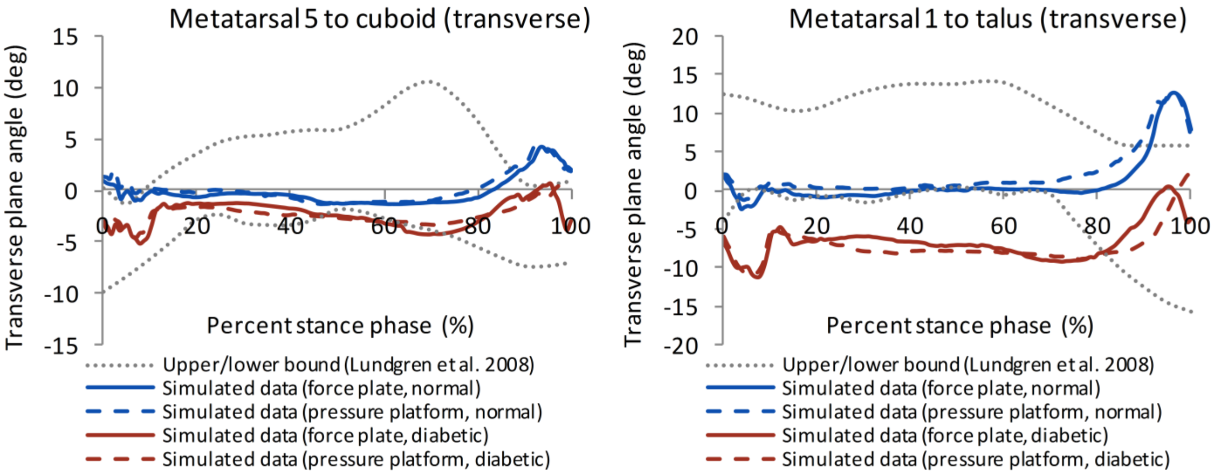

Figure C1: Bone-to-bone angle-time series from invasive *in vivo* experiment (Lundgren et al., 2008) (upper and lower bounds in dotted lines) and gait finite element simulations. The force plate and pressure platform results are represented by solid and dash lines, respectively. Results from the normal and diabetic subjects are shown in blue and red lines, respectively. Bone angles were defined as distal bone relative to the proximal bone. Zero degree angle was the position of the joint in the quiet stance trial. Positive change in the sagittal, transverse and frontal plane angle indicates plantarflexion, adduction and eversion of the distal bone relative to the proximal bone, respectively.

Supplementary Section D: Summary of root mean square (RMS) differences between the dynamic gait finite element simulations and the experimental/literature data.

Table D1: Summary of root mean square (RMS) differences between the dynamic gait finite element simulations and the experimental/literature data.

	Normal foot model		**Diabetic foot model**	
***In vivo* experimental vs. simulated data**	**Force plate**	**Pressure platform**	**Force plate**	**Pressure platform**
Ground reaction force				
RMS error vertical GRF (N)	138.6	147.7	135.5	113.8
RMS error AP GRF (N)	100.7	n/a	77.6	n/a
RMS error ML GRF (N)	59.1	n/a	28.2	n/a
First peak of vertical GRF error (%)	2.6	0.8	1.4	0.8
First peak time error (%)	7.2	0.2	16.4	19.1
Minimum vertical GRF error (%)	3.7	5.0	0.9	2.4
Minimum time error (%)	2.9	10.6	3.1	11.0
Second peak of vertical GRF error (%)	3.5	3.4	1.4	0.5
Second peak time error (%)	6.1	3.4	7.8	0.3
Plantar measurement				
<u>Peak pressure</u>				
RMS error total peak pressure (kPa)	n/a	412.2	n/a	289.5
RMS error hindfoot peak pressure (kPa ; medial, lateral)	n/a	74.7, 77.8	n/a	172.8, 141.3
RMS error midfoot peak pressure (kPa)	n/a	138.3	n/a	41.6
RMS error forefoot peak pressure (kPa; mh1,2,3,4,5)	n/a	50.0, 57.0, 283.2, 240.5, 100.2	n/a	55.3, 146.6, 116.0, 245.8, 155.1
RMS error toes peak pressure (kPa; hallux, toe2, toe3-5)	n/a	128.2, 316.5, 304.8	n/a	206.9, 237.9, 377.3
<u>Mean pressure</u>				
RMS error hindfoot mean pressure (kPa; medial, lateral)	n/a	49.7, 42.1	n/a	59.0, 40.0
RMS error midfoot mean pressure (kPa)	n/a	33.5	n/a	16.8
RMS error forefoot mean pressure (kPa; mh1,2,3,4,5)	n/a	26.3, 51.4, 64.7, 86.6, 55.1	n/a	34.4, 67.0, 41.1, 85.8, 59.8
RMS error toes mean pressure (kPa; hallux, toe2, toe3-5)	n/a	36.2, 97.7, 68.3	n/a	38.7, 71.6, 87.1
Force				
RMS error hindfoot force (N; medial, lateral)	n/a	93.0, 72.8	n/a	52.7, 41.2
RMS error midfoot force (N)	n/a	60.9	n/a	29.8
RMS error forefoot force (N; mh1,2,3,4,5)	n/a	49.6, 68.1, 44.5, 69.6, 12.3	n/a	50.2, 69.0, 17.5, 45.3, 15.8
RMS error toes force (N; hallux, toe2, toe3-5)	n/a	35.6, 36.0, 70.6	n/a	50.1, 27.0, 58.5
<u>Contact area</u>				
RMS error total contact area (cm^2)	n/a	10.3	n/a	8.8
RMS error hindfoot contact area (cm^2; medial, lateral)	n/a	1.6, 1.0	n/a	1.3, 1.1
RMS error midfoot contact area (cm^2)	n/a	2.7	n/a	3.2
RMS error forefoot contact area (cm^2; mh1,2,3,4,5)	n/a	3.3, 2.7, 1.6, 0.9, 1.3	n/a	3.3, 2.8, 2.2, 1.4, 1.5
RMS error toes contact area (cm^2; hallux, toe2, toe3-5)	n/a	1.7, 1.3, 2.8	n/a	2.4, 1.2, 1.6
Bone kinematics				
RMS error calcaneus-midfoot angle (deg; sagittal, frontal, transverse)	3.4, 0.1, 28.5	n/a	7.3, 0.3, 24.6	n/a
RMS error shank-foot angle (deg; sagittal, frontal, transverse)	2.8, 5.3, 3.0	n/a	9.9, 9.7, 4.5	n/a
RMS error medial longitudinal arch angle (deg)	5.7	n/a	8.2	n/a
RMS error metatarsal1-hallux sagittal angle (deg)	13.8	n/a	15.8	n/a
RMS error metatarsal1-hallux transverse angle (deg)	11.5	n/a	5.3	n/a
RMS error metatarsal1-ground sagittal angle (deg)	3.3	n/a	4.6	n/a
RMS error metatarsal2-ground sagittal angle (deg)	1.4	n/a	6.0	n/a

Table D1: (Cont'd) Summary of RMS differences between the dynamic gait finite element simulations and the experimental/literature data

	Normal foot model		**Diabetic foot model**	
***In vivo* experimental vs. simulated data**	**Force plate**	**Pressure platform**	**Force plate**	**Pressure platform**
Bone kinematics (Cont'd)				
RMS error midfoot-ground sagittal angle (deg)	2.5	n/a	7.0	n/a
RMS error metatarsal1-2 angle (deg)	1.2	n/a	0.5	n/a
RMS metatarsal2-5 angle (deg)	8.1	n/a	5.3	n/a
Literature vs. simulated data				
RMS error Achilles tendon force (BW)[a]	0.5	0.6	0.6	0.6
RMS error plantar aponeurosis force (BW)[a]	0.4	0.4	0.6	0.6
RMS error ankle joint force (BW)[b]	1.5	1.4	1.2	1.1

[a] Achilles tendon force and plantar aponeurosis force were from Erdemir et al. (Erdemir et al., 2004).

[b] Ankle joint force was from Sanford et al. (Sanford et al., 2014).

Supplementary Section E: Contour plots (frontal plane cross-section) of the internal von Mises and hydrostatic stresses from the normal and diabetic foot simulations under quiet stance and gait conditions. The cross-sectional plane for each region of interest (Figure 7.12) was defined by the anteroposterior axis and the lowest node of the each bony prominence (Figure E1). Note that only bones and plantar fat were shown.

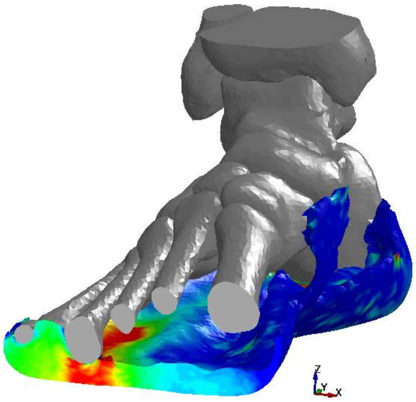

Figure E1: Example of a cross-sectional plane at the fourth metatarsal head region.

1) Quiet stance

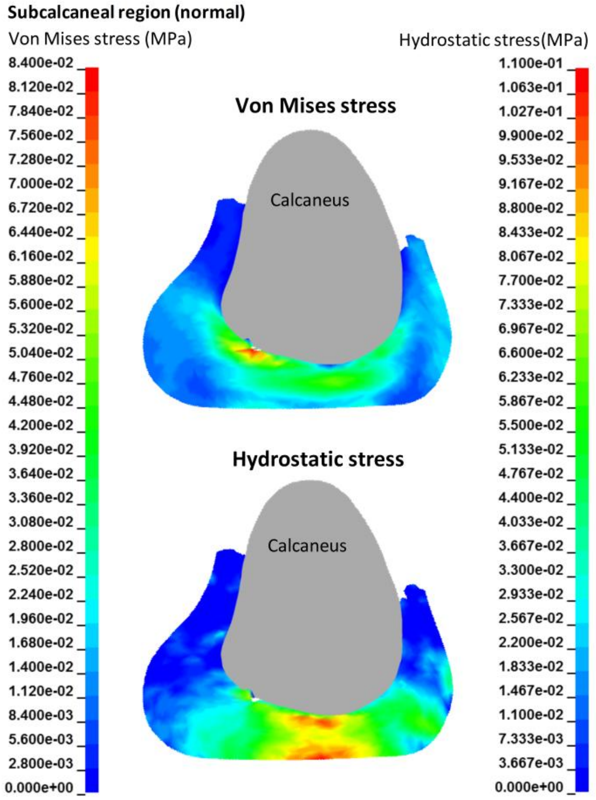

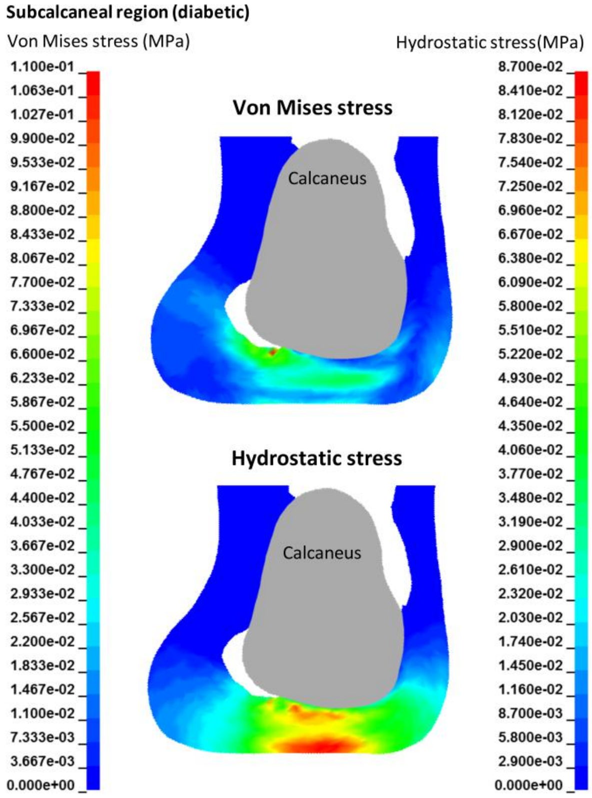

Fifth metatarsal base region (normal)

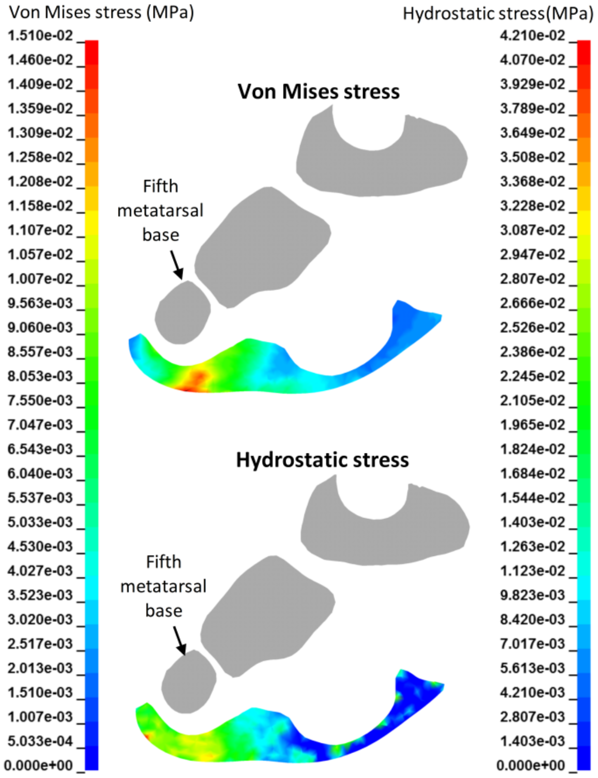

Fifth metatarsal base region (diabetic)

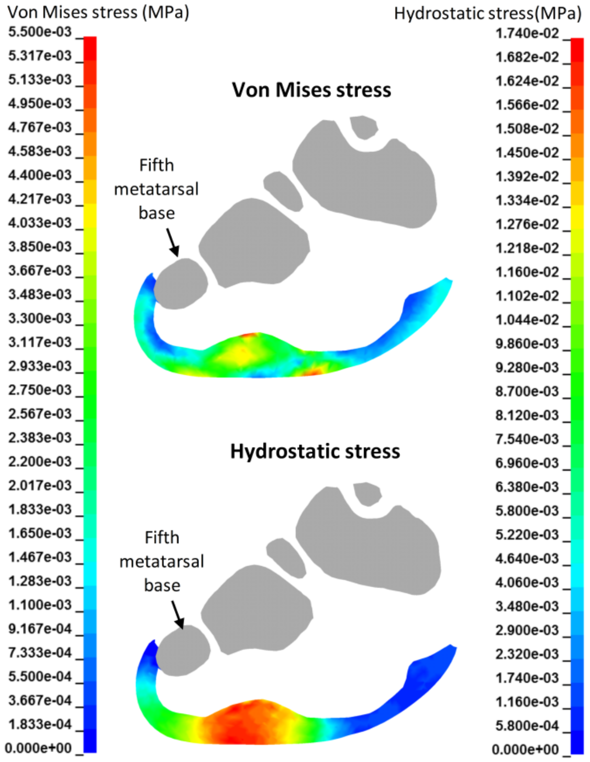

First metatarsal head region (normal)

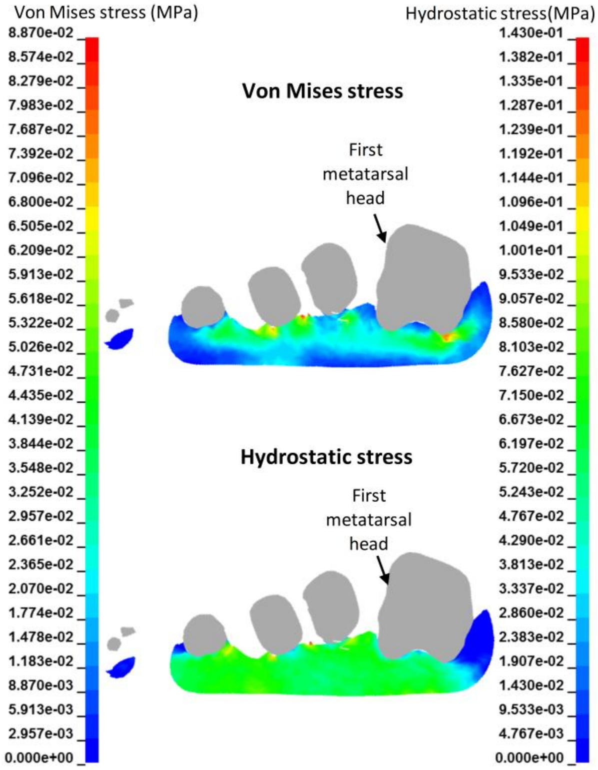

First metatarsal head region (diabetic)

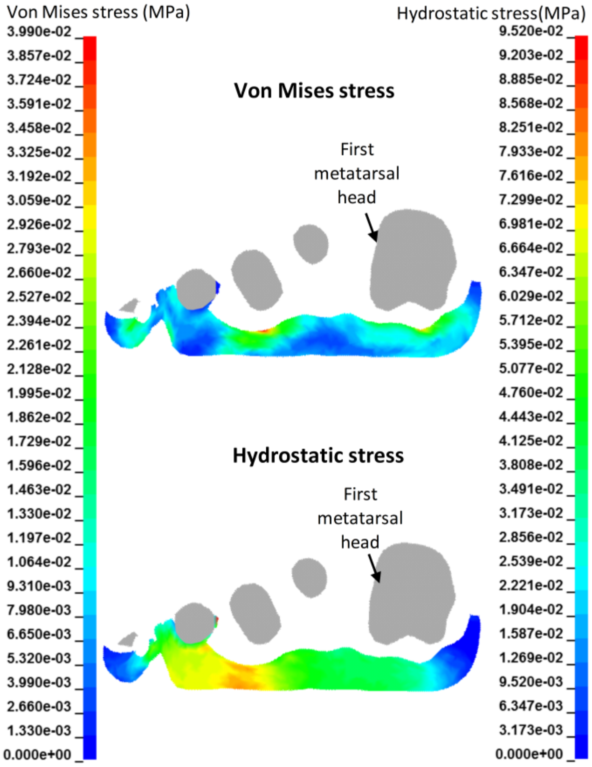

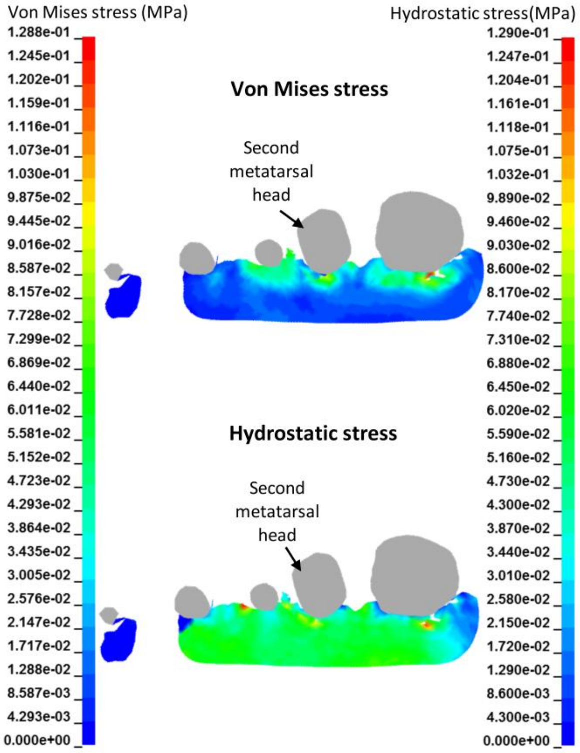

Second metatarsal head region (normal)

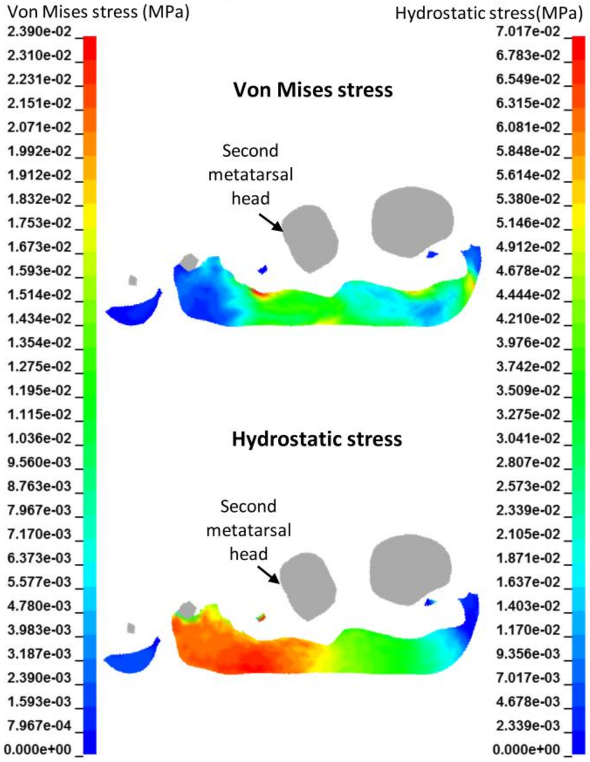

Second metatarsal head region (diabetic)

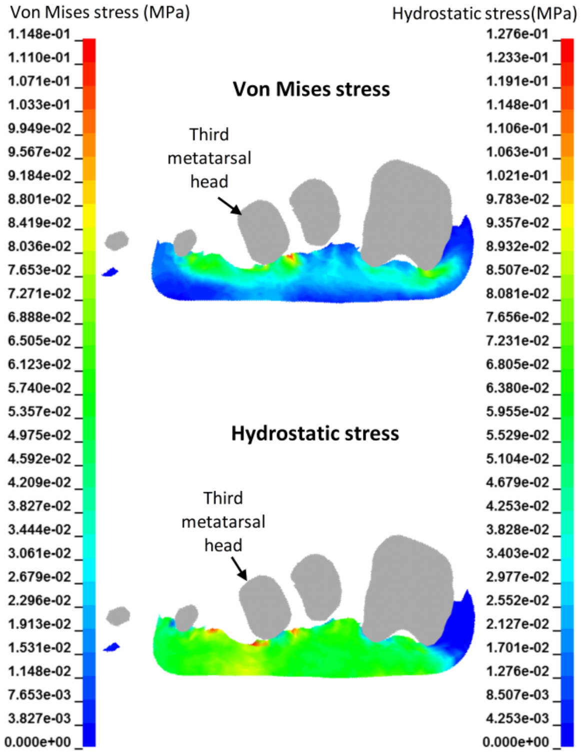

Third metatarsal head region (normal)

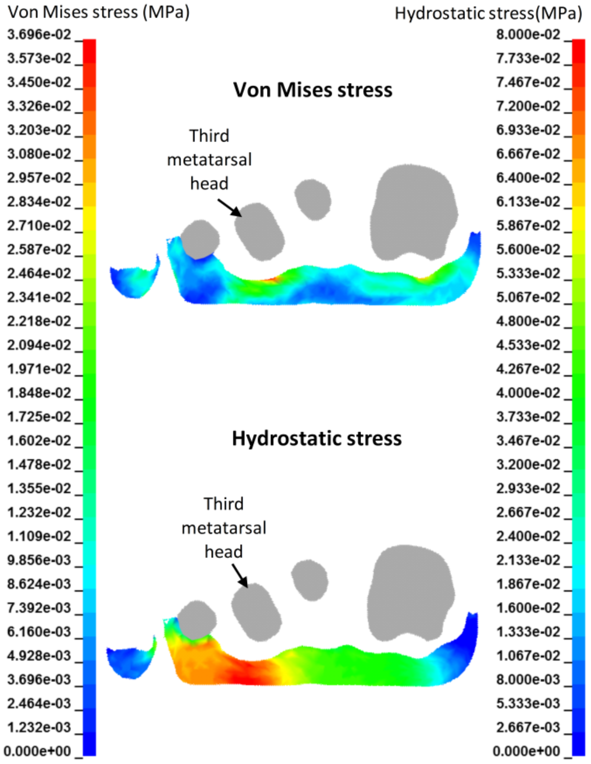

Third metatarsal head region (diabetic)

Fourth metatarsal head region (normal)

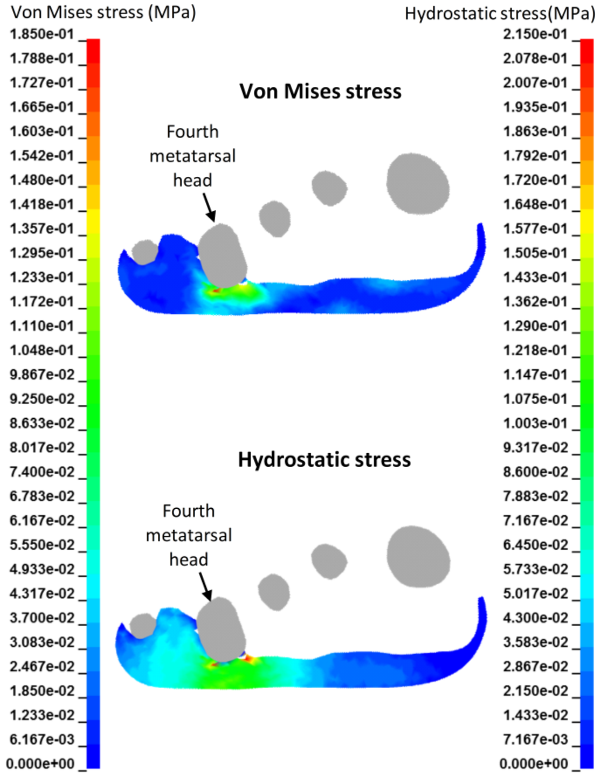

Fourth metatarsal head region (diabetic)

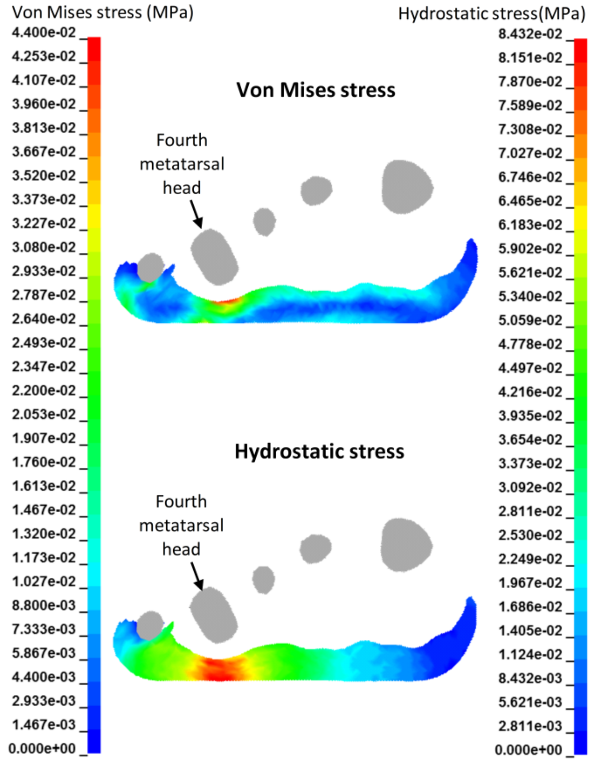

Fifth metatarsal head region (normal)

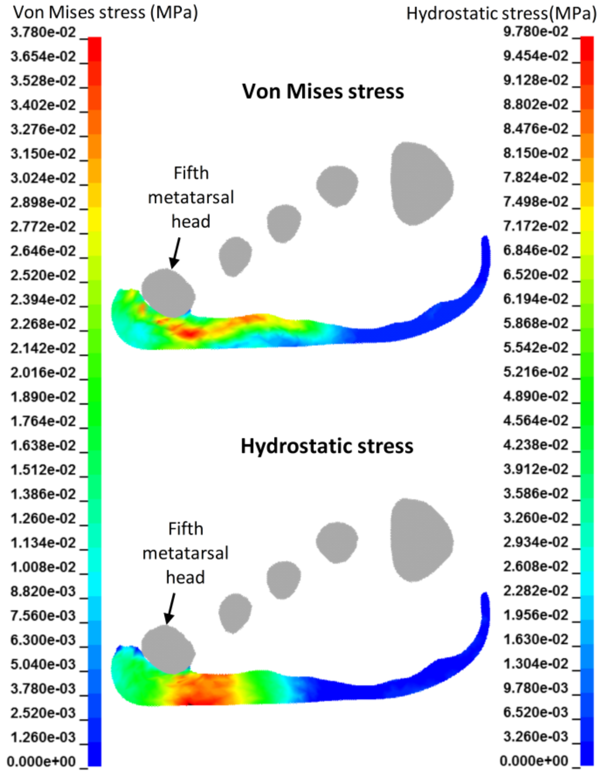

Fifth metatarsal head region (diabetic)

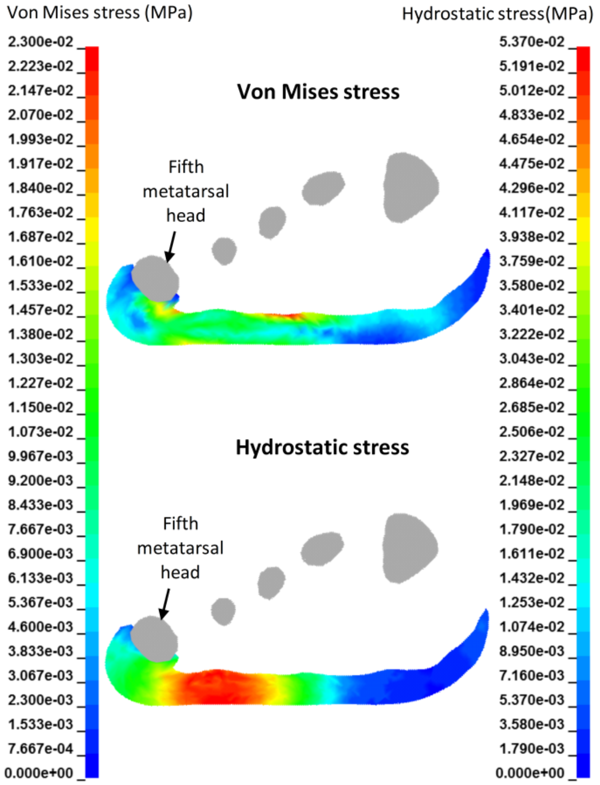

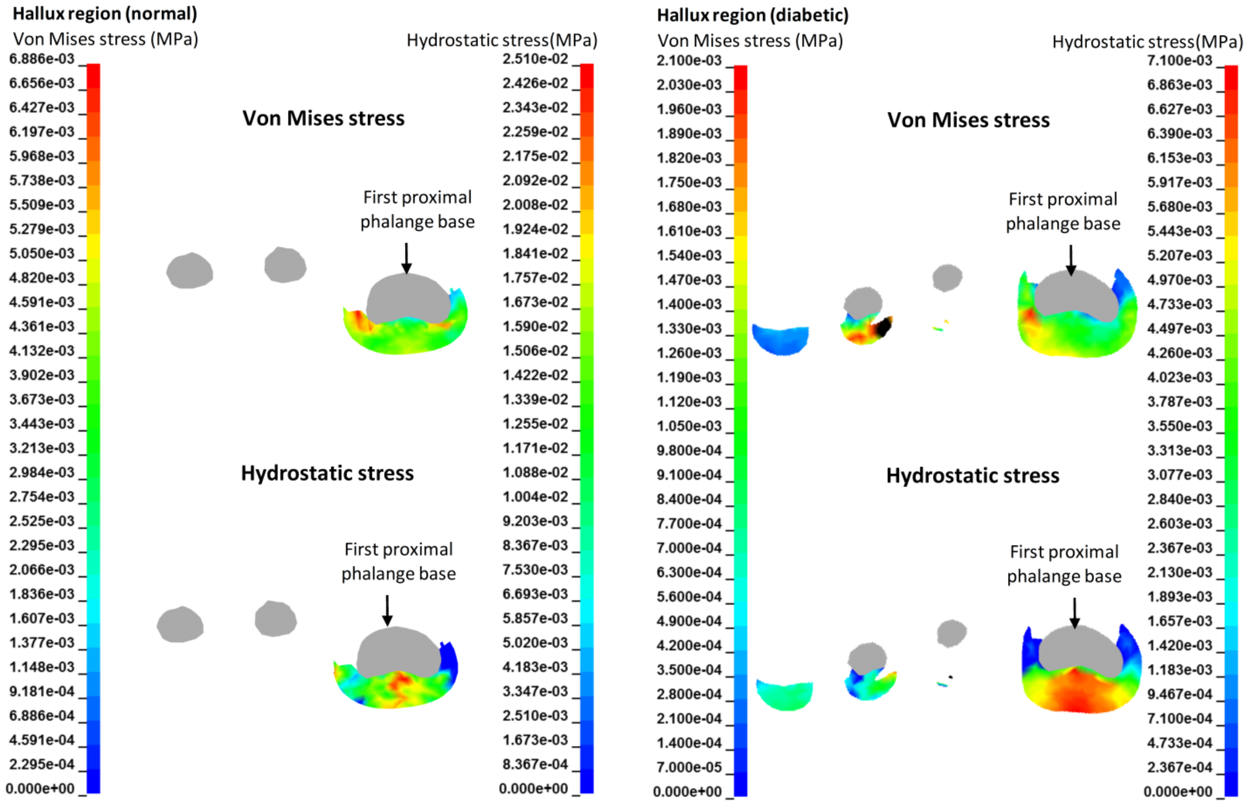

Figure E2: Contour plot of the internal von Mises and hydrostatic stresses in the frontal cross-sectional plane at eight regions of interest from quiet stance simulations.

2) Stance phase of gait

The contour plot at each region of interest was evaluated at the time of peak von Mises and hydrostatic stresses during gait. The cross-sectional cut plane was parallel to the frontal plane and located at the lowest point on each bony prominence.

2.1) Gait on force plate condition

Subcalcaneal region (normal)

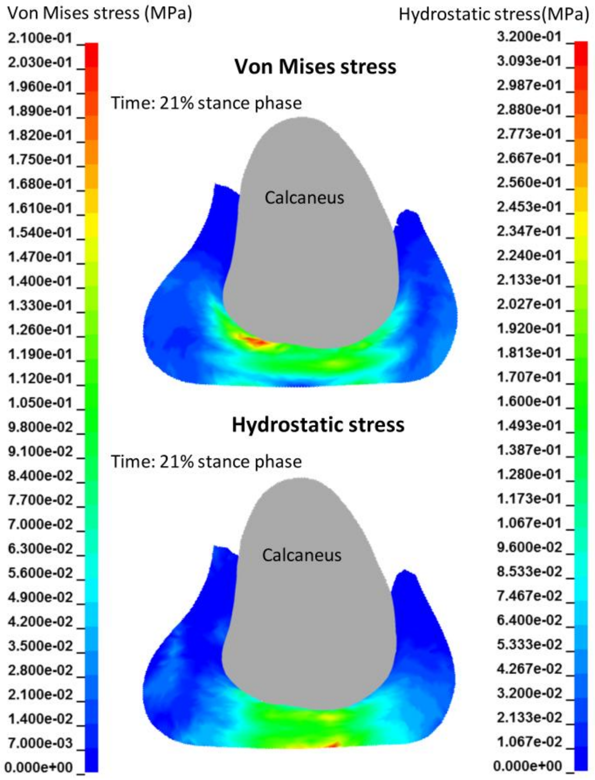

Subcalcaneal region (diabetic)

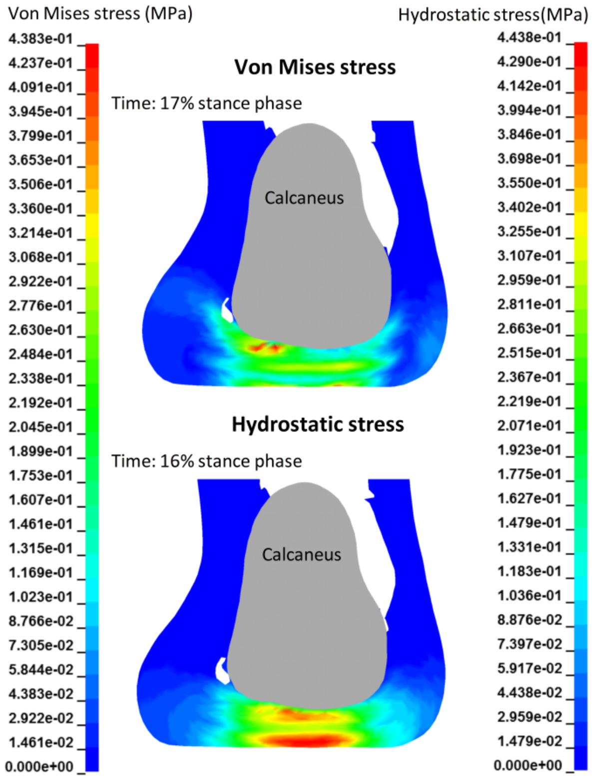

Fifth metatarsal base region (normal)

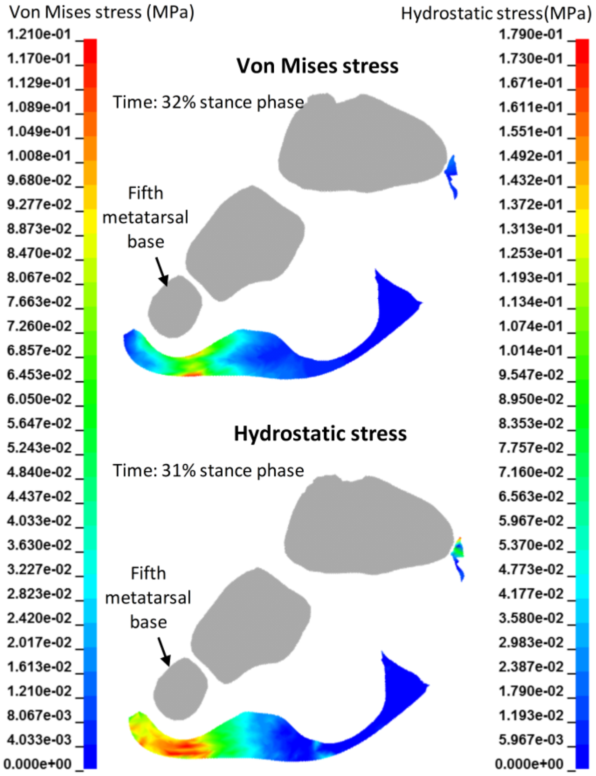

Fifth metatarsal base region (diabetic)

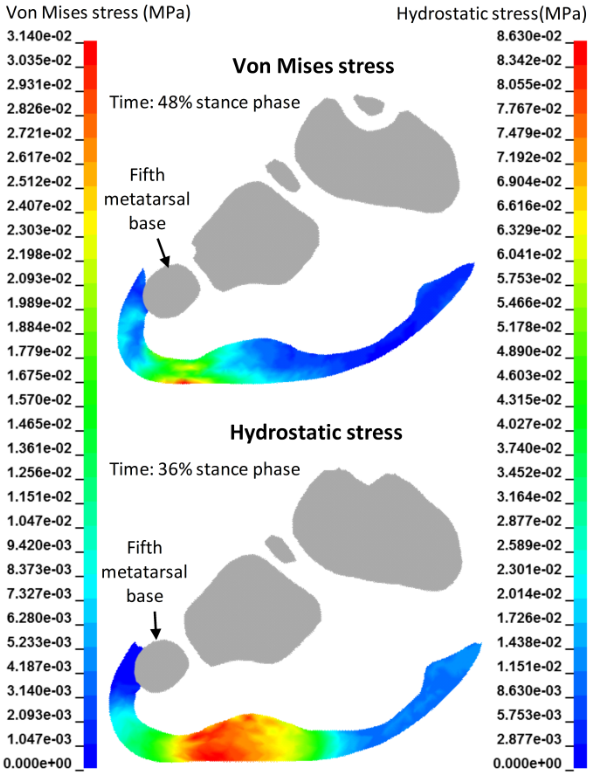

First metatarsal head region (normal)

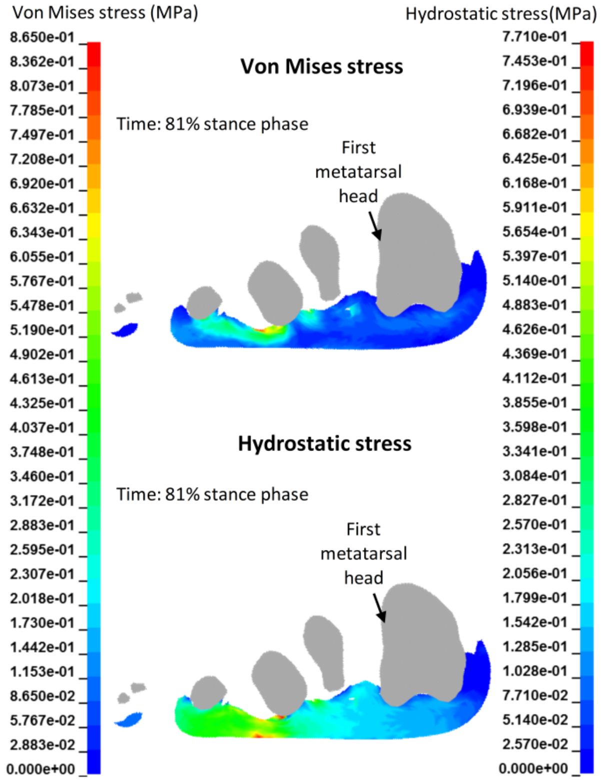

First metatarsal head region (diabetic)

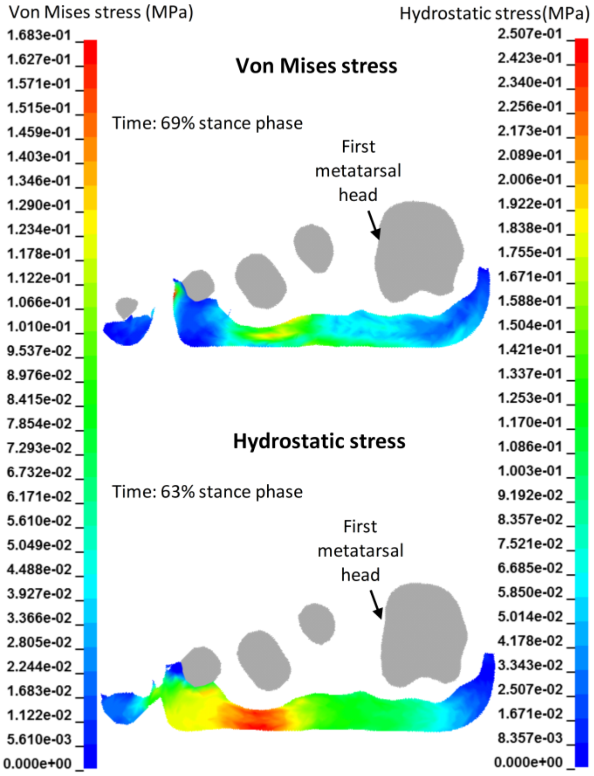

Second metatarsal head region (normal)

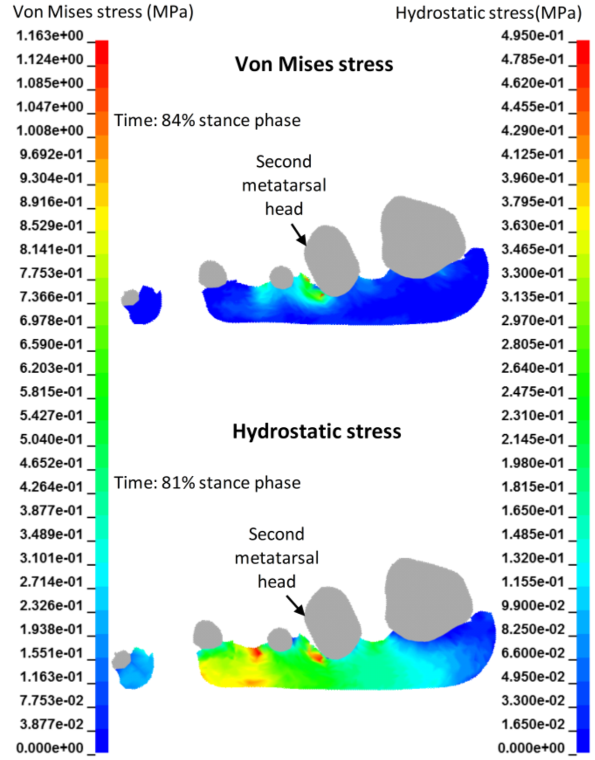

Second metatarsal head region (diabetic)

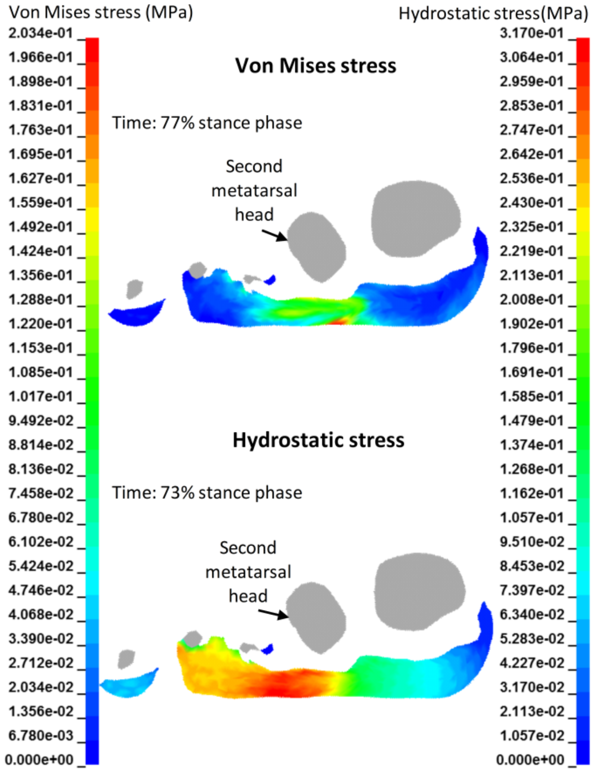

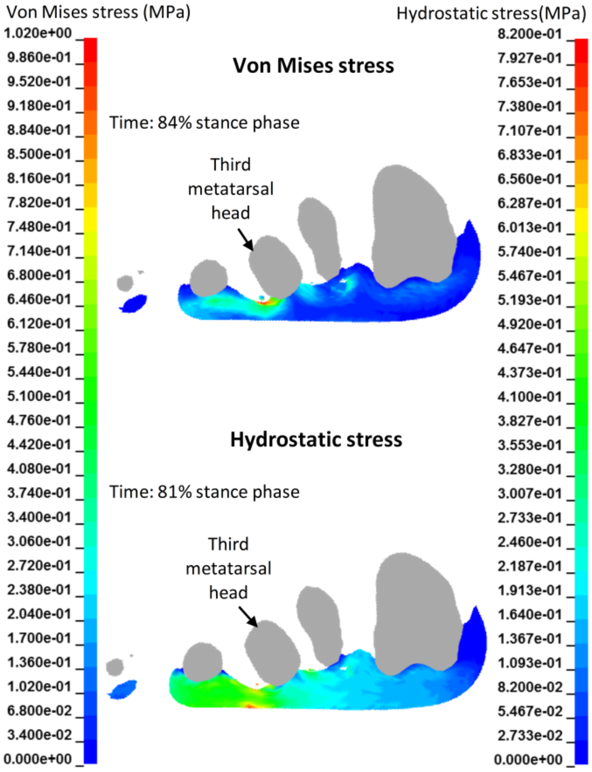

Third metatarsal head region (normal)

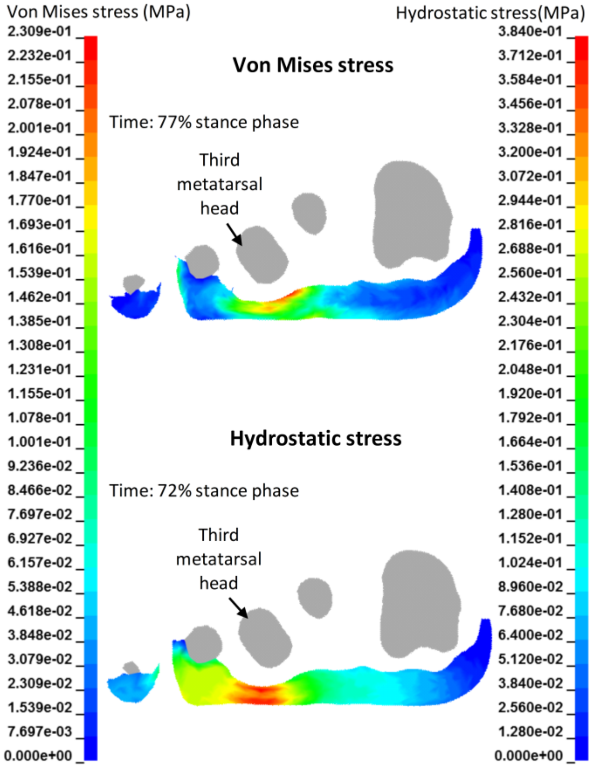

Third metatarsal head region (diabetic)

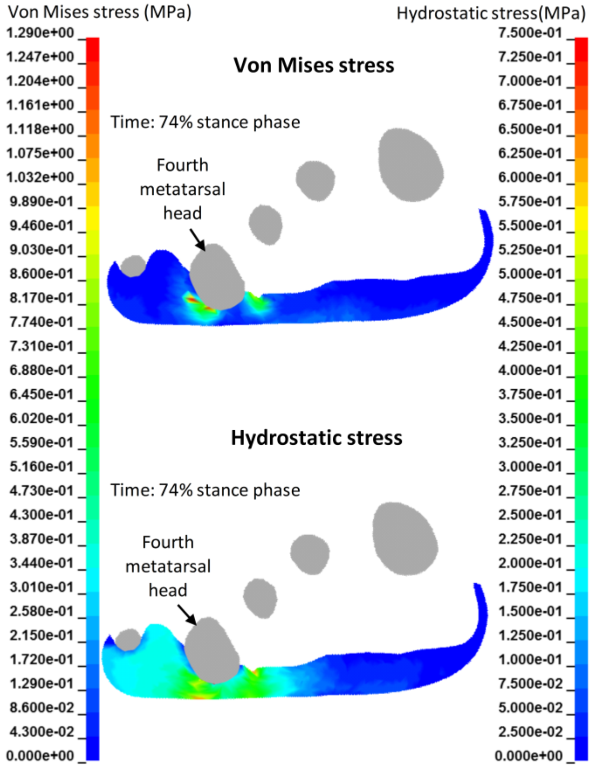

Fourth metatarsal head region (normal)

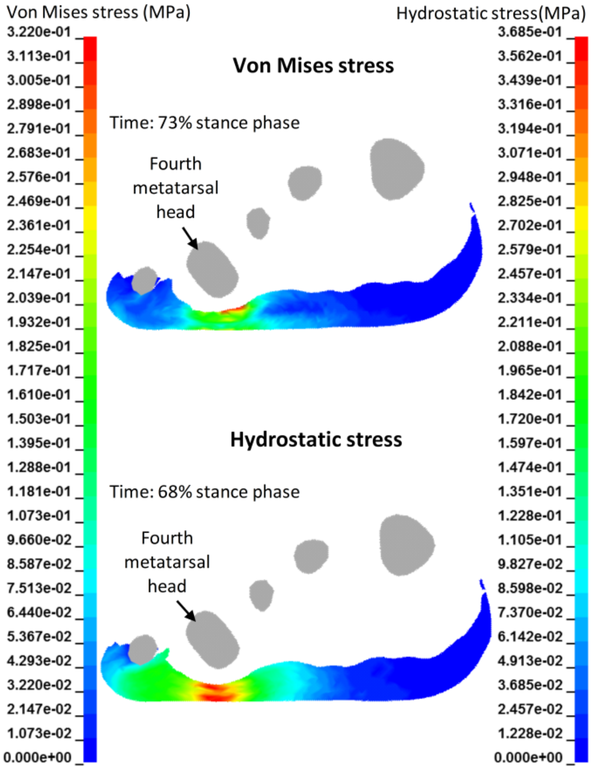

Fourth metatarsal head region (diabetic)

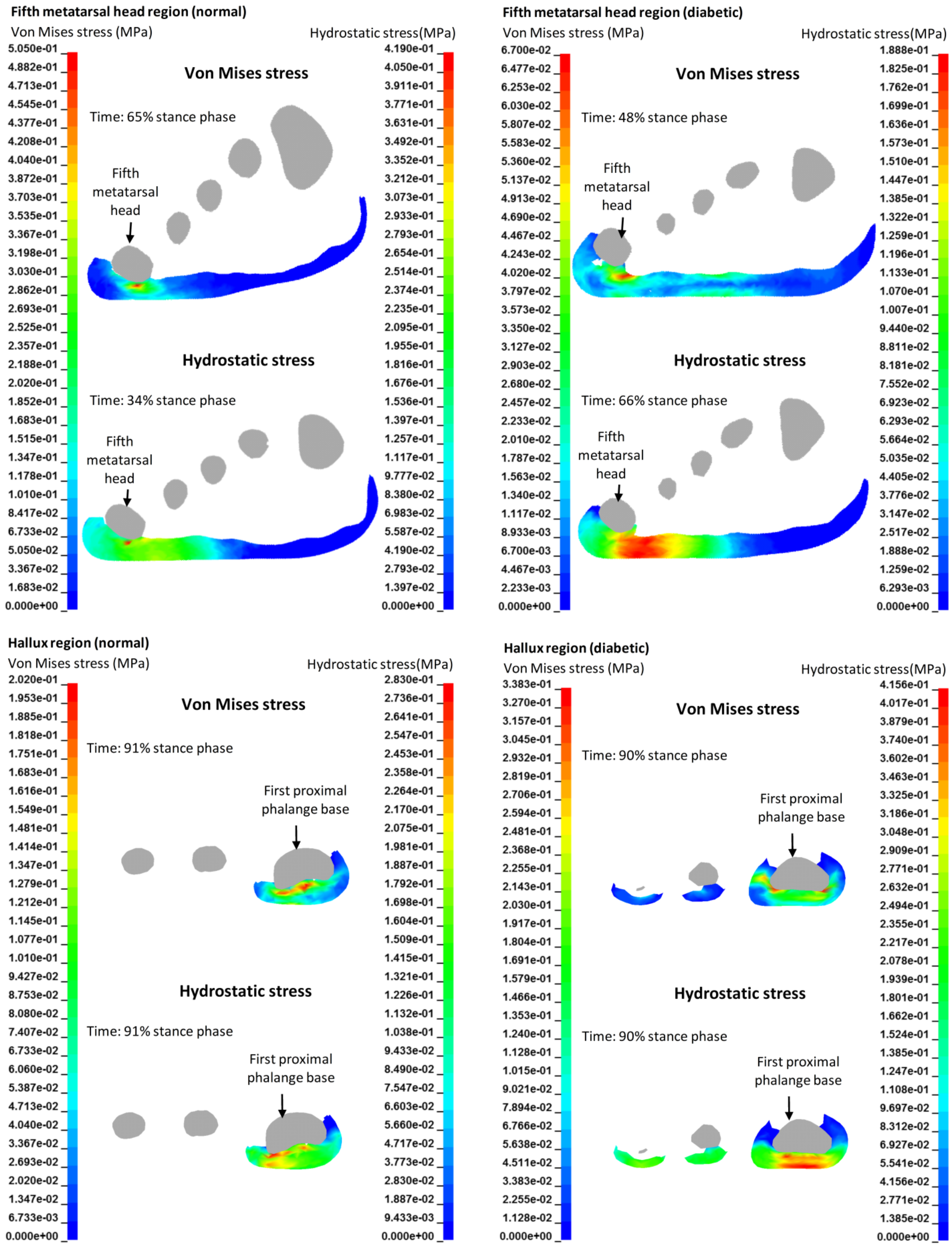

Figure E3: Contour plot of the internal von Mises and hydrostatic stresses in the frontal cross-sectional plane at eight regions of interest from gait on force plate simulations.

2.2) Gait on pressure platform condition

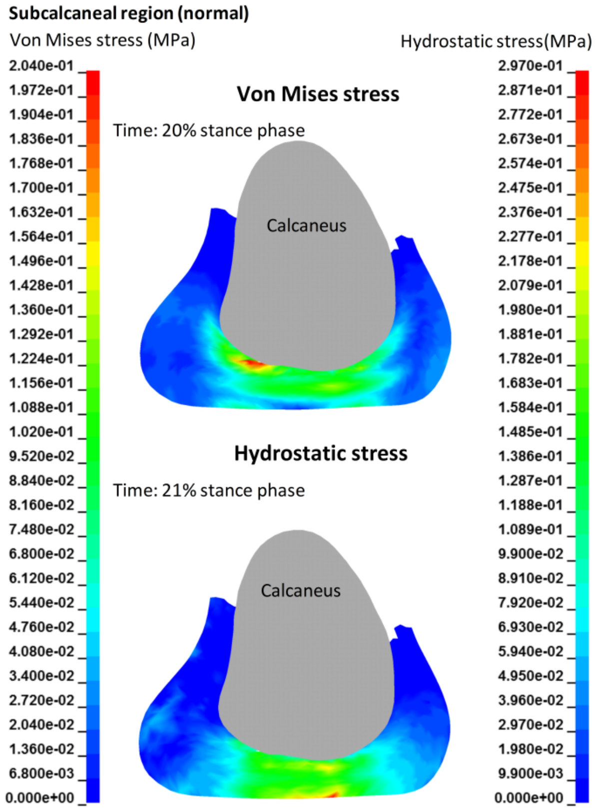

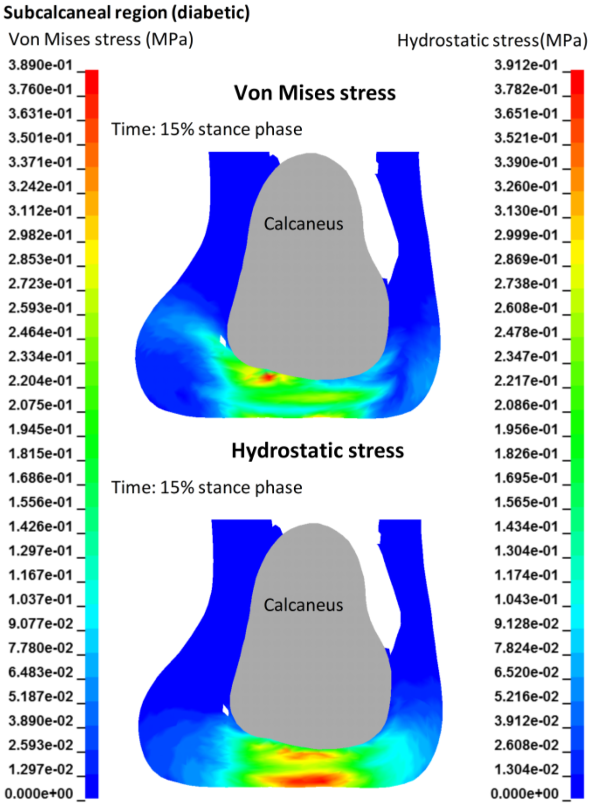

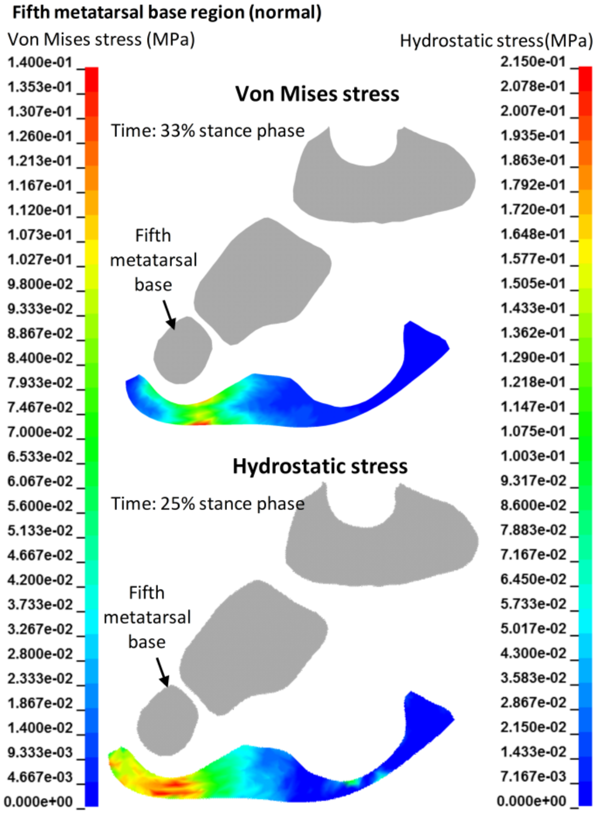

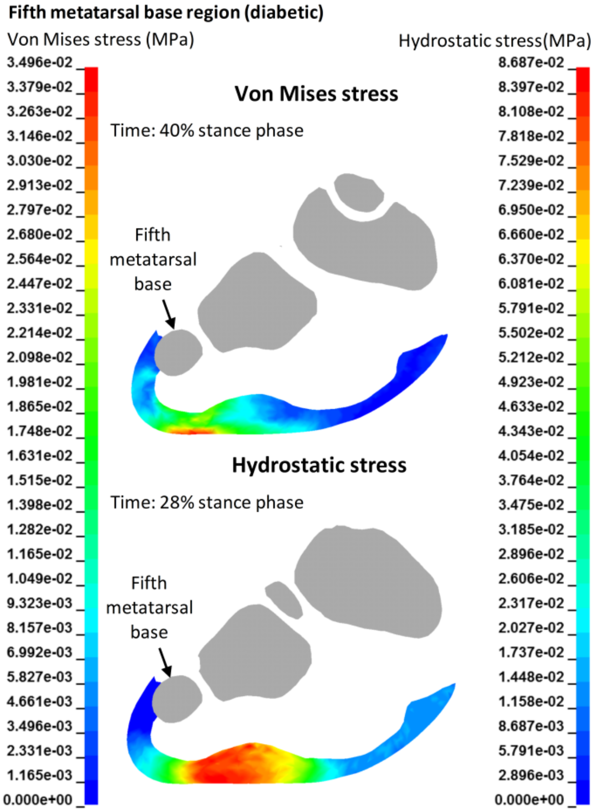

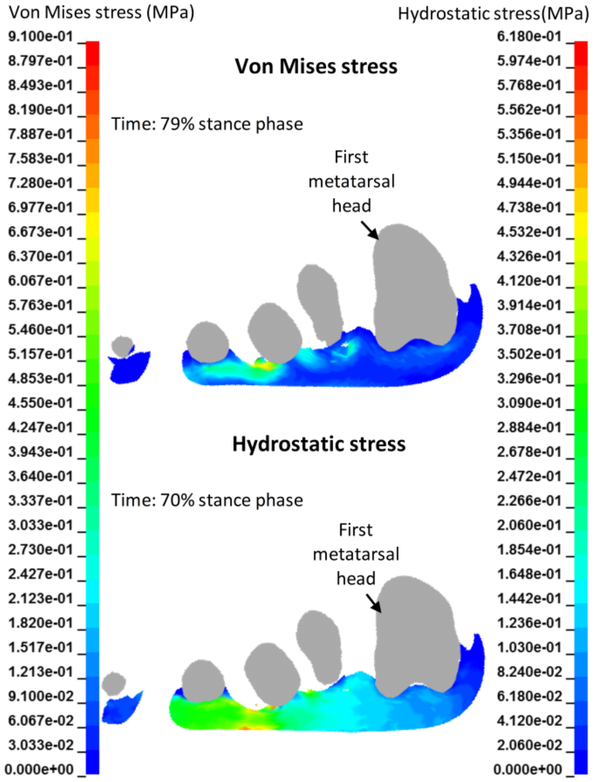

First metatarsal head region (normal)

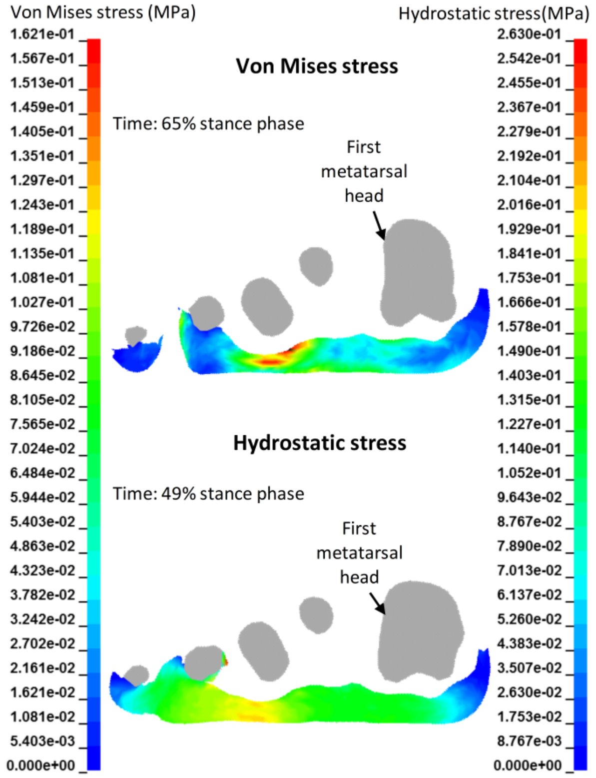

First metatarsal head region (diabetic)

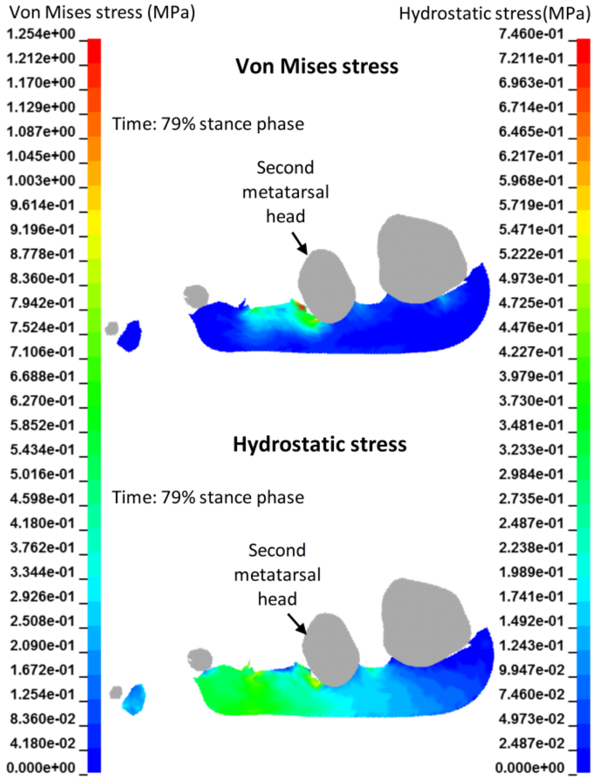

Second metatarsal head region (normal)

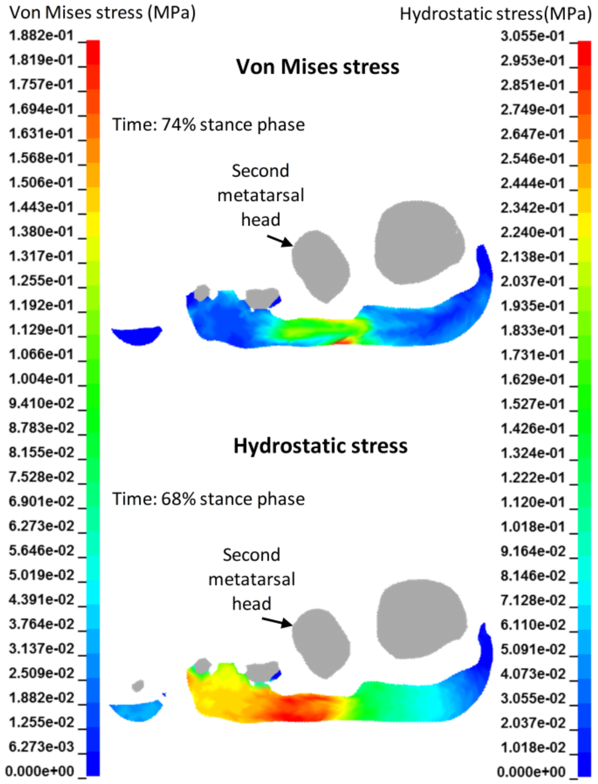

Second metatarsal head region (diabetic)

Third metatarsal head region (normal)

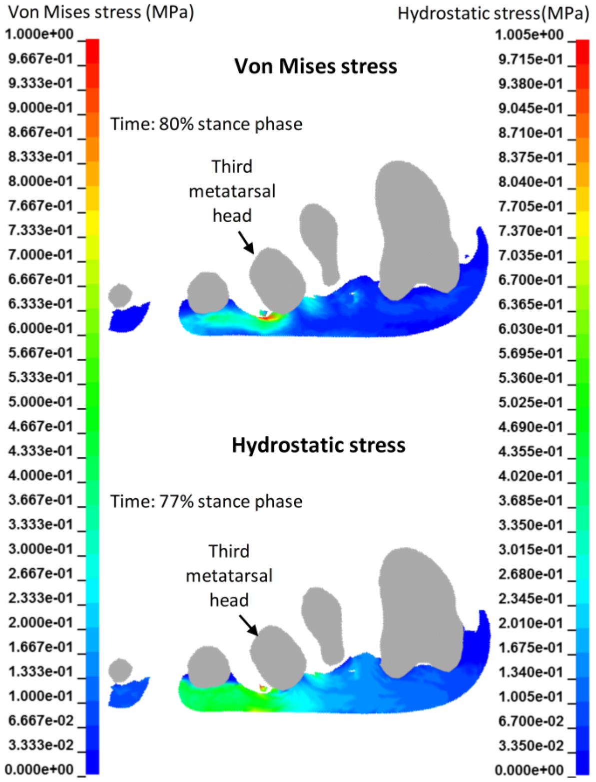

Third metatarsal head region (diabetic)

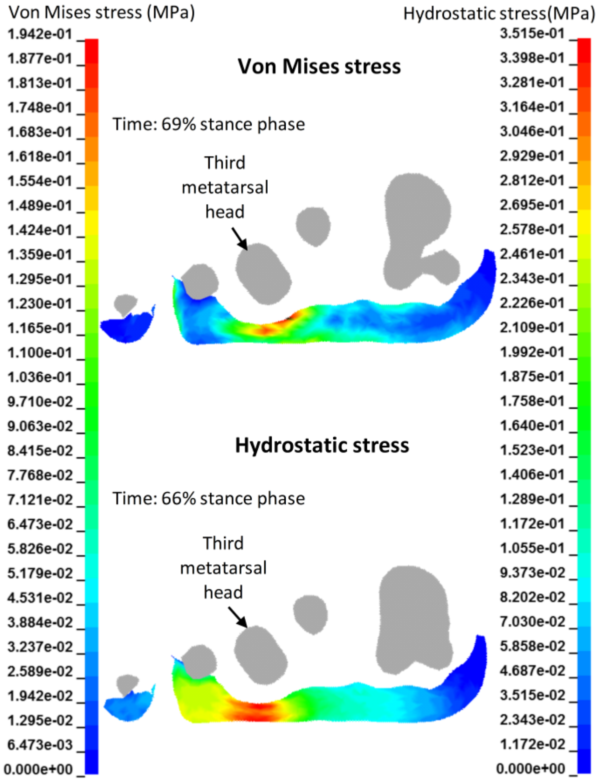

Fourth metatarsal head region (normal)

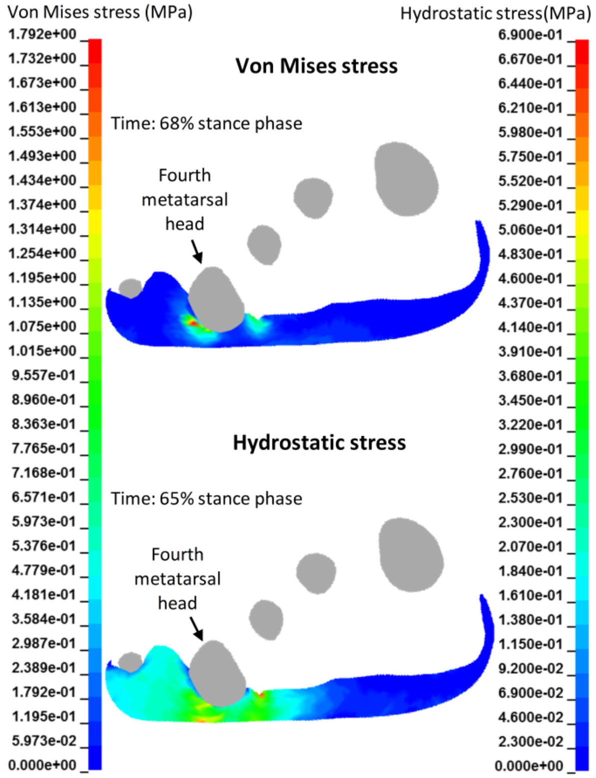

Fourth metatarsal head region (diabetic)

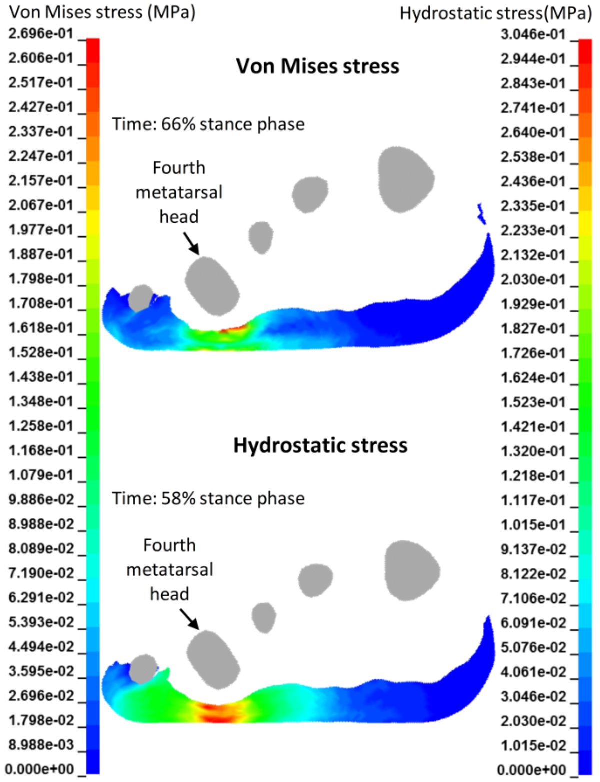

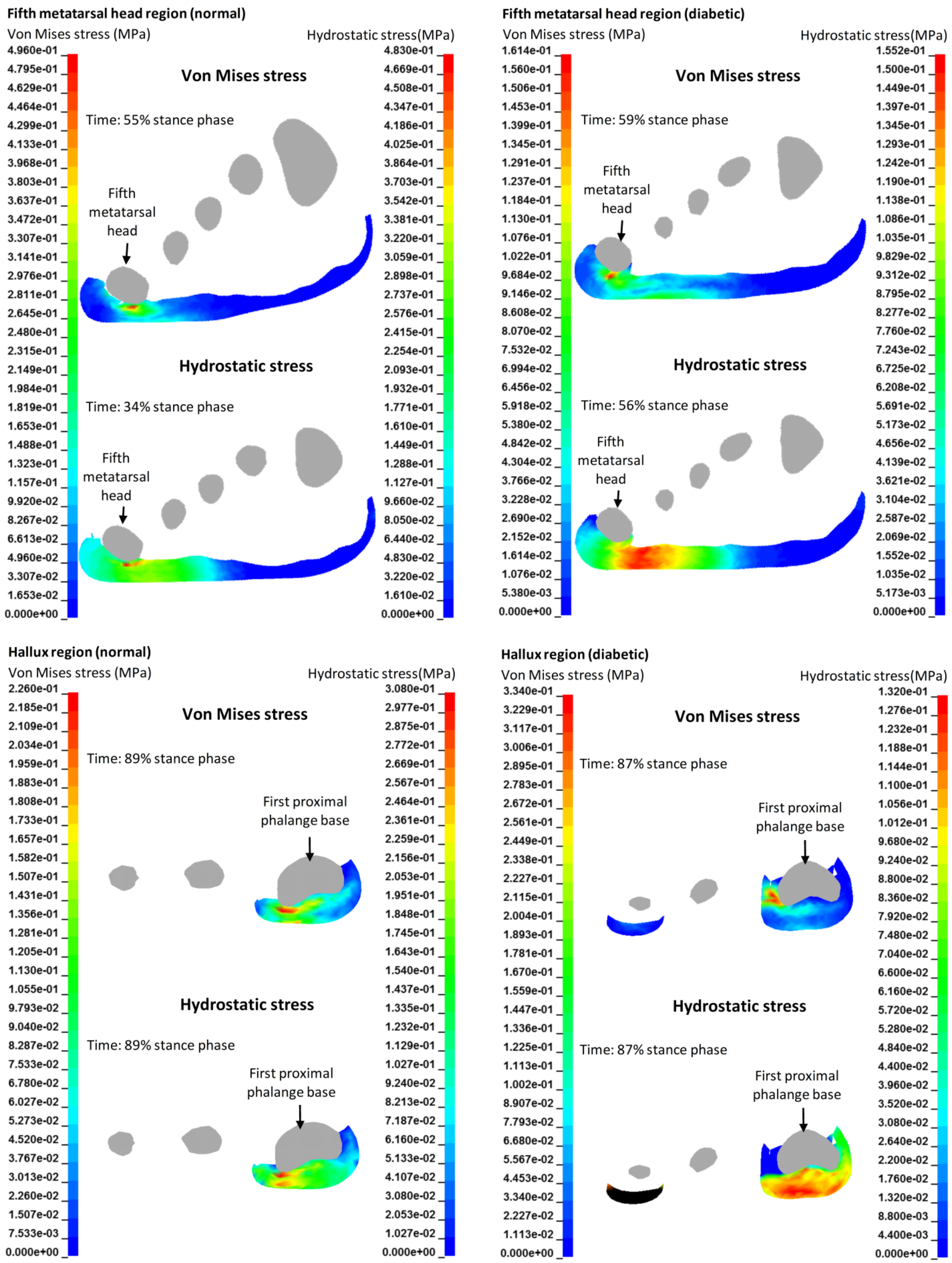

Figure E4: Contour plot of the internal von Mises and hydrostatic stresses in the frontal cross-sectional plane at eight regions of interest from gait on pressure platform simulations.

Chapter 8. Summary and contributions

The primary objective of this study was to develop two subject-specific computational foot models (normal and diabetic) that are capable of performing physiologic quiet stance and dynamic gait simulations, and provided insights into the internal soft tissue behavior of the normal and diabetic subjects. The detailed modeling and validation protocols outlined in Chapters 3 and 7 will serve as a guideline for the development of future FE foot models to better capture complexities of the foot. The FE foot models from this study will allow our research group to effectively perform parametric studies, thus overcoming current limitations frequently encountered in clinical or cadaveric studies. The mechanical characterization experiments on the plantar soft tissue (Chapter 4-5) and the plantar aponeurosis (Chapter 6) provided key geometric, material and structural information for the model, which were previously unavailable in the field. The following sections review the research performed, key findings, and future work.

8.1 Finite element foot model

8.1.1 Prior model utility and limitations

In Chapter 3, a previously-developed cadaveric FE foot model (Dengler, 2008) was improved and utilized in a parametric study focusing on two surgical treatments for correcting the clawed hallux deformity (Isvilanonda et al., 2012). The simulation results suggested that the modified Jones procedure, which altered the insertion of the EHL tendon, was more effective at correcting clawed hallux deformity generated from EHL overpull without FHL overpull. Conversely, the FHL transfer procedure was more effective when EHL and FHL overpull were both present.

A number of limitations were identified from this FE foot model. First, the foot was imaged under a compressive force, and so the unloaded anatomy could not be recreated. Second, the model did not incorporate a number of physiological features: it lacked physiologic soft tissue layers (skin and intrinsic muscle), and therefore internal stresses could not be accurately estimated. In addition, the plantar aponeurosis, which was the key component to stabilize the foot structure, could not be properly modeled because of inadequate material and anatomic data. Further, there was non-physiologic soft tissue in the joints which likely increased joint stiffness. Finally, the model was capable of only simulating the quasi-static condition. Nevertheless, this chapter demonstrated our group's fundamental background in FE foot modeling and provide the framework for our patient-specific modeling efforts.

8.1.2 Improvements in the subject-specific foot model

The limitations from the cadaveric FE foot model were addressed in Chapter 7 and resulted in two entirely new subject-specific FE foot models. These models were used to investigate plantar pressure and internal soft tissue stress during quiet stance and gait for a normal and a diabetic subject. Several key model improvements were incorporated. First, *in vivo* subject-specific (unloaded) anatomy obtained from medical imaging data was used to generate the model. Second, many of the soft tissue components were modeled more accurately: the material properties of the skin, fat, muscle, and dorsal generic soft tissue were obtained from inverse FE analyses (Chapter 5), the region-specific force-deformation response of the plantar aponeurosis (obtained directly from mechanical testing experiments, Chapter 6) was incorporated, and joint cavities were explicitly modeled (removing excess tissue from the joint spaces). Third, many ligaments were improved by defining multiple non-linear spring elements per ligament to better distribute the load. The Achilles tendon was physically modeled (instead of previously applying nodal forces to the calcaneus) to allow physiologic force vector during gait. Further, the model was extensively validated under three loading conditions—passive compression, quiet stance, and the stance phase of gait—using *in vivo* tibial kinematics measured for each subject.

8.1.3 Validation and performance

The subject-specific FE foot models were capable of simulating physiologic quiet stance and dynamic gait conditions. The vertical GRF, plantar pressure distribution, bone kinematics, plantar aponeurosis force and ankle joint force were reproduced in the model. The simulation results suggested that during gait the plantar soft tissue experienced substantially higher von Mises stress (up to 15 times) and hydrostatic stress (up to 4.6 times) compared to quiet stance. The location and time of the peak forefoot internal stresses were found to not always coincide with the peak plantar pressure or vertical GRF. Regions within the forefoot and hallux of higher internal von Mises and hydrostatic stresses were detected and persisted longer during gait, than such regions in the hindfoot. This disparity may account for the clinically observed incidences of forefoot and hallux ulceration in the diabetic neuropathic population. Under quiet stance condition, a foot model with multiple soft tissue layers predicted plantar pressure with better accuracy compared to a lumped tissue model. Non-subject specific material properties may be used when only plantar pressure is of interest (i.e., different internal stresses were found when subject-specific material properties were used). Generic soft tissue material simplification should be avoided.

8.1.4 Future model improvements

Future model improvements will involve the following goals: a) reduce development time and computation time by considering hexahedral elements and mesh morphing techniques; b) modify the tissue around joints to allow for buckling and therefore, a larger range of motion; c) implement unloaded ligament lengths by conducting additional cadaveric experiments; d) improve model stability by considering lower Poisson’s ratio of soft tissue; e) allow relative movement between soft tissue interfaces by utilizing contact instead of shared nodes; f) explicitly modeling the physical cartilage component to estimate joint pressure; and g) the incorporation of hyperviscoelastic material models, such that physiologic damping may be included in the model.

8.2 Soft tissue material characterization

Material property inputs (plantar soft tissue and plantar aponeurosis) were determined from two experiments for the subject-specific FE foot models.

8.2.1 Cadaveric subcalcaneal fat characterization

In Chapter 4, the feasibility of using inverse FE analysis to identify soft tissue material properties was explored. The *in vitro* subcalcaneal Ogden hyperelastic material properties were optimized from mean compression test data. The optimal material properties were μ_1 = 0.0235 kPa and α_1 = 12.07 using the first-order Ogden model and μ_1 = -4.629e-6 kPa and α_1 = -16.83, μ_2 = -1.613 kPa, α_2 = -1.04 using the second-order Ogden model. The predicted compression force was strongly affected by the Poisson's ratio and the strain hardening coefficient α. Future analysis may utilize a time-dependent material model to capture loading-unloading hysteresis in the experimental data.

8.2.2 *In vivo*, subject-specific hindfoot soft tissue characterization

In Chapter 5, the subject-specific skin, fat, muscle and generic soft tissue Ogden hyperelastic material properties were identified from *in vivo* MRI compression experiments using an inverse FE analysis. The optimal generic plantar soft tissue material properties were μ_G = 0.790 kPa, α_G = 21.08 for the normal subject and μ_G = 0.415 kPa, α_G = 25.25 for the diabetic subject. The optimal skin, fat and muscle material properties were μ_S = 0.156 kPa, α_S = 185.20, μ_F = 1.874 kPa, α_F = 8.29 and μ_M = 0.161 kPa, α_M = 31.95 for the normal subject. The analysis of diabetic subject utilized alternative method which yielded approximate optimal material properties of μ_S = 0.772 kPa, α_S = 163.56, μ_F = 0.200 kPa, α_F = 14.10 and μ_M = 0.321 kPa, α_M = 38.04. The diabetic soft tissue showed overall stiffer behavior compared to the normal tissue, however, statistical analyses cannot be conducted due to the small sample sizes. Potential areas for improvement in the experimental procedure include higher resolution MR images by using stronger magnets, a faster *in vivo* loading rate possibly by redesigning the loading jig, and a larger sample size. Computational improvements include using hexahedral elements to reduce solver time and the implementation of a viscohyperelastic material model to better capture the physiologic soft tissue behavior.

8.2.3 Plantar aponeurosis anatomy and biomechanical property characterization

In Chapter 6, the cross-sectional area and biomechanical properties at four regions of the plantar aponeurosis (i.e., proximal middle, distal middle, medial, and lateral) were measured from cadaveric specimens. Molding, casting and sectioning techniques were used to non-destructively obtain accurate specimen cross-sectional areas. The force-deformation responses of each region were measured at frequencies 0.5-10 Hz applied using a material testing machine. The digital image correlation was used to measure specimen strain. We found different cross-sectional areas and biomechanical properties across regions. The stress-strain responses were non-linear and nearly elastic. The final modulus, peak stress, and peak strain were not influenced by loading rate; however the energy loss was significantly affected. These anatomic information and material properties were utilized in the FE foot models to better represent this important component.

8.3 Future work

The developed FE foot model in this study provides a powerful research tool, especially for predicting internal soft tissue stress, performing high fidelity parametric studies on subject anatomy, and studying foot and ankle biomechanics. In addition to the potential future improvements to the model outlined above, the following topics of potential future research directions using the foot model have been identified:

- The effect of calluses and callus removal on plantar pressure and internal stress during standing and gait.

- The effect of total and partial plantar fascia release on medial longitudinal arch, plantar pressure and internal soft tissue stress.
- The effect of bone fusion (e.g., ankle joint, MTP joint or subtalar joint) and misalignment on bone kinematics, plantar pressure and internal soft tissue stress.

In addition, this model can be integrated with an implant or shoe FE models to determine their effect on foot biomechanics, and thus guide the design of these mechanical structures. Such studies could include:

- Stress analysis of a total ankle implant during quiet stance and gait and recommended designs to improve fatigue life.
- Parametric analyses of the effect of insole geometry and material properties on plantar pressure and internal soft tissue stress during quiet stance and gait.

These wide ranging of modeling applications, coupled with the current rate of advancement in computational power and image processing, will serve as a guide in the effort to generate clinically effective treatment techniques for foot and ankle pathology.

References

Actis, R., Ventura, L., Smith, K., Commean, P., Lott, D. J., Pilgram, T., et al., 2006. Numerical simulation of the plantar pressure distribution in the diabetic foot during the push-off stance. Medical and Biological Engineering and Computing 44**,** 653-663.

Apelqvist, J.Larsson, J., 2000. What is the most effective way to reduce incidence of amputation in the diabetic foot? Diabetes/Metabolism Research and Reviews 16 Suppl 1**,** S75-83.

Arangio, G. A., Chen, C.Kim, W., 1997. Effect of cutting the plantar fascia on mechanical properties of the foot. Clinical Orthopaedics and Related Research**,** 227-31.

Arinci Incel, N., Genc, H., Erdem, H. R.Yorgancioglu, Z. R., 2003. Muscle imbalance in hallux valgus: An electromyographic study. American Journal of Physical Medicine & Rehabilitation / Association of Academic Physiatrists 82**,** 345-9.

Athanasiou, K. A., Lui, G. T., Lavery, L. A., Lanctot, D. R.Schenck, R. C., 1998. Biomechanical topography of human articular cartilage in the first metatarsophalangeal joint. Clinical Orthopaedics and Related Research 348**,** 269-281.

Aubin, P., Whittaker, E.Ledoux, W. R., 2012. A robotic cadaveric gait simulator with fuzzy logic vertical ground reaction force control. IEEE T. Robot 28**,** 246-255.

Bandholm, T., Boysen, L., Haugaard, S., Zebis, M. K.Bencke, J., 2008. Foot medial longitudinal-arch deformation during quiet standing and gait in subjects with medial tibial stress syndrome. The Journal of Foot and Ankle Surgery 47**,** 89-95.

Bates, D., Maechler, M.Bolker, B. 2012. Lme4: Linear mixed-effects models using s4 classes. R package version 0.999999-0.

Bischof, J. E., Spritzer, C. E., Caputo, A. M., Easley, M. E., Deorio, J. K., Nunley, J. A., 2nd, et al., 2010. In vivo cartilage contact strains in patients with lateral ankle instability. Journal of Biomechanics 43**,** 2561-6.

Blanton, P. L.Biggs, N. L., 1970. Ultimate tensile strength of fetal and adult human tendons. Journal of Biomechanics 3**,** 181-189.

Boffeli, T. J., Bean, J. K.Natwick, J. R., 2002. Biomechanical abnormalities and ulcers of the great toe in patients with diabetes. The Journal of Foot and Ankle Surgery 41**,** 359-364.

Bojsen-Moller, F.Flagstad, K. E., 1976. Plantar aponeurosis and internal architecture of the ball of the foot. Journal of Anatomy 121**,** 599-611.

Bonet, J.Burton, A. J., 1998. A simple average nodal pressure tetrahedral element for incompressible and nearly incompressible dynamic explicit applications. Communications in Numerical Methods in Engineering 14**,** 437-449.

Boyle, J., Thompson, T., Gregg, E., Barker, L.Williamson, D., 2010. Projection of the year 2050 burden of diabetes in the us adult population: Dynamic modeling of incidence, mortality, and prediabetes prevalence. Popul Health Metrics 8**,** 29.

Brand, R. A., Pedersen, D. R.Friederich, J. A., 1986. The sensitivity of muscle force predictions to changes in physiologic cross-sectional area. Journal of Biomechanics 19**,** 589-596.

Buczek, F. L.Banks, S. A., 1996. High-resolution force plate analysis of utilized slip resistance in human walking. J Test. Eval. 24**,** 353-358.

Budhabhatti, S., Edmir, A., Petre, M., Sferra, J., Donley, B.Cavanagh, P. R., 2009. Finite element modeling of the first ray of the foot: A tool for the design of interventions. Journal of Biomechanical Engineering 129**,** 750-756.

Bummo, A.Jung, K., 2010. Measurement and characterization of soft tissue behavior with surface deformation and force response under large deformations. Medical Image Analysis 14**,** 138-148.

Bus, S. A., Maas, M., Cavanagh, P. R., Michels, R. P. J.Levi, M., 2004. Plantar fat-pad displacement in neuropathic diabetic patients with toe deformity. Diabetes Care 27**,** 2376-81.

Bus, S. A., Maas, M., De Lange, A., Michels, R. P.Levi, M., 2005. Elevated plantar pressures in neuropathic diabetic patients with claw/hammer toe deformity. Journal of Biomechanics 38**,** 1918-1925.

Camacho, D. L., Ledoux, W. R., Rohr, E. S., Sangeorzan, B. J.Ching, R. P., 2002. A three-dimensional, anatomically detailed foot model: A foundation for a finite element simulation and means of quantifying foot-bone position. Journal of Rehabilitation Research and Development 39**,** 401-10.

Cavanagh, P. R., Morag, E., Boulton, A. J. M., Young, M. J., Deffner, K. T.Pammer, S. E., 1997. The relationship of static foot structure to dynamic foot function. Journal of Biomechanics 30**,** 243-250.

Cavanagh, P. R., Rodgers, M. M.Iiboshi, A., 1987. Pressure distribution under symptom-free feet during barefoot standing. Foot & ankle 7**,** 262-276.

CDCP 2014. National diabetes fact sheet: General information and national estimates on diabetes in the united states. In: Services, D. O. H. A. H. (ed.).

Chen, D.-W., Li, B., Aubeeluck, A., Yang, Y.-F., Huang, Y.-G., Zhou, J.-Q., et al., 2014a. Anatomy and biomechanical properties of the plantar aponeurosis: A cadaveric study. PLoS ONE 9**,** e84347.

Chen, W.-M., Park, J., Park, S.-B., Shim, V. P.-W.Lee, T., 2012. Role of gastrocnemius–soleus muscle in forefoot force transmission at heel rise — a 3d finite element analysis. Journal of Biomechanics 45**,** 1783–1789.

Chen, W.-P., Ju, C.-W.Tang, F.-T., 2003. Effects of total contact insoles on the plantar stress redistribution: A finite element analysis. Clinical Biomechanics 18**,** S17-S24.

Chen, W.-P., Tang, F.-T.Ju, C.-W., 2001. Stress distribution of the foot during mid-stance to push-off in barefoot gait: A 3-d finite element analysis. Clinical Biomechanics 16**,** 614-620.

Chen, W. M., Lee, T., Lee, P. V. S., Lee, J. W.Lee, S. J., 2010. Effects of internal stress concentrations in plantar soft-tissue-a preliminary three-dimensional finite element analysis. Medical Engineering & Physics 32**,** 324-331.

Chen, Y.-N., Chang, C.-W., Li, C.-T., Chang, C.-H.Lin, C.-F., 2014b. Finite element analysis of plantar fascia during walking: A quasi-static simulation. Foot Ankle Int.

Cheng, H. Y. K., Lin, C. L., Wang, H. W.Chou, S. W., 2008. Finite element analysis of plantar fascia under stretch-the relative contribution of windlass mechanism and achilles tendon force. Journal of Biomechanics 41**,** 1937-1944.

Cheung, J. T.-M.Zhang, M., 2005. A 3-dimensional finite element model of the human foot and ankle for insole design. Archives of Physical Medicine and Rehabilitation 86**,** 353-358.

Cheung, J. T.-M., Zhang, M.An, K.-N., 2004. Effects of plantar fascia stiffness on the biomechanical responses of the ankle-foot complex. Clinical Biomechanics 19**,** 839-846.

Cheung, J. T.-M., Zhang, M.An, K.-N., 2006a. Effect of achilles tendon loading on plantar fascia tension in the standing foot. Clinical Biomechanics 21**,** 194-203.

Cheung, J. T.-M., Zhang, M., Leung, A. K.-L.Fan, Y.-B., 2005. Three-dimensional finite element analysis of the foot during standing--a material sensitivity study. Journal of Biomechanics 38**,** 1045-1054.

Cheung, J. T. M.Zhang, M., 2008. Parametric design of pressure-relieving foot orthosis using statistics-based finite element method. Medical Engineering & Physics 30**,** 269-277.

Cheung, Y. Y., Doyley, M., Miller, T. B., Kennedy, F., Lynch Jr, F., Wrobel, J. S., et al., 2006b. Magnetic resonance elastography of the plantar fat pads: Preliminary study in diabetic patients and asymptomatic volunteers. Journal of Computer Assisted Tomography 30**,** 321-326.

Chokhandre, S., Halloran, J. P., Van Den Bogert, A. J.Erdemir, A., 2012. A three-dimensional inverse finite element analysis of the heel pad. Journal of Biomechanical Engineering 134**,** 031002-9.

Chung, K. W., Suh, B. C., Shy, M. E., Cho, S. Y., Yoo, J. H., Park, S. W., et al., 2008. Different clinical and magnetic resonance imaging features between Charcot-Marie-Tooth disease type 1a and 2a. Neuromuscular Disorders 18**,** 610-618.

Clark, R. A., Franklyn-Miller, A., Falvey, E., Bryant, A. L., Bartold, S.Mccrory, P., 2009. Assessment of mechanical strain in the intact plantar fascia. Foot (Edinburgh, Scotland) 19**,** 161-4.

D'ambrogi, E., Giurato, L., D'agostino, M. A., Giacomozzi, C., Macellari, V., Caselli, A., et al., 2003. Contribution of plantar fascia to the increased forefoot pressures in diabetic patients. Diabetes Care 26**,** 1525-9.

Dengler, E. 2008. A finite element model of the human foot and ankle, Master of Science, University of Washington.

Dinh, T. L.Veves, A., 2005. A review of the mechanisms implicated in the pathogenesis of the diabetic foot. The International Journal of Lower Extremity Wounds 4**,** 154-159.

Döderlein, L., Breusch, S.Wenz, W., 2000. Transfer of extensor hallucis longus tendon (modified robert jones procedure). Orthopedics and Traumatology 8**,** 273-284.

Driver, V. R., Fabbi, M., Lavery, L. A.Gibbons, G., 2010. The costs of diabetic foot: The economic case for the limb salvage team. Journal of Vascular Surgery 52**,** 17S-22S.

Duck, F. A., 1990. Physical properties of tissue : A comprehensive reference book, Academic Press, London; San Diego

Dunn, J. E., Link, C. L., Felson, D. T., Crincoli, M. G., Keysor, J. J.Mckinlay, J. B., 2004. Prevalence of foot and ankle conditions in a multiethnic community sample of older adults. American Journal of Epidemiology 159**,** 491-498.

Eberl, C., Thompson, R., Gianola, D.Bundschuh, S. 2010. Digital image correlation and tracking [Online]. Available: http://www.mathworks.com/matlabcentral/fileexchange/12413 [Accessed April 26 2012].

Edmonds, M. E.Foster, A. V. M., 2006. Diabetic foot ulcers. British Medical Journal 332**,** 407-410.

Elias, F. N., Yuen, T. J., Olson, S. L., Sangeorzan, B. J.Ledoux, W. R., 2007. Correction of clawed hallux deformity: Comparison of the jones procedure and fhl transfer in a cadaver model. Foot Ankle Int. 28**,** 369-376.

Elliott, D. M.Setton, L. A., 2001. Anisotropic and inhomogeneous tensile behavior of the human anulus fibrosus: Experimental measurement and material model predictions. Journal of Biomechanical Engineering 123**,** 256-263.

Erdemir, A., Hamel, A. J., Fauth, A. R., Piazza, S. J.Sharkey, N. A., 2004. Dynamic loading of the plantar aponeurosis in walking. The Journal of Bone and Joint Surgery 86**,** 546-552.

Erdemir, A.Piazza, S. J., 2004. Changes in foot loading following plantar fasciotomy: A computer modeling study. Journal of Biomechanical Engineering 126**,** 237-243.

Erdemir, A., Saucerman, J. J., Lemmon, D., Loppnow, B., Turso, B., Ulbrecht, J. S., et al., 2005. Local plantar pressure relief in therapeutic footwear: Design guidelines from finite element models. Journal of Biomechanics 38**,** 1798-1806.

Erdemir, A., Viveiros, M. L., Ulbrecht, J. S.Cavanagh, P. R., 2006. An inverse finite-element model of heel-pad indentation. Journal of Biomechanics 39**,** 1279-1286.

Evans, S. L.Holt, C. A., 2009. Measuring the mechanical properties of human skin in vivo using digital image correlation and finite element modelling. The Journal of Strain Analysis for Engineering Design 44**,** 337-345.

Felton, N. 1996. A parametric study of the load distribution in the hindfoot, Master of Science, University of Washington.

Fukunaga, T., Roy, R. R., Shellock, F. G., Hodgson, J. A.Edgerton, V. R., 1996. Specific tension of human plantar flexors and dorsiflexors. Journal of Applied Physiology 80**,** 158-165.

Gao, Z.Desai, J. P., 2010. Estimating zero-strain states of very soft tissue under gravity loading using digital image correlation. Medical Image Analysis 14**,** 126-137.

Garcia-Aznar, J. M., Bayod, J., Rosas, A., Larrainzar, R., Garcia-Bogalo, R., Doblare, M., et al., 2009. Load transfer mechanism for different metatarsal geometries: A finite element study. Journal of Biomechanical Engineering 131**,** 021011.

Garcia-Gonzalez, A., Bayod, J., Prados-Frutos, J. C., Losa-Iglesias, M., Jules, K. T., De Bengoa-Vallejo, R. B., et al., 2009. Finite-element simulation of flexor digitorum longus or flexor digitorum brevis tendon transfer for the treatment of claw toe deformity. Journal of Biomechanics 42**,** 1697-1704.

Gefen, A., 2002. Stress analysis of the standing foot following surgical plantar fascia release. Journal of Biomechanics 35**,** 629-637.

Gefen, A., 2003. Plantar soft tissue loading under the medial metatarsals in the standing diabetic foot. Medical Engineering & Physics 25**,** 491-499.

Gefen, A., Megido-Ravid, M., Azariah, M., Itzchak, Y.Arcan, M., 2001a. Integration of plantar soft tissue stiffness measurements in routine mri of the diabetic foot. Clinical Biomechanics 16**,** 921-925.

Gefen, A., Megido-Ravid, M.Itzchak, Y., 2001b. In vivo biomechanical behavior of the human heel pad during the stance phase of gait. Journal of Biomechanics 34**,** 1661-1665.

Goske, S., Erdemir, A., Petre, M., Budhabhatti, S.Cavanagh, P. R., 2006. Reduction of plantar heel pressures: Insole design using finite element analysis. Journal of Biomechanics 39**,** 2363-2370.

Gould, J. S., 1988. The foot book, 1. Williams & Wilkins, Baltimore, MD

Gu, Y., Li, J., Ren, X., Lake, M. J.Zeng, Y., 2010. Heel skin stiffness effect on the hind foot biomechanics during heel strike. Skin Research and Technology 16**,** 291-296.

Guiotto, A., Sawacha, Z., Guarneri, G., Avogaro, A.Cobelli, C., 2014. 3d finite element model of the diabetic neuropathic foot: A gait analysis driven approach. Journal of Biomechanics 47**,** 3064-3071.

Guyton, G. P.Saltzman, C. L., 2001. The diabetic foot : Basic mechanisms of disease. The Journal of Bone and Joint Surgery 83**,** 1083-1096.

Halloran, J. P., Ackermann, M., Erdemir, A.Van Den Bogert, A. J., 2010. Concurrent musculoskeletal dynamics and finite element analysis predicts altered gait patterns to reduce foot tissue loading. Journal of Biomechanics 43**,** 2810-5.

Halloran, J. P.Erdemir, A., 2011. Adaptive surrogate modeling for expedited estimation of nonlinear tissue properties through inverse finite element analysis. Annals of Biomedical Engineering.

LS-DYNA theory manual, Livermore Software Technology Corporation, 2006.

Hedrick, M. R., 1996. The plantar aponeurosis. Foot Ankle Int. 17**,** 646-9.

Hibbeler, R. C., 1997. Mechanics of materials, Third ed. Prentice Hall, Upper Saddle River, NJ

Hibbit D., Karlsson B.P., S., 2007. Abaqus/standard analysis user's manual, Hibbit, Karlsson, Sorensen Inc.,

Hicks, J. H., 1954. The mechanics of the foot ii. The plantar aponeurosis and the arch. Journal of Anatomy 88**,** 25-30.

Hild, F.Roux, S., 2006. Digital image correlation: From displacement measurement to identification of elastic properties – a review. Strain 42**,** 69-80.

Hoffmeyer, P., Cox, J. N., Blanc, Y., Meyer, J. M.Taillard, W., 1988. Muscle in hallux valgus. Clinical Orthopaedics and Related Research**,** 112-8.

Hothorn, T., Bretz, F.Westfall, P., 2008. Simultaneous inference in general parametric models. Biometrical journal 50**,** 346-63.

Hsu, C. C., Tsai, W. C., Hsiao, T. Y., Tseng, F. Y., Shau, Y. W., Wang, C. L., et al., 2009. Diabetic effects on microchambers and macrochambers tissue properties in human heel pads. Clinical Biomechanics (Bristol, Avon) 24**,** 682-6.

Hsu, T.-C., Wang, C.-L., Tsai, W.-C., Kuo, J.-K.Tang, F.-T., 1998. Comparison of the mechanical properties of the heel pad between young and elderly adults. Archives of Physical Medicine and Rehabilitation 79**,** 1101-1104.

Hsu, T. C., Lee, Y. S.Shau, Y. W., 2002. Biomechanics of the heel pad for type 2 diabetic patients. Clinical Biomechanics (Bristol, Avon) 17**,** 291-6.

Hu, Y., Ledoux, W. R., Fassbind, M., Rohr, E. S., Sangeorzan, B. J.Haynor, D. R., 2011. Multi-rigid image segmentation and registration for the analysis of joint motion from 3d mri. Journal of Biomechanical Engineering 133**,** 101005.

Iaquinto, J. M.Wayne, J. S., 2010. Computational model of the lower leg and foot/ankle complex: Application to arch stability. Journal of Biomechanical Engineering 132**,** 021009.

Iaquinto, J. M.Wayne, J. S., 2011. Effects of surgical correction for the treatment of adult acquired flatfoot deformity: A computational investigation. Journal of Orthopaedic Research 29**,** 1047-1054.

Ishikawa, M., Komi, P. V., Grey, M. J., Lepola, V.Bruggemann, G. P., 2005. Muscle-tendon interaction and elastic energy usage in human walking. Journal of Applied Physiology 99**,** 603-608.

Isvilanonda, V., Dengler, E., Iaquinto, J. M., Sangeorzan, B. J.Ledoux, W. R., 2012. Finite element analysis of the foot: Model validation and comparison between two common treatments of the clawed hallux deformity. Clinical Biomechanics 27**,** 837-844.

Jacquemoud, C., Bruyere-Garnier, K.Coret, M., 2007. Methodology to determine failure characteristics of planar soft tissues using a dynamic tensile test. Journal of Biomechanics 40**,** 468-475.

James A. Birke, A. N., Elizabeth S. Hawkins, Charles Patout Jr., 1991. A review of causes of foot ulceration in patients with diabetes mellitus. Journal of Prosthetics & Orthotics 4**,** 13-22.

Kadel, N. J., Donaldson-Fletcher, E. A., Hansen, S. T.Sangeorzan, B. J., 2005. Alternative to the modified jones procedure: Outcomes of the flexor hallucis longus (fhl) tendon transfer procedure for correction of clawed hallux. Foot Ankle Int. 26**,** 1021-1026.

Ker, R. F., Bennett, M. B., Bibby, S. R., Kester, R. C.Alexander, R. M., 1987. The spring in the arch of the human foot. Nature 325**,** 147-149.

Kim, W.Voloshin, A. S., 1995. Role of plantar fascia in the load bearing capacity of the human foot. Journal of Biomechanics 28**,** 1025-1033.

Kitaoka, H. B., Luo, Z. P.An, K. N., 1997. Mechanical behavior of the foot and ankle after plantar fascia release in the unstable foot. Foot Ankle Int. 18**,** 8-15.

Kitaoka, H. B., Luo, Z. P., Growney, E. S., Berglund, L. J.An, K. N., 1994. Material properties of the plantar aponeurosis. Foot Ankle Int. 15**,** 557-560.

Klaesner, J. W., Hastings, M. K., Zou, D., Lewis, C.Mueller, M. J., 2002. Plantar tissue stiffness in patients with diabetes mellitus and peripheral neuropathy. Archives of Physical Medicine and Rehabilitation 83**,** 1796-1801.

Klingbeil, W.Shield, R., 1966. Large-deformation analyses of bonded elastic mounts. Journal of Applied Mathematics and Physics 17**,** 281-305.

Kogler, G. F., Veer, F. B., Verhulst, S. J., Solomonidis, S. E.Paul, J. P., 2001. The effect of heel elevation on strain within the plantar aponeurosis: In vitro study. Foot Ankle Int. 22**,** 433-9.

Kroon, D. J. 2009. Iterative closest point using finite difference optimization to register 3d point clouds affine [Online]. Available: http://www.mathworks.com/matlabcentral/fileexchange/24301-finite-iterative-closest-point [Accessed April 26 2012].

Kwon, O. Y., Tuttle, L. J., Johnson, J. E.Mueller, M. J., 2009. Muscle imbalance and reduced ankle joint motion in people with hammer toe deformity. Clinical Biomechanics (Bristol, Avon) 24**,** 670-5.

Lai, J. H.Levenston, M. E., 2010. Meniscus and cartilage exhibit distinct intra-tissue strain distributions under unconfined compression. Osteoarthritis and Cartilage 18**,** 1291-1299.

Lauret, C., Hrapko, M., Van Dommelen, J. A. W., Peters, G. W. M.Wismans, J. S. H. M., 2009. Optical characterization of acceleration-induced strain fields in inhomogeneous brain slices. Medical Engineering & Physics 31**,** 392-399.

Leardini, A., Benedetti, M. G., Berti, L., Bettinelli, D., Nativo, R.Giannini, S., 2007. Rear-foot, mid-foot and fore-foot motion during the stance phase of gait. Gait & posture 25**,** 453-462.

Ledoux, W. R.Blevins, J. J., 2007. The compressive material properties of the plantar soft tissue. Journal of Biomechanics 40**,** 2975-2981.

Lemmon, D., Shiang, T. Y., Hashmi, A., Ulbrecht, J. S.Cavanagh, P. R., 1997. The effect of insoles in therapeutic footwear-a finite element approach. Journal of Biomechanics 30**,** 615-620.

Li, G., Wan, L.Kozanek, M., 2008. Determination of real-time in-vivo cartilage contact deformation in the ankle joint. Journal of Biomechanics 41**,** 128-36.

Li, Y., Burrows, N. R., Gregg, E. W., Albright, A.Geiss, L. S., 2012. Declining rates of hospitalization for nontraumatic lower-extremity amputation in the diabetic population aged 40 years or older: U.S., 1988-2008. Diabetes Care 35**,** 273-7.

Lin, S.-C., Chen, W.-P., Hsu, C.-C., Hsieh, J.-H., Wang, J.-J., Chen, C.-W., et al., 2014. Stress distribution within the plantar aponeurosis during walking - a dynamic finite element analysis. Journal of Mechanics in Medicine and Biology 14**,** 1450053-1-17.

Lind, C., Schluder, H.Winklhofer, J. Optimization methodology in structural mechanics - comparison of ls-opt and hyperstudy. The Third German LS-DYNA Forum, 2005 Bamberg, Germany. 29-38.

LSTC. 2015. I have very long run times. What can i do? [Online]. Available: http://www.dynasupport.com/faq/general/i-have-very-long-run-times.-what-can-i-do [Accessed January 28 2015].

Lundgren, P., Nester, C., Liu, A., Arndt, A., Jones, R., Stacoff, A., et al., 2008. Invasive in vivo measurement of rear-, mid- and forefoot motion during walking. Gait & posture 28**,** 93-100.

Luo, G., Houston, V. L., Garbarini, M. A., Beattie, A. C.Thongpop, C., 2011. Finite element analysis of heel pad with insoles. Journal of Biomechanics 44**,** 1559-65.

Luo, Z. P., Kitaoka, H. B., Hsu, H. C., Kura, H.An, K. N., 1997. Physiological elongation of ligamentous complex surrounding the hindfoot joints: In vitro biomechanical study. Foot Ankle Int. 18**,** 277-83.

Maganaris, C. N.Paul, J. P., 1999. In vivo human tendon mechanical properties. The Journal of Physiology 521 Pt 1**,** 307-313.

Maganaris, C. N.Paul, J. P., 2002. Tensile properties of the in vivo human gastrocnemius tendon. Journal of Biomechanics 35**,** 1639-1646.

Manoogian, S. J., Bisplinghoff, J. A., Mcnally, C., Kemper, A. R., Santago, A. C.Duma, S. M., 2008. Dynamic tensile properties of human placenta. Journal of Biomechanics 41**,** 3436-3440.

Mccormick, N.Lord, J., 2010. Digital image correlation. Materials Today 13**,** 52-54.

Merkher, Y., Sivan, S., Etsion, I., Maroudas, A., Halperin, G.Yosef, A., 2006. A rational human joint friction test using a human cartilage-on-cartilage arrangement. Tribology Letters 22**,** 29-36.

Miller-Young, J. E., Duncan, N. A.Baroud, G., 2002. Material properties of the human calcaneal fat pad in compression: Experiment and theory. Journal of Biomechanics 35**,** 1523-1531.

Miller, K., 2005. Method of testing very soft biological tissues in compression. Journal of Biomechanics 38**,** 153-158.

Miller, K., 2011. Biomechanics of the brain, Springer, New York

Mills, G. P. 1924. The etiology and treatment of claw foot. Read before the British Orthopaedic Association, October, 1923.

Mkandawire, C., Ledoux, W. R., Sangeorzan, B. J.Ching, R. P., 2005. Foot and ankle ligament morphometry. Journal of Rehabilitation Research & Development 42**,** 809-819.

Mohamed, E. A., Abdulhakim, O. T., Seif, I. M., Abubakr, H. W.Mohamed, A. S., 2010. Hallux ulceration in diabetic patients. The Journal of Foot and Ankle Surgery 49**,** 2-7.

Moraes Do Carmo, C. C., Fonseca De Almeida Melao, L. I., Valle De Lemos Weber, M. F., Trudell, D.Resnick, D., 2008. Anatomical features of plantar aponeurosis: Cadaveric study using ultrasonography and magnetic resonance imaging. Skeletal Radiology 37**,** 929-35.

Muehleman, C., Berzins, A., Koepp, H., Eger, W., Cole, A. A., Kuettner, K. E., et al., 2002. Bone density of the human talus does not increase with the cartilage degeneration score. The Anatomical Record 266**,** 81-86.

Murray, H., Young, M., Hollis, S.Boulton, A., 1996. The association between callus formation, high pressures and neuropathy in diabetic foot ulceration. Diabetic Medicine 13**,** 979-82.

Myerson, M. S.Shereff, M. J., 1989. The pathological anatomy of claw and hammer toes. The Journal of Bone and Joint Surgery 71**,** 45-49.

Natali, A. N., Fontanella, C. G.Carniel, E. L., 2010. Constitutive formulation and analysis of heel pad tissues mechanics. Medical Engineering & Physics 32**,** 516-522.

Netter, F. H., 2005. Atlas of human anatomy, Fifth ed. Saunders, Philadelphia, PA

Nicolella, D. P., Moravits, D. E., Gale, A. M., Bonewald, L. F.Lankford, J., 2006. Osteocyte lacunae tissue strain in cortical bone. Journal of Biomechanics 39**,** 1735-1743.

Ogden, R. W., Saccomandi, G.Sgura, I., 2004. Fitting hyperelastic models to experimental data. Comput Mech 34**,** 484-502.

Olson, S. L., Ledoux, W. R., Ching, R. P.Sangeorzan, B. J., 2003. Muscular imbalances resulting in a clawed hallux. Foot Ankle Int. 24**,** 477-485.

Pai, S. 2011. Changes in the mechanical properties of the plantar soft tissue, Doctor of Philosophy, University of Washington.

Pai, S.Ledoux, W., 2011. The quasi-linear viscoelastic properties of diabetic and non-diabetic plantar soft tissue. Annals of Biomedical Engineering 39**,** 1517-1527.

Pai, S.Ledoux, W. R., 2010. The compressive mechanical properties of diabetic and non-diabetic plantar soft tissue. Journal of Biomechanics 43**,** 1754-1760.

Pai, S.Ledoux, W. R., 2012. The shear mechanical properties of diabetic and non-diabetic plantar soft tissue. Journal of Biomechanics 45**,** 364-370.

Palma, L. D., Colonna, E.Travasi, M., 1997. The modified jones procedure for pes cavovarus with claw hallux. The Journal of Foot and Ankle Surgery 36**,** 279-283.

Pavan, P. G., Pachera, P., Stecco, C.Natali, A. N., 2014. Constitutive modeling of time-dependent response of human plantar aponeurosis. Comput Math Methods Med 2014.

Pecoraro, R. E., Reiber, G. E.Burgess, E. M., 1990. Pathways to diabetic limb amputation. Basis for prevention. Diabetes Care 13**,** 513-521.

Perry, J., 1992. Gait analysis: Normal and pathological function, First ed. Slack, Thorofare, NJ

Petre, M., Erdemir, A.Cavanagh, P. R., 2008. An mri-compatible foot-loading device for assessment of internal tissue deformation. Journal of Biomechanics 41**,** 470-474.

Petre, M., Erdemir, A., Panoskaltsis, V. P., Spirka, T. A.Cavanagh, P. R., 2013. Optimization of nonlinear hyperelastic coefficients for foot tissues using a magnetic resonance imaging deformation experiment. Journal of Biomechanics 135**,** 061001.

Piaggesi, A., Romanelli, M., Schipani, E., Campi, F., Magliaro, A., Baccetti, F., et al., 1999. Hardness of plantar skin in diabetic neuropathic feet. Journal of Diabetes and Its Complications 13**,** 129-34.

Pierrynowski, M. R. 1982. A physiological model for the solution of individual muscle force during normal human walking, Doctor of Philosophy, Simon Fraser University.

Pinheiro, J., Bates, D., Saikatdebroy, D. S.Team, R. C. 2013. Nlme: Linear and non-linear mixed-effects models. R package version 3.1-108.

Pitei, D. L., Foster, A.Edmonds, M., 1999. The effect of regular callus removal on foot pressures. J Foot Ankle Surg. 38**,** 251-5; discussion 306.

Prichasuk, S., 1994. The heel pad in plantar heel pain. The Journal of Bone and Joint Surgery 76-B**,** 140-142.

Qian, Z., Ren, L., Ding, Y., Hutchinson, J. R.Ren, L., 2013. A dynamic finite element analysis of human foot complex in the sagittal plane during level walking. PLoS One 8**,** e79424.

Qiu, T. X., Teo, E. C., Yan, Y. B.Lei, W., 2011. Finite element modeling of a 3d coupled foot-boot model. Medical Engineering & Physics 33**,** 1228-33.

R Core Team 2013. R: A language and environment for statistical computing. R foundation for statistical computing, vienna, austria. Isbn 3-900051-07-0.

Ralphs, J. R.Benjamin, M., 1994. The joint capsule: Structure, composition, ageing and disease. Journal of Anatomy 184 (Pt 3)**,** 503-9.

Muscle atlas of the extremeties, Bare Bones Books, 2011.

Riddle, D. L.Schappert, S. M., 2004. Volume of ambulatory care visits and patterns of care for patients diagnosed with plantar fasciitis: A national study of medical doctors. Foot Ankle Int. 25**,** 303-310.

Roux, W. J., Stander, N.Haftka, R. T., 1998. Response surface approximations for structural optimization. Int. J. Numer. Meth. Engng 42**,** 517-534.

Sanford, B. A., Williams, J. L., Zucker-Levin, A. R.Mihalko, W. M. 2014. Hip, knee, and ankle joint forces in healthy weight, overweight, and obese individuals during walking. In: Doyle, B., Miller, K., Wittek, A.Nielsen, P. M. F. (eds.) Computational biomechanics for medicine. Springer New York.

Sangeorzan, B. J., Mosca, V.Hansen, S. T., Jr., 1993. Effect of calcaneal lengthening on relationships among the hindfoot, midfoot, and forefoot. Foot & Ankle 14**,** 136-41.

Sarrafian, S. K., 1993. Anatomy of the foot and ankle: Descriptive, topographic, functional, second ed. J. B. Lippincott, Philadelphia, PA

Sarrafian, S. K.Topouzian, L. K., 1969. Anatomy and physiology of the extensor apparatus of the toes. The Journal of Bone and Joint Surgery 51**,** 669-679.

Schechtman, H.Bader, D. L., 1994. Dynamic characterization of human tendons. Proceedings of the Institution of Mechanical Engineers 208**,** 241-248.

Schmidt, H. K. 2009. Foot ligament mechanical properties, Master of Science, University of Washington.

Schmidt, K. H.Ledoux, W. R., 2010. Quantifying ligament cross-sectional area via molding and casting. Journal of Biomechanical Engineering 132**,** 091012-6.

Schwenninger, D., Schumann, S.Guttmann, J., 2011. In vivo characterization of mechanical tissue properties of internal organs using endoscopic microscopy and inverse finite element analysis. Journal of Biomechanics 44**,** 487-493.

Sharkey, N. A., Donahue, S. W.Ferris, L., 1999. Biomechanical consequences of plantar fascial release or rupture during gait. Part ii: Alterations in forefoot loading. Foot & ankle international / American Orthopaedic Foot and Ankle Society [and] Swiss Foot and Ankle Society 20**,** 86-96.

Sharkey, N. A.Hamel, A. J., 1998. A dynamic cadaver model of the stance phase of gait: Performance characteristics and kinetic validation. Clinical Biomechanics 13**,** 420-433.

Sigal, I. A., Yang, H., Roberts, M. D.Downs, J. C., 2010. Morphing methods to parameterize specimen-specific finite element model geometries. Journal of Biomechanics 43**,** 254-62.

Singh, N., Armstrong, D. G.Lipsky, B. A., 2005. Preventing foot ulcers in patients with diabetes. Journal of the American Medical Association 293**,** 217-228.

Song, B., Chen, W., Ge, Y.Weerasooriya, T., 2007. Dynamic and quasi-static compressive response of porcine muscle. Journal of Biomechanics 40**,** 2999-3005.

Sophia Fox, A. J., Bedi, A.Rodeo, S. A., 2009. The basic science of articular cartilage: Structure, composition, and function. Sports health 1**,** 461-8.

Spears, I. R., Miller-Young, J. E., Sharma, J., Ker, R. F.Smith, F. W., 2007. The potential influence of the heel counter on internal stress during static standing: A combined finite element and positional mri investigation. Journal of Biomechanics 40**,** 2774-2780.

Spirka, T. A., Erdemir, A., Ewers Spaulding, S., Yamane, A., Telfer, S.Cavanagh, P. R., 2014. Simple finite element models for use in the design of therapeutic footwear. Journal of Biomechanics 47**,** 2948-2955.

Spyrou, L. A.Aravas, N., 2011. Muscle-driven finite element simulation of human foot movements. Computer Methods in Biomechanics and Biomedical Engineering.

Ls-opt user's manual, Livermore Software Technology Corporation, 2010.

Stebbins, M. J. 2012. Obtaining material properties of the plantar soft tissue for a patient-specific finite element model of the foot, Master of Science, University of Washington.

Steensma, M. R., Jabara, M., Anderson, J. G.Bohay, D. R., 2006. Flexor hallucis longus tendon transfer for hallux claw toe deformity and vertical instability of the metatarsophalangeal joint. Foot Ankle Int. 27**,** 689-92.

Sun, P. C., Shih, S. L., Chen, Y. L., Hsu, Y. C., Yang, R. C.Chen, C. S., 2011. Biomechanical analysis of foot with different foot arch heights: A finite element analysis. Computer Methods in Biomechanics and Biomedical Engineering**,** 1-7.

Tadepalli, S. C., Erdemir, A.Cavanagh, P. R., 2011. Comparison of hexahedral and tetrahedral elements in finite element analysis of the foot and footwear. Journal of Biomechanics.

Tao, K., Ji, W. T., Wang, D. M., Wang, C. T.Wang, X., 2010. Relative contributions of plantar fascia and ligaments on the arch static stability: A finite element study. Biomedizinische Technik 55**,** 265-71.

Then, C., Menger, J., Benderoth, G., Alizadeh, M., Vogl, T. J., Hübner, F., et al., 2007. A method for a mechanical characterisation of human gluteal tissue. Technology and Health Care 15**,** 385-398.

Thomas, J. L., Christensen, J. C., Kravitz, S. R., Mendicino, R. W., Schuberth, J. M., Vanore, J. V., et al., 2010. The diagnosis and treatment of heel pain: A clinical practice guideline - revision 2010. The Journal of Foot and Ankle Surgery 49**,** S1-S19.

Thomas, V. J., Patil, K. M.Radhakrishnan, S., 2003a. Three-dimensional stress analysis for the mechanics of plantar ulcers in diabetic neuropathy. Medical and Biological Engineering and Computing 42**,** 230-235.

Thomas, V. J., Patil, K. M.Radhakrishnan, S., 2004. Three-dimensional stress analysis for the mechanics of plantar ulcers in diabetic neuropathy. Medical and Biological Engineering and Computing 42**,** 230-235.

Thomas, V. J., Patil, K. M., Radhakrishnan, S., Narayanamurthy, V. B.Parivalavan, R., 2003b. The role of skin hardness, thickness, and sensory loss on standing foot power in the development of plantar ulcers in patients with diabetes mellitus--a preliminary study. The international Journal of Lower Extremity Wounds 2**,** 132-9.

Tong, J., Lim, C. S.Goh, O. L., 2003. Technique to study the biomechanical properties of the human calcaneal heel pad. The Foot 13**,** 83-91.

Tong, K. B.Furia, J., 2010. Economic burden of plantar fasciitis treatment in the united states. American Journal of Orthopedics (Belle Mead, N.J) 39**,** 227-31.

Veves, A., Murray, H., Young, M.Boulton, A., 1992. The risk of foot ulceration in diabetic patients with high foot pressure: A prospective study. Diabetologia 35**,** 660-663.

Wan, L., De Asla, R. J., Rubash, H. E.Li, G., 2008. In vivo cartilage contact deformation of human ankle joints under full body weight. Journal of Orthopaedic Research 26**,** 1081-9.

Wang, Y., Li, Z.Zhang, M., 2014. Biomechanical study of tarsometatarsal joint fusion using finite element analysis. Medical Engineering & Physics 36**,** 1394-1400.

Wang, Y. N., Lee, K.Ledoux, W. R., 2011. Histomorphological evaluation of diabetic and non-diabetic plantar soft tissue. Foot Ankle Int. 32**,** 802-10.

Ward, E. D., Smith, K. M., Cocheba, J. R., Patterson, P. E.Phillips, R. D., 2003. In vivo forces in the plantar fascia during the stance phase of gait: Sequential release of the plantar fascia. Journal of the American Podiatric Medical Association 93**,** 429-42.

Wickiewicz, T. L., Roy, R. R., Powell, P. L.Edgerton, V. R., 1983. Muscle architecture of the human lower limb. Clinical Orthopaedics and Related Research**,** 275-283.

Williams, D. S.Mcclay, I. S., 2000. Measurements used to characterize the foot and the medial longitudinal arch: Reliability and validity. Physical Therapy 80**,** 864-871.

Williams, E. D. 2015. Quantifying patient-specific plantar soft tissue stiffness using magnetic resonance imaging and a hydraulic loading device, Master of Science, University of Washington (In preparation).

Williams, E. D., Stebbins, M. J., Cavanagh, P. R., Haynor, D. R., Chu, B., Fassbind, M. J., et al., 2015. Design and verification of a gated mri technique to determine mechanical properties of plantar soft tissue. Proceedings of the Institution of Mechanical Engineers, Part H: Journal of Engineering in Medicine (In preparation).

Wright, D. G.Rennels, D. C., 1964. A study of the elastic properties of plantar fascia. The Journal of Bone and Joint Surgery 46**,** 482-92.

Wu, L., 2007. Nonlinear finite element analysis for musculoskeletal biomechanics of medial and lateral plantar longitudinal arch of virtual chinese human after plantar ligamentous structure failures. Clinical Biomechanics 22**,** 221-229.

Wülker, N., Stephens, M. M.Cracchiolo, A., 2005. An atlas of foot and ankle surgery, Taylor & Francis, London, UK

Xu, C., Zhang, M. Y., Lei, G. H., Zhang, C., Gao, S. G., Ting, W., et al., 2011. Biomechanical evaluation of tenodesis reconstruction in ankle with deltoid ligament deficiency: A finite element analysis. Knee Surg Sports Traumatol Arthrosc.

Young, M. J., Cavanagh, P. R., Thomas, G., Johnson, M. M., Murray, H.Boulton, A. J., 1992. The effect of callus removal on dynamic plantar foot pressures in diabetic patients. Diabet Med 9**,** 55-7.

Yu, J., Cheung, J. T.-M., Fan, Y., Zhang, Y., Leung, A. K.-L.Zhang, M., 2008. Development of a finite element model of female foot for high-heeled shoe design. Clinical Biomechanics 23**,** S31-S38.

Zhang, D., Eggleton, C.Arola, D., 2002. Evaluating the mechanical behavior of arterial tissue using digital image correlation. Experimental Mechanics 42**,** 409-416.

Zhang, M.Mak, A. F., 1999. In vivo friction properties of human skin. Prosthetics and Orthotics International 23**,** 135-141.

Zheng, Y. P., Choi, Y. K. C., Wong, K., Chan, S.Mak, A. F. T., 2000. Biomechanical assessment of plantar foot tissue in diabetic patients using an ultrasound indentation system. Ultrasound in Med. & Biol. 26**,** 451-456.

Zhou, S., Lawson, D. L., Morrison, W. E.Fairweather, I., 1995. Electromechanical delay in isometric muscle contractions evoked by voluntary, reflex and electrical stimulation. European Journal of Applied Physiology and Occupational Physiology 70**,** 138-145.

Zysset, P. K., Edward Guo, X., Edward Hoffler, C., Moore, K. E.Goldstein, S. A., 1999. Elastic modulus and hardness of cortical and trabecular bone lamellae measured by nanoindentation in the human femur. Journal of Biomechanics 32**,** 1005-1012.

Appendix I: Response Surface Method

The Response Surface Method (RSM) is one of the metamodeling optimization techniques often used in problems involving nonlinear simulation models (Lind et al., 2005; Stander et al., 2010). The RSM method constructs global approximation of the system behavior by fitting smooth, continuous function (e.g., linear or polynomial) to the response values obtained at various points in the multi-dimensional design space. The response surfaces are subsequently used to create an approximate design “sub-problem” that can be optimized. The RSM is suited to capturing global minimum because of their smoothness and global approximation properties, local minima caused by noisy response are suppressed. An optimization procedure utilizing RSM method can be divided into four steps:

i) Experimental design

Design points located within the user-defined design space (i.e., design of experiment (DOE)) need to be appropriately selected in order to ensure that proper response surfaces can be constructed. Several DOE criteria are available (e.g., full factorial, D-optimal, Koshal and Latin Hypercube). One of the most widely used criterion is D-optimal (Roux et al., 1998; Stander et al., 2010) because of its ability to handle design regions with irregular shapes, select any number of design points and consider the same point in different iterations. The D-optimal design select subset of all possible points (often from full factorial) such that $|\boldsymbol{X}^T\boldsymbol{X}|$ term in equation A1.6 is maximized, thus minimizes the variance of the regression parameter estimates.

ii) Response surface approximation

Response surface approximation involves least square fit of a function (*f*) to the response values (*y*) dependent upon a set of design variables (*X*). The exact functional relationship between these values are as follow:

$$y = \eta(X) \tag{A1.1}$$

The exact response is approximated by equation A1.2.

$$\eta(X) \cong f(X) \tag{A1.2}$$

The approximate function (*f*) can be written as a summation of *L* terms of the basis functions (ϕ). A linear (equation A1.4a) or quadratic (equation A1.4b) approximation is commonly used. Other approximation method such as neural networks and radial basis function networks are also available (Stander et al., 2010).

$$f(X) = \sum_{i=0}^{L} a_i \phi_i(X) \tag{A1.3}$$

where

$$\phi = [1, x_1, ..., x_n]^T \text{ for linear approximation or} \tag{A1.4a}$$

$$\phi = [1, x_1, ..., x_n, x_1^2, x_1 x_2, ..., x_1 x_n, ..., x_n^2]^T \text{ for quadratic approximation} \tag{A1.4b}$$

Unknown coefficient $\boldsymbol{a} = [a_1, a_2, ..., a_L]^T$ need to be determined such that the mean square error between the approximated function and the response at design points is minimized (equation A1.5).

$$\min\left[\sum_{p=0}^{P}\left\{\left[y(x_p) - \sum_{i=1}^{L} a_i \phi_i(x_p)\right]^2\right\}\right] \tag{A1.5}$$

where *P* is the number of design points and *y* is the exact response at the design points x_i. Rewrite equation A1.5 in matrix form as $\boldsymbol{y} = \boldsymbol{X}\,\boldsymbol{a}$, where $\boldsymbol{y}$ is ($y_1, y_2, \ldots, y_P$) and $\boldsymbol{X}$ is $[X_{ui}] = [\phi_i(x_u)]$. The solution for $\boldsymbol{a}$ is:

$$\boldsymbol{a} = (\boldsymbol{X}^T \boldsymbol{X})^{-1} \boldsymbol{X}^T y \tag{A1.6}$$

iii) Optimization

After a response surface is created, an optimum point on the surface is determined. Several optimization methods, such as Leapfrog optimizer for constrained minimization (LFOPC), genetic algorithm (GA), adaptive simulated annealing (ASA) and hybrid algorithms, are available in LS-OPT. Theory behind each algorithm is beyond the scope of this study and can be found elsewhere (Goel and Stander, 2009; Holland, 1992; Kirkpatrick et al., 1983; Snyman, 2000; Stander et al., 2010). For this study, the Hybrid Adaptive Simulated Annealing (Hybrid ASA) optimization algorithm is selected. This hybrid method uses ASA algorithm to reach the basin of the global optimum quickly, then switches to Leapfrog optimizer for constrained minimization (LFOPC) method to effectively determine an optimal solution from current starting solution.

iv) Iteration

The following strategies are recommended for automating the metamodel-based optimization process (Stander et al., 2010). For the current study, sequential strategy with domain reduction is used.

Single stage

In single stage approach, a large number of design points (as many as can be afforded) are selected only once to build a complete metamodel. The method is simple but time consuming because all the simulations need to be completed in order to perform optimization.

Sequential strategy

For this approach, a small number of points are selected for each iteration and multiple iterations are performed. The effect of this strategy (e.g., selecting 10 points for 30 iterations) is sometimes equivalent to single stage approach (e.g., selecting 300 points). However, the advantage is the iterative process can be stopped when the optimization has sufficient accuracy.

Sequential strategy with domain reduction

This approach is similar to the sequential strategy, but in each iteration the domain reduction method is used to reduce the size of the region of interest. Two approaches are available for sequential strategy with the domain reduction technique; the global and the local methods. The global approach or sequential adaptive metamodeling (SAM) constructs the response surface using all available design points, including from previous iterations. This method is good for evaluating global response of the problem. Good metamodel accuracy can be expected at the optimum point and becomes worse further away from the optimum. The local approach or sequential response surface method (SRSM), which is used in this study, allows the generation of a new response surface in each iteration. Responses from previous iterations are ignored. The convergence to the optimum point is achieved by moving the center of the region of interest to the optimum point of the previous iteration as well as reducing its size.

Iterative process is usually continued until the optimal solution is determined. The process is terminated when convergence criteria, equations A1.7 and A1.8, both became active.

$$\left| \frac{f^{(k)} - f^{(k-1)}}{f^{(k-1)}} \right| < \varepsilon_f \qquad \text{(A1.7)}$$

$$\frac{\left\| x^{(k)} - x^{(k-1)} \right\|}{\left\| d \right\|} < \varepsilon_x \qquad \text{(A1.8)}$$

where ε_f denotes the objective function accuracy, ε_x refers to the design accuracy, f is the normalized mean square error (MSE), x refers to the vector of design variables, d denotes the size of the design space, and *(k)* and *(k-1)* refer to two successive iteration numbers. Values ε_f, $\varepsilon_x < 0.01$ are typically used.

References:

Goel, T.Stander, N. Adaptive simulated annealing for global optimization in LS-OPT. 7th Europian LS-DYNA Conference, 2009 Filderstadt, Germany.

Holland, J. H., 1992. Adaptation in natural and artificial systems, MIT Press, Cambridge, MA

Kirkpatrick, S., Gelatt, C. D.Vecchi, M. P., 1983. Optimization by simulated annealing. Science 220**,** 671-680.

Lind, C., Schluder, H.Winklhofer, J. Optimization methodology in structural mechanics - comparison of ls-opt and hyperstudy. The 3rd German LS-DYNA Forum, 2005 Bamberg, Germany. 29-38.

Roux, W. J., Stander, N.Haftka, R. T., 1998. Response surface approximations for structural optimization. Int. J. Numer. Meth. Engng. 42**,** 517-534.

Snyman, J. A., 2000. The lfopc leap-frog algorithm for constrained optimization. Computers & Mathematics with Applications 40**,** 1085-1096.

LS-OPT user's manual, Livermore Software Technology Corporation, 2010.

Appendix II: Digital Image Correlation

Digital image correlation (DIC) is a type of non-contact, optical deformation measurement technique based on the concepts of pattern recognition method. In 2D analysis, series of images taken by a charge-coupled device (CCD) sensor as the specimen deforms are used as inputs to a DIC software program. A typical gray scale image can be described by a discrete function $g(x, y)$ representing the light intensity value at each pixel location (x, y). Multiple subsets of the reference image (i.e., undeformed) are selected by specifying a group of control points and the size of the subset (Figure A2.1). Each subset has a unique light intensity pattern which can be described by a matrix $F(x, y)$ about the center of the subset. On the deformed image, the reference subset is assumed to exist at a new location (x^*, y^*). The deformed location (x^*, y^*) is determined by searching for light intensity pattern $F^*(x^*, y^*)$ that most closely resemble the reference distribution $F(x, y)$ using normalized cross-correlation function C (equation A2.1) (Lewis, 1995; Zhang and Arola, 2004)

$$C = \frac{\langle FF^* \rangle - \langle F \rangle \langle F^* \rangle}{\sqrt{\left\langle \left(F - \langle F \rangle\right)^2 \right\rangle \left\langle \left(F^* - \langle F^* \rangle\right)^2 \right\rangle}} \qquad \text{(A2.1)}$$

where normalized cross-correlation coefficient (C) ranges from -1 (negative correlation), 0 (no correlation) to 1 (positive correlation). The $\langle\ \rangle$ symbol indicates the mean intensity value of elements in the matrix. The search for location (x^*, y^*) of maximum correlation coefficient can be performed at pixel integer level and continued in the sub-pixel domain (require interpolation methods, such as bilinear or bicubic interpolations). In plane displacements (u, v) are determined from (x^*, y^*) and (x, y) by solving equation A2.2 (Zhang et al., 2002). Displacement measurement precision up to 0.01 pixels has been reported previously (Jacquemoud et al., 2007; Zhang and Arola, 2004).

$$\begin{aligned} u &= x^* - x \\ v &= y^* - y \end{aligned} \qquad \text{(A2.2)}$$

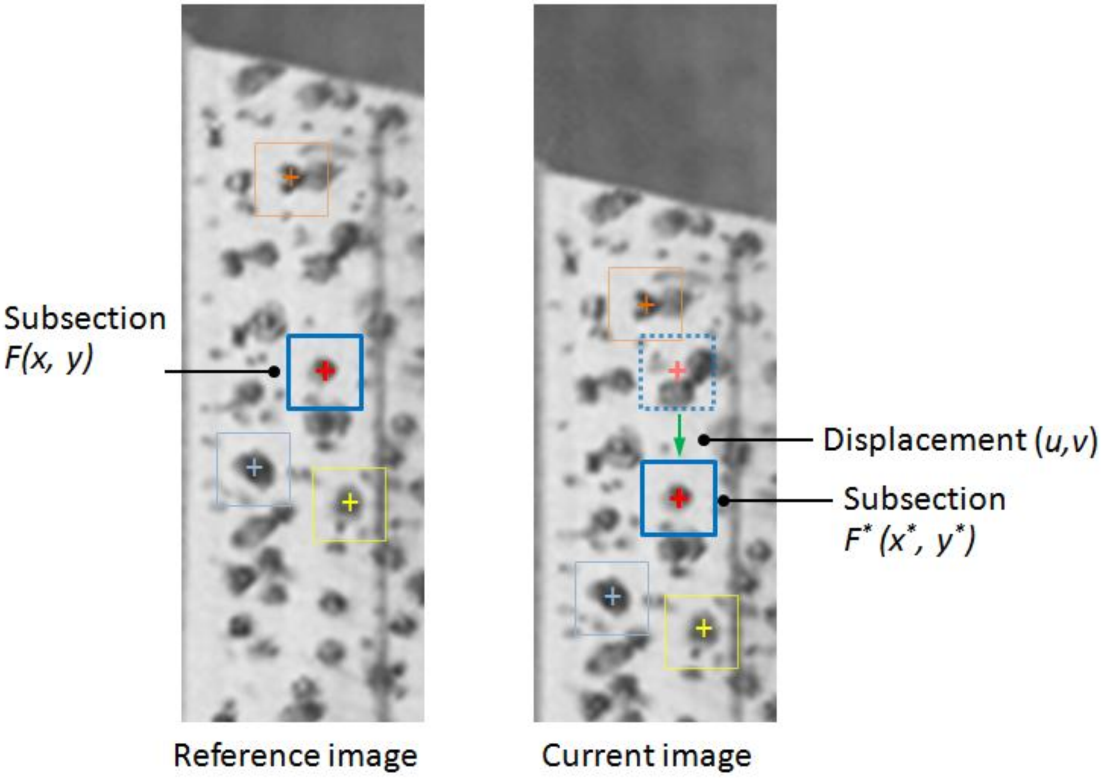

Figure A2.1: Digital image correlation (DIC) tracking of a rigid body movement

Several factors, including CCD sensor, lens, surface contrast, speckle pattern, and subset size can influence the robustness and accuracy of the DIC measurement. The CCD sensor size, effective pixel number, lens focal length control image pixel resolution, and field of view (FOV) are additional factors. Higher pixel resolution allows detection of smaller displacement and can be achieved by using a higher magnification lens (e.g., zoom or macro) and capturing a smaller FOV. Another factor affecting the DIC performance is image exposure, which is controlled by the frame rate (i.e., the shutter speed) and the lens aperture. Over and under exposed images result in wash out detail and low contrast, respectively, and potentially lead to false correlation. Random speckle pattern of black and white enamel paint is commonly used to improve the surface texture and contrast (Lauret et al., 2009; Zhang et al., 2002). It is necessary that the speckle size be smaller than the subset size in order to avoid decorrelation. A larger speckle diameter requires longer computation time due to an increased subset size.

References:

Jacquemoud, C., Bruyere-Garnier, K.Coret, M., 2007. Methodology to determine failure characteristics of planar soft tissues using a dynamic tensile test. Journal of Biomechanics 40**,** 468-475.

Lauret, C., Hrapko, M., Van Dommelen, J. A. W., Peters, G. W. M.Wismans, J. S. H. M., 2009. Optical characterization of acceleration-induced strain fields in inhomogeneous brain slices. Medical Engineering & Physics 31**,** 392-399.

Lewis, J. P., 1995. Fast template matching. Vision Interface**,** 120-123.

Zhang, D.Arola, D. D., 2004. Applications of digital image correlation to biological tissues. Journal of Biomedical Optics 9**,** 691-699.

Zhang, D., Eggleton, C.Arola, D., 2002. Evaluating the mechanical behavior of arterial tissue using digital image correlation. Experimental Mechanics 42**,** 409-416.

Appendix III: Ogden hyperelastic uni-axial stress-strain equation

The strain energy density function of a nearly-incompressible Ogden hyperelastic material is given by equation A3.1-A3.4 (LSTC, 2007).

$$W(\lambda_1, \lambda_2, \lambda_3) = \sum_{m=1}^{n} \frac{\mu_m}{\alpha_m}\left(\tilde{\lambda}_1^{\alpha_m} + \tilde{\lambda}_2^{\alpha_m} + \tilde{\lambda}_3^{\alpha_m} - 3\right) + \frac{1}{2}K(J-1)^2 \qquad \text{(A3.1)}$$

$$K = \frac{(1+v)}{3(1-2v)}\sum_{m=1}^{n}\mu_m\alpha_m \qquad \text{(A3.2)}$$

$$J = \lambda_1\lambda_2\lambda_3 \qquad \text{(A3.3)}$$

$$\tilde{\lambda}_i = J^{-1/3}\lambda_i \qquad \text{(A3.4)}$$

where $\lambda_1, \lambda_2, \lambda_3$ are the three principal stretches, the Jacobian, *J*, denotes the relative volume change, and $\tilde{\lambda}_i$ are the deviatoric principal stretches. Poisson's ratio (*v*) and hyperelastic coefficients (μ_m and α_m) are the material properties. Consider the first-order Ogden model (*n* = 1), substitute equation A3.4 into equation A3.1 yields:

$$W = \frac{\mu_1(\lambda_1\lambda_2\lambda_3)^{\frac{-\alpha_1}{3}}}{\alpha_1}\left(\lambda_1^{\alpha_1} + \lambda_2^{\alpha_1} + \lambda_3^{\alpha_1} - 3(\lambda_1\lambda_2\lambda_3)^{\frac{\alpha_1}{3}}\right) + \frac{K}{2}(\lambda_1\lambda_2\lambda_3 - 1)^2 \qquad \text{(A3.5)}$$

Three orthogonal stresses components (σ_1, σ_2, and σ_3) are defined by equation A3.6.

$$\frac{J\sigma_i}{\lambda_i} = \frac{\partial W}{\partial \lambda_i} \qquad \text{(A3.6)}$$

Substitute equation A3.5 into equation A3.6 results in:

$$\sigma_1 = \frac{\mu_1}{3J^{\left(1+\frac{\alpha_1}{3}\right)}}\left(2\lambda_1^{\alpha_1} - \lambda_2^{\alpha_1} - \lambda_3^{\alpha_1}\right) + K(J-1) \qquad \text{(A3.7)}$$

$$\sigma_2 = \frac{\mu_1}{3J^{\left(1+\frac{\alpha_1}{3}\right)}}\left(2\lambda_2^{\alpha_1} - \lambda_1^{\alpha_1} - \lambda_3^{\alpha_1}\right) + K(J-1) \tag{A3.8}$$

$$\sigma_3 = \frac{\mu_1}{3J^{\left(1+\frac{\alpha_1}{3}\right)}}\left(2\lambda_3^{\alpha_1} - \lambda_1^{\alpha_1} - \lambda_2^{\alpha_1}\right) + K(J-1) \tag{A3.9}$$

For a simplified uni-axial load, $\lambda_1 = \lambda = 1+\varepsilon$, $\lambda_2 = \lambda_3 = \sqrt{\frac{J}{1+\varepsilon}}$ and $\sigma_2 = \sigma_3 = 0$, equation A3.7-A3.9 becomes:

$$\sigma_1 = \frac{2\mu_1}{3J^{\left(1+\frac{\alpha_1}{3}\right)}}\left((1+\varepsilon)^{\alpha_1} - \left(\frac{J}{1+\varepsilon}\right)^{\frac{\alpha_1}{2}}\right) + K(J-1) \tag{A3.10}$$

$$\sigma_2 = \sigma_3 = \frac{\mu_1}{3J^{\left(1+\frac{\alpha_1}{3}\right)}}\left(\left(\frac{J}{1+\varepsilon}\right)^{\frac{\alpha_1}{2}} - (1+\varepsilon)^{\alpha_1}\right) + K(J-1) = 0 \tag{A3.11}$$

The uni-axial stress (σ_1) can be computed at each strain (ε) by substituting material properties (μ_1, α_1 and v) into equation A3.11 to solve for the Jacobian (J), then substitute J, ε and material properties into equation 3.10 and solve for σ_1.

References:

LS-DYNA keyword user's manual v971, Livermore Software Technology Corporation, 2007.

Appendix IV: Mesh Convergence Analysis

In this study, two mesh convergence analyses were conducted to determine optimal element type, element formulation and element size to ensure that the finite element (FE) solutions (e.g., force, deformation and stress) are not affected by changing these element settings. The first analysis used a simplified hindfoot model and the second analysis utilized the physiologic hindfoot model of the healthy, normal subject from Chapter 5 (Figure A4.1).

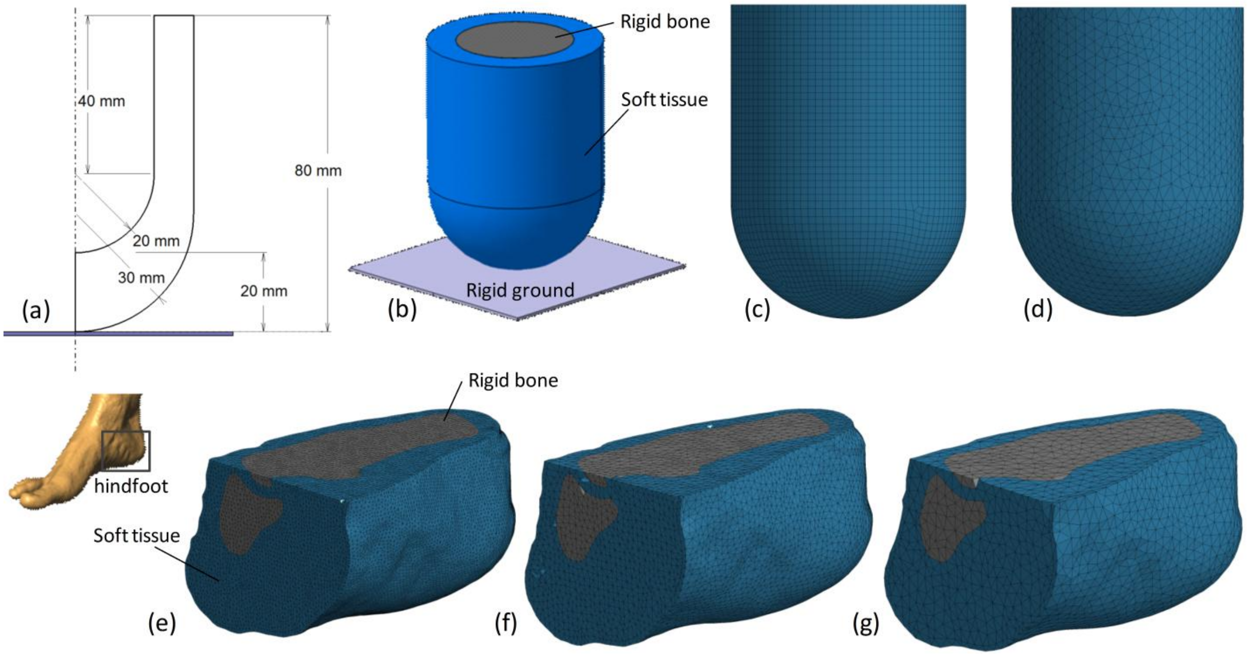

Figure A4.1: Hindfoot models used for mesh convergence analysis. (a) Cross-sectional dimension of the simplified hindfoot model. (b) The simplified hindfoot model consisted of rigid bone, rigid ground and an encapsulated soft tissue. The models were meshed with (c) hexahedral elements and (d) linear and second-order tetrahedral elements. The physiologic hindfoot models were meshed with (e) 1.5 mm, (f) 2.5 mm and (g) 4.0 mm tetrahedral elements. The model consisted of encapsulated soft tissue and a rigid calcaneus and cuboid.

A4.1 Methods

A4.1.1 Simplified hindfoot model

The simplified hindfoot model was created from two cylinders with two half-spheres on the inferior end (Figure A4.1 (a)), such that the soft tissue thickness at the centerline of the model was 20 mm (i.e., *in vivo* subcalcaneal soft tissue thickness). The rigid calcaneus was represented by the inner cylinder and half-sphere, and was fixed in all degrees of freedom. Global element size of 1.0 - 8.0 mm for the hexahedral models and 2.4 - 10.0 mm for the tetrahedral models were explored. The hexahedral models were mesh in LS-Prepost (Livermore Software, Livermore, USA) while tetrahedral models were meshed in ANSYS ICEM CFD (ANSYS Inc, Canonsburg, USA). The rigid ground was modeled with LS-DYNA (Livermore Software, Livermore, USA) rigid wall in LS-Prepost and compressed the soft tissue to 50% strain (i.e., 10 mm compression) via a prescribed displacement motion (linear ramp to the target displacement in 0.5s then hold until 1.0s). The soft tissue was modeled with the first-order Ogden hyperelastic material. Generic hindfoot material properties from Chokhandre et al. (2012) were used (μ = 0.222 kPa (after Abaqus-LS-DYNA conversion), α = 9.78 and v = 0.475).

Three element types (linear hexahedral, linear tetrahedral and second-order tetrahedral) were explored. The default LS-DYNA element formulations were used for the linear hexahedral (elform1 [constant stress solid element]) and the second-order tetrahedral (elform17 [10-noded composite tetrahedron]) models. Three element formulations for the linear tetrahedral model were investigated (elform1, elform10 [1-point tetrahedron], and elform13 [1-point nodal pressure tetrahedron for bulk forming]).

All models were solved in LS-DVNA (V971d R5.1.1). The platen reaction force, von Mises stress, hydrostatic stress and computation time from tetrahedral models were compared to the hexahedral model results (i.e., gold standard). The von Mises and hydrostatic stresses were measured by averaging four maximum stress elements. The stresses in these four elements are typically similar due to model symmetry.

A4.1.2 *In vivo* hindfoot model

The hindfoot FE model developed from an MRI compression experiment was described in Chapter 5. For this mesh convergence analysis, only linear tetrahedral element with elform13 were used.

Three global element sizes (1.5 mm, 2.5 mm and 4.0 mm) were simulated. The generic soft tissue material properties were arbitrarily selected (μ = 2.5 kPa, α = 22 and ν = 0.4999) such that the peak platen reaction force closely represent the MRI hindfoot compression (~215 N).

The predicted platen reaction force, muscle vertical displacement and skin bulging displacement were measured from a node set that represented the experimental measurement locations (Chapter 5). Note that although the model assumed generic hindfoot tissue, the material properties were assigned to the skin, fat and muscle layers, thus different tissue displacements could be measured. Computation time and simulated results from the models with element size 4.0 mm and 2.5 mm were compared to the results from the model with 1.5 mm element size (i.e., gold standard).

A4.2 Results and Discussion

A4.2.1 Simplified hindfoot model

The platen reaction force from all tetrahedral models except the linear tetrahedral with elform1 converged to within ±5% of the highly refined (element size 1.0 mm – 1.3 mm) hexahedral model solution (element size 6.5 mm for linear tetrahedral elform10, 10 mm for linear tetrahedral elform13 and 6.0 mm for second-order tetrahedral) (Figure A4.2a, Table A4.1). The hexahedral model converged to within ±5% and ±1% of the final solution at element size below 5 mm and 2.5 mm, respectively. The linear tetrahedral model with elform13 showed superior performance and converged to within ±5% of the final hexahedral solution at all element size tested and to within ±2% at element size below 4 mm. The linear tetrahedral model with elform10 also reached ±2% convergence at element size of 4.5 mm or smaller.

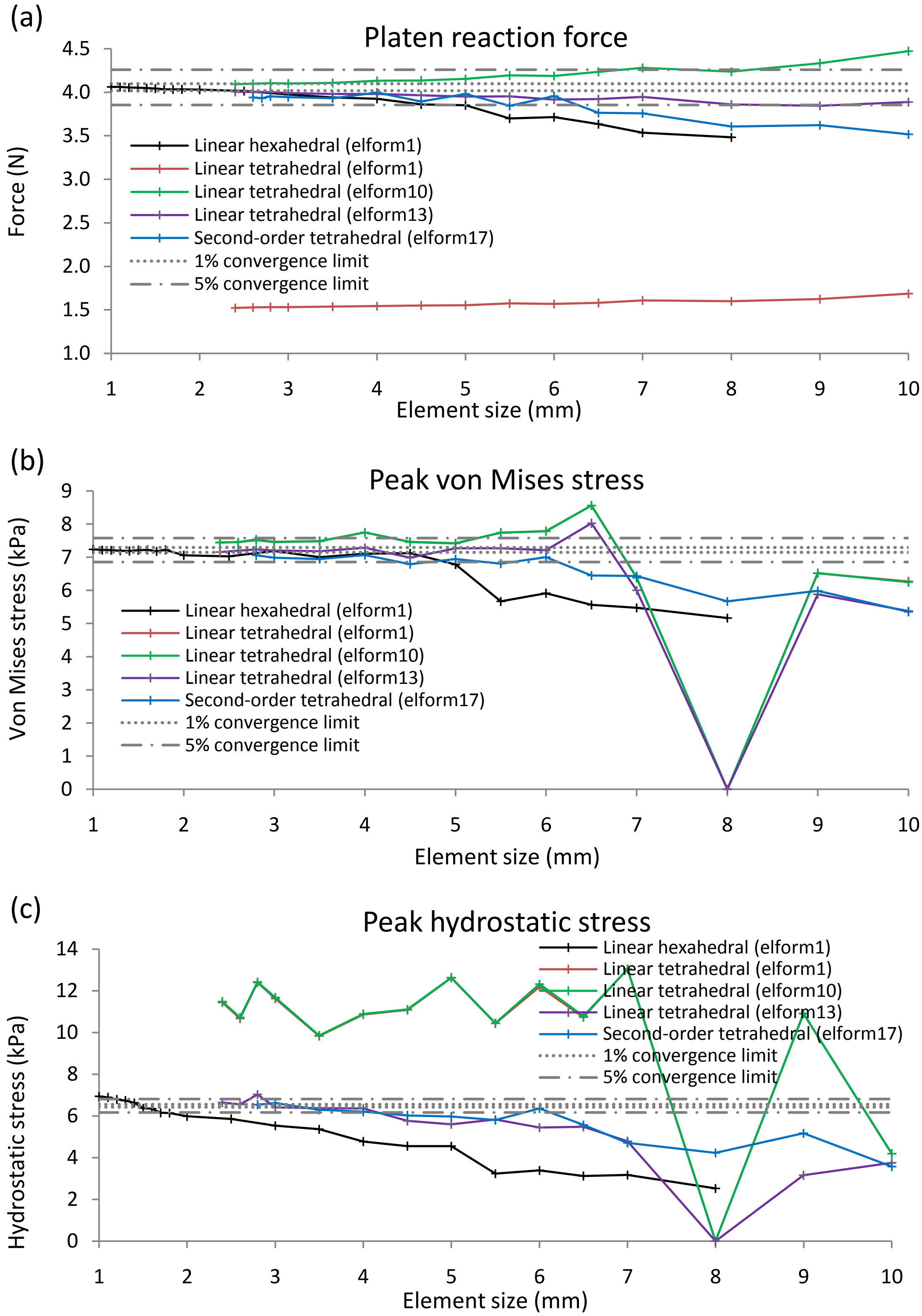

Figure A4.2: (a) Platen reaction force, (b) peak von Mises stress and (c) peak hydrostatic stress results from the simplified hindfoot mesh convergence analysis. Note that stress results from the linear tetrahedral models at 8.0 mm element size were unstable.

The predicted von Mises stress from all tetrahedral models showed convergence to within ±5% of the hexahedral model results (element size 5 mm for linear tetrahedral elform1 and 10, and 6 mm for linear tetrahedral elform13 and second-order tetrahedral) (Figure A4.2b, Table A4.1). However, only the linear tetrahedral model with elform13 converged to within ±1% (at element size 6.0 mm or smaller). The hexahedral model converged to within ±5% and ±1% of the final von Mises stress solution at element size below 4.5 mm and 1.8 mm, respectively.

The hydrostatic stress results from the hexahedral models did not converged (Figure A4.2c, Table A4.1). The linear tetrahedral model with elform13 and the second-order tetrahedral model showed ±5% convergence at element size of 4.0 and 3.5 mm, respectively. Results from other linear tetrahedral models over-estimated the hydrostatic stresses and showed oscillation in the peak values.

Using ±5% of the highly refined hexahedral model results as a convergence criteria, the simplified hindfoot models showed force and von Mises stress convergence at element size of 4.5 mm (hexahedral), 5.0 mm (linear tetrahedral elform10) and 6.0 mm (linear tetrahedral elform13 and second-order tetrahedral). At these element settings, the solving times were 48s (hexahedral), 113s (linear tetrahedral elform10), 47s (linear tetrahedral elform13) and 682s (second-order tetrahedral) (Figure A4.2, Table A4.1). Only the linear tetrahedral model with elform13 and the second-order tetrahedral model showed hydrostatic stress convergence.

Table A4.1: Number of element, simulation results (peak force, peak von Mises* and hydrostatic stresses*) and computation time from the simplified hindfoot mesh convergence analysis.

Element size (mm)	**Linear hexahedral element (elform1)**					**Number of tetrahedral element**	**Linear tetrahedral element (elform1)**				**Linear tetrahedral element (elform10)**				**Linear tetrahedral element (elform13)**				**Second-order tetrahedral element (elform1)**			
	Number of element	**Force (N)**	**V-M Stress (kPa)**	**H-S Stress (kPa)**	**Time (s)**		**Force (N)**	**V-M Stress (kPa)**	**H-S Stress (kPa)**	**Time (s)**	**Force (N)**	**V-M Stress (kPa)**	**H-S Stress (kPa)**	**Time (s)**	**Force (N)**	**V-M Stress (kPa)**	**H-S Stress (kPa)**	**Time (s)**	**Force (N)**	**V-M Stress (kPa)**	**H-S Stress (kPa)**	**Time (s)**
10.0	n/a	n/a	n/a	n/a	n/a	1,592	1.69	6.27	4.19	9	4.47	6.25	4.20	10	3.89	5.38	3.75	8	3.52	5.36	3.57	98
9.0	n/a	n/a	n/a	n/a	n/a	2,628	1.62	6.52	10.91	18	4.33	6.52	10.90	13	3.84	5.88	3.15	13	3.62	5.99	5.17	194
8.0	408	3.48	5.17	2.53	14	3,558	1.60	n/a	n/a	29	4.24	n/a	n/a	17	3.86	n/a	n/a	23	3.61	5.67	4.23	237
7.0	544	3.54	5.48	3.18	13	5,224	1.61	6.39	13.03	36	4.28	6.38	13.03	24	3.95	6.01	4.78	29	3.76	6.44	4.70	282
6.5	666	3.63	5.57	3.11	29	7,083	1.58	8.56	10.73	57	4.23	8.57	10.78	38	3.92	8.03	5.48	49	3.76	6.45	5.57	568
6.0	808	3.72	5.91	3.39	24	7,876	1.57	7.79	12.19	66	4.19	7.79	12.32	42	3.92	7.22	5.45	47	3.96	7.01	6.36	682
5.5	864	3.70	5.67	3.24	25	10,916	1.57	7.74	10.43	120	4.19	7.74	10.44	76	3.95	7.27	5.83	93	3.84	6.81	5.80	1,171
5.0	1,349	3.85	6.79	4.55	50	14,860	1.55	7.42	12.61	188	4.15	7.42	12.62	113	3.95	7.27	5.60	122	3.98	6.95	5.96	1,920
4.5	1,620	3.86	7.13	4.55	48	20,856	1.55	7.47	11.08	231	4.13	7.46	11.10	148	3.97	6.99	5.77	176	3.89	6.79	6.02	1,968
4.0	2,694	3.92	7.11	4.77	108	28,871	1.54	7.76	10.86	330	4.13	7.75	10.88	233	3.98	7.29	6.36	289	4.00	7.07	6.20	2,457
3.5	3,696	3.94	7.00	5.36	185	44,130	1.54	7.49	9.82	637	4.11	7.48	9.85	404	3.98	7.18	6.37	518	3.93	6.95	6.29	8,724
3.0	5,074	3.97	7.19	5.53	290	68,232	1.53	7.47	11.62	1,157	4.10	7.46	11.67	761	3.99	7.21	6.41	956	3.94	6.99	6.61	6,542
2.8	n/a	n/a	n/a	n/a	n/a	82,698	1.53	7.54	12.39	1,693	4.11	7.52	12.42	1,108	4.00	7.24	7.03	1,319	3.95	7.06	6.54	9,799
2.5	9,917	4.02	7.03	5.85	770	n/a	n/a	n/a	n/a	n/a	n/a	n/a	n/a	n/a	n/a	n/a	n/a	n/a	n/a	n/a	n/a	n/a
2.4	n/a	n/a	n/a	n/a	n/a	132,039	1.52	7.45	10.67	3,493	4.09	7.44	11.47	2,246	4.01	7.16	6.64	2,854	n/a	n/a	n/a	n/a
2.0	17,342	4.03	7.06	5.99	1,613	n/a	n/a	n/a	n/a	n/a	n/a	n/a	n/a	n/a	n/a	n/a	n/a	n/a	n/a	n/a	n/a	n/a
1.8	25,849	4.03	7.22	6.14	2,762	n/a	n/a	n/a	n/a	n/a	n/a	n/a	n/a	n/a	n/a	n/a	n/a	n/a	n/a	n/a	n/a	n/a
1.7	28,631	4.03	7.18	6.15	3,610	n/a	n/a	n/a	n/a	n/a	n/a	n/a	n/a	n/a	n/a	n/a	n/a	n/a	n/a	n/a	n/a	n/a
1.6	36,220	4.03	7.22	6.35	3,993	n/a	n/a	n/a	n/a	n/a	n/a	n/a	n/a	n/a	n/a	n/a	n/a	n/a	n/a	n/a	n/a	n/a
1.5	39,964	4.04	7.21	6.37	5,194	n/a	n/a	n/a	n/a	n/a	n/a	n/a	n/a	n/a	n/a	n/a	n/a	n/a	n/a	n/a	n/a	n/a
1.4	54,780	4.05	7.19	6.63	7,112	n/a	n/a	n/a	n/a	n/a	n/a	n/a	n/a	n/a	n/a	n/a	n/a	n/a	n/a	n/a	n/a	n/a
1.3†	66,356	4.05	7.20	6.73	8,094	n/a	n/a	n/a	n/a	n/a	n/a	n/a	n/a	n/a	n/a	n/a	n/a	n/a	n/a	n/a	n/a	n/a
1.2†	82,490	4.06	7.22	6.80	10,443	n/a	n/a	n/a	n/a	n/a	n/a	n/a	n/a	n/a	n/a	n/a	n/a	n/a	n/a	n/a	n/a	n/a
1.1†	112,660	4.06	7.22	6.88	13,541	n/a	n/a	n/a	n/a	n/a	n/a	n/a	n/a	n/a	n/a	n/a	n/a	n/a	n/a	n/a	n/a	n/a
1.0†	146,638	4.06	7.24	6.94	16,492	n/a	n/a	n/a	n/a	n/a	n/a	n/a	n/a	n/a	n/a	n/a	n/a	n/a	n/a	n/a	n/a	n/a

* V-M and H-S denotes von Mises and hydrostatic stresses, respectively.

† Platen reaction force and von Mises stress results from linear hexahedral models at 1.0 mm to 1.3 mm element size were averaged to determine the converged values (i.e., gold standard). The converged hydrostatic stress value was determined from the second-order tetrahedral model.

n/a indicated that no simulation was performed. For tetrahedral models at 8.0 mm element size, the von Mises stress results were unstable and excluded from analysis.

The mesh convergence analysis results using the simplified hindfoot model suggested that linear tetrahedral model with elform13 had superior performance in terms of hydrostatic stress prediction, optimal element size and solving time compared to other linear tetrahedral and second-order tetrahedral models. The tetrahedral model with elform13 also showed superior performance compared to the linear hexahedral model when considered hydrostatic stress, model generation time and optimal element size.

A4.2.2 *In vivo* hindfoot model

The global element size refinement from 4.0 mm to 2.5 mm and 1.5 mm showed less than 3% change in platen force, muscle vertical displacement and skin bulging displacement root mean square (RMS) error (Figure A4.3). However, the computation time increases exponentially at smaller element size (15,059s, 61,259s and 303,282s for models with element size of 4.0 mm, 2.5 mm and 1.5 mm, respectively). The global element size of 2.5 mm was found to be a good compromise between the ability to capture geometric details (e.g., skin thickness and small curvatures) and reasonable computation time.

A4.3 Conclusion

Based on this mesh convergence analysis, the linear tetrahedral element with elform13 and global element size of 2.5 mm were selected for this study.

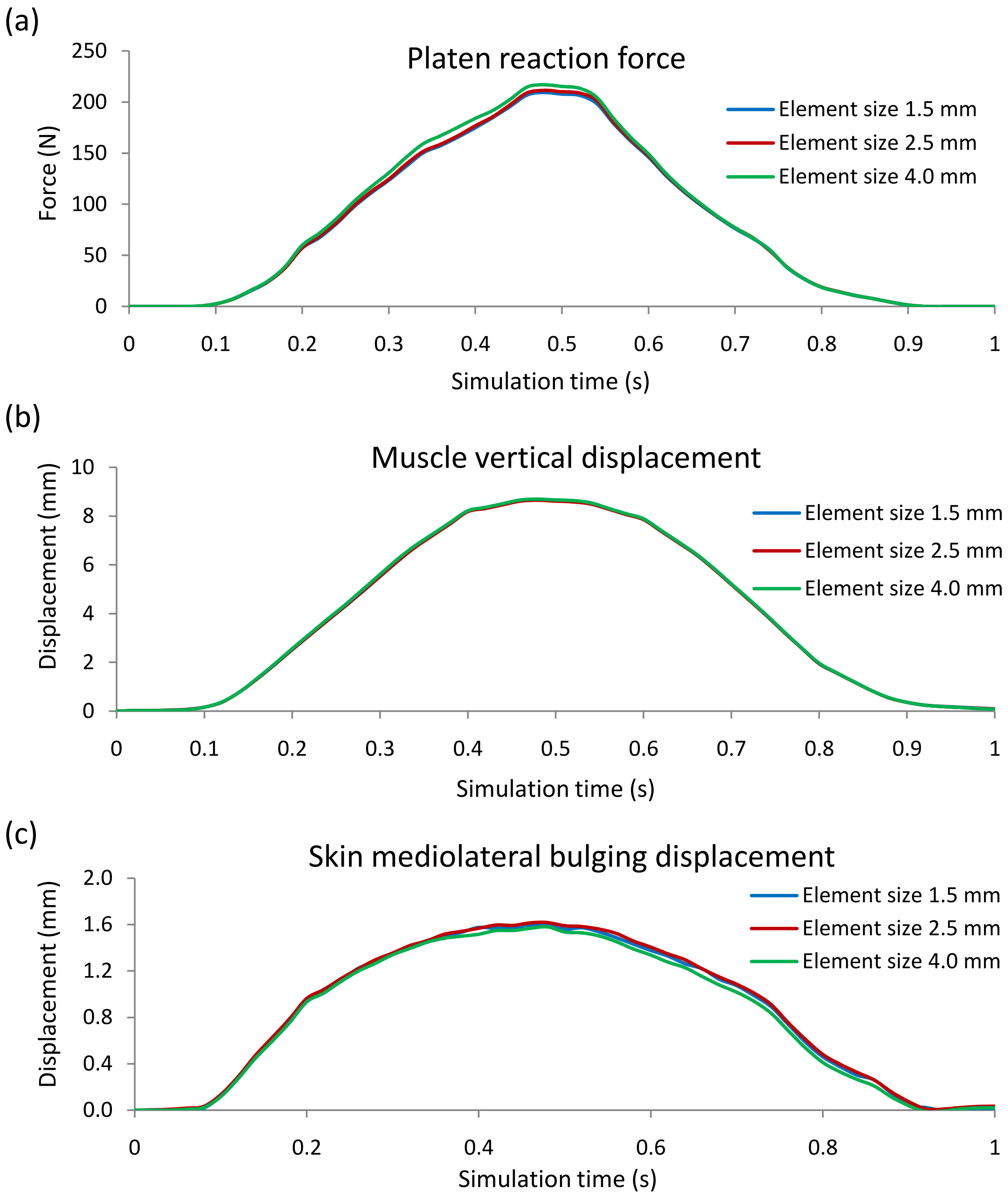

Figure A4.3: (a) Platen reaction force, (b) muscle vertical displacement and (c) skin bulging displacement results from an *in vivo* hindfoot model using three element sizes (4.0 mm, 2.5 mm and 1.5 mm).

References:

Chokhandre, S., Halloran, J. P., Van Den Bogert, A. J.Erdemir, A., 2012. A three-dimensional inverse finite element analysis of the heel pad. Journal of Biomechanical Engineering 134**,** 031002-9.

VITA

Vara Isvilanonda was born in Seattle, Washington and grew up in Bangkok, Thailand. After receiving his Bachelor of Engineering degree (first-class honours) from Chulalongkorn University in Bangkok in 2007, he went back to Seattle to pursue graduate education at the University of Washington. He earned his Master of Science in Mechanical Engineering in 2009 and Doctor of Philosophy in Mechanical Engineering in 2015.